Dynamics of quasi-two-dimensional turbulent jets

Julien Rémy Dominique Gérard Landel

Churchill College
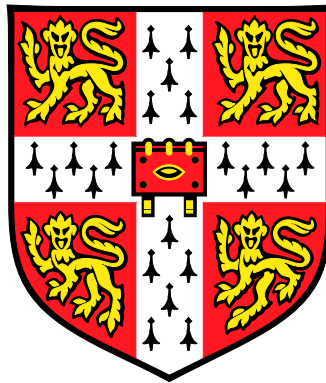
A dissertation submitted for the degree of Doctor of Philosophy

Department of Applied Mathematics and Theoretical Physics

and

BP Institute

The University of Cambridge

May 2012

Dynamics of quasi-two-dimensional turbulent jets

Julien Rémy Dominique Gérard Landel

Abstract

The study of quasi-two-dimensional turbulent jets is relevant to chemical reactors, the coking process in oil refinement, as well as rivers flowing into lakes or oceans. In the event of a spillage of pollutants into a river, it is critical to understand how these agents disperse with the flow in order to assess damage to the environment.

For such flows, characteristic streamwise and cross-stream dimensions can be much larger than the fluid-layer thickness, and so the flow develops in a confined environment. When the distance away from the discharge location is larger than ten times the fluid-layer thickness, the flow is referred to as a quasi-two-dimensional jet.

From experimental observations using dyed jets and particle image velocimetry, we find that the structure of a quasi-two-dimensional jet consists of a high-speed meandering core with large counter-rotating eddies developing on alternate sides of the core. The core and eddy structure is self-similar with distance from the discharge location. The Gaussianity of the cross-stream distribution of the time-averaged velocity is due, in part, to the sinuous instability of the core.

To understand the transport and dispersion properties of quasi-two-dimensional jets we use a time-dependent advection–diffusion equation, with a mixing length hypothesis accounting for the turbulent eddy diffusivity. The model is supported by experimental releases of dye in jets or numerical releases of virtual passive tracers in experimentally-measured jet velocity fields.

We consider the statistical properties of this flow by releasing and then tracking large clusters of virtual particles in the jet velocity field. The probability distributions of two-point properties (such as the distance between two particles) reveal large streamwise dispersion. Owing to this streamwise dispersive effect, a significant amount of tracers can be transported faster than the speed predicted by a simple advection model.

Using potential theory, we determine the flow induced by a quasi-two-dimensional jet confined in a rectangular domain. The streamlines of the induced flow predicted by the theory agree with experimental measurements away from the jet boundary.

Finally, we investigate the case of a quasi-two-dimensional particle-laden jet. Depending on the bulk concentration of dense particles, we identify different flow regimes. At low concentrations, the jet features the same core and eddy structure observed without the particles, and thus quasi-two-dimensional jet theory can apply to some extent. At larger concentrations, we observe an oscillating instability of the particle-laden jet.

Preface

This thesis, which is submitted for the degree of Doctor of Philosophy at Churchill College, University of Cambridge, describes work carried out from January 2009 to May 2012 in the Department of Applied Mathematics and Theoretical Physics and the BP Institute, University of Cambridge. This dissertation is the result of my own work and includes nothing which is the outcome of work done in collaboration, except where specifically indicated in the text. No part of this work has been, or is being submitted for any other qualification at this or any other university.

Acknowledgements

First of all, I would like to express my deep appreciation to my supervisor Dr Colm Caulfield and my advisor Prof. Andy Woods for giving me the opportunity to pursue my PhD research on this fascinating project, here at the University of Cambridge. I am particularly grateful for the constant support and useful advice I have received from Dr Colm Caulfield. He has taught me the rigour of mathematical modelling, and how it can be applied to physical problems. I wish to thank Prof. Andy Woods for all the fruitful and enthusiastic discussions. His unique way of simplifying any complex problem into its essential components will continue to serve me as a guide throughout my professional career.

I am very grateful to Dr Stuart Dalziel for his invaluable help in experimental and technical matters, and in the use of DigiFlow. He has always made himself available at any time during my PhD. His knowledge and expertise in experimental Fluid Dynamics is a wonderful source of inspiration.

I would like to extend my gratitude to my friend Samuel Rabin for helping me resolve numerous mathematical problems and equations throughout my PhD. I would like to thank my friends Megan Davies Wykes, Alan Jamieson, Antoine Julia, Hugh Lund and Dr Ben Maurer for proofreading parts of this document. I am also grateful to all my colleagues and friends at the G.K. Batchelor lab and

CONTENTS

List of Figures

CHAPTER 1

OVERVIEW

In turbulent jets, fluid is driven by momentum from an orifice into an environment filled with similar fluid. The complexity of this flow, which has been studied for more than 80 years (see e.g. List, 1982, for a detailed review), resides in its turbulent nature. Turbulence develops due to a shear instability at the boundary between the jet fluid and the ambient fluid. The transition of the flow from laminar to turbulent typically occurs at a Reynolds number $Re = bU/\nu$ (where b is the characteristic width of the jet, U is the jet characteristic streamwise velocity and ν is the kinematic viscosity of the fluid) of the order of 3000. From the equations of motion, the momentum flux is approximately conserved (see e.g. Kotsovinos, 1978, for a discussion on the conservation of momentum in turbulent jets), while its mean kinetic energy is dissipated by turbulence. Momentum spreads laterally due to entrainment of ambient fluid in the jet. The entrainment process is governed by the large-scale turbulent structures in the flow and is self-similar in the streamwise direction.

The capacity of turbulent jets to entrain ambient fluid and mix it efficiently with jet fluid accounts in large part for the attention this flow has received in both the scientific community and the industrial world. Also, behind the apparent simplicity of the jet mean motion lies the fascination for the elusive underlying physics of turbulence. Whether for their dilution properties, their efficient mixing properties or the thrust they can provide, jets have been used in various industrial applications, such as waste water disposal (Yannopoulos, 2006), chemical reactors (Jirka & Harleman, 1979), or as a means of propulsion (Stanley, Sarkar & Mellado, 2002). In geophysical flows, turbulent jets are, for instance, relevant to the study of explosive volcanic eruptions, where a mixture of gas, fluid lava and solid particles is initially driven by momentum out of the crater (Woods & Caulfield, 1992).

In this study we are interested in a particular type of turbulent jet called a quasi-two-dimensional steady turbulent jet (which we refer to, hereafter, as a quasi-two-dimensional jet). Giger, Dracos & Jirka (1991) gave the first description of quasi-two-dimensional jets (earlier studies of bounded plane jets include Foss & Jones, 1968; Holdeman & Foss, 1975, who focused on the near field of the flow). They observed that, in the far field of a plane turbulent jet confined between two close boundaries separated by a gap width W, the flow develops into a meandering core with large counter-rotating eddies growing on alternate sides of the core. A quasi-two-dimensional jet designates the region of the flow (starting from $z \approx 10W$, with z the streamwise distance from the source) where the meandering core and the large growing eddies appear. The sinuous instability of the jet is due to lateral transverse shear (Jirka & Uijttewaal, 2004). Dracos, Giger & Jirka (1992) found an inverse cascade of quasi-two-dimensional turbulence, which affects not only the structure of the flow but also transport, dispersion and mixing properties. The aim of this thesis is to investigate experimentally and theoretically the transport, dispersion and mixing properties of quasi-two-dimensional jets.

In figure 1.1(a), we show a picture of a typical quasi-two-dimensional dyed jet ($Re \approx 4000$) produced in our experimental apparatus (whose gap width is $W = 1$ cm). As we can see, for $z > 10$ cm, the jet meanders and large eddies form on alternate sides of the core. The same core and eddy structure has been observed in geophysical flows, such as rivers discharging into lakes or oceans. At the discharge location, the depth of a river is often much smaller than the other
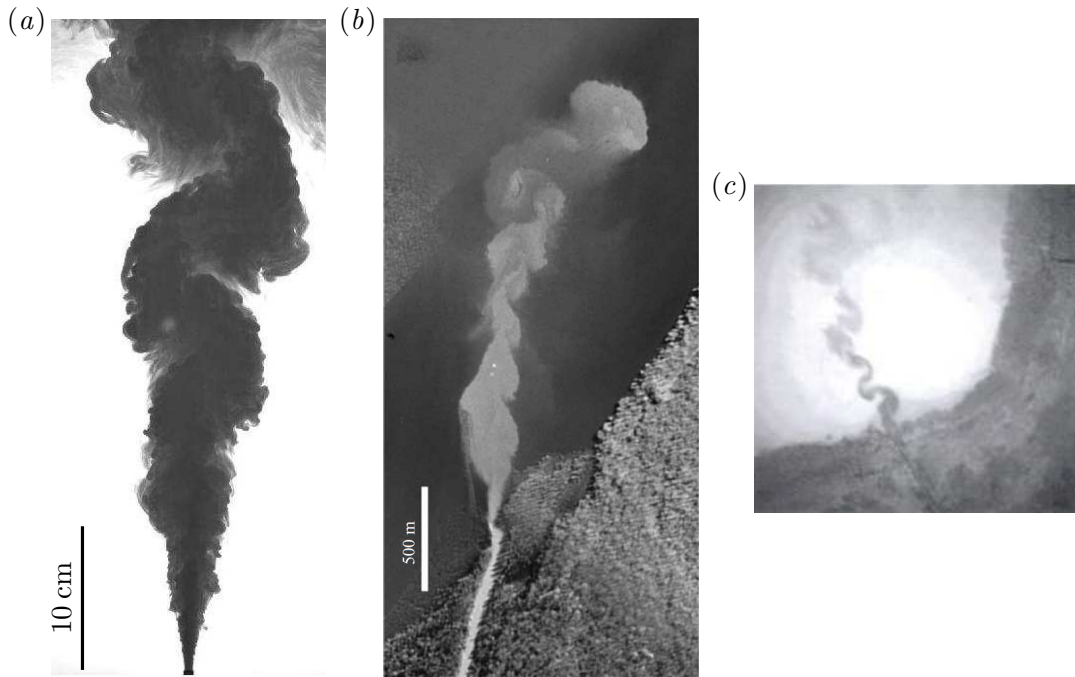
FIGURE 1.1: Meandering quasi-two-dimensional jets in the laboratory and in nature: (*a*) grey-scale picture of a dyed steady quasi-two-dimensional turbulent jet ($Re \approx 4000$) rising in our experimental apparatus; (*b*) photograph of a channel ($Re \approx 10^7$) discharging from the Lower Mississippi River (near Baton Rouge, LA, USA) into an oxbow lake, Image Source: 1998 US Geological Survey Digital Ortho-Quarter Quadrangle; (*c*) photograph of a river ($Re \approx 10^7$) flowing into Balaton Lake, Hungary (Jirka & Uijttewaal, 2004). In (*b*) and (*c*), the meanders are made visible by the sediment transported by the flow.

two characteristic dimensions of the environment in the horizontal plane. Thus, as depicted in figures 1.1(*b*) and 1.1(*c*), a river flow can develop into a quasi-two-dimensional jet flow. In figures 1.1(*b*) and 1.1(*c*), the core and eddy structures, displayed by the two rivers discharging into lakes ($Re \approx 10^7$), are revealed by the sediment transported by the flow.

The study of river flows is relevant to coastal engineering problems, such as sediment transport and coastal erosion (Joshi & Taylor, 1983), as well as environmental pollution. In the event of a spillage of pollutants in rivers, the prediction and monitoring of the transport and dispersion of the pollutants is crucial. Accurate models of the flow, tested against experimental evidence, are therefore needed to control this type of environmental pollution. The main objective of this thesis is to address these issues.

We compare the flow of a river discharging into a large basin with a (laboratory)

quasi-two-dimensional jet. In Chapter 2, we analyze and model the time-averaged velocity field of quasi-two-dimensional jets. We present a quantitative description of the characteristic core and eddy structure. We discuss the implications of this core and eddy structure on the velocity field and the entrainment mechanism of the flow. Based on this analysis, we propose a model, in Chapter 3, for the transport and dispersion of passive tracers in the flow. This model is derived from a general effective advection–diffusion equation, using a mixing length hypothesis to model the turbulent eddy diffusivity. The theoretical predictions are then compared with experimental data in Chapter 4. We also study the statistical significance of the experimental data, and describe a method, based on these data, to assess pollution risks in quasi-two-dimensional jet flows. In Chapter 5, we explore further the turbulent relative dispersion mechanisms of the core and eddy structures using two-point statistical analysis. Then, Chapter 6 presents a potential model for the flow induced by quasi-two-dimensional jets in a rectangular domain. We study the impact of the induced flow on the jet. In Chapter 7, we investigate particle-laden jets confined in a quasi-two-dimensional environment. We compare the case of a dilute particle-laden jet (i.e. a particle-laden jet with a small bulk concentration of particles) with a particle-free quasi-two-dimensional jet. Finally, we summarize the main findings of this thesis in Chapter 8 and discuss future work.

The results presented in Chapter 2 have been published in Landel, Caulfield & Woods (2012a). Most of the results described in Chapters 3 and 4 have been submitted for publication in *Journal of Fluid Mechanics*, in an article by Landel, Caulfield & Woods (2012b, *sub judice*). We adopt a similar structure in every chapter, except in Chapters 3 and 4 which have a combined structure. The problem studied in the chapter is introduced in the first section, which also includes a detailed review of past studies, and the last section is a conclusion of the chapter.

MEANDERING DUE TO LARGE EDDIES AND
THE STATISTICALLY SELF-SIMILAR DYNAMICS
OF QUASI-TWO-DIMENSIONAL JETS

2.1 Introduction

The study of turbulent plane jets is relevant to a wide variety of problems where both qualitative and quantitative knowledge of the concentration in time and space of tracers transported by the jet is needed (Kotsovinos, 1975). In many industrial applications, effluents, waste or even pollutants are released into large basins such as lakes or oceans. The source of the discharge can be rivers (see e.g. Rowland, Stacey & Dietrich, 2009, and references therein) or multiport diffusers (for an extensive study, see Jirka, 2006). In both situations, characteristic horizontal dimensions are much larger than the fluid-layer thickness and the flow

develops in a confined environment. Early experimental studies of bounded plane jets by Foss & Jones (1968) and Holdeman & Foss (1975) showed the influence of secondary flows on the mean flow. However, as Giger *et al.* (1991) and Dracos *et al.* (1992) pointed out, these secondary flows disappear beyond a distance of 10 flow thicknesses. The present work focuses on this far-field region ($z/W \geq 10$, where z is in the flow direction and W is the fluid-layer thickness), where the jet has been observed to meander due to the development of large eddies that grow on its sides. In this far-field region, the initially planar two-dimensional jet is referred to as a quasi-two-dimensional jet because of the influence of the spanwise restriction on the flow. The key characteristic of quasi-two-dimensional jets is the development of an instability (see Chen & Jirka, 1998, for a linear stability analysis of shallow-water jets) featuring large planar counter-rotating eddies. Dracos *et al.* (1992) noted that the spanwise distribution of the velocity was approximately uniform. Moreover, they found that in the far field the mean properties of the jet remained unchanged and turbulent energy was transferred to large scales thus indicating an inverse cascade characteristic of quasi-two-dimensional turbulence. Dracos *et al.* (1992) observed and studied the significance of large coherent eddy structures in the jet. However, using only point measurements, they could not provide a complete dynamical study of these structures. Recently, Shinneeb, Bugg & Balachandar (2011) conducted a statistical analysis of large vortical structures in shallow-water jets using particle image velocimetry. However, their layer thickness ($W \sim 5$–$15\,d$) was such that the flow evolution was inherently three-dimensional (albeit confined), and they did not focus on the far-field region because their measurements were taken only up to $z/W \leq 16$. Their study was also uncorrelated in time, and so they were unable to identify the inherent time dependence of the flow quantitatively.

We believe that a study of quasi-two-dimensional jets in the regime identified by Dracos *et al.* (1992) is necessary to assess the impact of the characteristic flow structures on the mixing, dispersion and diffusion of tracers in shallow jets, as suggested by Jirka (2001). For instance, undiluted patches of pollutants carried by a river discharging into the ocean can be disastrous for the local ecology. Information about the size, speed and typical travel distances of these patches is therefore crucial. To address this problem, we analyse the far field of a confined plane jet using particle image velocimetry. With a fully resolved velocity field in time and

space, we can characterize the jet structure phenomenologically. We are particularly interested in understanding quantitatively the relationship between the large-scale, and inevitably transient, flow structures and the long-time-averaged mean properties of the plane jet.

The rest of this chapter is organized as follows. In § 2.2 we describe the experimental procedure. In § 2.3 we then provide a qualitative overview of the flow structures observed from dyed-jet experiments and instantaneous velocity fields, while in § 2.4 we compare measurements of the time-averaged velocity field with classical theories for two-dimensional plane jets. In § 2.5 we present a quantitative study of the flow structures, in particular by tracking the large eddies as they interact with the high-speed core. We discuss how the frequency of occurrence of the eddies changes with distance due to eddy merger. The study of the probability density function of the core shows that the time-averaged mean distribution of the velocity is due to the large-scale dynamics of the core and eddy structure. Finally in § 2.6 we draw our conclusions.

2.2 Experimental procedure

The experimental apparatus is shown schematically in figure 2.1. Water jets were discharged vertically upwards in a $1\,\text{m}$ $(L) \times 0.01\,\text{m}$ $(W) \times 1\,\text{m}$ (H) tank made of $10\,\text{mm}$ thick Perspex sheets. An aluminium structure, made of two vertical beams located $0.4\,\text{m}$ apart on each side of the jet axis and one horizontal beam located $0.8\,\text{m}$ above the nozzle, was added on each side of the tank to increase the rigidity of the walls and ensure a uniform gap width. Two overflows on the side of the tank maintained a constant water depth at $0.915\,\text{m}$. The flow was driven by a constant-head tank and discharged via a $0.1\,\text{m}$ circular rigid tube of aspect ratio 20, leading to a $5\,\text{mm}$ $(d) \times 10\,\text{mm}$ $(W) \times 20\,\text{mm}$ chamber and finally into the tank. The aspect ratio of the tube was deemed sufficient to suppress any swirl in the flow. The flow rate was controlled through a valve and measured with a precision balance and a stopwatch for each experiment. The flow rate was found to be consistent in time with an accuracy of approximately $1\,\%$. We conducted two distinct sets of experiments using two qualitatively different techniques: dye tracking and particle image velocimetry (PIV).

7
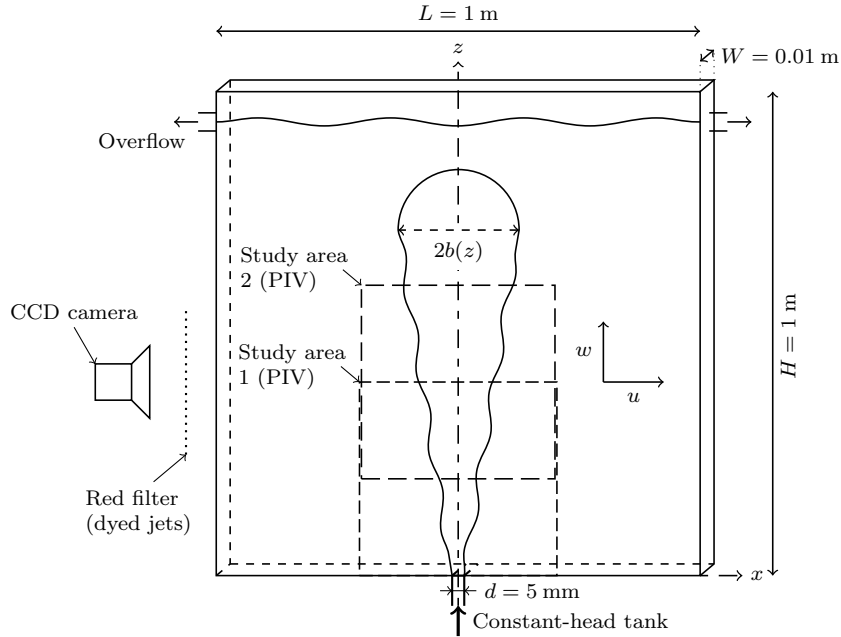
FIGURE 2.1: Schematic diagram of the experimental apparatus. The two PIV study areas are shown with overlapping dashed lines.

2.2.1 Dye tracking experiments

For the dye tracking experiments, we filled the tank with fresh tap water. We injected dark blue food dye through a needle placed $0.2\,\mathrm{m}$ upstream of the nozzle. Simultaneously, we pumped the same volume of fluid out to minimize the disturbance introduced into the flow. Also, we injected the dye after the flow reached a steady state in the tank. We used diffuse ambient lighting for these experiments. A red filter was placed between the objective of the camera and the tank, as shown in figure 2.1, to increase the contrast between the jets and the background. The flow motion was recorded with a high-speed 8 bit grey-scale camera (Fastcam SA1.1 – Photron), mounted with a $62\,\mathrm{mm}$ focal-length lens. We analysed 40 dyed jets with jet Reynolds number $2280 \leq Re_j = dw_s/\nu \leq 4030$, where w_s is the source velocity and ν is the kinematic viscosity of water, using the software code DigiFlow (Sveen & Dalziel, 2005). We determined the location of the edge of each dyed jet through an intensity criterion. Since the contrast between the dyed surface and the background was very strong but not saturated, the edge of the jet was very sharp.

2.2.2 Particle image velocimetry experiments

For PIV experiments the tank was filled with water mixed with Pliolite VTAC particles of average diameter 0.23 mm, which served as passive fluid tracers for the PIV. Approximately 2 mL of rinsing agent (Finish® rinse aid) was added to the mixture to prevent aggregation of Pliolite particles. The small change in surface tension had no influence on the measurements. The choice of this particle size depended on both hydrodynamic and optical criteria (see e.g. Drayton, 1993). We find that the particle diameter is of the order of the smallest Kolmogorov length scale found in the flow, $\eta_K \approx 0.2$ mm. Although this size is not optimal to study small-scale turbulence, it was the minimum size that could be detected by the image software while also capturing the largest length scales in the flow. The particle Stokes number based on the Kolmogorov time scale was $Stk_K \leq 10^{-1}$ (see Xu & Bodenschatz, 2008), which guaranteed that these particles followed the fluid motion closely. The particle concentration was kept relatively uniform at approximately 1.7×10^{-5} by volume due to the turbulence in the tank. Since the particle concentration was smaller than 10^{-3} by volume, particle–particle interactions and any changes in the fluid viscosity were insignificant (see Fung, 1990, for more discussion). We adjusted the water density to match the particle density of 1.03 g cm^{-3} by adding 35g of salt per litre of water. At rest, the particle distribution remained unchanged over 18 hours, thus confirming that the particles were neutrally buoyant. The mixture of salt water and particles recirculated in the experimental set-up in order to have identical conditions (particle concentration, water density and water temperature) for each experiment.

We performed the PIV experiments in a dark room. Two 1 kW filament photographic lamps, each mounted with a long focal-length spherical lens to focus the filament into a sheet, illuminated the tank from above through a 5 mm slit centred on the mid-plane ($y = 0$). Every effort was made to keep the width of the light sheet constant and smaller than the gap width in order to attenuate reflection issues with the tank walls. This also meant that we could not make any measurements away from the mid-plane ($y = 0$) because as we moved the light sheet closer to the wall in the narrow gap, reflection at the wall perturbed the measurements. From image inspection, the number of particles that appeared much slower than the rest, probably because they were trapped in the boundary layers, was sufficiently small (of the order of 10 %) not to affect the imaging analysis and corrupt

the computation of the velocity field. We recorded the flow motion using the same high-speed camera as described above. The camera filmed two $0.4\,\mathrm{m} \times 0.4\,\mathrm{m}$ study areas centred on the jet axis (as shown in figure 2.1). The frequency of image acquisition was set at 500 frames per second for a duration of $10.9\,\mathrm{s}$ for study area 1 and at 250 frames per second for a duration of $21.8\,\mathrm{s}$ for study area 2. The acquisition frequency was much higher than the largest Kolmogorov frequency scale. Moreover, the length of the video was long enough to compute meaningful temporal averages. Study area 1 covered a height from $z = 0$ to $0.4\,\mathrm{m}$, while study area 2 covered a height from $z = 0.2$ to $0.6\,\mathrm{m}$. Hence, the jet was studied from its source up to a distance of $120\,d$. The width of the study area is larger than the length scale of the jet at every height. The $1024 \times 1024\,\mathrm{pixel}$ images were analysed using DigiFlow (see Sveen & Dalziel, 2005, and references therein for more detail about the PIV algorithm used by DigiFlow). The spatial velocity resolution was at $6.6\,\mathrm{mm}$ based on interrogation areas of 17×17 pixels with $75\,\%$ overlapping. This resolution proved to be sufficiently small from $z = 20\,d$ upwards. Six steady turbulent jets of flow rates 33.2, 37.0 and 40.3 $\mathrm{cm^3\,s^{-1}}$ were investigated in both study areas. The jet Reynolds number was in the range $3320 \leq Re_j \leq 4030$.

2.3 Qualitative observations

A sequence of grey-scale pictures of a typical injection of dye in a steady-state jet with $Re_j = 3850$ is presented in figure 2.2 as the dye front rises through the full depth of the quasi-two-dimensional tank. These pictures reveal many interesting features of quasi-two-dimensional jets. The saturated dye clearly shows the maximum lateral extent of the turbulent jet. The dye gradually fills a triangle (plotted in black lines) which suggests that entrainment is self-similar with height, at least when averaged over sufficiently long times. Before filling the full triangle width, we can observe (especially in figures 2.2d and 2.2e) an oscillation of the jet, as the dye path is clearly sinuous. Large round structures corresponding to eddies can also be identified on either side of the centreline. Dracos *et al.* (1992) observed similar structures for a range of distances $10 \leq z/W \leq 120$. The curvy edge of the jet suggests a characteristic scale, typically half the width of the triangle (approximately 10 cm at mid-height). These eddies result from the instability of the shear layer at the border between the jet and the ambient fluid (Jirka,

2001). Furthermore, tongues of ambient fluid (in white or light grey) appear at the rear of the largest eddies (see arrow in figure 2.2*e*). This phenomenon was also observed by Dimotakis, Miake-Lye & Papantoniou (1983) in the far field of round turbulent jets, and by Thomas & Brehob (1986) for two-dimensional turbulent jets. The role played by the eddies in the entrainment, by means of engulfment mechanisms at their rear, was modelled by De Young (1997) in an attempt to determine quantitatively the mass inflow contribution of large-scale structures in two-dimensional mixing layers.

Although the eddies observed in quasi-two-dimensional jets, such as the jet presented in figure 2.2, have some similarities with eddies in planar two-dimensional jets, it is important to note that the latter are genuine three-dimensional eddies while the former should be referred to as quasi-two-dimensional eddies because of the restriction imposed on the flow in the spanwise direction. The growth dynamics of quasi-two-dimensional eddies is governed by an inverse cascade of turbulence, while three-dimensional eddies tend to grow with mean-flow length scales. On the other hand, quasi-two-dimensional eddies also differ from purely two-dimensional eddies because friction at the boundaries, although relatively weak, restrains the maximum size of the eddies (Jirka, 2001) and eventually leads to their disintegration (Dracos *et al.*, 1992). Finally, it is worth noting that at the leading edge the dye concentration attenuates suggesting that diffusion occurs in a steady jet. Diffusion in quasi-two-dimensional jets is likely to be the result of a complex interaction between the eddies and the sinuous turbulent core of the jet. We return to detailed investigation of this issue in Chapters 3 and 4.

The second batch of experiments involved quantitative measurements of the velocity field using the PIV technique. Typical results for a jet at Reynolds number 4030 analysed in study area 2 are depicted in figure 2.3. In figure 2.3(*a*), a superposition of 40 images of the filming of the experiment shows the tracers as streaks to help visualize Eulerian structures in the flow. The corresponding velocity field is presented in figure 2.3(*b*), and it is clear that the main structures of the jet have been captured by the PIV. A high-speed core undulates along the centreline and is bordered by alternating counter-rotating eddies on the sides. The eddies are responsible for the entrainment and detrainment of fluid to and from the central core in a time-dependent fashion. Owing to the particular geometry of the tank, the turbulence cannot develop isotropically and we observe rather

(a) (b) (c) (d) (e)
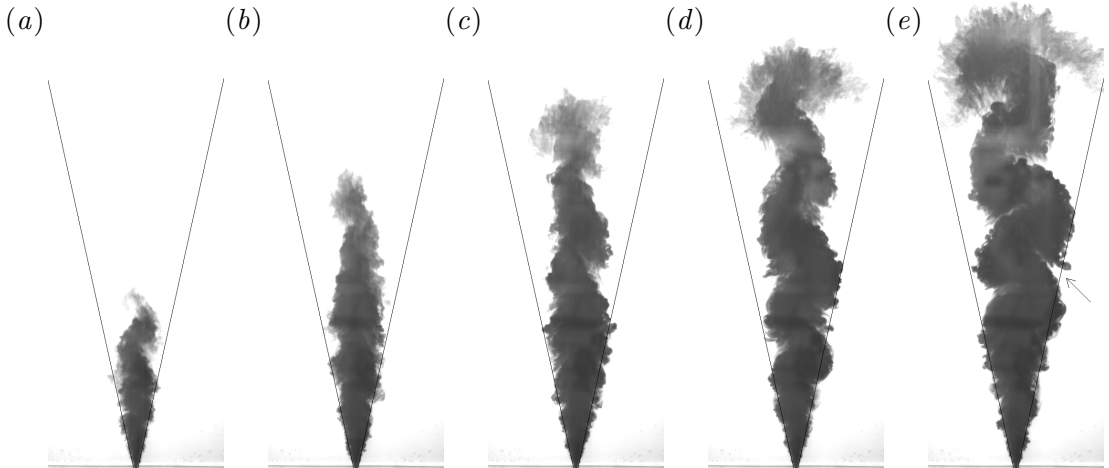
FIGURE 2.2: Sequence of grey-scale pictures of a dyed jet ($Re_j = 3850$) rising in the tank, at: (a) 1 s; (b) 2 s; (c) 3 s; (d) 4 s; and (e) 5 s. The average dye edge is plotted with black lines. The arrow in (e) points at the engulfment mechanism occurring at the rear of an eddy.

an inverse turbulent cascade in which quasi-two-dimensional eddies grow with height (De Young, 1997). This mechanism is confirmed in the experiment, as flow structures increase in size as they are advected upwards. The schematic cartoon displayed in figure 2.3(c) summarizes these ideas. The time-averaged mean picture of quasi-two-dimensional jets is associated with a triangular shape encapsulating all the flow structures, while the time-dependent picture shows a sinuous core flanked by large growing eddies. This two-part structure remains self-similar with height and its dynamics is responsible for the Gaussian distribution of the mean velocity, as we will discuss in § 2.5.

2.4 Time-averaged mean flow field

To characterize the mean behaviour of quasi-two-dimensional jets, we consider the ideal model of a turbulent momentum jet in a two-dimensional semi-infinite environment. Adopting the same conventions as Jirka & Harleman (1979), the flow is considered incompressible and steady in the mean. The x-direction is the lateral, cross-jet direction, the y-direction is the spanwise direction and the z-direction is the streamwise, axial direction. The velocity components are designated by (u, v, w) for the Cartesian system (x, y, z) with the origin at the nozzle exit. We assume a plane flow in the domain: the velocity field and any other
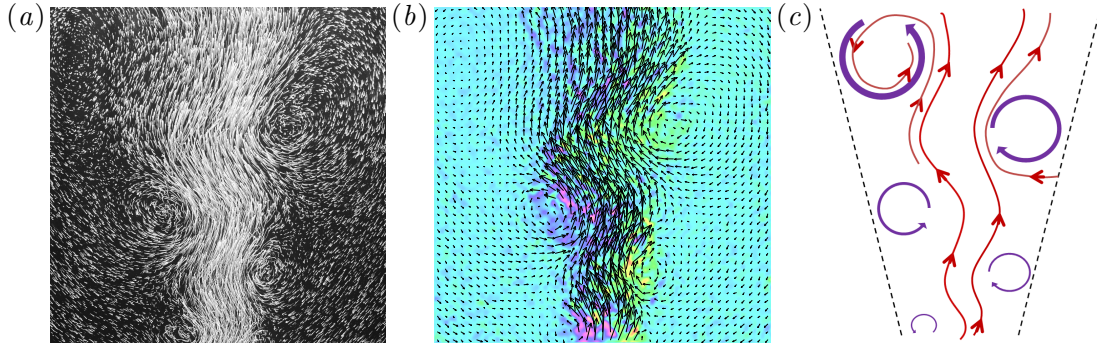
FIGURE 2.3: (*a*) Passive tracers (Pliolite particles) shown as streaks in a typical jet ($Re_j = 4030$) filmed in study area 2. (*b*) Velocity field (arrows) and vorticity field (background) of the same jet. (*c*) Schematic diagram describing the structure of quasi-two-dimensional jets.

quantities are invariant with y, and $v = 0$ everywhere. This hypothesis can be justified in three ways: the velocity profile across the gap must be self-similar in the core and the influence of the boundary layers is of second order at high Reynolds number; the v-component of the velocity is negligible compared to the other two components; and ambient fluid can only be entrained from the sides of the jet, i.e. in the x-direction. We also use the common hypothesis of a Gaussian profile (see, for instance, List, 1982) for the time-averaged streamwise velocity,

$$\overline{w}(x,z) = \overline{w}_m(z) \, \exp\left[-\left(\frac{x}{b(z)} \right)^2 \right], \tag{2.1}$$

where the over-bar represents an appropriate average in time, $w_m(z)$ is the maximum streamwise velocity at distance z from the source and $b(z)$ is a measure of the local lateral spread of the jet velocity. We derive briefly the governing equations for plane jets, based upon the conservation of volume and momentum (see, for instance, Kotsovinos & List, 1977, for more details). The time-averaged volume flux and the time-averaged momentum flux are expressed respectively as

$$\overline{Q}(z) = \int_{-\infty}^{\infty} \overline{w}(x,z) \, \mathrm{d}x \quad \text{and} \quad \overline{M}(z) = \int_{-\infty}^{\infty} (\overline{w})^2 (x,z) \, \mathrm{d}x. \tag{2.2a,b}$$

Solving the first-order integrated equations of motions

$$\frac{\mathrm{d}\overline{M}}{\mathrm{d}z} = 0, \quad \frac{\mathrm{d}\overline{Q}}{\mathrm{d}z} = 2\alpha \overline{w}_m, \tag{2.3a,b}$$

we find

$$\overline{M} = M_0, \quad \overline{Q} = Q_0 \left(4\sqrt{2}\alpha \frac{M_0 z}{Q_0{}^2} + 1 \right)^{1/2}, \qquad (2.4a,b)$$

where we assume in equation $(2.3b)$ that the entrainment velocity is proportional to the maximum time-averaged streamwise velocity, with α the entrainment co-efficient (Morton, Taylor & Turner, 1956), and Q_0 and M_0 are values at the origin for the volume flux and momentum flux, in $(2.4a)$ and $(2.4b)$ respectively. The e-folding value of the maximum time-averaged streamwise velocity and the maximum time-averaged streamwise velocity are, respectively,

$$b(z) = \frac{Q_0{}^2}{\sqrt{2\pi}M_0} \left(4\sqrt{2}\alpha \frac{M_0 z}{Q_0{}^2} + 1 \right) \text{ and } \overline{w}_m(z) = \frac{\sqrt{2}M_0}{Q_0} \left(4\sqrt{2}\alpha \frac{M_0 z}{Q_0{}^2} + 1 \right)^{-1/2}.$$
$$(2.5a,b)$$

We can infer the theoretical virtual origin of the jet

$$z_0 = -Q_0{}^2/(4\sqrt{2}\alpha M_0), \qquad (2.6)$$

which results from the choice of the boundary conditions (i.e. the distributions of the volume flux and momentum flux at $z = 0$).

Alternatively, solving the plane jet equations assuming momentum-flux conservation and similarity (see e.g. Pope, 2000) also leads to the same power laws for the e-folding value of the maximum time-averaged streamwise velocity, $b \propto (z - z_0)$, and the maximum time-averaged streamwise velocity, $\overline{w}_m \propto (z - z_0)^{-1/2}$. The constants of proportionality and the virtual origin can differ because of the assumptions we make for the x-distribution of $\overline{w}_m$ (essentially due to 'shape factors') and for the boundary conditions. As a direct comparison with the 'velocity spread rate' S defined as $\mathrm{d}x_{1/2}/\mathrm{d}z = S$ (where $x_{1/2}$ is the velocity half-width defined by $\overline{w}_m(z)/2 \equiv \overline{w}(x_{1/2}, z)$), we can remark that $S = 4(\ln 2/\pi)^{1/2}\alpha$ (see Pope, 2000, for further details about S).

Equations $(2.5a,b)$ suggest that the natural scalings for length and time scales in our problem are d, the source width, and $\tau = d^2/Q_0$, respectively. Therefore, when considering our experimental data, we will always scale quantities with these scalings, i.e.

$$\tilde{z} = \frac{z}{d}, \quad \tilde{x} = \frac{x}{d}, \quad \tilde{b} = \frac{b}{d}, \quad \tilde{t} = \frac{t}{\tau}, \quad \tilde{w} = \frac{\tau}{d}w, \qquad (2.7a{-}e)$$

where tildes denote non-dimensional variables.

For comparison with the theoretical model, we time-averaged the velocity field measured with PIV. We plot the lateral spread, the evolution with height and the lateral distribution of the time-averaged streamwise velocity. We also discuss the influence of the free surface at the top boundary, the impact of the lateral confinement and possible three-dimensional effects on the flow, such as friction at the walls constraining the flow.

In figure 2.4, we show the ensemble average of the edges of 40 dyed jets (plotted with dots). The evolution of the dye edge with height clearly indicates that above $z/d = 120$ the influence of the free surface becomes non-negligible. This height serves as a lower bound for the 'impingement region' (see Jirka & Harleman, 1979, for a detailed study). The zone of established flow is found to start at approximately $z/d = 20$, a value at which the streamwise velocity becomes self-similar. This value is commonly reported in the literature (see e.g. Kuang, Hsu & Qiu, 2001). A linear fit of the non-dimensional average dye edge (plotted with a thin line in figure 2.4) calculated for $20 \leq z/d \leq 120$ gives a slope of 0.22 ± 0.08 for the half-spreading angle. We can observe that the non-dimensional e-folding value of the maximum time-averaged streamwise velocity $\tilde{b}$ (plotted with crosses) is much narrower. We discuss this difference further below. We also compute the quantity $\tilde{b}$ from the ensemble average of the 12 jets studied with PIV. A linear fit (plotted with a thick line) calculated between $20 \leq z/d \leq 120$ gives the rate of change, $\mathrm{d}b/\mathrm{d}z = 0.154 \pm 0.016$, which is slightly above the value of 0.135 reported by Ramaprian & Chandrasekhara (1985) and very similar to the value reported by Albertson *et al.* (1950). Using (2.5a) the corresponding entrainment coefficient (determined to best-fit the streamwise variation of b) is $\alpha_b = 0.068 \pm 0.007$ (which is equivalent to $S_b = 0.125 \pm 0.015$), and we find that α_b is almost constant in the zone of established flow, thus confirming the entrainment assumption (Morton *et al.*, 1956).

In figure 2.5, we plot the non-dimensional maximum time-averaged streamwise velocity $\overline{w}_m/(Q_0/d)$ against height. The crosses are plots of an ensemble average over all the jets studied with PIV. Although the agreement is good, they lie slightly but systematically above the theoretical curve (plotted with a solid line) for $z/d \leq 100$. We compute the theoretical curve from (2.5b) and using $\alpha = \alpha_b$. The value of Q_0 was measured for each jet as described in the experimental procedure. On the other hand, since M_0 could not be measured directly, it was
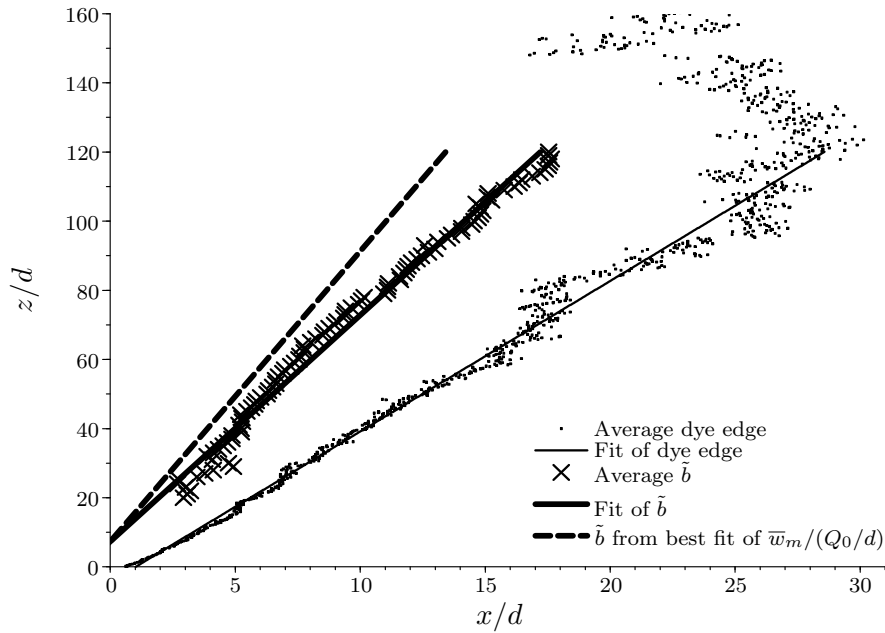
FIGURE 2.4: Non-dimensional average dye edge (dots) with a linear fit (thin line); non-dimensional e-folding value of the maximum time-averaged streamwise velocity $\tilde{b}$ (crosses) with a linear fit (thick line); and a non-dimensional average velocity spread rate (dashed line) using $\alpha = \alpha_{\overline{w}_m}$ computed from the best fit of $\overline{w}_m/(Q_0/d)$ (see figure 2.5).

replaced by $\overline{M}$ by virtue of (2.4a). As shown in figure 2.6, the momentum flux $\overline{M}$ (plotted with pluses) computed from the time-averaged streamwise velocity field using (2.2b) (the boundaries of the integral are chosen as the positions where $\overline{w}_m = 0$) is found to be approximately constant for $34 \leq z/d \leq 110$. For $z/d < 34$, the data do not seem accurate, probably because the frame rate is not high enough for the large velocity at that distance, and the resolution of the PIV could also not be optimal where the jet is very narrow. For $z/d > 110$, the influence of the impingement region as the jet approaches the free surface at the top seems to start affecting the momentum flux. The mean non-dimensional value of the momentum flux is $< \overline{M} > / \left(Q_0{}^2/d \right) = 0.55 \pm 0.03$ (plotted with a solid line in figure 2.6). Giger *et al.* (1991) reported and discussed the wide range of values for the non-dimensional momentum flux measured in plane jets from the literature: from 0.52 (Cervantes de Gortari & Goldschmidt, 1981) to 1.77 (Antonia, Satyaprakash & Hussain, 1980). We analysed the influence of friction at the rigid boundaries on the momentum flux and found a Fanning friction factor of $f \approx 0.007$ assuming
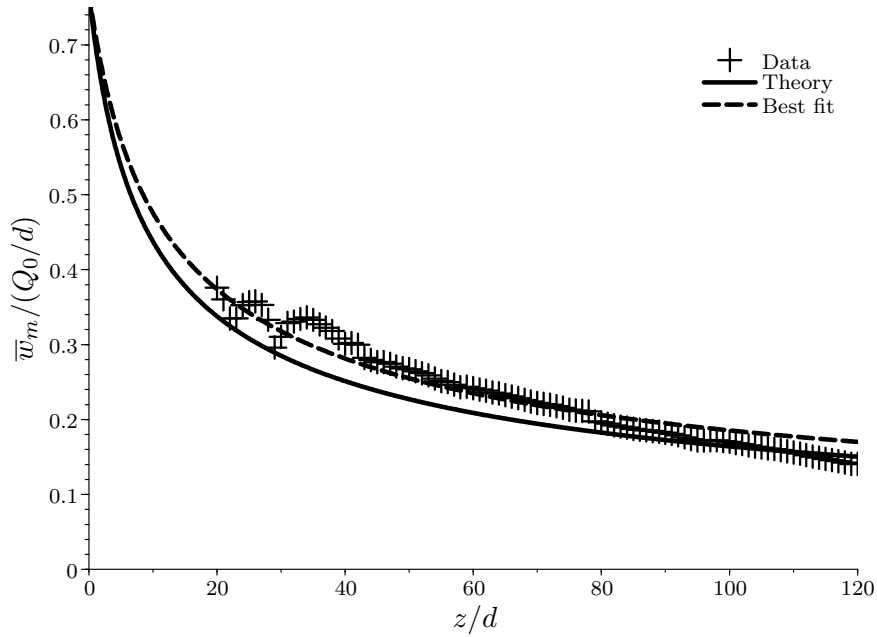
FIGURE 2.5: Non-dimensional maximum time-averaged streamwise velocity (pluses) versus height, theoretical curve (solid line, and using $\alpha_b = 0.068$) and best least-squares fit (dashed line) optimising with respect to α (using $\alpha_{\overline{w}_m} = 0.052$).

a wall stress of the form $\tau_w = f\rho < \overline{w} >^2 /2$, where ρ is the water density and $< \overline{w} >$ is the spatial averaged velocity in the y-direction (Bird, Stewart & Lightfoot, 2007). The influence of friction is relatively small compared to the mean value of the momentum flux (of the order of 10 %) and therefore has not been included in our constant momentum-flux model (see Giger *et al.*, 1991, for a detailed study). In figure 2.5, a least-squares fit of the data (plotted with a dashed line) assuming equation (2.5b) and optimising with respect to the entrainment coefficient yields an optimal choice for α from the z dependence of the maximum velocity $\alpha_{\overline{w}_m} = 0.052$ (which is equivalent to a velocity spread rate $S_{\overline{w}_m} = 0.098$). The fact that $\alpha_{\overline{w}_m}$ (also plotted with a dashed line in figure 2.4) is slightly smaller than α_b means that some assumptions of the model underlying (2.5a,b) (which should yield identical estimates for α using $b(z)$ and $\overline{w}_m(z)$) are not perfect. In particular, we believe that the Gaussian distribution hypothesis is not ideal, as slight deviations from Gaussianity could explain the mismatch.

In figure 2.7(a), we show the lateral distribution of the normalized time-averaged streamwise velocity $\overline{w}/\overline{w}_m$. The x-axis is centred on the position of the
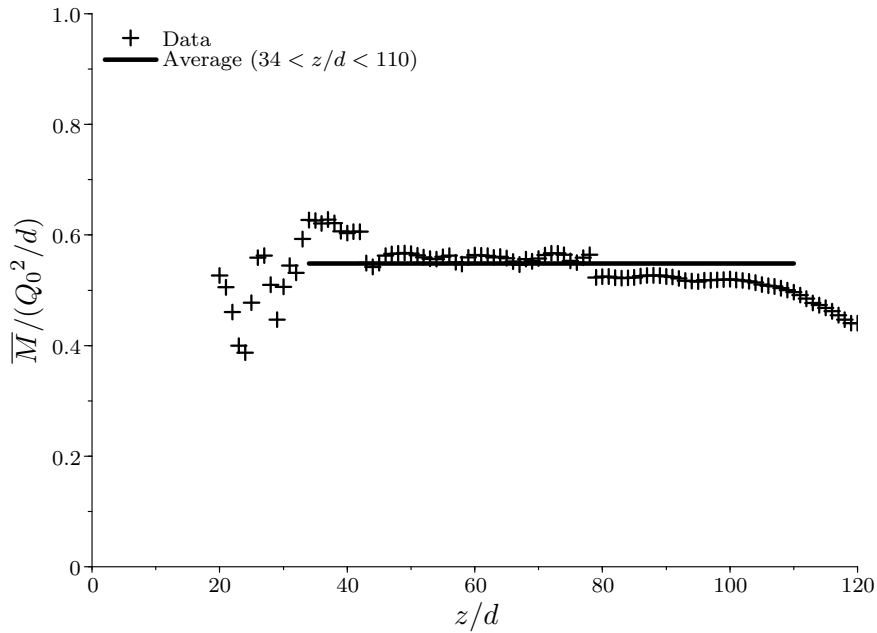
FIGURE 2.6: Non-dimensional time-averaged momentum flux (pluses) versus height and average value $< \overline{M} > / \left(Q_0{}^2/d \right) = 0.55$ (solid line).

maximum time-averaged streamwise velocity. All the curves result from an ensemble average of six or 12 jets, depending on where the z position of the curve lies with respect to the two study areas for the PIV. The experimental data (plotted with different colours) are in very good agreement with the theoretical curve (plotted with a thick red line) computed from equation (2.1) using $\alpha = \alpha_b$ and neglecting any consideration of virtual origin (Kotsovinos, 1976). Nevertheless, the experimental curves are somewhat narrower than the theoretical Gaussian velocity profile. This discrepancy is consistent with a smaller entrainment coefficient, as suggested by the best fit of $\overline{w}_m/(Q_0/d)$ in figure 2.5. The mismatch is probably caused by the return flow in the tank which is not accounted for by the model, where an infinitely wide domain is assumed.

The problem of the return flow in a domain of finite lateral extent is more prominent in plane jets than in (fully unconfined non-planar) three-dimensional jets. In plane jets, the entrainment velocity remains constant outside the jet, whereas it decreases with distance in the three-dimensional case. As a consequence, we can observe a negative shift in the lateral distribution of the time-averaged streamwise velocity (see figure 2.7a), which denotes the presence of the return flow. The flux
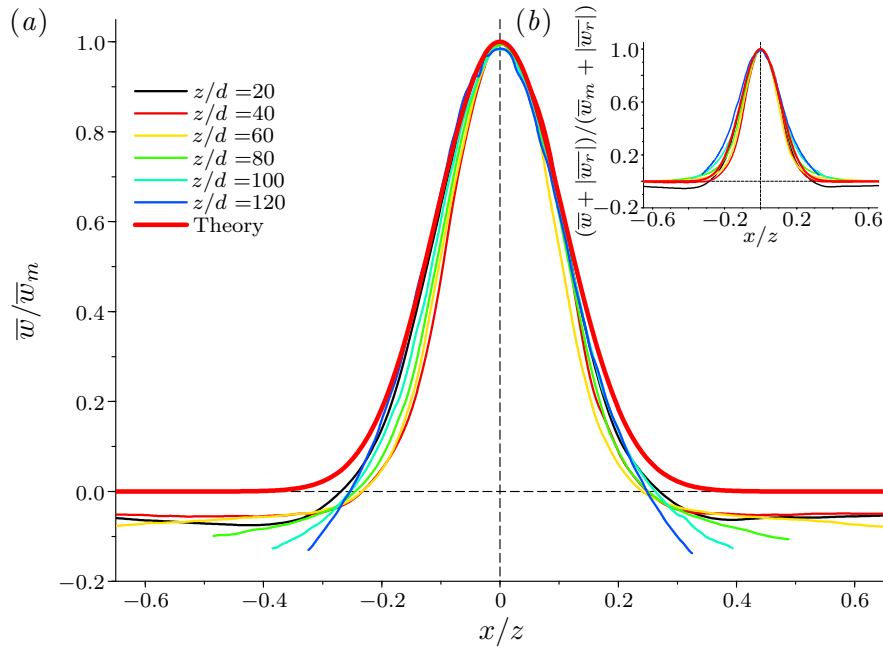
FIGURE 2.7: (a) Lateral distribution of the normalized time-averaged streamwise velocity at various heights (plotted with different colours) and theoretical prediction (plotted with a thick red line). (b) Lateral distribution of the normalized sum of the time-averaged streamwise velocity and the absolute value of the estimated time-averaged streamwise velocity of the return flow (defined by equation 2.8) at the same heights as in (a) (plotted with different colours) and theoretical prediction (plotted with a thick red line).

of the return flow, $\overline{Q_r}$, increases with height, as it matches the jet volume flux $\overline{Q}$ owing to conservation of volume at every height across the width of the tank. We can estimate the time-averaged streamwise velocity distribution of the return flow by applying volume conservation at each height. For all z, the total volume flux on both sides of the jet is $\overline{Q_r} = \overline{Q} - Q_0$. We assume that the return velocity is distributed uniformly along $-L/2 \leq x \leq -x_0$ and $x_0 \leq x \leq L/2$, where $x_0 \approx 0.25z$ is defined as the location where $\overline{w} = 0$. Therefore, using equations (2.4b) and (2.5b) we find that the time-averaged return velocity is

$$\frac{\overline{w_r}}{\overline{w}_m} = -\frac{Q_0^2}{2\sqrt{2}M_0(L/2 - x_0)}\left[\left(4\sqrt{2}\alpha\frac{M_0}{Q_0^2}z + 1\right) - \left(4\sqrt{2}\alpha\frac{M_0}{Q_0^2}z + 1\right)^{1/2}\right],$$
$$(2.8)$$

where we use $\alpha = \alpha_b = 0.068$ and $M_0 = <\overline{M}> = 0.55\,Q_0^2/d$ to plot figure 2.7(b).

19

As can be seen in figure 2.7(b), adding this simple estimate of the return-flow velocity $\overline{w_r}$ to the jet velocity $\overline{w}$ has corrected the negative shift in the experimental data. At every height, except $z/d = 20$, the velocity tends to a zero asymptotic value for large $|x/z|$.

From comparison with similar experiments that we conducted in a smaller domain (0.5 m × 0.01 m × 0.5 m) and with experimental results reported in the literature and obtained in larger tanks of various aspect ratios and with porous or non-porous lateral boundaries (Giger *et al.* (1991); Dracos *et al.* (1992); Rowland *et al.* (2009)), we believe that the impact of the return flow is limited and affects principally the distribution of the time-averaged streamwise velocity in the manner described above. From direct measurements we also find that the momentum flux associated with the return flow is small compared with the momentum flux in the jet (from 0 to 15 % for $z/d = 0$ to 110). We have not observed any qualitative or quantitative influence of the return flow on the time-dependent core and eddy structure described in § 2.3. We discuss the spatial structure of this return flow in more detail in Chapter 6.

The experimentally measured streamwise velocity field follows closely the predictions given by the derivation of the momentum and continuity equations for two-dimensional turbulent jets. The small difference due to the lateral confinement of the experimental jets leads us to the conclusion that the entrainment coefficient is within the range $0.052 \leq \alpha \leq 0.068$. The purpose of the study of the mean flow is not to understand all the details of this flow but rather to give us some insight about the flow field in this particular geometry. More refined models for the plane jet can be found in the literature (see e.g. Giger *et al.*, 1991; Hussein *et al.*, 1994; Wang & Law, 2002).

2.5 Quantitative analysis of the time-dependent core and eddy structure

2.5.1 Time-dependent eddy structure

We now analyse the core and eddy structure of the flow using the experimental results given by the PIV. We identify large vortical structures or 'eddies' in individual frames of the instantaneous velocity field using DigiFlow, as shown in

figure 2.8(a). Considering a specific frame, we find regions of the instantaneous flow field where streamlines form a complete loop. This technique is similar to the eddy identification method proposed by Robinson (1991). We plot the streamlines forming a complete loop in figure 2.8(a) with grey curves. We then analyse each patch, or eddy, to obtain statistical measurements such as the centroid (identified by the location of the black crosses) and the standard deviations in the lateral and streamwise directions (shown by the size of the crosses). The coordinates of the centroid $(x_{c,k}, z_{c,k})(t)$ of eddy 'k' at time t are computed numerically as

$$(x_{c,k}, z_{c,k})(t) = \frac{1}{\sum\limits_{x=0}^{L_x}\sum\limits_{z=0}^{L_z} \Delta_k(x,z,t)} \sum_{x=0}^{L_x}\sum_{z=0}^{L_z}(x,z)(t)\Delta_k(x,z,t), \qquad (2.9)$$

where L_x and L_z are the lateral and streamwise dimensions of the velocity field and $\Delta_k(x,z,t)$ is 1 if the point $(x,z)(t)$ belongs to a streamline identified as part of eddy k at time t and 0 otherwise. Similarly, the lateral and streamwise standard deviations $(x_{s,k}, z_{s,k})(t)$ of eddy k at time t are computed numerically as

$$(x_{s,k}, z_{s,k})(t) = \left(\frac{1}{\sum\limits_{x=0}^{L_x}\sum\limits_{z=0}^{L_z} \Delta_k(x,z,t)} \times \right.$$
$$\left. \sum_{x=0}^{L_x}\sum_{z=0}^{L_z}\left((x,z)(t) - (x_{c,k},z_{c,k})(t)\right)^2 \Delta_k(x,z,t) \right)^{1/2}. \quad (2.10)$$

We applied the algorithm every 10 frames to the six experimental velocity fields. The eddies are thus tracked in time at a frequency of 25 frames per second. As a quality control of the technique, we conducted a visual inspection of all the eddies identified by the algorithm. This showed that the algorithm was very robust. It did not appear to be subject to 'false positives', i.e. the misidentification of a non-eddy feature of the flow as an eddy. The algorithm only occasionally failed to detect eddies (i.e. there were very few 'false negatives') when the eddies partially

appeared at the edges of the frame.
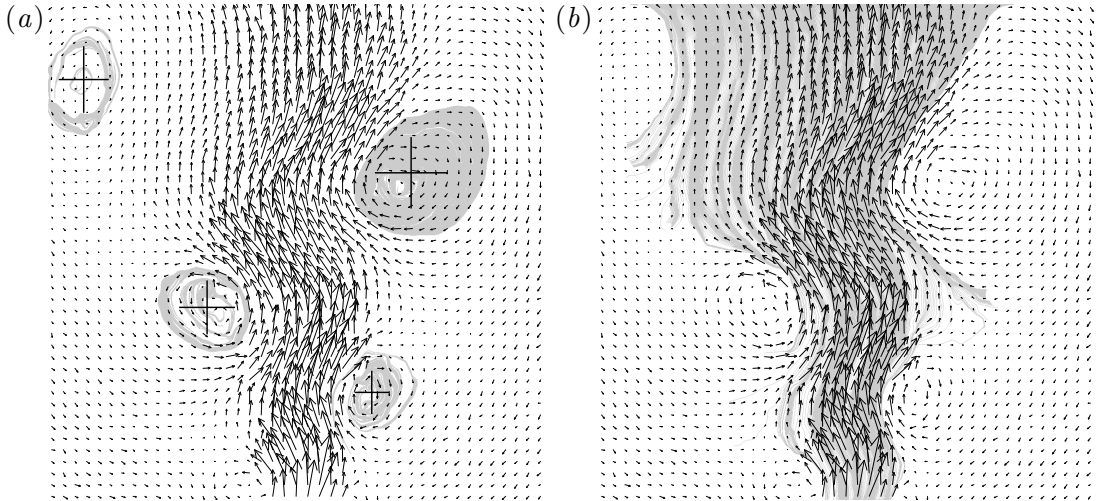
FIGURE 2.8: (*a*) Identification of the vortical structures in the instantaneous velocity field (plotted with black arrows). The streamlines identified within an eddy are plotted with grey curves. The black crosses designate the centroid of the eddies, and the size of the crosses represents their standard deviations in the lateral and streamwise directions. (*b*) Identification of the core structure in the same instantaneous velocity field (plotted with black arrows). The streamlines identified as part of the core structure are plotted with grey curves.

The trajectories of 48 eddies are shown in figure 2.9 (plotted with black dots). A linear fit (shown with a solid line) gives an average slope of 0.22 from the z-axis. We also plot the linear fits of the ensemble-averaged lateral standard deviation of the eddies, a measure of the average eddy width, with dashed lines. The lateral and streamwise standard deviations were found to be almost identical, showing that the eddies are close to circular in shape. They both have a linear trend increasing with height at a rate of 0.07.

The non-dimensional location of each eddy in time has been plotted in figure 2.10 with dots. We can see a general trend, which follows the power law $\tilde{z} \propto \tilde{t}^{2/3}$ (plotted with a solid curve) derived from the maximum time-averaged streamwise velocity formula (2.5*b*). The large scatter is due to the complex dynamics of individual eddies. We found that not all eddies travelled through the depth of the PIV window completely unperturbed. We observed merging of close successive eddies, with the first eddy slowing down considerably, sometimes even halting, and the following eddy accelerating substantially. Similarly to the observations made by Dracos *et al.* (1992), we did not see eddies rotating around
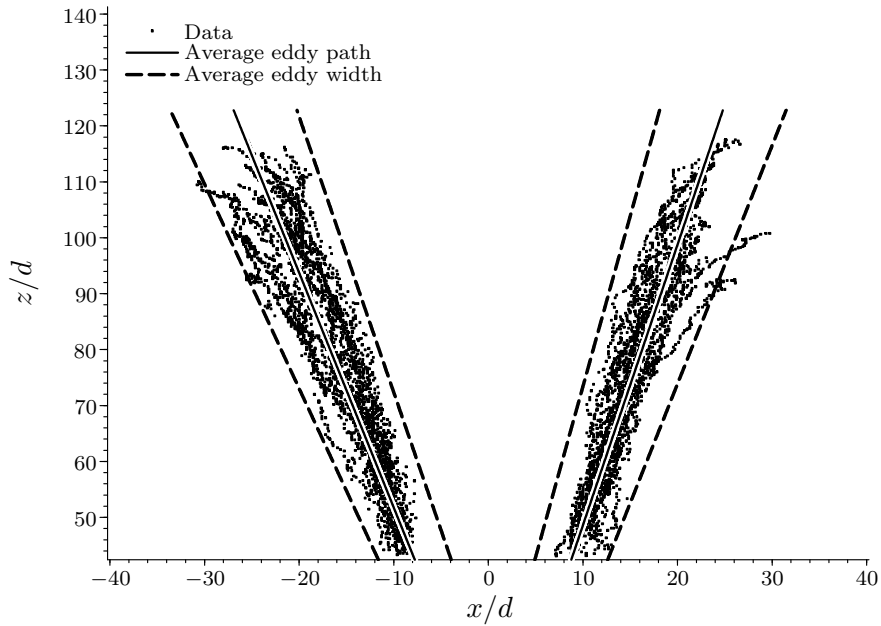
FIGURE 2.9: Eddy locations in PIV study area 2 (dots), linear fits of eddy locations (solid lines) and average eddy lateral standard deviations (dashed lines).

a common axis before merging. We also noticed some small eddies disappearing in the vicinity of the core. From the best fit of the eddy streamwise position in time, we find that the average eddy speed is 0.28 times the theoretical $\overline{w}_m$ and 0.24 times the best fit of $\overline{w}_m$. The fastest identified eddy rises approximately at the same speed as the centreline time-averaged streamwise velocity, whereas the slowest eddy rises at less than 15 % of $\overline{w}_m$.

To investigate the eddy frequency, we counted the number of eddies (identified by the algorithm described above) passing at a given height on either side of the core of the jet. We measured this number for the six PIV experiments performed in study area 2 and then divided it by the duration of the experiment, i.e. 21.8 s. The resulting non-dimensional eddy frequency $\tilde{f} = fd^2/Q_0$ is plotted with thin lines in figure 2.11(a). Dracos et al. (1992) found an empirical law for the eddy frequency, $\tilde{f} = 176\tilde{z}^{-3/2}$ (plotted in non-dimensional form with a dashed curve), and explained that f decreased as a result of the decrease of the eddy transport velocity and merging mechanisms. However, if we assume that eddies form periodically, then the eddy frequency should remain constant with height, since eddies travel on average at the same velocity. The frequency can only decrease
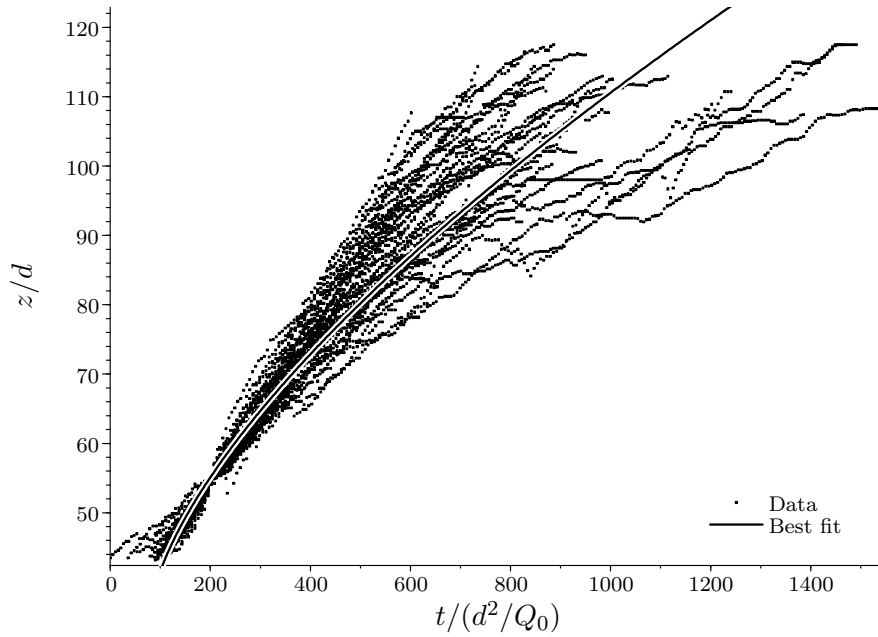
FIGURE 2.10: Eddy z-coordinate versus time (dots) and best least-squares fit (solid curve) assuming $\tilde{z} \propto \tilde{t}^{\,2/3}$.

if eddies merge (or, to a lesser extent, disappear). Merging occurs when the distance between two successive eddies is smaller than a critical value. The distance between two eddies decreases because their transport velocity decreases like $\tilde{z}^{-1/2}$ and because eddies grow approximately linearly with height due to entrainment of ambient fluid.

The punctuated decrease in frequency can actually be observed in figure 2.11(a) as we follow individual experiments (see the values of f for a typical experiment plotted with red crosses). The frequency f is constant over a certain distance and then drops by a discrete value in a stepwise way. This is also clearly shown by the evolution of the Strouhal number, $St = fb/\overline{w}_m$, plotted with dots in figure 2.11(b) and with red crosses for the same typical experiment. The Strouhal number increases like $St \propto \tilde{z}^{\,3/2}$ from a minimum value of $St = 0.07$ consistent with the value reported by Dracos *et al.* (1992) (plotted with a dashed curve) and then drops, somewhat chaotically but consistently, to this minimum value as merging occurs. Because merging becomes less frequent as z/d increases, the length of time over which f is constant (and hence St increases) increases with z/d. This leads to the increase in both typical values of the Strouhal number and
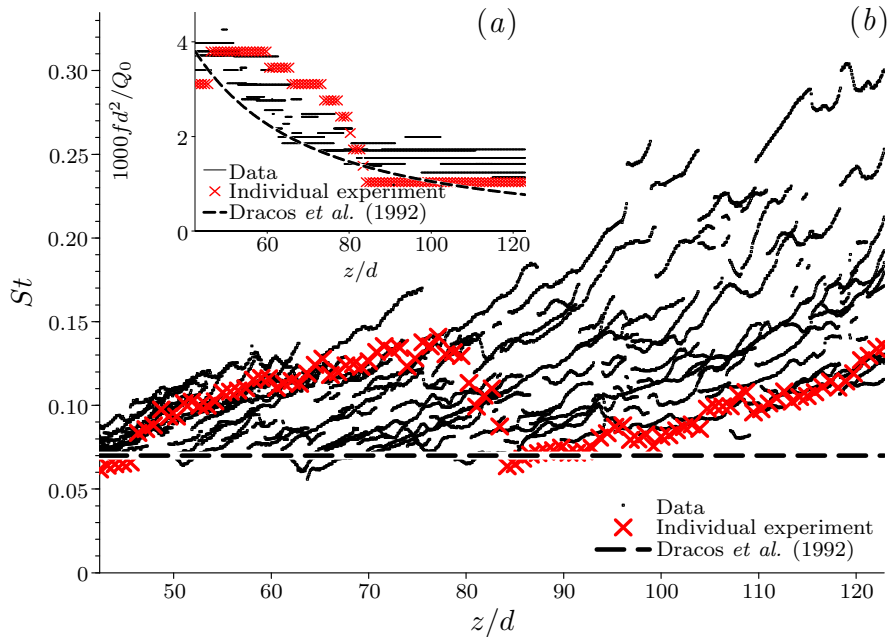
FIGURE 2.11: (a) Data for the non-dimensional eddy frequency fd^2/Q_0 versus height (thin lines) and best fit of Dracos *et al.* (1992) (dashed curve). The values of fd^2/Q_0 for a typical individual experiment have been highlighted with red crosses. (b) Data for the Strouhal number $St = fb/\overline{w}_m$ versus height (dots) and Strouhal number reported by Dracos *et al.* (1992) (dashed line). The values of St for the same experiment have also been highlighted with red crosses.

its variance, as is apparent in figure 2.11(b). The actual value of the minimum Strouhal number appears to depend on the eddy formation frequency, the travel speed of the eddies, the growth of the eddies due to entrainment and the dynamics of merging, in ways that are not as yet fully understood.

To summarize, the eddies have on average a linear trajectory, a constant growth with height and a velocity similar to the time-averaged mean streamwise velocity of the jet. All these findings lead to the conclusion that the dynamics of the eddies is essentially self-similar with height, at least within the region of the flow that we have studied. From the analysis of the time evolution of the streamlines leading to the eddies, we can also attribute the growth of the eddies mainly to the entrainment of ambient flow. Eddy merging occurs irregularly and is responsible for the decrease of the long-time-averaged eddy frequency, with an apparently well-defined minimum Strouhal number $St \geq 0.07$.

2.5.2 Time-dependent core structure

Similarly, we identify the core of the jet by plotting all the streamlines that exit through the top of a specific velocity field. Effectively, the algorithm follows the streamlines backwards starting from the points at the top horizontal boundary of the velocity field. However, in the following discussion, we consider the streamlines in the forward direction with their endpoint at the top of the velocity field. The identification of the streamlines of the core is repeated every 10 frames for each PIV velocity field, thus giving a dynamical picture of the core at a frequency of 25 frames per second. It can be seen in figure 2.8(b) that some streamlines (plotted with grey curves) start at the bottom boundary of the window while others come laterally inwards. The streamlines coming from the bottom of the frame reveal the volume flux brought by the jet itself into the frame. The streamlines coming from the sides of the jet show the entrained volume flux. They actually reveal how entrainment of ambient fluid occurs as they wrap around eddies and then are incorporated into the core. It is clear that eddies constitute an essential entrainment mechanism by engulfing ambient fluid at their rear. The starting point of entrained streamlines (i.e. the location at which we consider them as part of the core) is chosen where the streamwise component of their gradient changes sign.

This choice raises the more fundamental question about the boundaries of the core. The boundary between the core and the eddy is clearly defined since the algorithms used to identify both structures ensure mutual exclusion. However, at the top and bottom of the window, this boundary can be ambiguous if large eddies are not entirely seen in the image frame. At the top of the frame, the error zone is actually restricted to $z > 118\,d$, which is approximately where the self-similarity region of the jet ends. At the bottom of the frame, the error zone is insignificant since the eddies are much smaller. Moreover, we found that the starting point chosen for entrained streamlines has no effect on the time-averaged distribution of the core and negligible impact on time-dependent distributions. Therefore, although somewhat arbitrary, we believe that our criterion determining the boundary between the core and the ambient flow reflects the diffusion of momentum from the jet to the ambient flow.

We present the lateral (or x-) distribution of the probability $P_{core}(x, z)$ of being in the core in time (plotted with thick solid curves) at different heights in

figure 2.12. The discrete formulation of the probability P_{core} is

$$P_{core}(x, z) = \frac{1}{N} \sum_{n=0}^{N} \Delta_n(x, z), \qquad (2.11)$$

where N is the total number of frames for a given experiment, n designates the nth frame and $\Delta_n(x, z)$ is 1 if the point (x, z) belongs to a streamline identified as part of the core of the jet in the nth frame and 0 otherwise. Its shape is Gaussian-like on the edges and flatter in the middle. The flat portion where $P_{core}(x, z) = 1$ corresponds to the section of the jet always occupied by the core in time. The width of this section grows linearly with height on average, as shown by the standard deviation measurement $\overline{x}_{std}$ (plotted with thin solid curves for the experimental data and dashed lines for the linear fits), at a rate of 0.12. Furthermore, the momentum flux of this portion remains constant with height at a value of 78 % of the total momentum of the jet. The edges of the probability P_{core} correspond to the lateral excursions of the core through time. It is interesting to note a similarity between the distribution of the probability P_{core}, as presented in figure 2.12, and a typical distribution of the intermittency function measured in quasi-two-dimensional jets (see e.g. Dracos *et al.*, 1992). Both display a plateau equal to 1 in the interior of the jet and a Gaussian-like decrease tending towards 0 as $|x/z|$ increases. Nevertheless, the intermittency function and the probability P_{core} are different, both in the way they are computed and in their meaning. The probability P_{core} is a measure of the likelihood of being in the core in time (which is identified by the algorithm described above). On the other hand, the intermittency criterion measures the probability of being in a turbulent region in time. The similarity observed between these two functions is probably due to the fact that the core is a region where the amplitude of the turbulent fluctuations increases towards the jet centreline. However, the lateral spreading of the two functions should differ because, contrary to the intermittency function, the probability P_{core} excludes the eddies, which are also regions of large velocity fluctuations.

A typical standard deviation $x_{std}(t)$ of the distribution of the core streamlines at the time instant corresponding to the jet shown in figure 2.8(b) is plotted with dashed curves in figure 2.13. The undulations of the jet, which we already observed on dyed jet pictures, are primarily a feature of the edges of the core. The
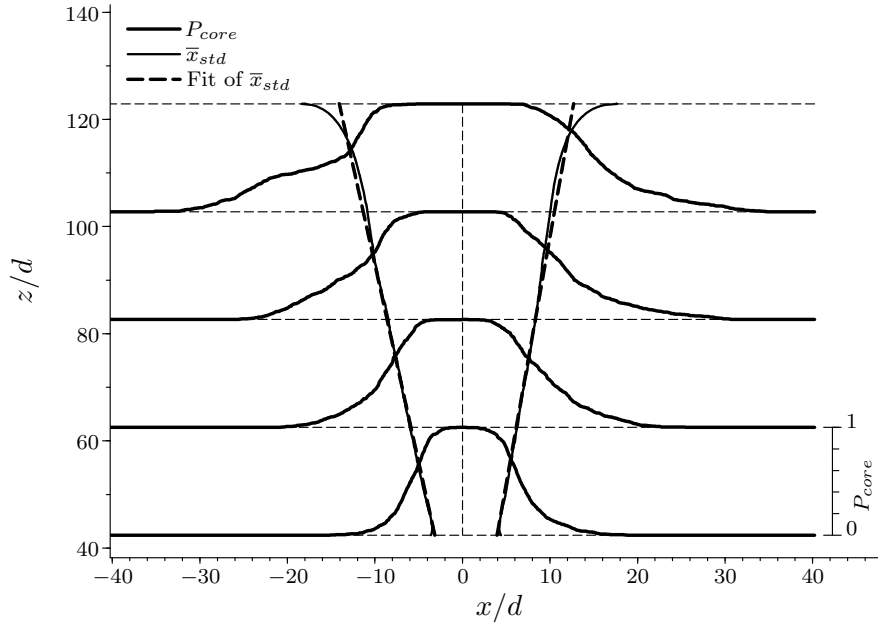
FIGURE 2.12: Time-averaged mean core structure in PIV study area 2. Lateral distribution of the probability P_{core} of being in the core in time (thick solid curves) at different heights, and data (thin solid curves) and linear fits (dashed lines) of the time-averaged standard deviation $\overline{x}_{std}$ of the probability P_{core}.

distribution of the instantaneous streamwise velocity $w(t)$ corresponding to the same time instant is plotted with solid curves at different heights in figure 2.13. We normalize $w(t)$ with the maximum instantaneous streamwise velocity w_n measured at the lowest height in the frame, $\tilde{z}_n = 42.4$. We can observe that the instantaneous velocity decreases with height and spreads laterally as expected from the self-similar theoretical model. Furthermore, the velocity distribution is not centred on the z-axis but follows the undulations of the core described by $x_{std}(t)$. The velocity within the core is much larger than the velocity outside, thus underlying the presence of this high-speed core in the jet. It is also very interesting to note that the lateral decrease of the velocity is slower in the interiors of the undulations than in the exteriors. This is due to the presence of the eddies (shown as crosses, with the size of the crosses representing the lateral and streamwise eddy standard deviations) located in the curves of the core structure and which carry some upwards momentum flux (slightly less than a quarter of the total momentum flux on average).
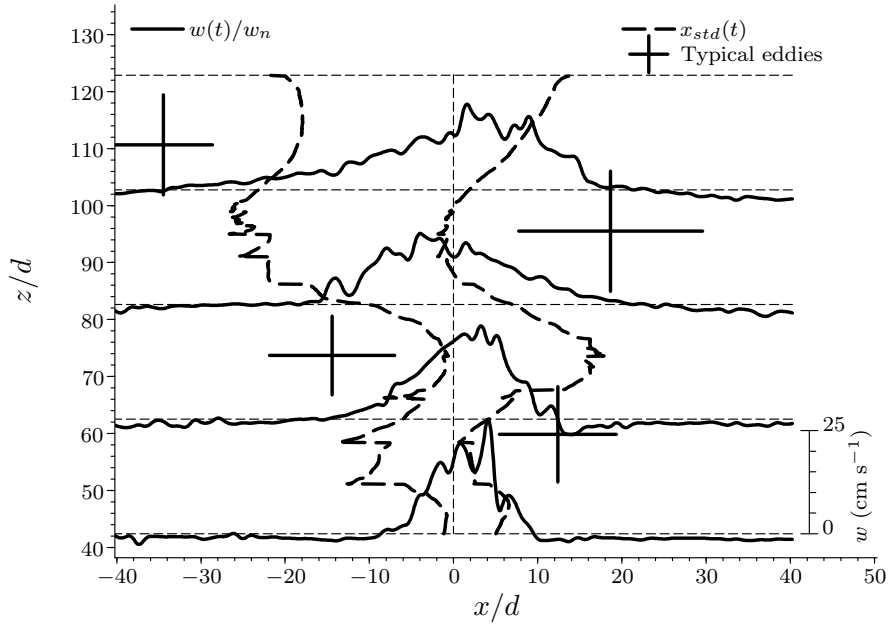
FIGURE 2.13: Distribution of the instantaneous normalized streamwise velocity $w(t)/w_n$ (solid curves) at different heights and corresponding to the jet presented in figure 2.8(b). Instantaneous standard deviation $x_{std}(t)$ (dashed curves) of the core of the jet presented in figure 2.8(b) with its eddies (crosses, with the size representing the lateral and streamwise eddy standard deviations).

The linear growth of the core shows that it is self-similar with height within the flow region studied, as we found for the eddies. The spatial statistical distribution of the location of the core is due to its particular wave-like dynamics. The undulations along the centreline of this high-velocity core are characterized by an essentially self-similar spatial probability distribution P_{core}. The standard deviation of the probability P_{core} increases with height at a rate of 0.12, which is quite close to the rate of change with height of the mean velocity spread rate $\mathrm{d}b/\mathrm{d}z = 0.15$. The spatial Gaussian distribution of the time-averaged mean streamwise velocity is therefore the result of the statistical spatial distribution of the undulating core. It is difficult to assess whether the eddies have a direct contribution to this statistical process. However, their role in the large-scale dynamics of the core is essential.

2.6 Conclusion

In this experimental study of quasi-two-dimensional turbulent jets (and similarly to Giger *et al.* (1991) and Dracos *et al.* (1992)), we have observed that the flow organizes into a very interesting structure with a sinuous core of high streamwise velocity oscillating about the centreline and eddies rising and growing along the undulations. As predicted by the theoretical model, we find that: the mean velocity field measured with PIV is self-similar with height (see figure 2.14); the normalized time-averaged streamwise velocity profile $\overline{w}/\overline{w}_n$ (plotted with thick solid curves, where $\overline{w}_n$ is the maximum time-averaged streamwise velocity at the lowest height, $\tilde{z}_n = 42.4$) is close to a Gaussian distribution; and the velocity peak decreases as $\tilde{z}^{-1/2}$ with height. The return flow due to the lateral confinement of the jet could explain the small mismatch between the theory and the experimental results. Friction at the bounding walls has only a second-order effect on the momentum flux (of the order of 10 % compared to the average value of the momentum flux) and thus on the velocity field. Within the flow region studied, we also find that both the eddies (average eddy paths plotted with dashed lines) and the core (time-averaged standard deviation plotted with thin solid lines) are on average self-similar with height, which is not described by the theory and is fundamentally different from either a (fully unconfined planar) two-dimensional jet or a (fully unconfined non-planar) three-dimensional jet, where the turbulence is unconfined and three-dimensional.

The confinement of the jet in a narrow gap undoubtedly changes the structure of the turbulence in the flow with a quasi-two-dimensional inverse cascade allowing large eddies to grow. This persistent growth of eddies is contrary to three-dimensional turbulence. The eddies form within the intense shear layer at the boundary between the jet and the ambient flow when the width b of the jet is larger than the thickness W of the flow (Dracos *et al.*, 1992). Then, the eddy structures appear periodically at a given height. The eddy frequency decreases with height due to merging and we find a well-defined minimum Strouhal number $St \geq 0.07$. The dynamics of these eddies is strongly coupled with the dynamics of the core. The core, which moves on average four times faster and carries approximately 75 % of the momentum flux, flows round the eddies. The consequence of these lateral excursions is seen in the mean velocity field. We believe that the unstable dynamics of the core characterized by its probability density distribution

is principally responsible for the Gaussian profile of the time-averaged stream-wise velocity. In this flow, it is the two-dimensional macrostructure and not the three-dimensional small-scale turbulence that produces the Gaussian distribution.

Therefore, analysing the instantaneous flow field is key to understanding how entrainment, mixing and dispersion occur in the jet. The eddies play a leading role in the entrainment by engulfing ambient fluid at their rear, as we noticed from the study of the streamlines in the core and eddy structure. This entrainment mechanism ensures the linear growth of both the core and the eddies, therefore explaining the self-similarity of these structures. The exchange of fluid between the core and the eddies is permanent and in both directions as streamlines evolve in time from being closed within an eddy to being open and stretched in the core. It is perhaps surprising that the entrainment assumption of Morton *et al.* (1956), modelling entrainment due to three-dimensional turbulent mechanisms, can also describe the fundamentally different two-dimensional case. We find that the entrainment coefficient is $0.052 \leq \alpha \leq 0.068$, depending on how it is calculated. This range of values for the entrainment coefficient is very similar to the values reported in the literature for (fully unconfined planar) two-dimensional jets: for example, 0.060 (Ramaprian & Chandrasekhara, 1985), 0.069 (Albertson *et al.*, 1950). The dyed jet experiments revealed the vigorous mixing effect of the eddies. It is also worth noting that the average dye edge (shown with dotted lines in figure 2.14) coincides with the average outer boundaries of the eddies, which is the physical maximum lateral extent of the jet. Mixing is apparently not as strong in the core, but intense stretching leading to large streamwise dispersion occurs at the interface with the eddies. This region is delimited between the thin solid lines and the dashed lines shown in figure 2.14.

In conclusion, a probabilistic description of the core–eddy structure of quasi-two-dimensional jets leads to a self-similar Gaussian description of the time-averaged flow. The instantaneous flow has a very different character from either (fully unconfined planar) two-dimensional flows or (fully unconfined non-planar) three-dimensional flows. Bulk long-time-averaged properties are consistent with conventional theoretical models, but the mixing and dispersion cannot be accounted for by these time-averaged models. We present a model for this mixing and dispersion in the next chapter.
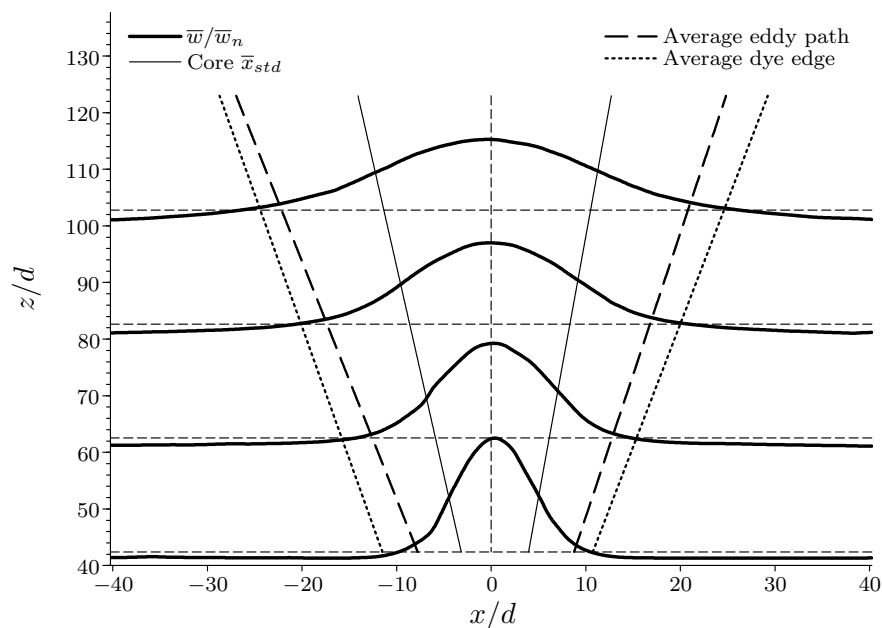
FIGURE 2.14: Distribution at different heights of: normalized time-averaged streamwise velocity $\overline{w}/\overline{w}_n$ (thick solid curves); time-averaged standard deviation of the mean core $\overline{x}_{std}$ (thin solid lines); ensemble-averaged mean trajectory of eddies (dashed lines); and average dye edge (dotted lines).

CHAPTER 3

ADVECTION–DIFFUSION MODEL FOR THE STREAMWISE TRANSPORT, DISPERSION AND MIXING IN QUASI-TWO-DIMENSIONAL JETS

3.1 Introduction

In the event of a spill of pollutants, waste or any other tracers into a river, it is crucial to predict how the tracers are advected and dispersed by the flow after they reach a relatively shallow basin, such as a lake or the sea shelf. Such predictions can be used to monitor the spread of the tracers, control their impact on the environment and assess any potential damage. One of the most important aspects of these shallow river flows, and one which has raised the interest of scientists for more than 20 years, is the emergence of large-scale eddy structures and meanders at some distance away from the river mouth. These eddies and

meanders have been visualized in nature on several occasions due to sediments transported by the flow (see e.g. Giger *et al.*, 1991; Jirka & Uijttewaal, 2004; Rowland *et al.*, 2009). Giger *et al.* (1991) were interested in the entrainment and mixing in shallow water flows, whose characteristic streamwise dimensions were much larger than the fluid-layer thickness and where the flow developed in a confined environment. They showed that these geophysical flows could be reproduced in laboratory experiments by confining plane turbulent jets in the spanwise direction (i.e. the direction parallel to the line source of the jet). Giger *et al.* (1991) observed that in the far field, or for $z/W > 10$ where z is the spatial coordinate in the streamwise direction and W is the fluid-layer thickness in the spanwise direction (i.e. W corresponded to the depth of the basin), the jet produced similar large eddies and meanders as observed in shallow river flows. In Chapter 2, we referred to turbulent plane jets in such a confined geometry in the far field as quasi-two-dimensional jets and considered in detail the meandering flow due to the large-scale eddy structures. The present chapter focuses on the advection and dispersion properties of such quasi-two-dimensional jets, particularly when considering the transport of a passive scalar.

The essential characteristics of quasi-two-dimensional jets have been described previously. Dracos *et al.* (1992) showed that the large planar counter-rotating eddies observed in quasi-two-dimensional jets developed due to an inverse cascade of quasi-two-dimensional turbulence. Chen & Jirka (1998) proved through linear stability analysis that the meanders of the jet were the result of a sinuous instability. According to Jirka & Uijttewaal (2004) the sinuous instability of the jet originated from internal transverse shear across the jet. In Chapter 2, we showed that the time-averaged velocity field of quasi-two-dimensional jets could be modelled using two-dimensional plane jet theory. We also studied the instantaneous velocity field and revealed the interactions between the high-speed meandering core of the jet and the large eddies alternating on its sides. We showed that these core and eddy structures were self-similar with distance and continuously exchanged fluid between themselves, as well as with the ambient fluid surrounding the jet. In particular, the eddies played a key role in the entrainment of ambient fluid by means of engulfment at their rear. Entrained fluid could either be trapped for a brief period in an eddy, where it experienced strong mixing, or be directly incorporated in the core of the jet, where it was advected downstream much more

rapidly. We further hypothesized that because of the difference in advection speed between the core and the eddies (we measured that on average eddies travelled at approximately 1/4 of the speed of the core), initially relatively close fluid parcels entrained by the jet should experience large streamwise dispersion depending on whether they were drawn into the eddies or the core.

In order to study and model the transport, mixing and dispersion of tracers in shallow river flows, we investigate in this chapter the temporal and spatial evolution of the concentration of tracers released in quasi-two-dimensional jets. The mixing properties of turbulent jets have been studied experimentally many times. Uberoi & Singh (1975) measured instantaneous temperature profiles in plane jets and found that they differed from typical time-averaged Gaussian profiles. They reported a relatively well-mixed interior while most of the mixing was performed at the turbulent–non-turbulent interface of the jet. Schefer *et al.* (1994) also noted a difference between the instantaneous distribution and the time-averaged distribution of tracers in the case of three-dimensional round turbulent jets. They attributed this discrepancy to the development of large-scale vortical structures. Arguably, the dynamics of large-scale vortical structures is different in quasi-two-dimensional jets from the case of three-dimensional round or plane jets due to the confinement of the flow in one direction (see Jirka, 2001, for a discussion on large-scale flow structures in shallow flows, or Chapter 2 for quasi-two-dimensional jets specifically). Nevertheless, large-scale vortical structures do have an influence on the mixing and dilution properties of quasi-two-dimensional jets. Giger *et al.* (1991) reported that mixing efficiency and dilution in quasi-two-dimensional jets tended to diminish with distance. From turbulence spectral analysis and intermittency analysis, Dracos *et al.* (1992) argued that the decrease of mixing efficiency was due to the development of quasi-two-dimensional turbulence. Using laser-induced fluorescence in quasi-two-dimensional jets, Chen & Jirka (1999) showed that quasi-two-dimensional turbulence induced patchiness in the time-dependent distribution of the tracer concentration. They found distinct regions of large concentration which corresponded to the large-scale turbulent structures. Jirka (2001) reflected upon the impact of large vortical structures in shallow river flows and emphasized their ability to transport relatively unmixed fluid over large distances.

Despite the large number of experimental studies, there appear to have been

relatively few attempts to provide a comprehensive model of the advection and dispersion processes in quasi-two-dimensional jets. Moreover, most models assume a steady state. Paranthoën *et al.* (1988) suggested a limited model for the initial phase of the dispersion process in a turbulent plane jet. Then, from conservation of mass in a classical plane jet, Chen & Jirka (1999) showed that the decay of the time-averaged concentration of passive tracers $\overline{C}$ along the centreline of quasi-two-dimensional jets followed $\overline{C} \propto z^{-1/2}$. Using conservation of mass and the Reynolds-averaged Navier–Stokes equation with the boundary-layer approximation for three-dimensional round and plane jets, Law (2006) proposed an analytic solution for the time-averaged concentration distribution across the jet. To close the problem, he used the common assumption that the turbulent diffusive term was proportional to the gradient of the time-averaged concentration across the jet. He also assumed that the coefficient of proportionality between these two quantities (i.e. the turbulent diffusivity) was constant across the jet and depended only on the eddy diffusivity and the turbulent Schmidt number (see e.g. Mathieu & Scott, 2000, for more details).

Previous models often assume purely lateral entrainment, and then simple time-averaged streamwise motion. Owing to the cross-stream variation in along-stream velocity (due to the time-dependent core–eddy interaction and the time-averaged Gaussian streamwise velocity distribution) quasi-two-dimensional jets inevitably have significant along-stream dispersion. We want to investigate the implications of this along-stream dispersion for tracer transport and how it affects advection in quasi-two-dimensional jets.

In this chapter, we propose a new one-dimensional model solving the time-dependent effective advection–diffusion equation along the direction of the flow, based on mixing-length theory. Mixing-length theory is appropriate because of the central role of large eddies (scaling with the local jet width) on the dispersion within the flow. We find analytical solutions in similarity form for the case of a constant-flux release and the case of a finite-volume release of tracers, which appear to describe correctly some new experimental measurements of tracer transport. We are able to formulate the general solution for any time-dependent release in integral form, effectively by means of a Green's-function-like solution. We also show the importance of along-stream dispersion mechanisms in quasi-two-dimensional jets, by comparing our full effective advection–diffusion

model with a simple advection model. In § 3.2, we present our model hypothesis starting from the advection–diffusion equation, where the diffusive term models the dispersion by the turbulent flow field of quasi-two-dimensional jets. In § 3.3, we derive analytical solutions for both a constant volume-flux release and an instantaneous finite-volume release. We also show how to generalize the analytical solution for an instantaneous finite-volume release into a solution for an arbitrary time-dependent release. In the next chapter, we compare the theoretical results obtained in this chapter with experimental data. In § 4.1, we describe our experimental procedure. In § 4.2, we first provide a qualitative assessment of our model hypothesis, then we compare our theoretical predictions with experimental data obtained using dye tracking experiments and virtual particle tracking experiments in both the constant-flux and the finite-volume cases. In § 4.3, we analyse the statistical significance of the experimental measurements presented in § 4.2 for the cases of constant-flux releases of dye and instantaneous finite-volume releases of virtual particles. Finally, in § 4.4 we draw our conclusions for both Chapters 3 and 4.

3.2 Turbulent model hypothesis

To characterize the evolution of the concentration of tracers released in quasi-two-dimensional jets, we consider the ideal model of a turbulent momentum jet in a two-dimensional semi-infinite environment. Adopting the same conventions to those used in § 2.4, the flow is considered incompressible and statistically steady. The x-direction is the lateral, cross-jet direction and the z-direction is the streamwise, axial direction. Assuming a plane flow in the domain, the velocity is labelled $\boldsymbol{u} = (u, w)$ in a Cartesian coordinate system (x, z) with the origin at the nozzle exit. The temporal and spatial evolution of the concentration of tracers $C(x, z, t)$ (where t is time) in a two-dimensional steady turbulent jet satisfies (see e.g. Itô, 1992)

$$\partial_t C + \boldsymbol{\nabla} \cdot (\boldsymbol{u} C) = \kappa \Delta C, \tag{3.1}$$

where $\boldsymbol{\nabla}$ is the gradient operator, κ is the molecular diffusivity and Δ is the Laplacian in two dimensions. We take a point-wise ensemble average (i.e. an

ensemble average at each point (x, z, t) in space and time) of equation (3.1)

$$\partial_t C_\mathrm{E} + \boldsymbol{\nabla} \cdot (\boldsymbol{u}_\mathrm{E} C_\mathrm{E}) + \boldsymbol{\nabla} \cdot ([\boldsymbol{u}_\mathrm{F} C_\mathrm{F}]_\mathrm{E}) = \kappa \Delta C_\mathrm{E}, \tag{3.2}$$

where the subscript in X_E denotes the ensemble average of a quantity X and X_F denotes the fluctuations such that $X = X_\mathrm{E} + X_\mathrm{F}$, $[X_\mathrm{F}]_\mathrm{E} = 0$. Thus, the ensemble-averaged concentration is defined as

$$C_\mathrm{E}(x, z, t) = \frac{1}{N} \sum_{n=1}^{N} C_n(x, z, t), \tag{3.3}$$

where N is the total number of realisations of an experiment and n designates the nth realisation. We then make the modelling assumptions that $\boldsymbol{u}_\mathrm{E} C_\mathrm{E}$ behaves as an advective contribution and is equal to $\lambda_1 \overline{\boldsymbol{u}} C_\mathrm{E}$ (where the overbar represents an appropriate average in time and λ_1 is a constant), while $[\boldsymbol{u}_\mathrm{F} C_\mathrm{F}]_\mathrm{E}$ effectively acts diffusively so that $[\boldsymbol{u}_\mathrm{F} C_\mathrm{F}]_\mathrm{E} = -\boldsymbol{D} \cdot \boldsymbol{\nabla} C_\mathrm{E}$ (with $\boldsymbol{D}$ a turbulent eddy diffusive tensor). We expect that advection is governed by the mean flow and dispersion by eddy processes. The term $[\boldsymbol{u}_\mathrm{F} C_\mathrm{F}]_\mathrm{E}$ can be seen as a turbulent flux, which is usually defined as $\overline{\boldsymbol{u}' C'}$ with $\overline{\boldsymbol{u}'} = \overline{C'} = 0$ (Mathieu & Scott, 2000), where $\boldsymbol{u}'$ and C' designate the temporal fluctuations of the velocity field and the temporal fluctuations of the concentration field, respectively. In other words, we assume that the statistical diffusive effect of the turbulent fluctuations is equivalent whether averaged in time or over many realisations. The diffusive effect of $[\boldsymbol{u}_\mathrm{F} C_\mathrm{F}]_\mathrm{E}$ describes and parameterizes physically the interaction between the high-speed core and the growing eddies described in Chapter 2. Therefore, neglecting molecular diffusion under the assumption that it is less significant than eddy diffusion processes (Mathieu & Scott, 2000), equation (3.2) becomes

$$\partial_t C_\mathrm{E} + \lambda_1 \boldsymbol{\nabla} \cdot (\overline{\boldsymbol{u}} C_\mathrm{E}) = \boldsymbol{\nabla} \cdot (\boldsymbol{D} \cdot \boldsymbol{\nabla} C_\mathrm{E}), \tag{3.4}$$

We believe that the interaction between the high-speed core and the growing eddies has a strong streamwise dispersive effect. On the other hand, the cross-jet distribution of the concentration remains confined laterally by two linearly-expanding straight-sided boundaries (as observed in Chapter 2). As we already mentioned, the transport and dispersion of tracers in quasi-two-dimensional jets is more critical along the streamwise direction (Jirka, 2001). Therefore, we choose

to integrate equation (3.4) across the jet

$$\partial_t \phi + \lambda_1 \int_{-\infty}^{\infty} \left(\partial_x \left(\overline{u} C_{\mathrm{E}} \right) + \partial_z \left(\overline{w} C_{\mathrm{E}} \right) \right) \mathrm{d}x = \int_{-\infty}^{\infty} \boldsymbol{\nabla} \cdot \left(\boldsymbol{D} \cdot \boldsymbol{\nabla} C_{\mathrm{E}} \right) \mathrm{d}x, \qquad (3.5)$$

where

$$\phi(z, t) = \int_{-\infty}^{\infty} C_{\mathrm{E}}(x, z, t) \, \mathrm{d}x. \qquad (3.6)$$

Since C_{E} vanishes as $x \to \pm\infty$ and $\overline{u}$ remains finite we have

$$\partial_t \phi + \lambda_1 \partial_z \left(\int_{-\infty}^{\infty} \overline{w} C_{\mathrm{E}} \, \mathrm{d}x \right) = \int_{-\infty}^{\infty} \boldsymbol{\nabla} \cdot \left(\boldsymbol{D} \cdot \boldsymbol{\nabla} C_{\mathrm{E}} \right) \mathrm{d}x. \qquad (3.7)$$

We assume that the eddy diffusive coefficient is independent of x and that, in the streamwise direction, it scales like the local characteristic velocity $\overline{w}_m(z)$ (the maximum time-averaged streamwise velocity in the jet at height z) and the local characteristic size $b(z)$ (the velocity spread rate or e-folding distance of the time-averaged streamwise velocity at height z) of this core and eddy structure, such that

$$D_{zz}(z) \propto b(z)\overline{w}_m(z). \qquad (3.8)$$

This is essentially a 'mixing-length' model (Prandtl, 1925), where the mixing length is the local characteristic width of the jet, and where streamwise transport and dispersion are dominant. Therefore, since $\partial_x C_{\mathrm{E}}$ and $\partial_z C_{\mathrm{E}}$ vanish as $x \to \infty$ and $\boldsymbol{D}$ remains finite equation (3.7) becomes

$$\partial_t \phi + \lambda_1 \partial_z \left(\int_{-\infty}^{\infty} \overline{w} C_{\mathrm{E}} \, \mathrm{d}x \right) \propto \partial_z \left(\overline{w}_m b \, \partial_z \phi \right). \qquad (3.9)$$

We found in (2.5a,b)

$$b(z) = \frac{Q_0{}^2}{\sqrt{2\pi} M_0} \left(4\sqrt{2}\alpha \frac{M_0 z}{Q_0{}^2} + 1 \right) \text{ and } \overline{w}_m(z) = \frac{\sqrt{2} M_0}{Q_0} \left(4\sqrt{2}\alpha \frac{M_0 z}{Q_0{}^2} + 1 \right)^{-1/2},$$
$$(3.10a,b)$$

where α is the entrainment coefficient (Morton *et al.*, 1956), Q_0 is the initial volume flux of the jet, and M_0 is the initial momentum flux, which is conserved with distance in the z-direction (see figure 2.6). The time-averaged streamwise velocity can be further decomposed into a spatial-averaged part and a fluctuating

part:

$$\overline{w} = <\overline{w}> + \hat{\overline{w}}, \tag{3.11}$$

where

$$<\overline{w}> = \frac{1}{2b}\left(\int_{-\infty}^{\infty} \overline{w}\,\mathrm{d}x\right). \tag{3.12}$$

Therefore, we obtain

$$\partial_t\phi + \lambda_1\partial_z\left(<\overline{w}>\phi + \int_{-\infty}^{\infty}\hat{\overline{w}}C_{\mathrm{E}}\,\mathrm{d}x\right) \propto \partial_z\left(\overline{w}_m b\,\partial_z\phi\right). \tag{3.13}$$

We again face a closure problem with the third term on the left-hand side of (3.13), which we address by assuming that this term has an advective effect of the form $<\overline{w}>\phi$. Therefore, considering that $<\overline{w}>\propto\overline{w}_m$, we can introduce two constants k_a and k_d to obtain

$$\partial_t\phi + k_a\,\partial_z\left(\overline{w}_m\phi\right) = k_d\,\partial_z\left(\overline{w}_m b\,\partial_z\phi\right). \tag{3.14}$$

We can rewrite the quantities b and $\overline{w}_m$ using the power laws $(2.5a)$ and $(2.5b)$ (neglecting the virtual origins) respectively, to obtain the effective advection–diffusion equation for the laterally-integrated ensemble-averaged concentration ϕ

$$\partial_t\phi + K_a M_0^{1/2}\,\partial_z\left(\frac{\phi}{z^{1/2}}\right) = K_d M_0^{1/2}\,\partial_z\left(z^{1/2}\partial_z\phi\right), \tag{3.15}$$

where the constants K_a and K_d are a dimensionless advection parameter and a dimensionless dispersion parameter, respectively, which we will determine experimentally. The parameters K_a and K_d can be related to k_a and k_d using $(2.5a)$ and $(2.5b)$ (and, again, neglecting the virtual origins) in the following manner

$$K_a = \frac{k_a}{\left(2\alpha\sqrt{2}\right)^{1/2}} \quad\text{and}\quad K_d = 2k_d\left(\frac{\alpha\sqrt{2}}{\pi}\right)^{1/2}, \tag{3.16a,b}$$

with $\alpha \approx 0.068$ (as calculated in Chapter 2). It is interesting to note that in (3.15) the dispersion term increases with distance like $z^{1/2}$, whereas the advection term decreases with distance like $z^{-1/2}$.

3.3 Mathematical model

In order to test our turbulent model hypothesis, we impose different, appropriate initial, boundary and integral conditions on solutions to the general effective advection–diffusion equation (3.15), for example,

$$\phi(z,0) = 0,\ z > 0, \quad \phi(z,t) \to 0 \ \text{ as } \ z \to \infty, \quad \text{and} \quad \int_0^\infty \phi(z,t)\,\mathrm{d}z \propto t^\vartheta,\ t > 0.$$
$$(3.17a\text{–}c)$$

Equation (3.17a) imposes that the concentration is 0 everywhere initially; equation (3.17b) imposes that, at all time, the concentration vanishes at infinity; and equation (3.17c) imposes that, for $t > 0$, the total integrated concentration evolves as a power law of time. The integral condition (3.17c) effectively controls the release of the passive tracers in the jet.

In this theoretical section, we solve analytically equation (3.15) for three different sets of initial boundary and integral conditions. We consider the simple case of a constant-flux release of passive tracers (i.e. we impose $\vartheta = 1$ in (3.17c)), which we solve by analysing either the concentration (see § 3.3.2) or the concentration flux (see § 3.3.3). In the second case, presented in § 3.3.4, we consider an instantaneous release of a finite volume of passive tracers at the origin of the jet (i.e. we impose $\vartheta = 0$ in (3.17c)). Then, based on the solution for the instantaneous finite-volume release, we show in § 3.3.5 how to formulate, in integral form, the solution for a general and more realistic time-dependent release of tracers governed by an arbitrary source function (i.e. not limited to a power law of time). We give an analytical solution in the case where the source function models a constant-flux release over a finite period of time T_0. We further show that the solutions for the first two simpler cases of a constant-flux release and an instantaneous finite-volume release are the two asymptotic limits of the more general solution when $T_0 \to \infty$ and $t \gg T_0$, respectively.

We choose to solve the problems of a constant-flux release and a finite-volume release because we can reproduce them experimentally, and thus test our turbulent model hypothesis and the various associated assumptions, stated in § 3.2, against experimental measurements (presented in § 4.2). Before deriving the solutions of the three cases, we use below a similarity transformation to simplify the partial differential equation (3.15) into an ordinary differential equation (ODE), which we can then solve.

3.3.1 Similarity transformation

We introduce the dilation transformation

$$\check{z} = \varepsilon^a z, \quad \check{t} = \varepsilon^b t, \quad \check{\phi} = \varepsilon^c \phi(\varepsilon^{-a}\check{z}, \varepsilon^{-b}\check{t}), \tag{3.18}$$

and so equation (3.15) becomes

$$\varepsilon^{b-c}\partial_{\check{t}}\check{\phi} + \varepsilon^{\frac{3}{2}a-c} K_a M_0^{1/2} \, \partial_{\check{z}} \left(\frac{\check{\phi}}{\check{z}^{1/2}} \right) = \varepsilon^{\frac{3}{2}a-c} K_d M_0^{1/2} \, \partial_{\check{z}} \left(\check{z}^{1/2}\partial_{\check{z}}\check{\phi} \right). \tag{3.19}$$

If $b = 3a/2$, then equation (3.15) is invariant under this transformation. This suggests that we look for a solution for (3.15) of the form

$$\phi(z,t) = t^{2c/3a} \, y(\eta) \quad \text{with} \quad \eta = \frac{z}{t^{2/3} M_0^{1/3}}. \tag{3.20}$$

Thus (3.15) becomes

$$\left(\frac{2c}{3a} - \frac{K_a}{2\eta^{3/2}} \right) y + \left(\frac{(2K_a - K_d)}{2\eta^{1/2}} - \frac{2\eta}{3} \right) y' - K_d \eta^{1/2} y'' = 0. \tag{3.21}$$

The general effective advection–diffusion problem has thus been simplified to the ODE (3.21). This second-order ODE, written in similarity form, captures both the temporal and spatial streamwise evolution of the concentration of tracers in quasi-two-dimensional steady turbulent jet. Most importantly, (3.21) allows not only for streamwise advection transport, but also for streamwise turbulent dispersion (based on a mixing-length assumption). Furthermore, we can note that (3.21) depends on the ratio of two dilation constants, c/a. This ratio can be determined using the integral condition (3.17c), which becomes, using (3.20), for $t > 0$,

$$\int_0^\infty \phi(z,t) \, \mathrm{d}z = t^{2c/3a} \int_0^\infty y \left(\frac{z}{t^{2/3}} \right) t^{2/3} M_0^{1/3} \mathrm{d}\eta = M_0^{1/3} t^{\left(\frac{2c}{3a} + \frac{2}{3} \right)} \int_0^\infty y(\eta) \, \mathrm{d}\eta \propto t^\vartheta. \tag{3.22}$$

Therefore, this condition can hold for all $t > 0$ if and only if

$$\frac{c}{a} = \frac{3\vartheta - 2}{2}. \tag{3.23}$$

3.3.2 Constant-flux release: concentration

In the case of a release of tracers at a constant source flux F, if the general effective advection–diffusion equation (3.15) is satisfied for $z > 0$, $t > 0$ and if, in addition, $\phi(z, t)$ satisfies (following (3.17a–c) with $\vartheta = 1$)

$$\phi(z, 0) = 0, \; z > 0, \quad \phi(z, t) \to 0 \; \text{ as } \; z \to \infty, \quad \text{and} \quad \int_0^\infty \phi(z, t)\, \mathrm{d}z = Ft, \; t > 0,$$
$$(3.24a\text{–}c)$$

then the condition (3.24c) can hold for all $t > 0$ if and only if $a = 2c$ according to (3.23) with $\vartheta = 1$. Thus, (3.20) becomes

$$\phi(z, t) = t^{1/3} y(\eta) \quad \text{with} \quad \eta = \frac{z}{t^{2/3} M_0^{1/3}}. \tag{3.25}$$

In this case, the initial boundary value problem for $\phi(z, t)$, defined by (3.21) with $a = 2c$, (3.24a–c) and (3.25), reduces to

$$\left(\frac{1}{3} - \frac{K_a}{2\eta^{3/2}} \right) y + \left(\frac{(2K_a - K_d)}{2\eta^{1/2}} - \frac{2\eta}{3} \right) y' - K_d\, \eta^{1/2} y'' = 0, \tag{3.26}$$

subject to the conditions

$$y(\eta) \to 0 \; \text{ as } \; \eta \to \infty, \quad \int_0^\infty y(\eta)\, \mathrm{d}\eta = \frac{F}{M_0^{1/3}}, \; t > 0. \tag{3.27a,b}$$

Equation (3.26) can then be rewritten using

$$y(\eta) = s^{\frac{1}{3}\left(\frac{K_a}{K_d} - 1\right)} p(s), \quad \text{with} \quad s = \frac{4\eta^{3/2}}{9K_d}, \tag{3.28}$$

to obtain

$$p'' + p' + \left(\frac{\frac{1}{3}\left(\frac{K_a}{K_d} - 2\right)}{s} + \frac{\frac{1}{4} - \left(\frac{1}{3}\left(\frac{K_a}{K_d} - \frac{1}{2}\right)\right)^2}{s^2} \right) p = 0. \tag{3.29}$$

Making the change of variable $p = e^{-s/2}W$, we obtain the Whittaker differential equation (Gradshteyn & Ryzhik, 2007). The Whittaker functions $W_{k,m}[s]$ and $M_{k,m}[s]$ are two linearly independent solutions of the Whittaker differential

equation where

$$k = \frac{1}{3}\left(\frac{K_a}{K_d} - 2\right), \quad m = \frac{1}{3}\left(\frac{K_a}{K_d} - \frac{1}{2}\right). \tag{3.30a,b}$$

Therefore, the solution of (3.29) is

$$p(s) = e^{-s/2}\left(J_W W_{k,m} + J_M M_{k,m}\right)[s], \tag{3.31}$$

where J_W and J_M are constants of integration which will be determined using the boundary conditions (3.27a,b). We can rewrite equation (3.31) in the similarity form

$$y(\eta) = \left(\frac{4\eta^{3/2}}{9K_d}\right)^{\frac{1}{3}\left(\frac{K_a}{K_d}-1\right)} e^{-\frac{2\eta^{3/2}}{9K_d}} \left(J_W W_{k,m} + J_M M_{k,m}\right)\left[\frac{4\eta^{3/2}}{9K_d}\right] = J_W \mathcal{W} + J_M \mathcal{M}, \tag{3.32}$$

defining two linearly independent solutions: $\mathcal{W}$ (involving $W_{k,m}$), and $\mathcal{M}$ (involving $M_{k,m}$) of the underlying equation (3.31). Since $m - k - 1/2 = 0$, we can actually simplify the Whittaker functions $W_{k,m}$ and $M_{k,m}$ (see equations (13.18.5) and (13.18.4) for $W_{m-1/2,m}$ and $M_{m-1/2,m}$, respectively, in National Institute of Standards and Technology, 2011-08-29) to find

$$\mathcal{W}(\eta) = \left(\frac{4\eta^{3/2}}{9K_d}\right)^{1/3} \Gamma\left[\frac{2}{3}\left(\frac{K_a}{K_d} - \frac{1}{2}\right), \frac{4\eta^{3/2}}{9K_d}\right], \tag{3.33}$$

$$\mathcal{M}(\eta) = \frac{2}{3}\left(\frac{K_a}{K_d} - \frac{1}{2}\right)\left(\frac{4\eta^{3/2}}{9K_d}\right)^{1/3} \gamma\left[\frac{2}{3}\left(\frac{K_a}{K_d} - \frac{1}{2}\right), \frac{4\eta^{3/2}}{9K_d}\right], \tag{3.34}$$

where $\Gamma[g, \iota] = \int_\iota^\infty h^{g-1} e^{-h}\, dh$ is the upper incomplete Gamma function and $\gamma[g, \iota] = \int_0^\iota h^{g-1} e^{-h}\, dh$ is the lower incomplete Gamma function. We can prove that, as $\eta \to \infty$,

$$\mathcal{W} \sim e^{-\eta^{3/2}} \eta^{\left(\frac{K_a}{K_d} - \frac{3}{2}\right)}, \quad \mathcal{M} \sim \eta^{1/2}, \tag{3.35a,b}$$

(see equation (8.11.2) in National Institute of Standards and Technology, 2011-08-29, for the asymptotic expansion of the upper incomplete Gamma function) for $K_a > K_d/2$ (we will find later that for our experimental data, K_a appears to be substantially greater than K_d). So, in order to satisfy the far-field boundary condition (3.27a) requiring decay of y, we must have $J_M = 0$ with the solution depending on $\mathcal{W}$ alone. J_W can then be determined using the boundary condition

(3.27b):

$$J_W = \frac{F}{M_0^{1/3} \int_0^\infty \mathcal{W}(\eta) \, \mathrm{d}\eta}. \tag{3.36}$$

Therefore, the general solution of the effective advection–diffusion problem for the case of a constant flux release at the source is, in similarity form, for $K_a > K_d/2$

$$y_F(\eta) = \frac{2F}{3K_d M_0^{1/3} \Gamma\left[\frac{2}{3}\left(\frac{K_a}{K_d} + 1\right)\right]} \eta^{1/2} \Gamma\left[\frac{2}{3}\left(\frac{K_a}{K_d} - \frac{1}{2}\right), \frac{4\eta^{3/2}}{9K_d}\right], \tag{3.37}$$

where $\Gamma[g] = \int_0^\infty h^{g-1} e^{-h} \, \mathrm{d}h$ is the Gamma function. We can note that the laterally-integrated concentration $\phi_F(z, t) = t^{1/3} y_F(\eta)$ (according to equation (3.25) with y_F described in (3.37)) tends towards a simple asymptotic distribution $\phi_F \propto z^{1/2}$ as $t^{2/3} M_0^{1/3} \gg z$ (or $\eta \ll 1$). In the limit $t^{2/3} M_0^{1/3} \gg z$, it appears that the laterally-integrated concentration ϕ_F depends only on z and increases with distance like $z^{1/2}$. On the other hand, we will see in the next chapter that the ensemble-averaged concentration $C_{\mathrm{E},F}$ (see (3.6)) should actually decrease like $z^{-1/2}$, because the experimental cross-jet distribution of ϕ_F spreads linearly with distance (see figure 4.5a). Since the asymptotic distribution of the concentration $C_{\mathrm{E},F}$ is independent of time in the limit $t^{2/3} M_0^{1/3} \gg z$, this asymptotic distribution represents the steady state solution. This finding is in agreement with Chen & Jirka (1999), who also showed that the time-averaged concentration of passive tracers in quasi-two-dimensional jets decays like $\overline{C} \propto z^{-1/2}$ along the jet axis. Note that in the steady-state case, the ensemble average is equivalent to the time average. Mathematically, the concentration $C_{\mathrm{E},F}$ is singular at the origin $z = 0$ and tends to infinity. However, this is not the case in practice because the concentration of tracers must be finite at the source and the jet has a virtual origin z_0.

Interestingly, in the purely advective limit where $K_d \to 0$ (corresponding to a so-called 'top-hat' velocity profile, see e.g. Turner, 1986) equation (3.26) becomes

$$\left(\frac{1}{3} - \frac{K_a}{2\eta^{3/2}}\right) y + \left(\frac{K_a}{\eta^{1/2}} - \frac{2\eta}{3}\right) y' = 0, \tag{3.38}$$

which integrates to

$$y_{F,a}(\eta) = \begin{cases} J_1 \eta^{1/2}, & 0 \leq \eta < \eta_a \\ J_2 \eta^{1/2}, & \eta_a < \eta \end{cases}, \tag{3.39}$$

where J_1 and J_2 are integration constants, and

$$\eta_a = \left(\frac{3K_a}{2}\right)^{2/3} \tag{3.40}$$

is the location of the advective front considering 'top-hat' velocity profiles in the jet. Using the boundary condition at infinity (3.27a), we obtain $J_2 = 0$. J_1 can be determined using the integral condition (3.27b). Therefore, the similarity solution of the purely advective problem for the case of a constant-flux release at the source is

$$y_{F,a}(\eta) = \begin{cases} \dfrac{F}{K_a M_0^{1/3}} \eta^{1/2}, & 0 \leq \eta < \eta_a \\ 0, & \eta_a < \eta \end{cases}. \tag{3.41}$$

We have plotted in figure 3.1 the non-dimensional quantities $y_F / \left(F/M_0^{1/3}\right)$ and $y_{F,a} / \left(F/M_0^{1/3}\right)$. The five different curves show the concentration profile in similarity form for different values of K_a and K_d. As we increase K_a (determining the advection strength), the maximum of the curve is displaced upwards, further away from the origin, while if we increase K_d (determining the dispersion strength), the front drops less rapidly, and there is still asymmetry about the maximum. As expected, without dispersion (i.e. in the 'top-hat' limit $K_d \to 0$) the distribution of tracers $y_{F,a} / \left(F/M_0^{1/3}\right)$ has a discontinuity at η_a, the location of the advective front (defined in (3.40)), where it vanishes.

To study the distribution of y_F, we can compute the location of its centroid normalized with the advective front η_a

$$\mu_F = \frac{\displaystyle\int_0^\infty y_F(\eta) \eta \, \mathrm{d}\eta}{\eta_a \displaystyle\int_0^\infty y_F(\eta) \, \mathrm{d}\eta} \tag{3.42}$$

$$= \frac{3}{5} \left(\frac{3K_d}{2K_a}\right)^{2/3} \frac{\Gamma\left[\frac{2K_a}{3K_d} + \frac{4}{3}\right]}{\Gamma\left[\frac{2K_a}{3K_d} + \frac{2}{3}\right]}, \tag{3.43}$$
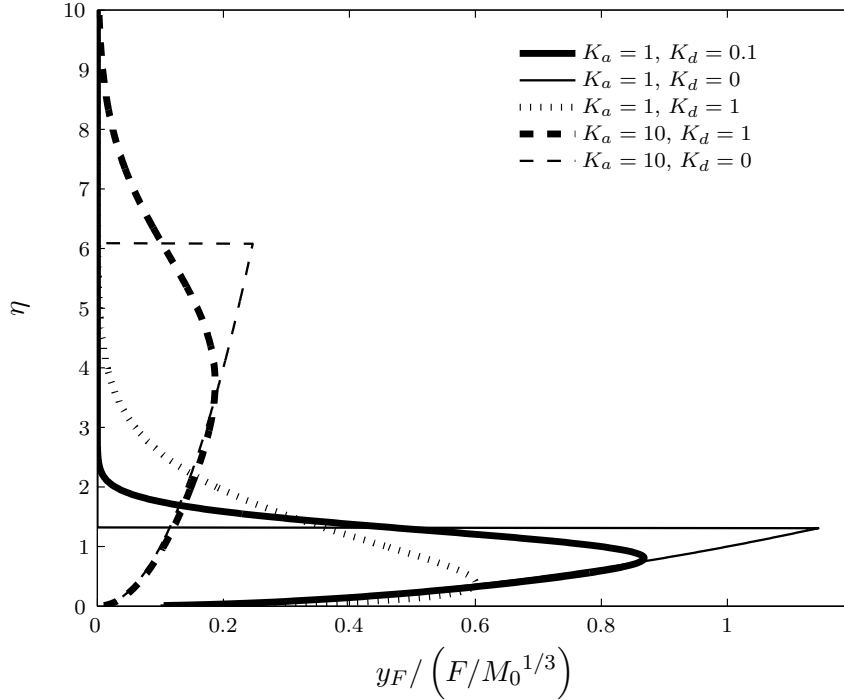
FIGURE 3.1: Variation of the non-dimensional similarity solution $y_F/\left(F/M_0^{1/3}\right)$, defined in (3.37), against the similarity variable $\eta = z/\left(t^{2/3}M_0^{1/3}\right)$ for the problem of advection–dispersion in the case of a constant flux at the source and for different values of the advection and dispersion parameters, K_a and K_d respectively. In the 'top-hat' limit $K_d \to 0$, we use the non-dimensional similarity solution $y_{F,a}/\left(F/M_0^{1/3}\right)$ defined in (3.41).

and its standard deviation normalized with the advective front η_a

$$\sigma_F = \left(\frac{\int_0^\infty y_F(\eta)\eta^2 \, d\eta}{\eta_a{}^2 \int_0^\infty y_F(\eta) \, d\eta} - \mu_F{}^2\right)^{1/2} \tag{3.44}$$

$$= \left(\frac{3K_d}{2K_a}\right)^{2/3}\left(\frac{3\Gamma\left[\frac{2K_a}{3K_d}+2\right]}{7\Gamma\left[\frac{2K_a}{3K_d}+\frac{2}{3}\right]} - \left(\frac{3\Gamma\left[\frac{2K_a}{3K_d}+\frac{4}{3}\right]}{5\Gamma\left[\frac{2K_a}{3K_d}+\frac{2}{3}\right]}\right)^2\right)^{1/2}. \tag{3.45}$$

We plot μ_F in figure 3.2(a). We can see that μ_F decreases when K_a/K_d increases. We can prove that $\mu_F \to 3/5$ as $K_a/K_d \to \infty$ (using equation (5.11.7) in National Institute of Standards and Technology, 2011-08-29), thus meaning that the centroid of y_F recedes behind the advective front at a fixed relative distance. The
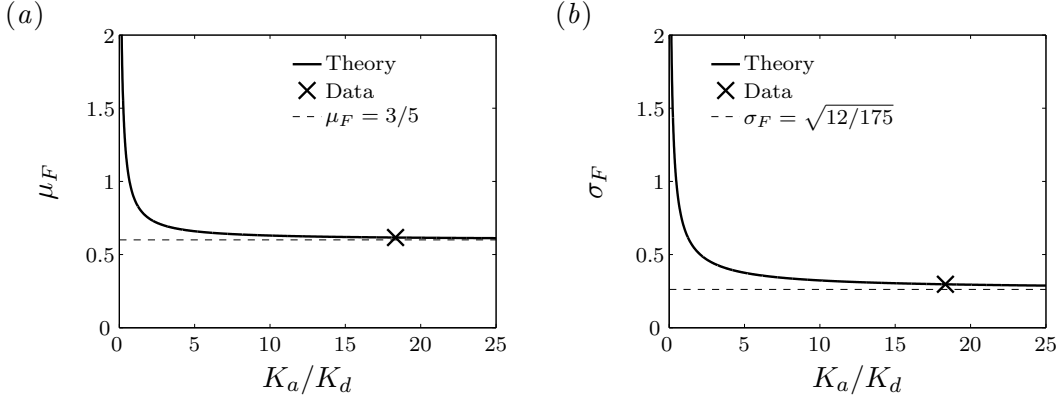
FIGURE 3.2: Constant-flux case for the tracer concentration: (a) plot of the theoretically predicted variation of μ_F (defined in (3.43)), the centroid of y_F (defined in (3.37)) normalized with the advective front η_a (defined in (3.40)), as a function of K_a/K_d (plotted with a solid line), with the experimentally determined value (obtained from the best fit of the constant-flux case shown in figure 4.7) marked with a cross, the asymptotic value of μ_F is plotted with a dashed line; (b) plot of the theoretically predicted variation of σ_F (defined in (3.45)), the standard deviation of y_F normalized with the advective front η_a, as a function of K_a/K_d (plotted with a solid line), with the experimentally determined value (obtained from the best fit of the constant-flux case shown in figure 4.7) marked with a cross, the asymptotic value of σ_F is plotted with a dashed line.

normalized standard deviation σ_F is plotted in figure 3.2(b). σ_F also decreases when K_a/K_d increases. We can prove that $\sigma_F \to \sqrt{12/175}$ as $K_a/K_d \to \infty$ (using equation (5.11.7) in National Institute of Standards and Technology, 2011-08-29).

Moreover, we can observe in figure 3.1 that for the solution y_F of the general effective advection–diffusion problem a non-negligible portion of the volume of tracers is transported faster than the advective speed due to the combined effects of advection and dispersion processes. We can compute the portion of the total volume of tracers β_F which travels ahead of the advective front

$$\beta_F = \frac{\displaystyle\int_{\eta_a}^{\infty} y_F \, \mathrm{d}\eta}{\displaystyle\int_{0}^{\infty} y_F \, \mathrm{d}\eta},$$

(3.46)

using equation (3.37), we obtain

$$\beta_F = \frac{\Gamma\left[\frac{2}{3}\left(\frac{K_a}{K_d}+1\right), \frac{2K_a}{3K_d}\right] - \left(\frac{2K_a}{3K_d}\right)\Gamma\left[\frac{2}{3}\left(\frac{K_a}{K_d}-\frac{1}{2}\right), \frac{2K_a}{3K_d}\right]}{\Gamma\left[\frac{2}{3}\left(\frac{K_a}{K_d}+1\right)\right]}.$$

(3.47)

The ratio β_F remains constant in time and space because (3.47) does not depend on η. Moreover, β_F depends only on the ratio K_a/K_d. We have plotted β_F against K_a/K_d in figure 3.3(a). We can prove that β_F tends asymptotically towards 0 at large K_a/K_d (see equation (8.11.10) in National Institute of Standards and Technology, 2011-08-29), thus meaning that the portion of tracers in the dispersive front becomes smaller as K_a/K_d increases (see figure 3.1 for the change in the distribution of y_F with various K_a and K_d). We can also compute the normalized distance between the average location of the volume of tracers travelling ahead of the advective front and the location of the advective front η_a

$$\xi_F = \frac{1}{\eta_a} \left(\frac{\displaystyle\int_{\eta_a}^{\infty} y_F \, \eta \, \mathrm{d}\eta}{\displaystyle\int_{\eta_a}^{\infty} y_F \, \mathrm{d}\eta} - \eta_a \right), \tag{3.48}$$

which yields

$$\xi_F = \frac{3}{5} \left(\frac{3K_d}{2K_a} \right)^{2/3} \frac{\Gamma\left[\frac{2}{3}\left(\frac{K_a}{K_d} + 2 \right), \frac{2K_a}{3K_d} \right] - \left(\frac{2K_a}{3K_d} \right)^{5/3} \Gamma\left[\frac{2}{3}\left(\frac{K_a}{K_d} - \frac{1}{2} \right), \frac{2K_a}{3K_d} \right]}{\Gamma\left[\frac{2}{3}\left(\frac{K_a}{K_d} + 1 \right), \frac{2K_a}{3K_d} \right] - \left(\frac{2K_a}{3K_d} \right) \Gamma\left[\frac{2}{3}\left(\frac{K_a}{K_d} - \frac{1}{2} \right), \frac{2K_a}{3K_d} \right]} - 1. \tag{3.49}$$

We plot ξ_F against K_a/K_d in figure 3.3(b). The distance ξ_F can be considered as the normalized distance between the dispersive front (average location of the particles travelling ahead of the advective front) and the advective front η_a (defined in (3.40)). In time and space coordinates, the distance between the dispersive front z_F and the advective front z_a is $z_F - z_a = \xi_F \eta_a t^{2/3}$. So the distance between the dispersive front and the advective front increases with time like $t^{2/3}$. We can also see in figure 3.3(b) that $\xi_F \to 0$ as $K_a/K_d \to \infty$, thus meaning that the front becomes sharper as K_a/K_d increases (see also figure 3.1).

3.3.3 Constant-flux release: concentration flux

A somewhat more physically relevant quantity, which we can now study in space and time for the case of a constant-flux release at the source, is the streamwise

(a)

(b)
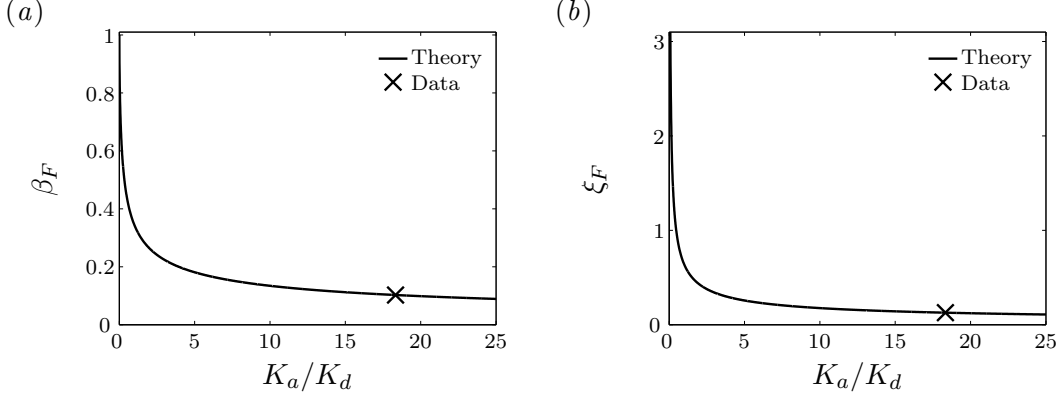
FIGURE 3.3: Constant-flux case for the tracer concentration: (a) plot of the theoretically predicted variation of β_F (defined in (3.47)), the portion of the total volume of tracers released which travels ahead of the advective front η_a (defined in (3.40)), as a function of K_a/K_d (plotted with a solid line), with the experimentally determined value (obtained from the best fit of the constant-flux case shown in figure 4.7) marked with a cross; (b) plot of the theoretically predicted variation of ξ_F (defined in (3.49)), the normalized distance between the average location of the volume of tracers travelling ahead of the advective front and the location of the advective front η_a, as a function of K_a/K_d (plotted with a solid line), with the experimentally determined value (obtained from the best fit of the constant-flux case shown in figure 4.7) marked with a cross.

concentration flux of tracers in a steady quasi-two-dimensional jet, defined as:

$$M_\phi = \int_{-\infty}^{\infty} wC \, \mathrm{d}x. \tag{3.50}$$

We can take the point-wise ensemble average (as defined in (3.3) for the concentration) of (3.50) and, neglecting the second-order turbulent contribution to the flux (Wang & Law, 2002, found that the turbulent mass flux for round turbulent jets was approximately 7.6 % of the mean mass flux, so can be ignored to leading order), we find

$$M_{\phi_\mathrm{E}} = \int_{-\infty}^{\infty} w_\mathrm{E} C_\mathrm{E} \, \mathrm{d}x. \tag{3.51}$$

Using the same modelling assumptions we made in § 3.2, (3.51) becomes

$$M_{\phi_\mathrm{E}} = \lambda_1 \int_{-\infty}^{\infty} \overline{w} C_\mathrm{E} \, \mathrm{d}x, \tag{3.52}$$

where we assume that the ensemble-averaged streamwise velocity is proportional to the time-averaged streamwise velocity. Then, the time-averaged streamwise

velocity can be further decomposed into a spatially-averaged part $< \overline{w} >$, defined in (3.12), and a fluctuating part $\hat{\overline{w}}$, so that

$$M_{\phi_{\mathrm{E}}} = \lambda_1 < \overline{w} > \phi + \lambda_1 \int_{-\infty}^{\infty} \hat{\overline{w}} C_{\mathrm{E}} \, \mathrm{d}x, \qquad (3.53)$$

Again, if we assume that the term $\int_{-\infty}^{\infty} \hat{\overline{w}} C_{\mathrm{E}} \, \mathrm{d}x$ in (3.53) has an advective effect similar to $< \overline{w} > \phi$, M_ϕ can be related to K_a and ϕ as (hereafter omitting the subscript E for simplicity)

$$M_\phi = K_a M_0^{1/2} \frac{\phi}{z^{1/2}}. \qquad (3.54)$$

Therefore, the solution of the concentration flux of tracers for the case of a constant source flux is, for $K_a > K_d/2$,

$$M_\phi(z,t) = y_M(\eta) = \frac{F}{1 - \frac{K_d}{2K_a}} \frac{\Gamma\left[\frac{2}{3}\left(\frac{K_a}{K_d} - \frac{1}{2}\right), \frac{4\eta^{3/2}}{9K_d}\right]}{\Gamma\left[\frac{2}{3}\left(\frac{K_a}{K_d} - \frac{1}{2}\right)\right]}, \ \text{with } \eta = \frac{z}{t^{2/3} M_0^{1/3}}, \quad (3.55)$$

where we use the solution for the laterally-integrated concentration $\phi = \phi_F = t^{1/3} y_F$, with y_F defined in (3.37). In the limit $t^{2/3} M_0^{1/3} \gg z$ (or $\eta \ll 1$), the concentration flux is independent of time or space and tends towards a constant $M_\phi \to F (1 - K_d/(2K_a))$.

For comparison with a purely advective flow, in the limit $K_d \to 0$ (relevant, as already noted, to 'top-hat' velocity profiles) the concentration flux is

$$y_{M,a}(\eta) = \begin{cases} F, & 0 \leq \eta < \eta_a \\ 0, & \eta_a < \eta \end{cases}, \qquad (3.56)$$

according to $y_{F,a}$, defined in (3.41), and (3.54) with $\phi = \phi_{F,a} = t^{1/3} y_{F,a}$.

We have plotted the normalized tracer flux y_M/F as well as $y_{M,a}/F$ in figure 3.4. The five different curves show the concentration profile in similarity form for different values of K_a and K_d. As we increase the advection parameter the flux of tracers extends from the origin into a plateau before dropping smoothly at the front and eventually vanishing at large η. In the purely advective case (i.e. in the 'top-hat' limit $K_d \to 0$), the solution $y_{M,a}/F$ has a discontinuity at the location of the advective front η_a (defined in (3.40)). The steepness of the front tends
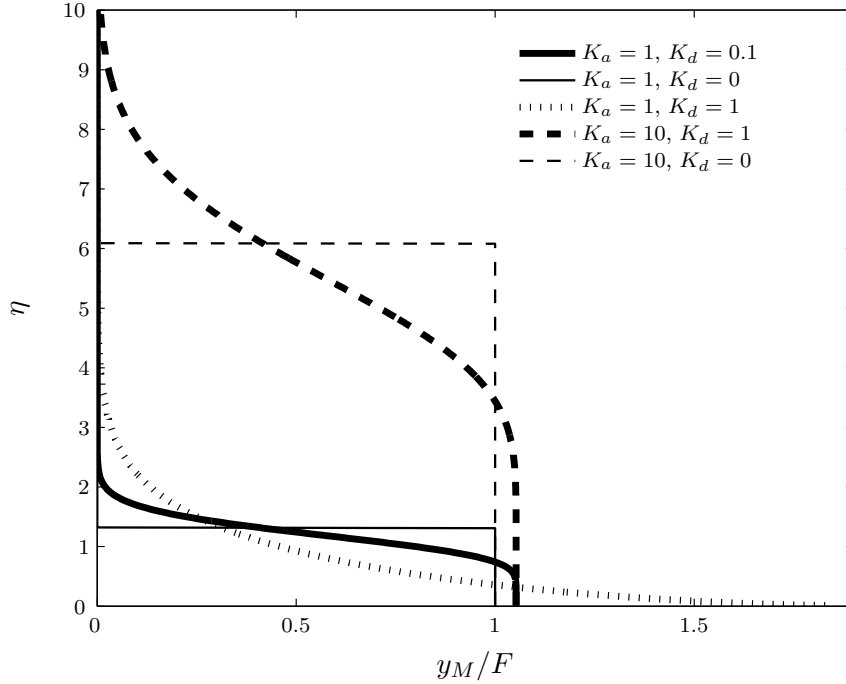
FIGURE 3.4: Plot of the variation of the normalized similarity solution y_M/F, defined in (3.55), against the similarity variable $\eta = z / \left(t^{2/3} M_0{}^{1/3} \right)$ for the concentration flux of tracers in the case of a constant flux at the source F and for different values of the advection and dispersion parameters, K_a and K_d respectively. In the 'top-hat' limit $K_d \to 0$, we use the normalized piecewise-constant similarity solution $y_{M,a}/F$, defined in (3.56).

to decrease with increasing dispersion parameter. Moreover, we can see that the value at the origin $y_M(\eta = 0)/F$ decreases with K_a/K_d, from $y_M(0)/F \to \infty$ as $K_a/K_d \to 0$ to $y_M(0)/F \to 1$ as $K_a/K_d \to \infty$.

Similarly to the previous section, we can compute the centroid of the distribution of y_M normalized with the advective front η_a

$$\mu_M = \frac{\displaystyle\int_0^\infty y_M(\eta)\eta \, \mathrm{d}\eta}{\eta_a \displaystyle\int_0^\infty y_M(\eta) \, \mathrm{d}\eta} \tag{3.57}$$

$$= \frac{1}{2}\left(\frac{3K_d}{2K_a}\right)^{2/3} \frac{\Gamma\left[\frac{2K_a}{3K_d} + 1\right]}{\Gamma\left[\frac{2K_a}{3K_d} + \frac{1}{3}\right]}, \tag{3.58}$$

and its standard deviation normalized with the advective front η_a

$$\sigma_M = \left(\frac{\int_0^\infty y_M(\eta)\eta^2 \, d\eta}{\eta_a{}^2 \int_0^\infty y_M(\eta) \, d\eta} - \mu_M{}^2 \right)^{1/2} \tag{3.59}$$

$$= \left(\frac{3K_d}{2K_a} \right)^{2/3} \left(\frac{\Gamma\left[\frac{2K_a}{3K_d} + \frac{5}{3} \right]}{3\Gamma\left[\frac{2K_a}{3K_d} + \frac{1}{3} \right]} - \left(\frac{\Gamma\left[\frac{2K_a}{3K_d} + 1 \right]}{2\Gamma\left[\frac{2K_a}{3K_d} + \frac{1}{3} \right]} \right)^2 \right)^{1/2}. \tag{3.60}$$

We plot μ_M against K_a/K_d in figure 3.5(a). We can see that, similarly to μ_F (defined in (3.43)), μ_M decreases when K_a/K_d increases. We can prove that $\mu_M \to 1/2$ as $K_a/K_d \to \infty$ (using equation (5.11.7) in National Institute of Standards and Technology, 2011-08-29), thus meaning that the centroid of y_M recedes behind the advective front at a fixed relative distance. The normalized standard deviation σ_M is plotted in figure 3.5(b) against K_a/K_d. Similarly to σ_F (defined in (3.45)), σ_M decreases when K_a/K_d increases. We can prove that $\sigma_M \to \sqrt{3}/6$ as $K_a/K_d \to \infty$ (using equation (5.11.7) in National Institute of Standards and Technology, 2011-08-29).

In a similar fashion to the previous subsection (cf. (3.46) and (3.48)), we can compute the portion of the total concentration flux of tracers β_M which is ahead of the advective front η_a

$$\beta_M = \frac{\int_{\eta_a}^\infty y_M \, d\eta}{\int_0^\infty y_M \, d\eta}, \tag{3.61}$$

using equation (3.55), we obtain

$$\beta_M = \frac{\Gamma\left[\frac{2}{3}\left(\frac{K_a}{K_d} + \frac{1}{2} \right), \frac{2K_a}{3K_d} \right] - \left(\frac{2K_a}{3K_d} \right)^{2/3} \Gamma\left[\frac{2}{3}\left(\frac{K_a}{K_d} - \frac{1}{2} \right), \frac{2K_a}{3K_d} \right]}{\Gamma\left[\frac{2}{3}\left(\frac{K_a}{K_d} + \frac{1}{2} \right) \right]}. \tag{3.62}$$

As before, the ratio β_M remains constant in time and space because (3.62) does not depend on η; and β_M depends only on the ratio K_a/K_d. We have plotted β_M against K_a/K_d in figure 3.6(a). Similarly to β_F, β_M appears to vanish at large K_a/K_d, thus meaning that the portion of the tracer flux in the dispersive front becomes smaller as K_a/K_d increases (see figure 3.4 for the change in the

(a) (b)
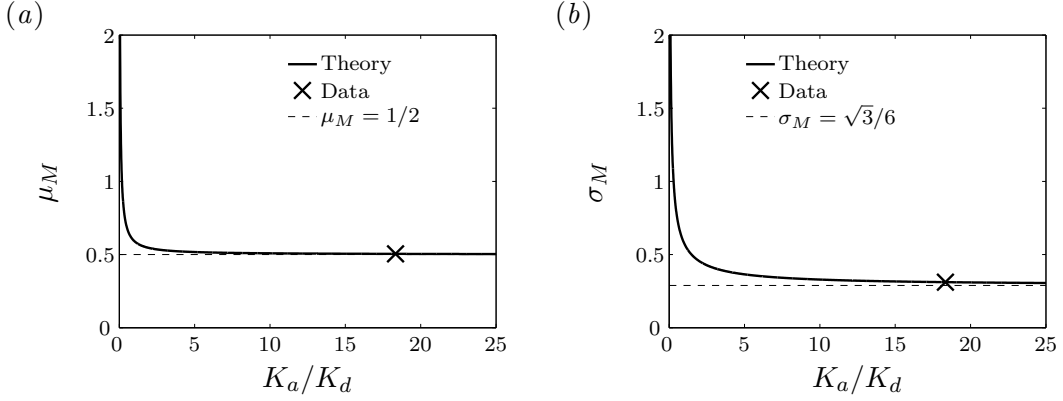
FIGURE 3.5: Constant-flux case for the tracer concentration flux: (a) plot of the theoretically predicted variation of μ_M (defined in (3.58)), the centroid of y_M (defined in (3.55)) normalized with the advective front η_a (defined in (3.40)), as a function of K_a/K_d (plotted with a solid line), with the experimentally determined value (obtained from the best fit of the constant-flux case shown in figure 4.7) marked with a cross, the asymptotic value of μ_M is plotted with a dashed line; (b) plot of the theoretically predicted variation of σ_M (defined in (3.60)), the standard deviation of y_M normalized with the advective front η_a, as a function of K_a/K_d (plotted with a solid line), with the experimentally determined value (obtained from the best fit of the constant-flux case shown in figure 4.7) marked with a cross, the asymptotic value of σ_M is plotted with a dashed line.

distribution of y_M with various K_a and K_d). We can also compute the normalized distance between the average location of the tracer flux ahead of the advective front and the location of the advective front η_a

$$\xi_M = \frac{1}{\eta_a}\left(\frac{\displaystyle\int_{\eta_a}^{\infty} y_M\,\eta\,\mathrm{d}\eta}{\displaystyle\int_{\eta_a}^{\infty} y_M\,\mathrm{d}\eta} - \eta_a\right), \tag{3.63}$$

which yields

$$\xi_M = \frac{1}{2}\left(\frac{3K_d}{2K_a}\right)^{2/3}\frac{\Gamma\left[\frac{2}{3}\left(\frac{K_a}{K_d}+\frac{3}{2}\right),\frac{2K_a}{3K_d}\right] - \left(\frac{2K_a}{3K_d}\right)^{4/3}\Gamma\left[\frac{2}{3}\left(\frac{K_a}{K_d}-\frac{1}{2}\right),\frac{2K_a}{3K_d}\right]}{\Gamma\left[\frac{2}{3}\left(\frac{K_a}{K_d}+\frac{1}{2}\right),\frac{2K_a}{3K_d}\right] - \left(\frac{2K_a}{3K_d}\right)^{2/3}\Gamma\left[\frac{2}{3}\left(\frac{K_a}{K_d}-\frac{1}{2}\right),\frac{2K_a}{3K_d}\right]} - 1. \tag{3.64}$$

We plot ξ_M against K_a/K_d in figure 3.6(b). Similarly to ξ_F (see figure 3.3b), we can also see in figure 3.6(b) that $\xi_M \to 0$ as $K_a/K_d \to \infty$, thus meaning that the front becomes sharper as K_a/K_d increases.
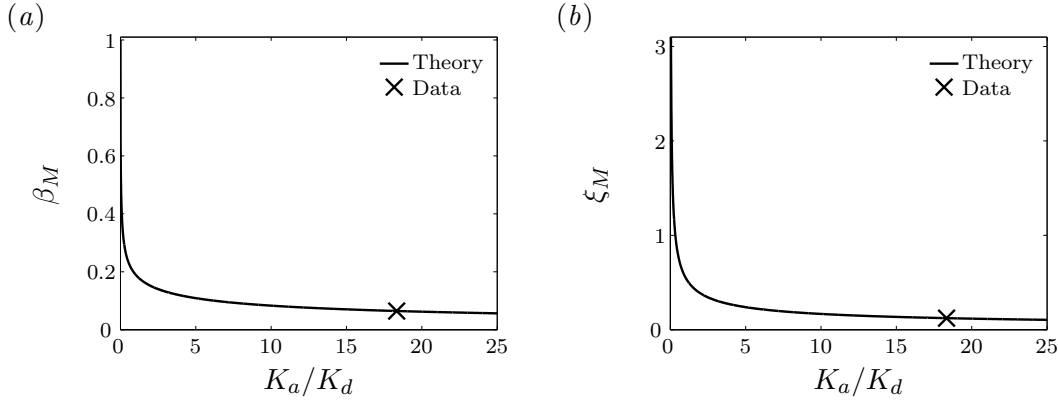
FIGURE 3.6: Constant-flux case for the tracer flux: (*a*) plot of the theoretically predicted variation of β_M (defined in (3.62)), the portion of the total concentration flux of tracers ahead of the advective front η_a (defined in (3.40)), as a function of K_a/K_d (plotted with a solid line), with the experimentally determined value (obtained from the best fit of the constant-flux case shown in figure 4.7) marked with a cross; (*b*) plot of the theoretically predicted variation of ξ_M (defined in (3.64)), the normalized distance between the average location of the concentration flux of tracers ahead of the advective front and the location of the advective front η_a, as a function of K_a/K_d (plotted with a solid line), with the experimentally determined value (obtained from the best fit of the constant-flux case shown in figure 4.7) marked with a cross.

3.3.4 Finite-volume release: instantaneous release fundamental solution

We can also consider an instantaneous finite-volume release localized at the source of a quasi-two-dimensional steady turbulent jet. If the general equation (3.15) is satisfied for $z > 0$, $t > 0$ and if, in addition, $\phi(z,t)$ satisfies (following (3.17a–c) with $\vartheta = 0$)

$$\phi(z,0) = B\delta(z), \quad \phi(z,t) \to 0 \ \text{ as } \ z \to \infty, \quad \int_0^\infty \phi(z,t)\,\mathrm{d}z = B, \ t > 0,$$
$$(3.65a\text{–}c)$$

where B is a constant representing the total volume of tracers released and $\delta(z)$ is a Dirac delta function, then the condition (3.65c) can hold for all $t > 0$ if and only if $c = -a$ according to (3.23) with $\vartheta = 0$. Thus, (3.20) becomes

$$\phi(z,t) = t^{-2/3}y(\eta) \quad \text{with} \quad \eta = \frac{z}{t^{2/3}M_0^{1/3}}. \tag{3.66}$$

In this case, the initial boundary value problem for $\phi(z, t)$, defined by (3.21) with $c = -a$, (3.65a–c) and (3.66), reduces to

$$\left(-\frac{2}{3} - \frac{K_a}{2\eta^{3/2}} \right) y + \left(\frac{(2K_a - K_d)}{2\eta^{1/2}} - \frac{2\eta}{3} \right) y' - K_d \, \eta^{1/2} y'' = 0, \tag{3.67}$$

subject to the conditions

$$y(\eta) \to 0 \ \text{ as } \ \eta \to \infty, \quad \int_0^\infty y(\eta) \, \mathrm{d}\eta = \frac{B}{M_0^{1/3}}, \ t > 0. \tag{3.68a,b}$$

Equation (3.67) can be rearranged

$$-\frac{2}{3} (\eta y)' + K_a \left(\frac{y}{\eta^{1/2}} \right)' - K_d \left(\eta^{1/2} y' \right)' = 0, \tag{3.69}$$

and thus integrated twice to obtain

$$\begin{aligned}
y(\eta) \ &= \ \eta^{K_a/K_d} \exp\left[-\frac{4}{9K_d} \eta^{3/2} \right] \Bigg(J_4 \\
&+ \frac{2J_3}{3} \left(-\frac{4}{9K_d} \right)^{\frac{2}{3}\left(\frac{K_a}{K_d} - 1 \right)} \gamma \left[\frac{2}{3} \left(1 - \frac{K_a}{K_d} \right), -\frac{4}{9K_d} \eta^{3/2} \right] \Bigg),
\end{aligned} \tag{3.70}$$

where J_3 and J_4 are two integration constants and $\gamma[g, \iota] = \int_0^\iota h^{g-1} e^{-h} \, \mathrm{d}h$ is the lower incomplete gamma function. Since $\eta > 0$ and the function $\gamma[g, \iota]$ is complex for $\iota < 0$, J_3 must equal 0. J_4 can be determined by integrating equation (3.70)

$$\int_0^\infty y(\eta) \, \mathrm{d}\eta = J_4 \left(\frac{3}{2} \right)^{\frac{4}{3}\left(\frac{K_a}{K_d} + \frac{1}{4} \right)} K_d^{\frac{2}{3}\left(\frac{K_a}{K_d} + 1 \right)} \Gamma \left[\frac{2}{3} \left(\frac{K_a}{K_d} + 1 \right) \right], \tag{3.71}$$

and applying the integral condition (3.68b) to obtain

$$J_4 = \frac{B}{\left(\frac{3}{2} \right)^{\frac{4}{3}\left(\frac{K_a}{K_d} + \frac{1}{4} \right)} K_d^{\frac{2}{3}\left(\frac{K_a}{K_d} + 1 \right)} \Gamma \left[\frac{2}{3} \left(\frac{K_a}{K_d} + 1 \right) \right] M_0^{1/3}}. \tag{3.72}$$

Therefore, the 'fundamental' solution of the effective advection–diffusion problem for the case of an instantaneous finite-volume release initially localized as a delta

function at $z = 0$ is, in similarity form,

$$y_\delta(\eta) = \frac{B}{\left(\frac{3}{2}\right)^{\frac{4}{3}\left(\frac{K_a}{K_d}+\frac{1}{4}\right)} K_d^{\frac{2}{3}\left(\frac{K_a}{K_d}+1\right)} \Gamma\left[\frac{2}{3}\left(\frac{K_a}{K_d}+1\right)\right] M_0^{1/3}} \eta^{K_a/K_d} \exp\left[-\frac{4}{9K_d}\eta^{3/2}\right].$$

(3.73)

We can note that the concentration $\phi_\delta = t^{-2/3} y_\delta(\eta)$ (from (3.66) with y_δ described in (3.73)) vanishes in time for all values of η, because of the streamwise dispersion (i.e. for $K_d > 0$). Furthermore, we expect the actual concentration C_δ to vanish even more rapidly due to the cross-jet dispersion as the flow transports the finite volume of tracers (see the experimental results in figure 4.5a for finite-volume releases in quasi-two-dimensional jets).

We have plotted the non-dimensional quantity $y_\delta / \left(B/M_0^{1/3}\right)$ in figure 3.7. The three different curves show the concentration profile in similarity form for different values of K_a and K_d. Unsurprisingly, we find that the location of the peak, $\eta_{max} = (3K_a/2)^{2/3}$, only depends on K_a. Thus, increasing K_a shifts the peak upwards (away from the origin), while increasing K_d spreads the width of the distribution. There is always to a greater or lesser extent asymmetry, with the leading edge being more diffuse than the rear.

Interestingly, in the 'top-hat', purely advective limit $K_d \to 0$ equation (3.69) integrates to

$$\left(\frac{K_a}{\eta^{1/2}} - \frac{2\eta}{3}\right) y = J_5,$$

(3.74)

where J_5 is a constant of integration. In order to satisfy the boundary condition at infinity (3.68a) as well as the integral condition (3.68b) we must have $J_5 = 0$ for all $0 \le \eta < \eta_a$ and $\eta_a < \eta$, where $\eta_a = (3K_a/2)^{2/3}$ is the location of the advective front as defined in (3.40) (note that η_a is the same in both the constant-flux case and the finite-volume case). Therefore, the similarity solution of the purely advective problem for the case of an instantaneous finite-volume release initially localized as a delta function at $z = 0$ is

$$y_{\delta,a} = B\delta\left(\eta - \eta_a\right).$$

(3.75)

As expected, without dispersion (i.e. in the 'top-hat' limit $K_d \to 0$) the distribution of tracers remains the same in time (i.e. distributed as the initial Dirac delta function). The delta function is located in the similarity domain at
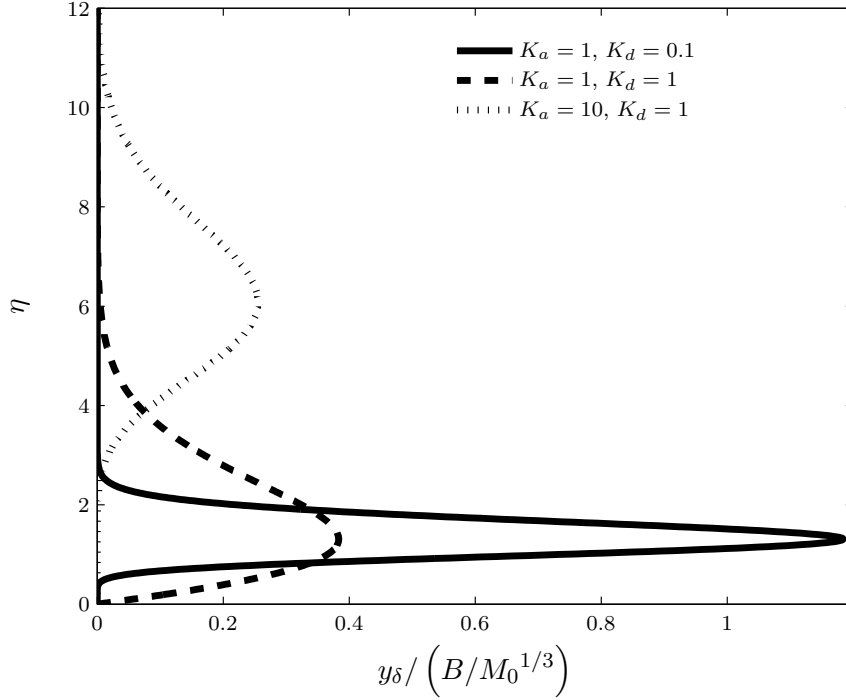
FIGURE 3.7: Plot of the variation of the non-dimensional fundamental similarity solution $y_\delta / \left(B/M_0^{1/3} \right)$, defined in (3.73), against the similarity variable $\eta = z / \left(t^{2/3} M_0^{1/3} \right)$ for the problem of advection–dispersion in the case of an instantaneous finite-volume release at the source and for different values of the advection and dispersion parameters, K_a and K_d respectively.

$\eta_a = (3K_a/2)^{2/3}$, the location of the (purely) advective front. In time and space coordinates, it means that the volume of tracers is located at $z_a = (3K_a/2)^{2/3} t^{2/3}$ and travels at the speed $w_a = K_a M_0^{1/2} z^{-1/2}$ in the streamwise direction. We can notice that the location of the advective front η_a is the same as the location of the peak of the tracer concentration in the general effective advection–diffusion problem: $\eta_a = \eta_{max} = (3K_a/2)^{2/3}$.

Similarly to the previous section, we can compute the centroid of the distribution of y_δ normalized with the advective front η_a

$$\mu_B = \frac{\displaystyle\int_0^\infty y_\delta(\eta)\eta \,\mathrm{d}\eta}{\eta_a \displaystyle\int_0^\infty y_\delta(\eta) \,\mathrm{d}\eta} \tag{3.76}$$

$$\mu_B = \left(\frac{3K_d}{2K_a}\right)^{2/3} \frac{\Gamma\left[\frac{2K_a}{3K_d} + \frac{4}{3}\right]}{\Gamma\left[\frac{2K_a}{3K_d} + \frac{2}{3}\right]}, \tag{3.77}$$

and its standard deviation normalized with the advective front η_a

$$\sigma_B = \left(\frac{\int_0^\infty y_\delta(\eta)\eta^2\,\mathrm{d}\eta}{\eta_a{}^2 \int_0^\infty y_\delta(\eta)\,\mathrm{d}\eta} - \mu_B{}^2\right)^{1/2} \tag{3.78}$$

$$= \left(\frac{3K_d}{2K_a}\right)^{2/3} \left(\frac{\Gamma\left[\frac{2K_a}{3K_d} + 2\right]}{\Gamma\left[\frac{2K_a}{3K_d} + \frac{2}{3}\right]} - \left(\frac{\Gamma\left[\frac{2K_a}{3K_d} + \frac{4}{3}\right]}{\Gamma\left[\frac{2K_a}{3K_d} + \frac{2}{3}\right]}\right)^2\right)^{1/2}. \tag{3.79}$$

We plot μ_B against K_a/K_d in figure 3.8(a). We can see that, similarly to μ_F (defined in (3.43)) and μ_M (defined in (3.58)), μ_B decreases when K_a/K_d increases. We can prove that $\mu_B \to 1$ as $K_a/K_d \to \infty$ (using equation (5.11.7) in National Institute of Standards and Technology, 2011-08-29), thus meaning that the centroid of y_B recedes precisely to the location of the advective front, which is also the location of the peak. It is also important to note that μ_B does not only depend on K_a but actually on the ratio K_a/K_d. Since the distribution is not symmetric with respect to its centroid, then both advection and dispersion processes can affect the centroid. We believe that the underlying physical interpretation of this asymmetry can be related to the asymmetry between the advective and the dispersive terms in the general effective advection–diffusion equation (3.15). The advection term decreases with distance like $z^{-1/2}$, whereas the diffusion term increases with distance like $z^{1/2}$. The normalized standard deviation σ_B is plotted in figure 3.8(b) against K_a/K_d. Similarly to σ_F (defined in (3.45)) and σ_M (defined in (3.60)), σ_B decreases when K_a/K_d increases. We can prove that $\sigma_B \to 0$ as $K_a/K_d \to \infty$ (using equation (5.11.7) in National Institute of Standards and Technology, 2011-08-29). σ_B vanishes at large K_a/K_d because, as we mentioned previously, the concentration becomes distributed spatially according to a Dirac delta function $\delta(z)$.

Similarly to the constant-flux case, in the general effective advection–diffusion problem a non-negligible portion of the volume of tracers is transported faster than the advective speed due to the combined effects of advection and dispersion

(a) (b)
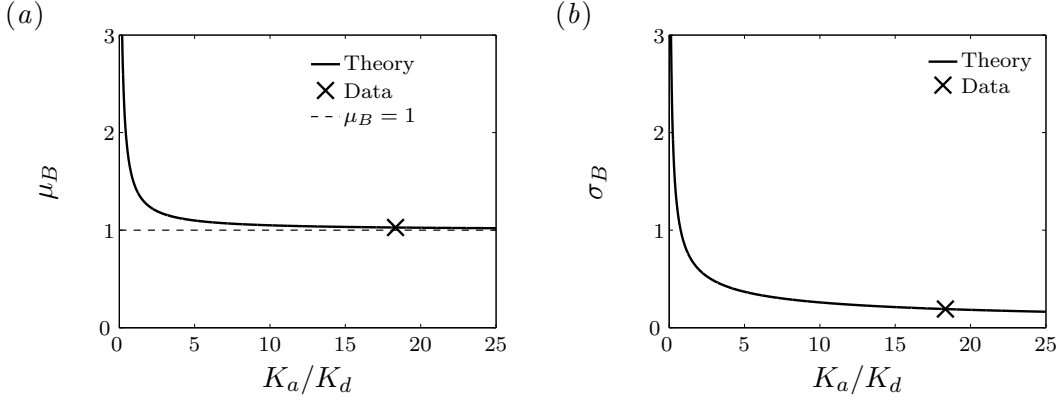
FIGURE 3.8: Instantaneous finite-volume case for the tracer concentration: (a) plot of the theoretically predicted variation of μ_B (defined in (3.77)), the centroid of y_δ (defined in (3.73)) normalized with the advective front η_a (defined in (3.40)), as a function of K_a/K_d (plotted with a solid line), with the experimentally determined value (obtained from the best fit of the constant-flux case shown in figure 4.7) marked with a cross, the asymptotic value of μ_B is plotted with a dashed line; (b) plot of the theoretically predicted variation of σ_B (defined in (3.79)), the standard deviation of y_δ normalized with the advective front η_a, as a function of K_a/K_d (plotted with a solid line), with the experimentally determined value (obtained from the best fit of the constant-flux case shown in figure 4.7) marked with a cross.

processes. We can compute the portion of the total volume of tracers β_B which travels ahead of the advective front

$$\beta_B = \frac{\displaystyle\int_{\eta_a}^{\infty} y_\delta \, \mathrm{d}\eta}{\displaystyle\int_{0}^{\infty} y_\delta \, \mathrm{d}\eta}, \qquad (3.80)$$

using equation (3.73), we obtain

$$\beta_B = \frac{\Gamma\left[\frac{2}{3}\left(\frac{K_a}{K_d}+1\right), \frac{2K_a}{3K_d}\right]}{\Gamma\left[\frac{2}{3}\left(\frac{K_a}{K_d}+1\right)\right]}, \qquad (3.81)$$

where, once again, $\Gamma[g, \iota] = \int_{\iota}^{\infty} h^{g-1} e^{-h} \, \mathrm{d}h$ is the upper incomplete Gamma function. As in the constant-flux release case β_F defined in (3.47), the ratio β_B remains constant in time and space because (3.81) does not depend on η. Moreover, β_B depends only on the ratio K_a/K_d. We have plotted β_B against K_a/K_d in figure 3.9(a). However, in contrast to β_F, we can prove that $\beta_B \to 1/2$ (plotted with a

dashed line) as $K_a/K_d \to \infty$ (see equation (8.11.10) in National Institute of Standards and Technology, 2011-08-29), thus meaning that the distribution of tracers y_δ becomes more symmetrical with respect to the peak value as K_a/K_d increases (see figure 3.7 for the change in the distribution of y_δ with various K_a and K_d). We can also compute the normalized distance between the average location of the volume of tracers travelling ahead of the advective front and the location of the advective front η_a

$$\xi_B = \frac{1}{\eta_a} \left(\frac{\displaystyle\int_{\eta_a}^{\infty} y_\delta \, \eta \, \mathrm{d}\eta}{\displaystyle\int_{\eta_a}^{\infty} y_\delta \, \mathrm{d}\eta} - \eta_a \right), \tag{3.82}$$

which yields

$$\xi_B = \left(\frac{3K_d}{2K_a} \right)^{2/3} \frac{\Gamma\left[\frac{2}{3}\left(\frac{K_a}{K_d} + 2 \right), \frac{2K_a}{3K_d} \right]}{\Gamma\left[\frac{2}{3}\left(\frac{K_a}{K_d} + 1 \right), \frac{2K_a}{3K_d} \right]} - 1. \tag{3.83}$$

We plot ξ_B against K_a/K_d in figure 3.9(b). Similarly to the constant-flux case ξ_F defined in (3.49), the normalized distance ξ_B can also be considered as the distance between the dispersive front (average location of the particles travelling ahead of the advective front) and the advective front η_a. In time and space coordinates, the distance between the dispersive front z_B and the advective front z_a is $z_B - z_a = \xi_B \eta_a t^{2/3}$. This distance increases with time as $t^{2/3}$, as we observed in the constant-flux case. We can also see in figure 3.9(b) that $\xi_B \to 0$ as $K_a/K_d \to \infty$, thus meaning that the spreading of the tracer distribution becomes small compared with the distance between the peak and the origin as K_a/K_d increases (see also figure 3.7).

3.3.5 Finite-volume release: time-dependent release general solution

The solution $\phi_\delta(z, t) = t^{-2/3} y_\delta(\eta)$ is the response of the system described by the effective advection–diffusion equation (3.15) to a finite volume released instantaneously at $t = 0$ and distributed spatially according to a Dirac delta function $\delta(z)$. Due to the linearity of equation (3.15), we can construct from this 'fundamental' solution ϕ_δ an integral expression for the general solution ϕ_g for a finite volume B being released at the origin $z = 0$ over a period of time such that $\phi_g(0, t) = f(t)$.

(a) (b)
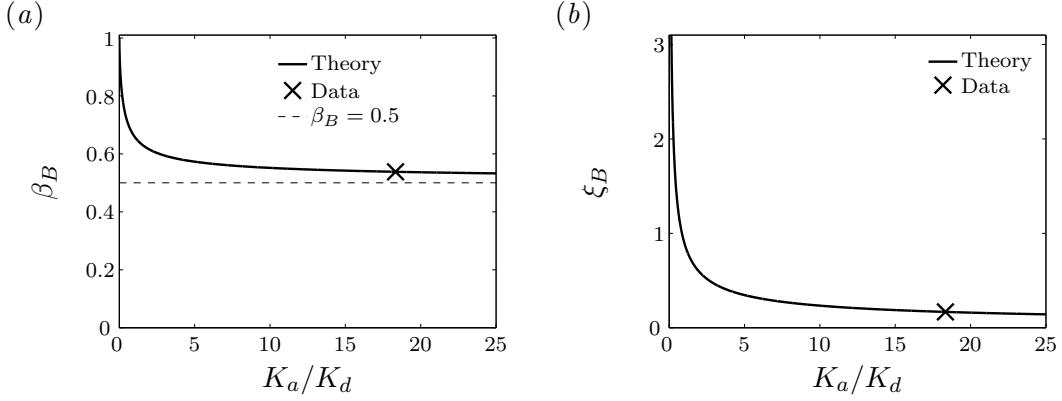
FIGURE 3.9: Finite-volume case for an instantaneous release: (a) plot of the theoretically predicted variation of β_B (defined in (3.81)), the portion of the total volume of tracers released which travels ahead of the advective front η_a (defined in (3.40)), as a function of K_a/K_d (plotted with a solid line), with the experimentally determined value (obtained from the best fit of the constant-flux case shown in figure 4.7) marked with a cross, and the asymptotic value $\beta_B = 0.5$ is plotted with a dashed line; (b) plot of the theoretically predicted variation of ξ_B (defined in (3.83)), the normalized distance between the average location of the volume of tracers travelling ahead of the advective front and the location of the advective front η_a, as a function of K_a/K_d (plotted with a solid line), with the experimentally determined value (obtained from the best fit of the constant-flux case shown in figure 4.7) marked with a cross.

Without loss of generality, we choose to normalize the source function $f(t)$:

$$\int_{-\infty}^{\infty} f(t)\, \mathrm{d}t = 1. \tag{3.84}$$

Therefore, the general solution ϕ_g can be expressed as the following integral

$$\phi_g(z,t) = \int_0^t (t-\tau)^{-2/3}\, y_\delta(\eta_\tau) f(\tau)\, \mathrm{d}\tau, \quad \text{with} \quad \eta_\tau = \frac{z}{(t-\tau)^{2/3} M_0^{1/3}}. \tag{3.85}$$

The case of a truly instantaneous release of a finite volume at $(z,t) = (0,0)$ is physically impossible to realize in an experiment. It is also not ideal in the modelling of real flows. A more realistic set of initial boundary conditions is to have a finite volume released at a constant flux over a finite period of time $0 \le t \le T_0$. This problem can be defined in terms of the following conditions

$$\phi_{T_0}(z,t) \to 0 \ \text{ as } \ z \to \infty, \quad \int_0^\infty \phi_{T_0}(z,t)\, \mathrm{d}z = \begin{cases} \dfrac{Bt}{T_0}, & 0 \le t \le T_0 \\ B, & T_0 < t \end{cases}, \tag{3.86a,b}$$

with ϕ_{T_0} satisfying the general equation (3.15) for $z > 0$, $t > 0$. The solution to this initial boundary value problem can be computed using equation (3.85) with the source function

$$f_{T_0}(t) = \frac{H(t) - H(t - T_0)}{T_0},\tag{3.87}$$

where H is the Heaviside function (i.e. $H(t) = 0$ for all $t < 0$ and $H(t) = 1$ for all $t > 0$). We find that the solution to the integral (3.85) with the source function f_{T_0} described by (3.87) is

$$\phi_{T_0}(z, t) = \frac{2Bz^{1/2}}{3K_d M_0^{1/2} T_0 \Gamma\left[\frac{2}{3}\left(\frac{K_a}{K_d} + 1\right)\right]} \left(\Gamma\left[\frac{2}{3}\left(\frac{K_a}{K_d} - \frac{1}{2}\right), \frac{4z^{3/2}}{9K_d M_0^{1/2} t}\right] \right.$$

$$\left. - \begin{cases} 0, & 0 < t \leq T_0 \\ \Gamma\left[\frac{2}{3}\left(\frac{K_a}{K_d} - \frac{1}{2}\right), \frac{4z^{3/2}}{9K_d M_0^{1/2}(t - T_0)}\right], & T_0 < t \end{cases} \right). \tag{3.88}$$

The upper incomplete Gamma function, $\Gamma[g, \iota] = \int_{\iota}^{\infty} h^{g-1}e^{-h}\, dh$, requires $g > 0$, hence this solution is well-defined only for $K_a > K_d/2$. As we mentioned previously, we will find later that for our experimental data K_a appears to be substantially greater than K_d. Note that this solution cannot be written in similarity form because of the dependence on the time constant T_0.

We can prove (see Appendix A.1) that the solution $\phi_{T_0}(z, t)$, described in (3.88), satisfies

$$\phi_{T_0}(z, t) = \phi_\delta(z, t), \quad \text{for} \quad \frac{t}{T_0} \gg 1. \tag{3.89}$$

So, the general solution for a rectangular source function converges asymptotically to the fundamental solution $\phi_\delta(z, t)$ (defined by (3.73) and (3.66)) in the limit $t \gg T_0$. It is interesting to study how fast ϕ_{T_0} converges towards ϕ_δ. We can non-dimensionalize the distance z and the time t using the scalings for length and time scales $T_0^{1/3}M_0^{1/3}$ and T_0, respectively, such that

$$z = T_0^{1/3}M_0^{1/3}\breve{z}, \quad t = T_0\breve{t}, \tag{3.90a,b}$$

where breves denote non-dimensional variables. The evolution in time of the normalized absolute deviation of the general solution ϕ_{T_0} from the fundamental

63
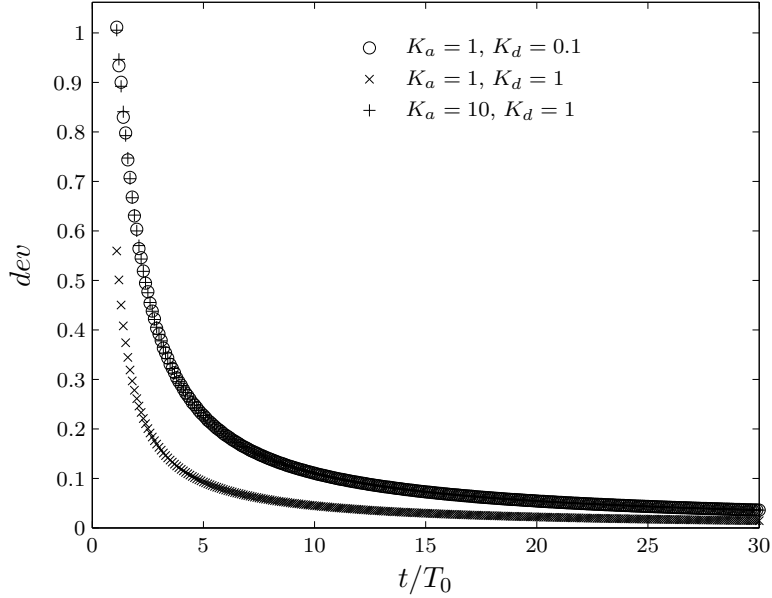
FIGURE 3.10: Variation with scaled time $\check{t} = t/T_0$ of the normalized absolute deviation $dev(\check{t})$, defined in (3.91), of the general solution $\phi_{T_0}(z, t)$, defined in (3.88), and the fundamental solution $\phi_\delta(z, t)$ (defined by (3.73) and (3.66)). The data are computed numerically for different values of the advection and dispersion parameters.

solution ϕ_δ is

$$dev(\check{t}) = \frac{\int_0^\infty |\phi_{T_0}(\check{z}, \check{t}) - \phi_\delta(\check{z}, \check{t})| \, \mathrm{d}\check{z}}{\int_0^\infty \phi_\delta(\check{z}, \check{t}) \, \mathrm{d}\check{z}}, \quad \text{for} \quad \frac{t}{T_0} \geq 1, \tag{3.91}$$

a non-dimensional quantity which only depends on the advection and dispersion parameter K_a and K_d, and in particular does not depend on the total injected volume of tracers B, on the initial momentum M_0 or on the period of injection T_0. We plot $dev(\check{t})$ in figure 3.10 for $1 \leq t/T_0 \leq 30$. We compute the deviation numerically for three different sets of values of K_a and K_d. We can see that all the curves decrease asymptotically towards 0 as t/T_0 increases. The deviation is smaller than 0.1 (which can be considered as a threshold value of near convergence) for $t/T_0 > 11$, $t/T_0 > 4.7$ and $t/T_0 > 11$ for the sets of advection and dispersion parameters $(K_a = 1, K_d = 0.1)$, $(K_a = 1, K_d = 1)$ and $(K_a = 10, K_d = 1)$, respectively. It appears that the deviation depends mainly on the ratio K_a/K_d and only very weakly on K_d.

Furthermore, we can note that in equation (3.88), if we take the limit $T_0 \to \infty$

and define $F = B/T_0$, then we find

$$\phi_{T_0 \to \infty}(z, t) = t^{1/3} y_F(\eta), \qquad (3.92)$$

with $\eta = z/\left(t^{2/3} M_0^{1/3}\right)$ consistently with (3.25). So, equation (3.37) is equivalent to the asymptotic solution of the general solution ϕ_{T_0} if the period of release T_0 extends to infinity.

We have developed in this chapter a theoretical model, for various source conditions, describing the streamwise transport and dispersion in quasi-two-dimensional jets. In the following chapter we test the predictions of this model through comparison with a range of experimental measurements.

STREAMWISE TRANSPORT, DISPERSION AND MIXING IN QUASI-TWO-DIMENSIONAL JETS: EXPERIMENTAL RESULTS

4.1 Experimental procedure

We conduct our experiments in a slight modification of the experimental apparatus we presented in Chapter 2, as shown schematically in figure 4.1. We conduct three distinct sets of experiments using two qualitatively different techniques. Each set of experiments is designed to provide experimental data that can be compared with the three theoretical predictions derived in Chapter 3 for: a constant-flux release; an instantaneous finite-volume release; and a non-instantaneous finite-volume release. In the first set of experiments (whose results are presented in § 4.2.2), we measure the distribution of the concentration of dye
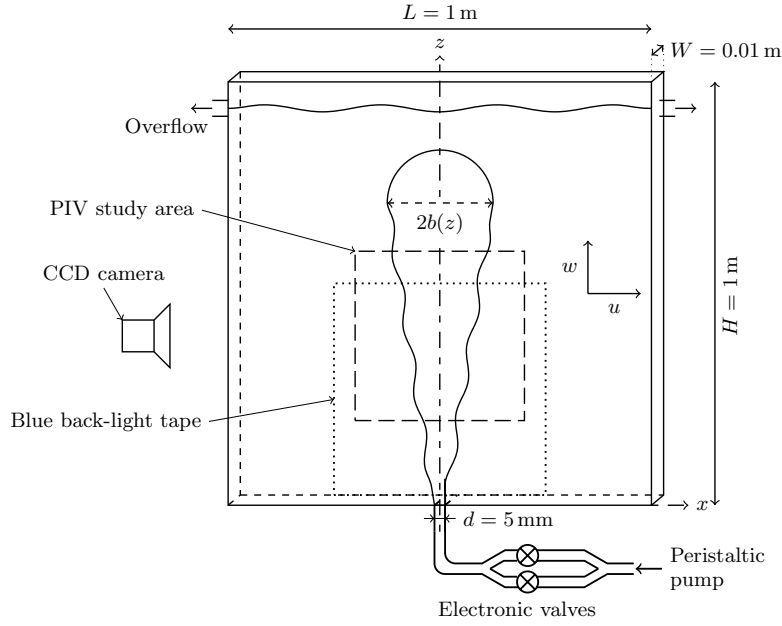
FIGURE 4.1: Schematic diagram of the experimental apparatus.

as it is released at a constant flux at the source of quasi-two-dimensional steady turbulent jets. The second set of experiments (whose results are presented in § 4.2.3) involves what we believe to be a new technique, which consists of tracking large quantities of virtual particles evolving as passive tracers in the velocity field of quasi-two-dimensional steady turbulent jets. The velocity field is measured in experiments with real jets (as opposed to numerically computed jets) by using particle image velocimetry. We designed this technique, which we designate as virtual particle tracking, to obtain data for an instantaneous release to compare with our mathematical model (derived in Chapter 3). In the third set of experiments (whose results are presented in § 4.2.4), we measure the distribution of the concentration of dye as it is released as finite volumes at the origin of quasi-two-dimensional steady turbulent jets. For physical reasons, which will be detailed below, we cannot release finite volumes of dye instantaneously in the jets, and so such physical dye releases inevitably extended over a finite time interval.

4.1.1 Constant-flux releases of dye

We fill the $1\,\mathrm{m}$ $(L) \times 0.01\,\mathrm{m}$ $(W) \times 1\,\mathrm{m}$ (H) tank displayed in figure 4.1 with fresh tap water. A vertical jet of constant source volume flow rate is discharged into the

tank using a peristaltic pump (520DU/R2 Watson-Marlow variable speed pump) fed by a constant-head tank.

The injection mechanism for the constant-flux releases of dye in steady turbulent quasi-two-dimensional jets consists of a syringe-pump connected to a small needle inserted into a single main tube. The needle is located 0.2 m upstream of the nozzle. After the jet has reached a steady state in the tank, a mixture of red food dye 'Fiesta Red' (Allura Red AC, E129) and tap water (with a dye concentration of 1.8 % per weight) is injected at a constant flow rate, 0.11 cm^3 s^{-1} . We study 19 constant-flux releases of dye in steady turbulent jets with jet Reynolds number $2240 \leq Re_j = dw_s/\nu \leq 3870$, where w_s is the source velocity and ν is the kinematic viscosity of water.

To measure the dye concentration, we perform the experiments in a dark room. Following Dalziel *et al.* (2008) we attach a 0.54 m × 0.54 m electroluminescent Light Tape (Electro-LuminX Lighting Corporation) to the external surface of the rear side of the tank, centred on the jet axis and with the bottom of the tape at the height of the nozzle. It provides a constant and uniform source of near-monochromatic cyan light of approximately 400 cd m^{-2}. This wave length is close to the peak of the 'Fiesta Red' dye absorption spectrum. We measure the transmitted light intensity with a high-speed 8 bit grey-scale camera (Fastcam SA1.1 - Photron) mounted with an 85 mm focal-length lens (f-stop 5.6). The camera is located 3 m away from the tank, which is sufficient to have negligible parallax error. We also take care to reduce any light pollution from reflection or other sources, in particular by installing a black frame around the study area. The camera records 640 × 848 pixel images covering the entire study area, which spans $-40 \leq x/d \leq 40$ and $0 \leq z/d \leq 100$ (where x is the coordinate in the lateral, cross-jet direction, and z is the coordinate in the streamwise direction; the origin is at the centre of the nozzle slot and $d = 5$ mm is the nozzle width), and part of the black frame (in order to have a black intensity reference). For each video we set the origin in time, $t = 0$, at the image preceding the first image in which dye is seen by the camera. The frequency of image acquisition is set at 60 frames per second. Following the calibration method and the algorithm described by Coomaraswamy (2011) and based on Cenedese & Dalziel (1998), we perform the calibration in situ. We record the intensity measured by the camera for 23 known concentrations of dye, ranging from 0 to 2 % per weight. A fitting

curve using a third-order polynomial in the logarithm of the normalized intensity gives us a continuous and monotonic relationship between the intensity and the spanwise- (or y-) integrated concentration. All the images recorded by the camera, either for the calibration process or for the experiments, are analysed using the software code DigiFlow (Sveen & Dalziel, 2005). This procedure enables us to obtain accurate measurements of the (spanwise-integrated) dye concentration in time and space for each experiment.

4.1.2 Instantaneous finite-volume releases of clusters of virtual particles

We track virtual particles in experimentally measured velocity fields of quasi-two-dimensional steady turbulent jets. We use the velocity fields measured by us previously as presented in Chapter 2 and obtained using a particle-image-velocimetry technique (as described in Sveen & Dalziel, 2005). We measure the jet velocity in a $0.4\,\mathrm{m} \times 0.4\,\mathrm{m}$ study area centred on the jet axis (as shown in figure 4.1) and covering a height from $z = 0.2$–0.6 m. We use the camera described above (mounted with a $62\,\mathrm{mm}$ focal-length lens) at a frequency of image acquisition 250 frames per second and for a duration of 21.8 s. The 1024×1024 pixel images provide us with spatially and temporally resolved velocity fields for six steady turbulent jets at source volume flow rates 33.2, 37.0 and $40.3\,\mathrm{cm}^3\,\mathrm{s}^{-1}$. The jet Reynolds number ranges from $3320 \leq Re_j \leq 4030$. We find that the divergence of each velocity field is insignificant (typically $mean(|\boldsymbol{\nabla} \cdot \boldsymbol{u}|)/mean(|\boldsymbol{\nabla} \times \boldsymbol{u}|) \approx 5\,\%$, where $mean(\cdot)$ represents an average in time and space), so they can be considered as incompressible. Using these computed velocity fields, we seed in each of them 201×51 pixel clusters of (massless) virtual particles located in a rectangular evenly-distributed cluster at $-8.8 \leq x/d \leq 7$ and $44.4 \leq z/d \leq 48.3$ (i.e. within the characteristic local width of the jet). The release can be considered instantaneous as a cluster of virtual particles is injected in the flow field within a single time step. The possibility of releasing instantaneously a large number of particles constitutes the main reason for the use of this technique in this study. This important advantage, compared with the non-instantaneous dye finite-volume releases (discussed below), allows us to reproduce more easily the instantaneous release constraint imposed in the mathematical model in (3.65a).

We release individual clusters every 0.4s in each experiment and study a total of

256 clusters representing 2,624,256 virtual particles. For each cluster the virtual particles evolve in time and space as passive tracers transported by the flow. For each simulation we set the origin in time, $t = 0$, at the first image in which the particle cluster is seeded. The simulation of a cluster stops as soon as a virtual particle reaches the top boundary of the velocity field. Finally, we record the location in time and space of the tracers and analyse the results using DigiFlow. By averaging 256 virtual-particle experiments we obtain a smooth distribution of the particle concentration in time and space, which we compare with the dye experiments and the theoretical prediction in § 4.2.

Different techniques involving particle tracking have been used to study dispersion, mixing and transport in jets or other types of flows. In previous studies, the particles were either real and tracked by imaging analysis technique (see e.g. Yang *et al.*, 2000; Sveen & Dalziel, 2005), or purely numerical and evolving in numerically resolved flows (see e.g. Dutkiewicz *et al.*, 1993; Luo *et al.*, 2006; Picano *et al.*, 2010). However, we have not been able to find any mention in the literature of using virtual particles in the velocity field of real flows. This technique requires a spatially and temporally resolved computation of the velocity field, which can be done, for example, using a particle-image-velocimetry technique. We can then seed some (massless) virtual particles in the velocity field and track their trajectory as they are transported as passive tracers by the flow. The advantages of this technique are numerous: the resolution is only limited by the resolution of the acquisition of the velocity field; it is not restricted to the computation limitations encountered in full numerical simulations, but can be used for any laboratory experiments; a large quantity of virtual particles can be seeded instantaneously in the jet (thus satisfying, in our case, the constraint imposed in the theoretical model for an instantaneous finite-volume release); and their initial distribution can be completely arbitrary.

4.1.3 Finite-volume releases of dye

The experimental procedure for the finite-volume releases of dye in steady turbulent quasi-two-dimensional jets is very similar to the experimental procedure for the constant-flux releases of dye (described in § 4.1.1). We fill the tank displayed in figure 4.1 with fresh tap water. A vertical jet of constant source volume flow rate is discharged into the tank using the same peristaltic pump described above

and fed by a constant-head tank.

For the injection mechanism of the finite-volume releases of dye, the main tube divides into two approximately 80 cm before the nozzle (see figure 4.1). The two tubes are recombined approximately 15 cm before the nozzle. Two valves located just before the recombining junction control the flow for each pipe separately. We monitor the valves to allow the flow to go through one section or the other exclusively. We open and close the valves electronically so that a steady jet flow is maintained in the tank before and after switching the valves. Although we observe a small perturbation (a pressure wave) in the tank we believe it does not perturb the experiment significantly. The purpose of this two-tube system is to release a finite volume of dye in a steady turbulent jet. The procedure for each experiment is as follows. We inject a 5 cm^3 mixture of the same red food dye described above and tap water (with a dye concentration of 2 % per weight) into the closed tube approximately 5 mm upstream of the valve. Meanwhile, water flows at a constant source volume flow rate through the other tube to produce a turbulent jet in the tank. After the jet reaches a steady state, we switch the valves to redirect the whole flow into the section containing the red dye, thus releasing a finite volume of dye into the established jet. We conduct 26 finite-volume releases of dye in steady turbulent jets with jet Reynolds number $2170 \leq Re_j \leq 4870$. It is important to note that, although great care is taken during the experiments and different protocols have been tested, instantaneous finite-volume releases of dye cannot be achieved for practical reasons. We find that the time of injection, although relatively short (of the order of 0.5 s), cannot be considered as instantaneous, as we will discuss in § 4.2.4. We believe that the main reason for this injection delay is due to some Taylor dispersion (Taylor, 1953) of the dye as it is transported in the short section of tube (approximately 0.2 m long) leading to the tank.

We perform the measurements of the dye concentration for the finite-volume releases using exactly the same technique as described for the constant-flux releases. From the transmitted light intensity recorded by the high-speed camera described above, we can compute the dye concentration in the study area, spanning $-40 \leq x/d \leq 40$ and $0 \leq z/d \leq 100$, at a frequency of 60 frames per second. We obtain accurate measurements of the dye concentration in time and space for each experiment.

4.2 Experimental results

Similarly to $(2.7a,d)$, we find that the natural scalings for length and time in our problem are d, the source width, and (d^2/Q_0), respectively. Therefore when considering our experimental data we will always scale quantities with these scalings, i.e.

$$z = d\tilde{z}, \quad t = \left(\frac{d^2}{Q_0}\right)\tilde{t}, \tag{4.1a,b}$$

where tildes denote non-dimensional variables. Although the initial momentum flux M_0 is also a natural scaling parameter in the theoretical model (see equations $(2.5b)$, (3.15) and (3.20)), we do not use it as a scaling parameter in this section because we could not measure it directly in the experiments. Instead of M_0, we use the equivalent ratio Q_0^2/d (in § 2.4, we found $M_0 \approx < \overline{M} > = 0.55 \left(Q_0^2/d\right)$, where $< \overline{M} >$ is the space- and time-averaged momentum flux in quasi-two-dimensional jets). In particular, the non-dimensional similarity variable $\eta = z/\left(t^{2/3}M_0^{1/3}\right)$, defined in the model (see § 3.3.1), is replaced by $\eta_{exp} = z/\left(t^{2/3}\left(Q_0^2/d\right)^{1/3}\right)$, so that

$$\frac{\eta_{exp}}{\eta} = \left(\frac{dM_0}{Q_0^2}\right)^{1/3} \approx 0.82. \tag{4.2}$$

This non-dimensionalization also affects slightly the advection and dispersion parameters K_a and K_d, defined in the model (see § 3.2). As a consequence, the advection and dispersion parameters $K_{a,exp}$ and $K_{d,exp}$, that we use in this section, are related to K_a and K_d such that

$$\frac{K_{a,exp}}{K_a} = \frac{K_{d,exp}}{K_d} = \left(\frac{dM_0}{Q_0^2}\right)^{1/2} \approx 0.74. \tag{4.3}$$

We omit the subscript exp in η_{exp}, $K_{a,exp}$ and $K_{d,exp}$ hereafter in this section.

To test our turbulent model hypothesis developed in § 3.2 and which led to the general effective advection–diffusion (3.15), we choose to compare the theoretical predictions, developed in § 3.3, first with experiments realized in the constant-flux case. The initial boundary and integral conditions $(3.24a–c)$ imposed in the constant-flux case are simpler to satisfy experimentally than the initial boundary and integral conditions imposed in the finite-volume case $(3.65a–c)$, which require an instantaneous release of finite volumes of tracers. Instantaneous finite-volume releases of virtual particles are then tested against the theoretical prediction,

before studying the more challenging case of a non-instantaneous finite-volume release of dye. In each case, we are particularly interested in whether the natural scaling of the model $z \propto t^{2/3}$ agrees with the experimental results and, if so, we then estimate from the experimental data the two key parameters: the advection parameter K_a and the dispersion parameter K_d. Since the experiments in the constant-flux case are simpler to realize, we believe that the estimates of K_a and K_d measured in this case are more accurate than in the other two cases. Therefore, we consider the values of K_a and K_d measured in the constant-flux case as reference values, while the values measured in the other two cases are used to determine the confidence interval of K_a and K_d. Before presenting the quantitative experimental results, we give below a qualitative assessment of our turbulent model hypothesis and motivate the utility of the virtual-particle-tracking technique (described in § 4.1.2) in understanding the transport, dispersion and mixing properties of quasi-two-dimensional jets.

4.2.1 Qualitative assessment

The purpose of this qualitative assessment is two-fold. Firstly, we want to study how the dynamical structure of steady turbulent quasi-two-dimensional jets affects their transport and dispersion properties. We have developed our turbulent model hypothesis, stated in § 3.2, from the qualitative understanding of these properties. Secondly, we use in this study a new technique to analyse the transport and dispersion properties of the jets, which we introduced in the previous section as virtual particle tracking. We give a qualitative overview of this technique, as well as some justifications and motivations for its use in a more systematic and rigorous approach to obtain quantitative results (which will be presented in § 4.2.3).

As we discussed in Chapter 2, in the far-field of quasi-two-dimensional jets (i.e. $z \geq 20\,d$ for $W = 2\,d$ Dracos *et al.*, 1992), the core forms a high-speed undulating region, which grows on average in an expanding straight-sided triangular section. Outside the core we observe large counter-rotating eddies, which develop on alternate sides of the core and grow linearly with distance. Moreover, we showed in Chapter 2 that the core–eddy structure is self-similar with distance z. The characteristic sinuous core and the large growing eddies can be observed in figure 4.2(a), which is an instantaneous grey-scale picture of a constant-flux release of dye in a steady-state quasi-two-dimensional jet with $Re_j = 3850$ (shown five
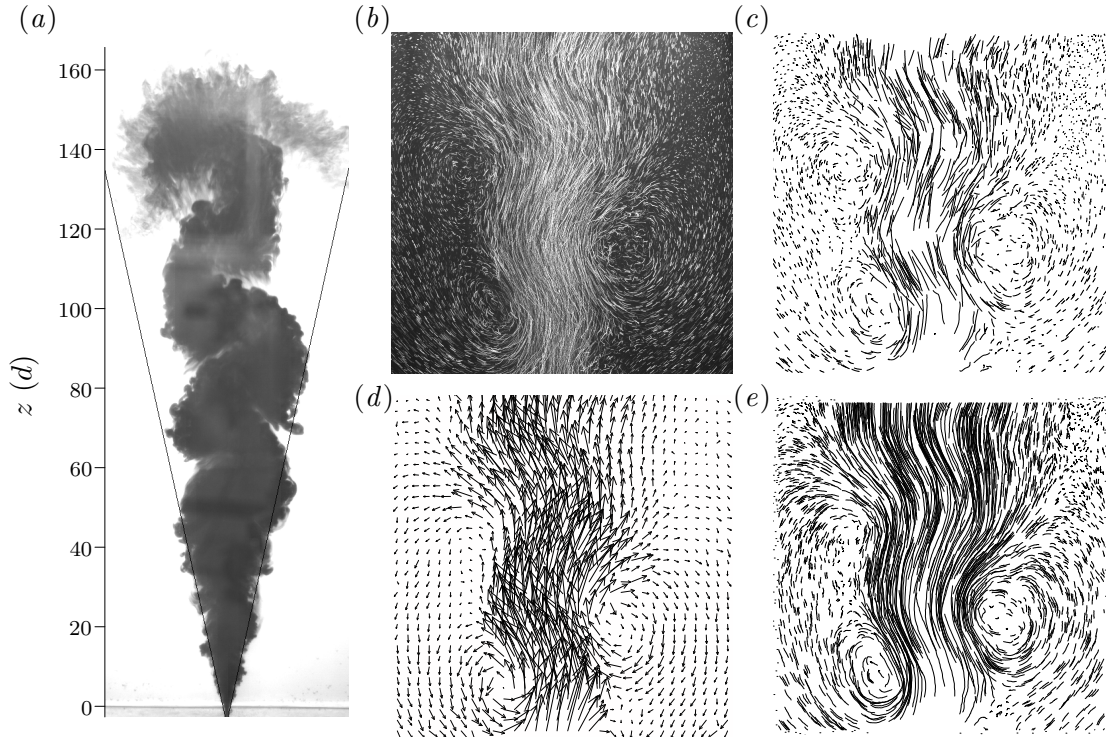
FIGURE 4.2: (*a*) Grey-scale picture of a dyed jet ($Re_j = 3850$) rising in the tank. The average dye edges are plotted with black lines (half-spreading angle, $< \theta_{dye} >= 12.4°$, as measured in figure 2.5). (*b*) Passive tracers (Pliolite particles) shown as streaks in a typical jet ($Re_j = 4080$). (*c*) Trajectories of the passive tracers shown in (*b*) and identified by imaging analysis (for a duration of 0.2 s). (*d*) Instantaneous velocity field (arrows) of the jet shown in (*b*). (*e*) Trajectories of virtual particles (for approximately 0.3 s) seeded at the same initial locations as the particles identified in (*c*) and evolving as passive tracers in the time-dependent velocity field shown in (*d*).

seconds after injection; the average dye edges are plotted with black lines, half-spreading angle $< \theta_{dye} >= 12.4°$, as measured in figure 2.4). The instantaneous core–eddy structure can also be seen in figure 4.2(*b*). In figure 4.2(*b*), a superposition of 50 images (i.e. for a duration of 0.2 s) of the filming of an experiment (see § 2.2), where passive tracers (0.23 mm Pliolite VTAC particles) were mixed with a quasi-two-dimensional jet ($Re_j = 4080$), depicts the tracers as streaks, thus revealing the Eulerian structures in the flow (see discussion in § 2.5).

We compute two different types of results from the experiment with passive tracers shown in figure 4.2(*b*). We can consider the tracers as Lagrangian particles and track their trajectory in time using a particle tracking algorithm implemented in DigiFlow (Dalziel, 1992; Sveen & Dalziel, 2005). Figure 4.2(*c*) shows

the trajectories identified by the algorithm, at the same time instant as the jet displayed in figure 4.2(*b*). Particles have been tracked for 50 images (i.e. for a duration of 0.2 s) and reveal very similar flow patterns to the streaks in figure 4.2(*b*). However, this technique has some limitations as the number of particles tracked for a certain time period decreases quickly with increasing time period. We have also very little control over the initial distribution of the particles (usually spatially homogeneous), and cannot, for example, reproduce an instantaneous finite-volume release of these particles. To remedy these limitations, we have developed a virtual-particle-tracking technique, which we presented in § 4.1.2. We seed in the velocity field (displayed in figure 4.2*d*) of the experimental jet shown in figure 4.2(*b*) some virtual particles in order to track their trajectory as they are advected as passive tracers by the flow. As a qualitative validation of this technique, we have seeded the virtual particles so that their initial distribution is identical to the initial distribution of the (real) particles identified in figure 4.2(*c*). The resulting trajectories of the virtual particles are plotted in figure 4.2(*e*) for a period of approximately 0.3 s. The trajectories of the virtual particles are very similar to the trajectories of the particles in figures 4.2(*b*) and 4.2(*c*), and thus reveal the same core–eddy structure. We believe that the virtual-particle-tracking technique can provide meaningful information about the transport and dispersion properties of quasi-two-dimensional jets.

The schematic diagram displayed in figure 4.3(*a*) summarizes the structure of quasi-two-dimensional jets. The time-averaged mean picture of quasi-two-dimensional jets is associated with a triangular shape encapsulating all the flow structures, while the time-dependent picture shows a sinuous core flanked by large growing eddies. We believe that the interaction between the core and the eddies results in large streamwise dispersion as the fluid experiences intense stretching at the interface between the core and the eddies. The eddies also play a crucial role in the entrainment and mixing of ambient fluid. From the observations of dyed jets such as the jet illustrated in figure 4.2(*a*), we find that fluid can be entrained from the ambient by the eddies and then either drawn within the eddies or incorporated into the core. We also believe that fluid can be exchanged between the eddies and the core. On the other hand, we have not observed any dyed fluid being detrained completely from the jet to the ambient.

These processes can be revealed by applying the virtual-particle-tracking tech-

nique to the core and the eddies of a quasi-two-dimensional jet. In the velocity field of the jet presented in figure 4.2(*d*) and reproduced in figure 4.3(*b*), we seed three clusters of virtual particles. The first cluster, composed of 3721 virtual particles, distributed in a square and initially seeded at the centre of an eddy is shown in light grey in figure 4.3(*b*). The second cluster, composed of 7381 virtual particles, distributed in a rectangle and initially seeded between the eddy and the core is shown in grey in figure 4.3(*b*). The last cluster, composed of 3721 virtual particles, distributed in a square and initially seeded in the core of the jet is shown in dark grey in figure 4.3(*b*). Figure 4.3(*c*) shows the typical trajectories of one single particle from each cluster. The particle locations are plotted every 0.02 s and each colour corresponds to a time period of 0.2 s (see colour scale). The particle starting in the eddy (plotted with pluses) moves slower than the other two particles and its trajectory forms two loops characteristic of the fact that it is transported within the eddy. The particle starting in the core (plotted with crosses) is transported quickly and has a slightly sinuous trajectory, which is characteristic of the transport within the core. On the other hand, the trajectory of the particle chosen approximately at the interface between the eddy and the core (see § 2.5 for a thorough discussion on the identification of the core and eddy structures) is often more complex (plotted with squares) and can be transported from the core to the eddy, or indeed from the eddy to the core. In the present case the particle starts in the core and then is drawn into the neighbouring eddy as the trajectory forms one loop. This is a simple illustration of the possible exchange of fluid parcels between the different structures.

Figure 4.4 shows the simultaneous evolution in time of all the particles in the three clusters as they are passively transported by the jet velocity field shown in figure 4.3(*b*). Each colour corresponds to a particular time instant, starting from black and finishing with white and with a time step of 0.2 s between each colour (we use the same colour scale to that used in figure 4.3c). Again, we can clearly see that the virtual particles are transported much faster in the core of the jet (see figure 4.4*c*) than in the eddy (see figure 4.4*a*). On the other hand, mixing is more intense in the eddy than in the core. The cluster initially seeded in the eddy disintegrates very rapidly compared to the cluster initially seeded in the core. The cluster initially seeded between the eddy and the core (see figure 4.4*b*) experiences considerable stretching in the streamwise direction (its streamwise
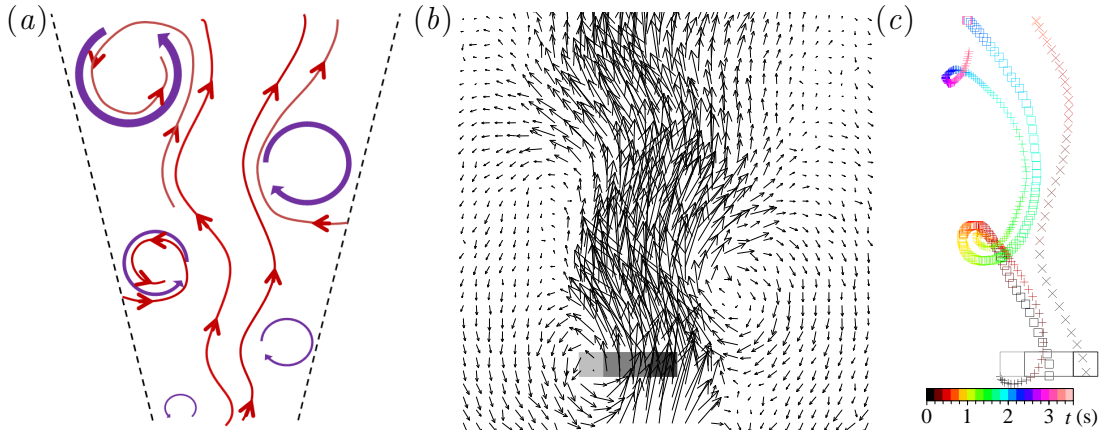
FIGURE 4.3: (*a*) Schematic diagram describing the structure of quasi-two-dimensional jets. (*b*) Instantaneous velocity field displayed in figure 4.2(*d*) with three rectangular clusters of virtual particles initially seeded: at the centre of an eddy (plotted in light grey); between the eddy and the core (plotted in grey); and in the core of the jet (plotted in dark grey). (*c*) Typical trajectories of three virtual particles evolving in the time-dependent velocity field shown in (*b*) and initially seeded: in an eddy (cluster outlined in light grey) (plotted with pluses); between the eddy and the core (cluster outlined in grey) (plotted with squares); and in the core (cluster outlined in dark grey) (plotted with crosses). The particle locations are plotted every 0.02 s and each colour corresponds to a time period of 0.2 s (see colour scale).

maximum extent is ten times larger than its cross-stream maximum extent after a few time steps), owing to the shear layer at the interface between the core and the eddy. We can notice that some virtual particles are drawn into the eddy while others remain in the core. This emphasizes the time-dependent exchange of fluids between the core and the eddies pointed out above. We can also observe the delaying effect (with the colour scheme) of the eddies, in which tracers have a longer residency time than in the core. In Chapter 5, we investigate further the turbulent relative dispersion of the particle clusters presented in figure 4.4.

When ensemble-averaged, we believe that the streamwise dispersive mechanisms revealed by the virtual particles in figure 4.4 can be modelled as an enhanced dispersion coefficient, as stated in the turbulent hypothesis presented in § 3.2. The main assumption we make in equation (3.8), pertaining to the turbulent eddy diffusive coefficient ($D_{zz} \propto b\,\overline{w}_m$, where D_{zz} is the streamwise component of the turbulent eddy diffusive tensor), can be physically justified from the study of both the structures and the velocity profile of quasi-two-dimensional jets (see figures 2.5, 2.7 and 2.13 for velocity measurements in quasi-two-dimen-
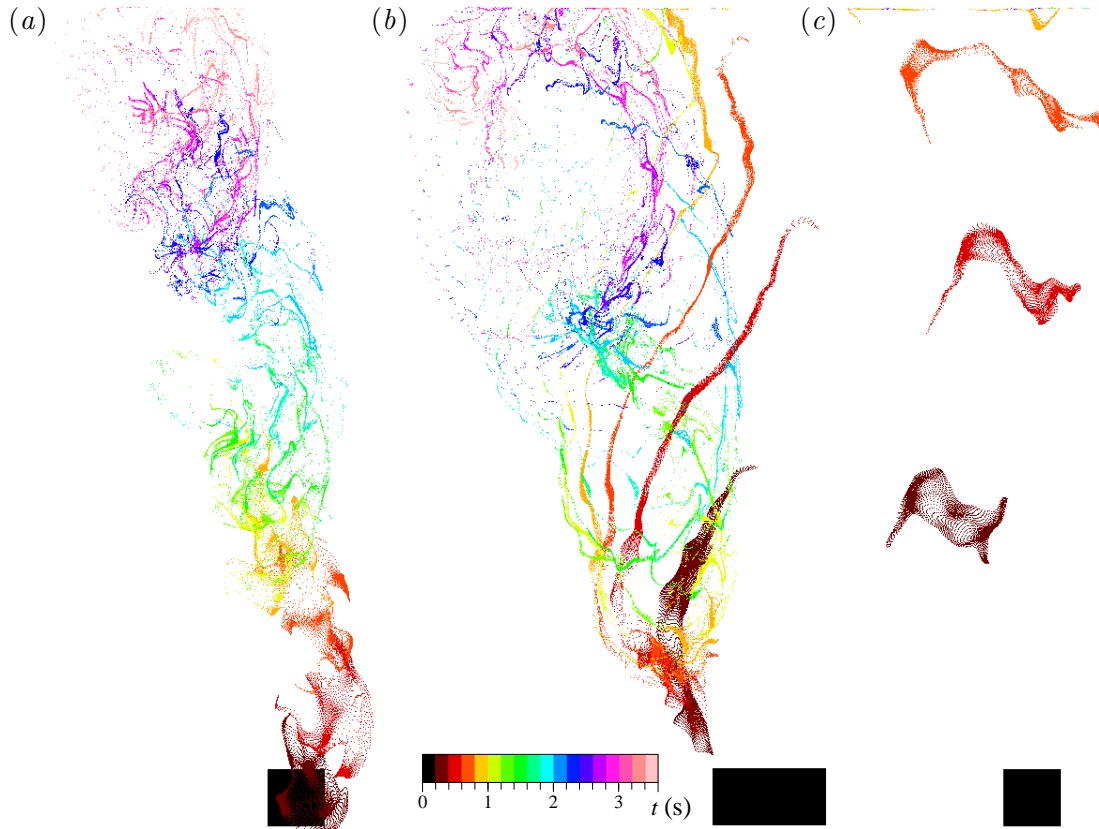
FIGURE 4.4: Evolution in time of the virtual particles seeded in the velocity field shown in figure 4.3(b) as they are transported by the flow (each colour corresponds to a particular time instant): (a) cluster initially distributed at the centre of an eddy and shown in light grey in figure 4.3(b); (b) cluster initially distributed between the eddy and the core and shown in grey in figure 4.3(b); (c) cluster initially distributed in the core of the jet and shown in dark grey in figure 4.3(b). Each colour corresponds to a time period of 0.2 s, the colour scale shown at the bottom of (b) is the same to that used in figure 4.3(c).

sional jets). The core–eddy structure is self-similar with height, thus the local characteristic size of the jet, $b(z)$, appears as a relevant length-scale. Moreover, the local maximum time-averaged streamwise velocity is the second physically meaningful variable in the problem of dispersion, because all mixing and dispersive mechanisms should scale like $\overline{w}_m(z)$. In the rest of this section, we compare ensemble-averaged experimental results with the theoretical predictions found in § 3.3 and based on our turbulent model hypothesis.

4.2.2 Constant-flux releases of dye

We present in figures 4.5(a–c) experimental results and theoretical predictions of constant-flux releases of dye in quasi-two-dimensional steady turbulent jets. The spatial distribution of the concentration $C(x, z, t)$ is plotted using a colour scale (see colour scale at the top of figures 4.5a–c) at different non-dimensional times, $74 \leq \tilde{t} \leq 374$, to show the evolution of the dye concentration in the jet. In figure 4.5(a), we plot the ensemble-averaged concentration of the 19 experiments, which were conducted at different jet Reynolds number, $2240 \leq Re_j \leq 3870$ (see § 4.1.1). We also plot the average dye edges (half-spreading angle, $< \theta_{dye} >= 12.4°$) with thick white lines and the average boundaries of the core (half-spreading angle, $7°$ starting from $z = 20$ d) with thin white lines. We can observe some dispersion of the dye at the leading edge, which indicates the streamwise dispersion discussed above. It is also apparent that the dye is transported first through the core (i.e. within the thin white lines) before mixing across the full width of the jet (i.e. filling the triangle delimited by the average dye edges shown with thick white lines). The characteristic sinuous instability of the core (clearly visible in figure 4.2a) does not appear in figure 4.5(a) because of the averaging process.

Our model is inherently one-dimensional, and so obviously cannot predict the distribution of the concentration across the jet (i.e. in the x-direction). In order to be able to solve the partial differential equation (3.4), we integrate the concentration along the x-axis and study the evolution of $\phi(z, t)$ rather than $C(x, z, t)$. We present the laterally-integrated experimental concentration $\phi_{F,exp}(z, t)$ in figure 4.5(b) in normalized and re-distributed form using

$$C(x, z, t) = \begin{cases} \dfrac{\phi_{F,exp}(z, t)}{2l(z)}, & -l(z) \leq x \leq l(z) \\ 0, & \text{otherwise} \end{cases} , \qquad (4.4)$$

where

$$l(z) = \tan\left(< \theta_{dye} >\right)(z - z_0), \quad \text{for} \quad z \geq 0 \qquad (4.5)$$

is the local lateral distance between the average dye edges (plotted with thick white lines in figure 4.5a) and z_0 is the space virtual origin defined below in (4.7a). Alongside in figure 4.5(c), we show the equivalent theoretical prediction
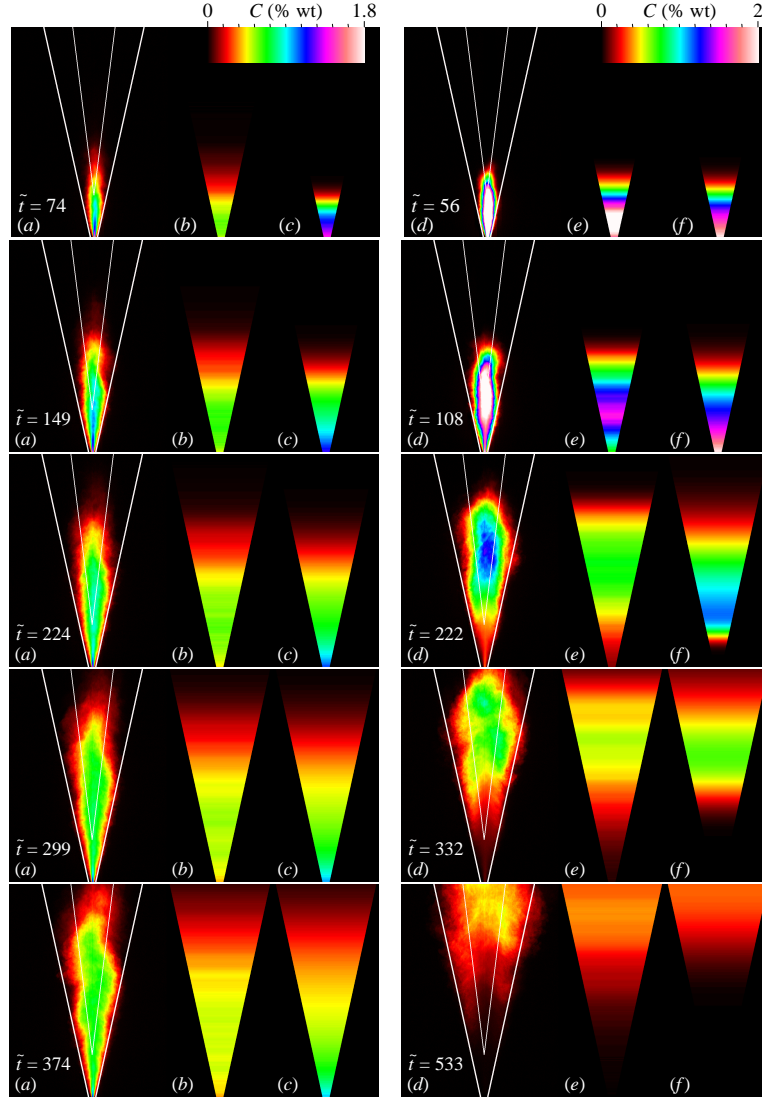
FIGURE 4.5: Distribution in space and non-dimensional time $\tilde{t} = t/(d^2/Q_0)$ of the concentration of dye (plotted using the two colour scales shown at the top for figures a–c and d–f, respectively) in the case of constant-flux releases (a–c) and finite-volume releases (d–f) in quasi-two-dimensional jets for: (a) ensemble average of 19 experiments, the average dye edges are plotted with thick white lines (half-spreading angle, $< \theta_{dye} >=$ 12.4°, as measured in figure 2.4) and the average boundaries of the core are plotted with thin white lines (half-spreading angle, 7° starting from $z = 20\,d$, as measured in figure 2.12); (b) spatial lateral average of the distribution shown in (a) (defined in (4.4)); (c) theoretical prediction based on (3.37) and using $K_a = 1.65$ and $K_d = 0.09$; (d) ensemble average of 26 experiments, similarly to (a) the average dye edges are plotted with thick white lines and the average boundaries of the core are plotted with thin white lines; (e) spatial lateral average of the distribution shown in (d) (defined in (4.9)); (f) theoretical prediction based on (3.88) using $K_a = 1.65$, $K_d = 0.09$ and $T_0 = 183\,\left(d^2/Q_0\right)$.

computed from equation (3.37) for $y_F(\eta)$, based on the assumption of a constant-flux release at the origin of the jet. To compute the theoretical prediction y_F, we use $K_a = 1.65$ and $K_d = 0.09$ for the advection and dispersion parameters, respectively. These parameters are optimized by obtaining the best least-squares fit between the experimental concentration $y_{F,exp}$ (i.e. the similarity form of $\phi_{F,exp}(z,t)$, transformed using (3.25)), and the theoretical prediction y_F. Before plotting the theoretical prediction y_F in figure 4.5(c), we transform y_F into its physical form $\phi_F(z,t)$ using (3.25), then normalize it (similarly to $\phi_{F,exp}(z,t)$) with the local distance $2l(z)$ between the average dye edges, and finally re-distribute it uniformly, assuming a top-hat spatially-averaged profile, within these boundaries, i.e.

$$C(x,z,t) = \begin{cases} \dfrac{\phi_F(z,t)}{2l(z)}, & -l(z) \leq x \leq l(z) \\ 0, & \text{otherwise} \end{cases}, \tag{4.6}$$

where $l(z)$ is defined in (4.5). As we noted in § 3.3.2, we can see that the cross-stream distribution of the concentration spreads linearly with distance. Law (2006) modelled mathematically the cross-stream distribution of the concentration of passive tracers in round and plane turbulent jets. He also found that the cross-stream distribution spreads linearly with distance. The model predicts that, in steady state, the laterally-integrated concentration ϕ_F increases like $z^{1/2}$. However, due to the cross-stream dispersion, the concentration C should decrease like $z^{-1/2}$. We can actually see in figure 4.5(b,c) that the experimental and theoretical concentrations, respectively, decrease with distance.

Comparing the data (figure 4.5b) with the theoretical prediction (figure 4.5c), we can see that the propagation of the front as well as its dispersion appear to have been correctly modelled (i.e. the scaling is correct), with only a small difference near the source. This mismatch is probably due to the zone of flow establishment of the jet (see e.g. Yannopoulos & Noutsopoulos, 1990). There is a necessary time and distance of adjustment before the experimental data can match the theoretical prediction, because the theoretical prediction is based around the assumption that the jet characteristic properties are given by the similarity power laws (2.5a,b). Giger *et al.* (1991) and Dracos *et al.* (1992) reported that the structure of quasi-two-dimensional jets was different near the source, where three-dimensional effects were important. They found that the self-similar core and eddy structure

(which is key in the dispersion mechanisms of the jet) only developed beyond approximately $z \geq 20\,d$ (for the aspect ratio $W/d = 2$). Therefore, we might expect our model to be appropriate for $z \geq 20\,d$.

We display in figure 4.6(a) the evolution in time of the non-dimensional integrated concentration of dye released in the experiments shown in figure 4.5(a). We can see that the experimental data (plotted with pluses) increase approximately linearly in time (a linear fit is plotted with a black line). Therefore, the constant-flux integral condition (3.24c) assumed in the model is satisfied experimentally.

We show in figure 4.6(b) the evolution in time of the distribution in similarity space of the normalized experimental data $y_{F,exp}$, plotted for nine successive time periods in the range $2 \leq \tilde{t} \leq 353$. As we explained earlier, $y_{F,exp}$ is computed from the ensemble-averaged laterally-integrated experimental concentration for the constant-flux releases $\phi_{F,exp}$ using equation (3.25) at every instant in time $\tilde{t}$. We also use the following virtual origins in space (see equation (2.6)) and time:

$$z_0 = -\frac{Q_0{}^2}{4\sqrt{2}\alpha M_0}, \quad t_0 = \frac{z_0 d}{Q_0}. \qquad (4.7a,b)$$

The space virtual origin z_0 is simply the virtual origin of quasi-two-dimensional jets. The time virtual origin t_0 represents the time needed to travel the distance $|z_0|$, from the jet virtual origin to the nozzle, at the average source jet velocity Q_0/d. We shift the origins in space and time from $(z = 0, t = 0)$ (where $z = 0$ corresponds to the height of the nozzle and $t = 0$ corresponds to the time instant when the dye first appears from the nozzle) to (z_0, t_0) by applying the following transformation between the new and old coordinates

$$z_{new} = z_{old} - z_0, \quad t_{new} = t_{old} - t_0. \qquad (4.8a,b)$$

For simplicity, we omit the subscripts *new* and *old* hereafter. In Chapter 2, we found $\alpha \approx 0.068$ and $M_0 \approx\, <\overline{M}> =\, 0.55\left(Q_0{}^2/d\right)$. So, the non-dimensional virtual origins in space and time are $\tilde{z}_0 = \tilde{t}_0 \approx -4.7$. Except for the data in the time interval, $2 \leq \tilde{t} \leq 118$ (plotted with dashed curves), the data corresponding to the time interval, $118 \leq \tilde{t} \leq 353$ (plotted with thin solid curves), seem to have a similar distribution. The experimental concentration distribution converges rapidly, in time, towards an asymptotic profile in similarity space (y, η). We

(a)

(b)
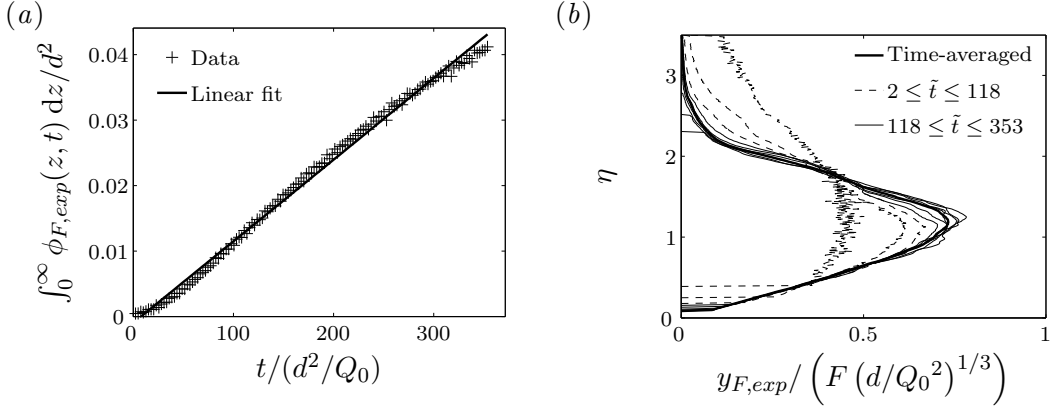
FIGURE 4.6: (a) Evolution in time of the non-dimensional integrated concentration of dye: the experimental data are plotted with pluses, a linear fit is plotted with a black line. (b) Evolution in time of the distribution of the normalized ensemble-averaged laterally-integrated experimental concentration shown in similarity form $y_{F,exp}$ in the case of constant-flux releases (plotted with dashed curves against the similarity variable $\eta = z/\left(t^{2/3}\left(Q_0{}^2/d\right)^{1/3}\right)$ for the time interval $2 \leq \tilde{t} \leq 118$ and with thin solid curves for the time interval $118 \leq \tilde{t} \leq 353$). The time-averaged data $\overline{y}_{F,exp}$, for $118 \leq \tilde{t} \leq 353$, are plotted with a thick solid curve.

approximate this asymptotic distribution by the time-averaged distribution $\overline{y}_{F,exp}$ for $118 \leq \tilde{t} \leq 353$ (plotted with a thick solid curve in figure 4.6b). The rapid convergence of the data in similarity space is very important because it means that the similarity scalings derived from the model, $\phi_F(z,t) = t^{1/3}y_F(\eta)$ (with $\eta \propto z/t^{2/3}$), are the appropriate scalings for this phenomenon. We can notice in figure 4.6(b) that near $\eta = 0$ the data are incomplete. Small values of $\eta \propto z/t^{2/3}$ are equivalent to small values of z compared with $t^{2/3}$, or large values of $t^{2/3}$ compared with z. The incomplete data near $\eta = 0$ are simply due to a lack of spatial resolution near the source and a finite time of observation in the experiments.

We present the experimental data $\overline{y}_{F,exp}$ in figure 4.7 (the ensemble average is plotted with pluses and the standard deviation, std, with dotted curves). We compute the best least-squares fit using the theoretical formula (3.37), where K_a and K_d are optimized under the constant-flux constraint (3.27b). The best fit (plotted with a solid curve) is found for $K_a = 1.65$ and $K_d = 0.09$. We can see that the model captures the main characteristics of the data. The concentration increases from zero at the origin (where the first derivative is infinite) to a peak value and then decreases smoothly at the front. The front of the curve agrees with
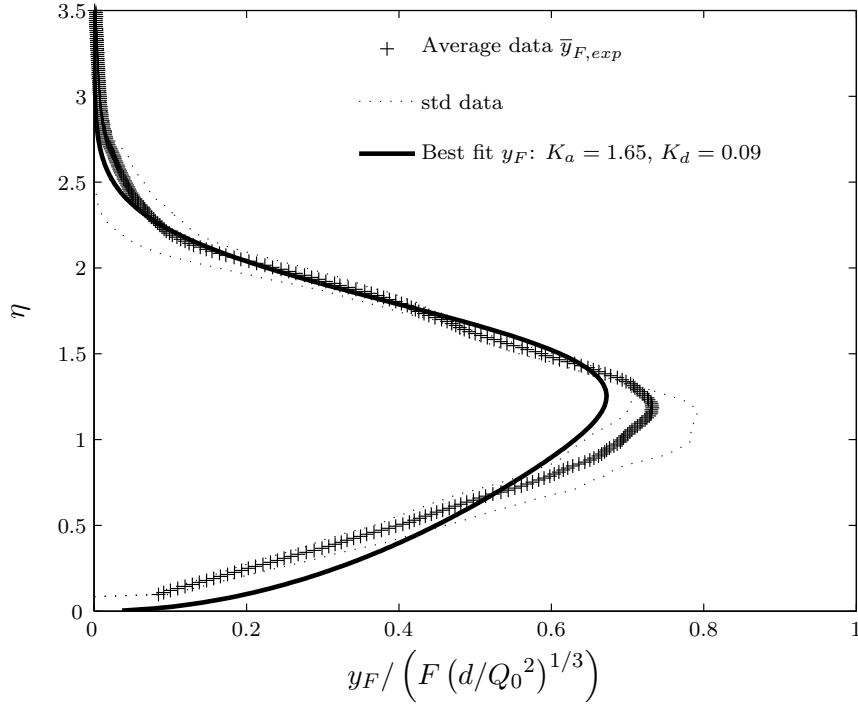
FIGURE 4.7: Constant-flux case, in similarity form: plots of the ensemble average (pluses) and standard deviation (std) (thin dotted curves) of the normalized experimental dye concentration $\overline{y}_{F,exp}$ (pluses) and best least-squares fit using y_F from (3.37) and with $K_a = 1.65$ and $K_d = 0.09$ (solid curve) against the similarity variable $\eta = z/\left(t^{2/3}\left(Q_0{}^2/d\right)^{1/3}\right)$.

the theoretical fit, and so, the dispersion processes appears to have been correctly modelled. The rear of the experimental data appears slightly more linear than the theoretical prediction. This mismatch is probably due to the zone of flow establishment discussed above.

The ratio between the advection parameter and the dispersion parameter is approximately $K_a/K_d = 18.3$. Using the advection parameter, we can compute theoretically the location of the advective front (considering 'top-hat' velocity profiles in the jet), $\eta_a = 1.83$, based on (3.40). We find that the position of the centroid relative to η_a is, for the experimental data, $\mu_{F,exp} = 0.65$ (computed using (3.42)), which is close to the theoretical prediction $\mu_F = 0.62$ (shown with a cross in figure 3.2a and computed using (3.43) with $K_a/K_d = 18.3$). The standard deviation of $\overline{y}_{F,exp}$ is $\sigma_{F,exp} = 0.29$ (computed using (3.44)), which is almost identical to the theoretical prediction $\sigma_F = 0.30$ (shown with a cross in figure 3.2b and computed using (3.45) with $K_a/K_d = 18.3$). We can also

measure from the experimental data the portion of the dye which travels ahead of the advective front $\beta_{F,exp} = 0.12$ (computed using (3.46)), which is close to the theoretical prediction $\beta_F = 0.10$ (shown with a cross in figure 3.3a) based on the ratio $K_a/K_d = 18.3$ and using (3.47). Thus, at each instant in time a non-negligible proportion of the total volume of tracers having been released travels ahead of the advective front η_a. Finally, we can also determine from the experimental data the normalized distance between the average location of the volume of tracers travelling ahead of the advective front and the location of the advective front η_a, $\xi_{F,exp} = 0.16$ (computed using (3.48)). This value is slightly larger than the theoretical prediction based on the ratio $K_a/K_d = 18.3$ and using (3.49), $\xi_F = 0.13$ (shown with a cross in figure 3.3b). ξ_F is a measure of the spread of the front of the distribution compared with the distance of the peak from the origin.

All these agreements between the data $\overline{y}_{F,exp}$ and the best least-squares fit y_F suggest that our model can predict the shape of the concentration distribution of a finite-volume release of tracers in quasi-two-dimensional jets. We believe that the constant-flux experiments are the most straightforward experiments performed in this chapter. Therefore, the values of the advection and the dispersion parameters $K_a = 1.65$ and $K_d = 0.09$, respectively, found in this case will be used in the next cases as reference values. Furthermore, these results clearly reveal the importance of dispersion processes in the transport of passive tracers by quasi-two-dimensional jets. As is clear in figure 4.7, the front of the distribution of the concentration in the similarity space (y, η) is not sharp but smooth due to dispersion. Were the transport of passive tracers by quasi-two-dimensional jets purely governed by advective processes alone, the distribution of the concentration in similarity space would drop much more rapidly at the front, as shown by the distributions of $y_{F,a}$ in figure 3.1 (plotted with a thin solid curve and a thin dashed curve). It is also important to note that more than $10\,\%$ of the total volume of tracers released, at any time, propagates ahead of the advective front.

We plot the normalized ensemble-averaged experimental results for the concentration flux of dye $\overline{y}_{M,exp}/F$ in figure 4.8 with pluses, while the standard deviation of the data (std) is plotted with thin dotted curves. The experimental concentration flux of dye $M_{\phi,exp}$ is computed using the expression (3.54) with $K_a = 1.65$ (as found above for the best fit of $\overline{y}_{F,exp}$ in the constant-flux case, see figure 4.7)

and the virtual origins described in (4.7a) and (4.7b). Then, according to (3.55), the similarity form is $\overline{y}_{M,exp} = M_{\phi,exp}$. We compute the theoretical prediction y_M (plotted with a solid curve) using the theoretical formula (3.55) with $K_a = 1.65$ and $K_d = 0.09$ (the reference values obtained in the constant-flux case for y_F, see figure 4.7). We also compute the best least-squares fit $y_{M,fit}$ using the theoretical formula (3.55), where $K_{a,fit}$ and $K_{d,fit}$ are optimized. The best fit (plotted with a dashed curve) is found for $K_{a,fit} = 1.55$ and $K_{d,fit} = 0.07$. (The values of the advection and dispersion parameters for the best fit and the theoretical prediction are actually very similar.) The theoretical prediction matches with the data at the front, with the dispersion processes appearing to have been correctly modelled, but near the origin the data drop towards zero instead of remaining constant. The absence of a plateau near the origin in the experimental results is presumably due to the time and distance of adjustment before the experimental data can match the theoretical prediction, which we mentioned previously as being associated with the zone of flow establishment.

We find that the position of the centroid relative to $\eta_a = 1.83$ (computed using (3.40) with $K_a = 1.65$) is, for the experimental data, $\mu_{M,exp} = 0.58$ (computed using (3.57)), which is somewhat larger than the theoretical prediction $\mu_M = 0.50$ (shown with a cross in figure 3.5a and computed using (3.58) with $K_a/K_d = 18.3$). The standard deviation of $\overline{y}_{M,exp}$ is $\sigma_{M,exp} = 0.31$ (computed using (3.59)), which is identical to the theoretical prediction $\sigma_M = 0.31$ (shown with a cross in figure 3.5b and computed using (3.60) with $K_a/K_d = 18.3$). We can also measure from the experimental data the proportion of the dye flux being ahead of the advective front $\beta_{M,exp} = 0.09$ (computed using (3.61)), which is close to the theoretical prediction $\beta_M = 0.06$ (shown with a cross in figure 3.6a) based on the ratio $K_a/K_d = 18.3$ and using (3.62). We can also determine from the experimental data the normalized distance between the average location of the volume of tracers travelling ahead of the advective front and the location of the advective front (considering 'top-hat' velocity profiles in the jet) η_a, $\xi_{M,exp} = 0.19$ (computed using (3.63)). This value is somewhat larger than the theoretical prediction based on the ratio $K_a/K_d = 18.3$ and using (3.64), $\xi_M = 0.12$ (shown with a cross in figure 3.6b).

The study of the flux of dye in the constant-flux case also demonstrates the ability of the model to predict both advective and diffusive processes. It is clear
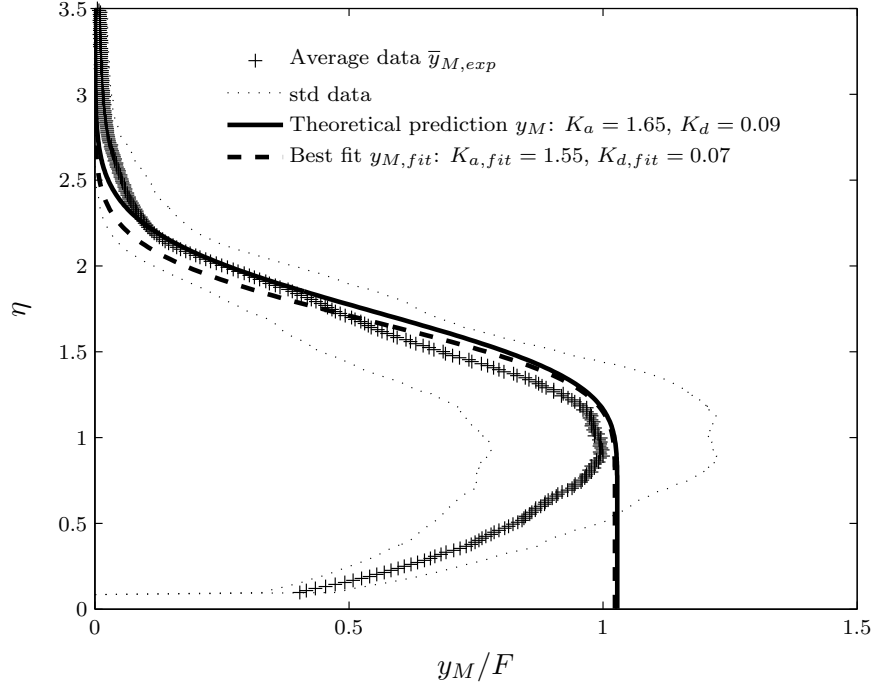
FIGURE 4.8: Constant-flux case, in similarity form: plots of the ensemble average (pluses) and standard deviation (std) (thin dotted curves) of normalized experimental dye flux $\overline{y}_{M,exp}$, theoretical prediction y_M using (3.55) and with $K_a = 1.65$ and $K_d = 0.09$ (solid curve), and best least-squares fit $y_{M,fit}$ using (3.55) and with $K_{a,fit} = 1.55$ and $K_{d,fit} = 0.07$ (dashed curve) against the similarity variable $\eta = z/\left(t^{2/3}\left(Q_0^2/d\right)^{1/3}\right)$.

from the observation of the front of the profile in figure 4.8 that quasi-two-dimensional jets diffuse tracers in a qualitatively different manner from the 'top-hat' purely advective case $y_{M,a}$ presented in figure 3.4 (plotted with a thin solid curve and a thin dashed curve). Moreover, we measure that approximately 10% of the total concentration flux of tracers is located ahead of the advective front.

4.2.3 Instantaneous finite-volume releases of clusters of virtual particles

We now compare our effective advection–diffusion model with experiments conducted using finite-volume releases of tracers in quasi-two-dimensional jets. The initial boundary and integral conditions imposed in the finite-volume case (3.65a–c) are more difficult to reproduce experimentally because they require an instantaneous release. An instantaneous release is not physically possible in laboratory

experiments (as we discussed in § 4.1.3), but it can be achieved using virtual particles. So, we first investigate the case of finite volumes of virtual particles released in the velocity field of quasi-two-dimensional jets, before analysing the more difficult problem of finite-volume releases of dye (presented in § 4.2.4).

Figure 4.9(a) shows the dimensionless streamwise profile, at different times, of the laterally-integrated normalized concentration $\phi_{v,exp}\left(\tilde{z},\tilde{t}\right)/\phi_{max}(\tilde{t})$ (where $\phi_{max}(\tilde{t})$ is the maximum value of $\phi_{v,exp}(\tilde{z},\tilde{t})$ in time, and $\tilde{z} = z/d$ and $\tilde{t} = t/\left(d^2/Q_0\right)$ as defined in (4.1a) and (4.1b), respectively) of the ensemble average of 256 virtual-particle clusters released instantaneously, as finite volumes, in the experimental velocity field of quasi-two-dimensional jets with source volume flow rates 33.2, 37.0 and 40.3 $\text{cm}^3\,\text{s}^{-1}$ (see § 4.1.2). At each time, we bin the data into 100 evenly-spaced intervals extending from the origin to the maximum streamwise extent of the ensemble-averaged cluster. The thick dashed curve shows the location of the front z_f of the ensemble-averaged cluster in time, which reaches the top boundary of the velocity field at approximately $\tilde{t} = 290$, after the release time. The location of the front follows the expected power law $z_f \propto t^{2/3}$, derived from (2.5b). As we can see, the ensemble-averaged cluster rapidly changes from an initial rectangular shape to a smoother rounded profile as it is advected by the jet. At early times $\tilde{t} \leq 150$, the dispersion of the particles appears to differ slightly between the front and the rear of the ensemble-averaged cluster. The front is sharper and drops more rapidly, while the rear has a longer tail. This is probably due to the fact that at the beginning most particles are advected quickly by the core of the jet, while the rest are trapped in the lateral eddies where they move more slowly (the time-averaged streamwise speed of an eddy is approximately 25 % of the maximum speed of the core, as measured in § 2.5). However, at later times the cluster seems to spread more symmetrically between the front and the rear. We believe this is due to the continuous exchange of material between the core and the eddies.

We apply the similarity transformation (3.66) to the ensemble-averaged experimental concentration $\phi_{v,exp}$ to obtain the similarity form $y_{v,exp}$, normalized by the total volume of virtual particles $B_{v,exp} = 2{,}624{,}256$. We use the space virtual origin z_0 defined in (4.7a). The time virtual origin cannot be the same as defined in the simple equation (4.7b) because the jet velocity is not constant between the jet virtual origin z_0 and the location of release of the virtual particles
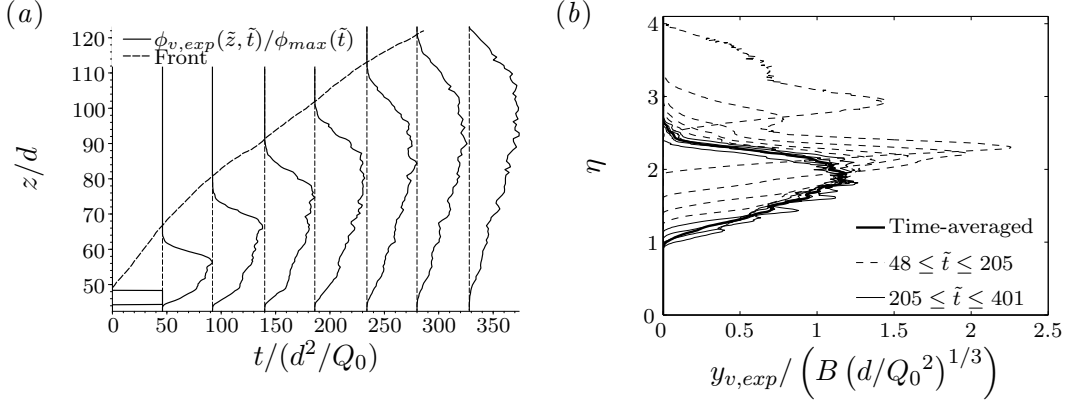
FIGURE 4.9: (*a*) Streamwise distribution of the normalized laterally-integrated concentration of virtual particles $\phi_{v,exp}(z,t)/\phi_{max}(t)$ (solid curves) at different non-dimensional times. The results have been averaged for 256 releases of identical clusters in the velocity fields of quasi-two-dimensional turbulent jets of source volume flow rates 33.2, 37.0 and 40.3 cm^3 s^{-1} . The location of the front of the ensemble-averaged cluster is plotted versus time with a thick dashed curve. (*b*) Evolution in time of the distribution in similarity form of the normalized ensemble-averaged laterally-integrated experimental concentration of virtual particles $y_{v,exp}$ (dashed curves for the time interval $48 \leq \tilde{t} \leq 205$ and with thin solid curves for the time intervals $205 \leq \tilde{t} \leq 401$) against the similarity variable $\eta = z/\left(t^{2/3}\left(Q_0{}^2/d\right)^{1/3}\right)$. The time-averaged data $\overline{y}_{v,exp}$, for $205 \leq \tilde{t} \leq 401$, are plotted with a thick solid curve.

(i.e. $44.4 \leq z/d \leq 48.3$). We determine the time virtual origin so that the location of the front in time $\tilde{z}_f(\tilde{t})$ (plotted with a thick dashed curve in figure 4.9*a*) best fits (using a least-squares fit) a straight line in a log–log plot. We show in figure 4.9(*b*) the evolution in time of the distribution in similarity space of the normalized experimental data $y_{v,exp}$, plotted for nine successive time periods in the range $48 \leq \tilde{t} \leq 401$. We can see that $y_{v,exp}$ seems to converge towards an asymptotic distribution after $205 \leq \tilde{t}$ (the data for $48 \leq \tilde{t} \leq 205$ are plotted with dashed curves, while the data for $205 \leq \tilde{t} \leq 401$ are plotted with thin solid curves). We approximate the asymptotic distribution by the time-averaged distribution $\overline{y}_{v,exp}$ for $205 \leq \tilde{t} \leq 401$ (plotted with a thick solid curve in figure 4.9*b*). Similarly to the constant-flux case, the convergence of these finite-volume data in similarity space implies that the similarity scalings derived from the model, $\phi_\delta(z,t) = t^{-2/3}y_\delta(\eta)$ (with $\eta \propto z/t^{2/3}$), are the appropriate scalings for this phenomenon.

In figure 4.10, we compare the time-averaged ensemble-averaged virtual particle data $\overline{y}_{v,exp}$ (the ensemble average is plotted with crosses and the standard

deviation, std, is plotted with dotted curves) with the theoretical prediction of the fundamental solution y_δ (plotted with a solid curve), which assumes an instantaneous release. We compute the theoretical prediction y_δ using equation (3.73) with $K_a = 1.65$ and $K_d = 0.09$ (the reference values obtained in the constant-flux case for y_F, see figure 4.7). We also compute the best least-squares fit $y_{\delta,fit}$ (plotted with a dashed curve in figure 4.10) using (3.73), where $K_{a,fit}$ and $K_{d,fit}$ are optimized under the finite-volume constraint (3.68b). The best least-squares fit between $\overline{y}_{v,exp}$ and $y_{\delta,fit}$ is obtained for $K_{a,fit} = 1.62$ and $K_{d,fit} = 0.09$. Once again, these best-fit values are quite similar to the reference values.

We can see that the model captures the main characteristics of the data. The concentration increases from zero at the origin (where the first and second derivatives also vanish) to a peak value and then decreases at the front, following the theoretical prediction y_δ. The location of the peak of $\overline{y}_{v,exp}$ (which is also the location of the advective front) is at $\eta_{a,exp} = 1.83$. Using the advection parameter $K_a = 1.65$, we can compute theoretically a very similar value $\eta_a = 1.83$, based on (3.40). We find that the position of the centroid relative to η_a is, for the experimental data, $\mu_{B,exp} = 0.99$ (computed using (3.76)), which is slightly smaller than the theoretical prediction $\mu_B = 1.03$ (shown with a cross in figure 3.8a and computed using (3.77) with $K_a/K_d = 18.3$). Thus, the centroid is very close to the location of the concentration peak. The standard deviation of $\overline{y}_{v,exp}$ is $\sigma_{B,exp} = 0.17$ (computed using (3.78)), which is close to the theoretical prediction $\sigma_B = 0.19$ (shown with a cross in figure 3.8b and computed using (3.79) with $K_a/K_d = 18.3$). We can also measure from the experimental data the portion of the virtual particles which travels ahead of the advective front $\beta_{B,exp} = 0.49$ (computed using (3.80)), which is very close to the theoretical prediction $\beta_B = 0.54$ (shown with a cross in figure 3.9a) based on the ratio $K_a/K_d = 18.3$ and using (3.81). (A value β_B of 0.5 means that the virtual particles are symmetrically distributed with respect to the concentration peak.) Finally, we can also determine from the experimental data the normalized distance between the average location of the volume of tracers travelling ahead of the advective front and the location of the advective front (considering 'top-hat' velocity profiles in the jet) η_a, $\xi_{B,exp} = 0.13$ (computed using (3.82)). This value is somewhat smaller than the theoretical prediction based on the ratio $K_a/K_d = 18.3$ and using (3.83), $\xi_B = 0.17$ (shown with a cross in figure 3.9b). ξ_B is a measure of the spread of

the distribution compared with the distance of the peak from the origin.
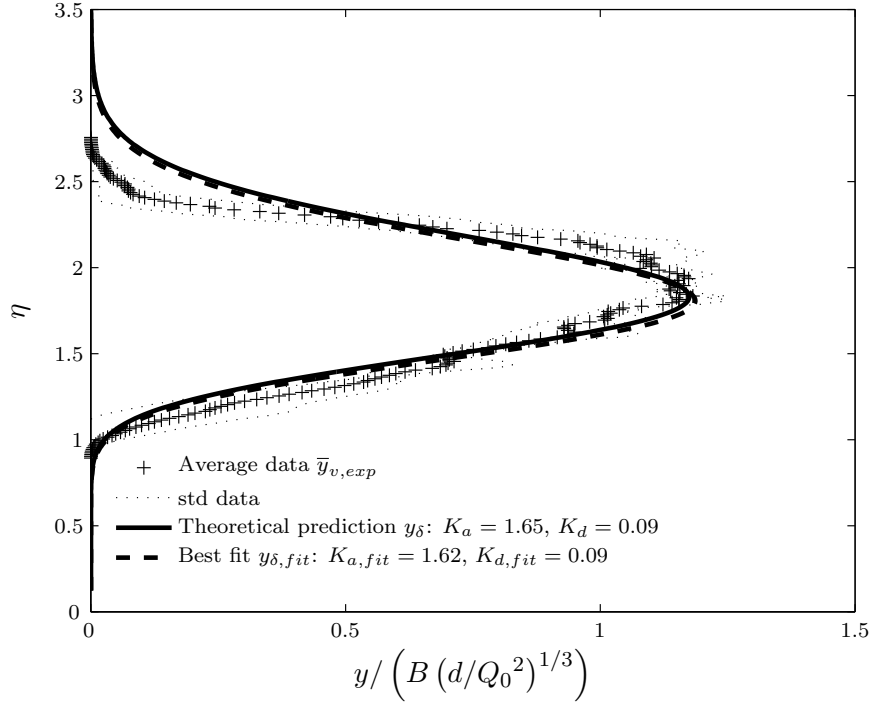
FIGURE 4.10: Finite-volume case, instantaneous release, in similarity form: plots of the variation with similarity variable $\eta = z/\left(t^{2/3}\left(Q_0{}^2/d\right)^{1/3}\right)$ of the ensemble average (pluses) and standard deviation (std) (thin dotted curves) of the normalized time-averaged experimental concentration of virtual particles $\overline{y}_{v,exp}$ (pluses), theoretical prediction y_δ defined by (3.73) with $K_a = 1.65$ and $K_d = 0.09$ (solid curve), and best least-squares fit using $y_{\delta,fit}$ defined by (3.73) with $K_{a,fit} = 1.62$ and $K_{d,fit} = 0.09$ (dashed curve).

All these agreements between the data $\overline{y}_{v,exp}$ and the theoretical prediction y_δ, and between the advection and dispersion parameters of the constant-flux case and the finite-volume case, suggest that our model can predict the shape of the concentration distribution of an instantaneous finite-volume release of tracers in quasi-two-dimensional jets. Furthermore, it clearly reveals the importance of dispersion processes in the transport of passive tracers by quasi-two-dimensional jets. As is clear in figure 4.9(b), the distribution of the concentration in the similarity space (y, η) converges in time towards a distribution with a finite width. Were the transport of passive tracers by quasi-two-dimensional jets purely governed by advective processes alone, the distribution of the concentration in similarity space would rather shrink towards a distribution of negligible width (similar to a Dirac delta function), even with a non-instantaneous release of tracers. It is

also important to note that approximately half of the total volume of tracers in figure 4.10 travels ahead of the advective front, at a normalized averaged distance $\xi_B \approx 0.17$ (defined in (3.83) with $K_a/K_d = 18.3$).

4.2.4 Finite-volume releases of dye

We also present in figures 4.5(d–f) experimental results and theoretical predictions of finite-volume releases of dye in quasi-two-dimensional steady turbulent jets. The spatial distribution of the concentration $C(x, z, t)$ is plotted using a colour scale (see colour scale at the top of figures 4.5d–f) at different non-dimensional times, $56 \leq \tilde{t} \leq 533$, to show the evolution of the patch of dye as it is advected, mixed and dispersed by the jet. In figure 4.5(d) we plot the ensemble average of the 26 experiments, which were conducted at different jet Reynolds number, $2170 \leq Re_j \leq 4870$ (see § 4.1.3). We also plot the average dye edges (half-spreading angle, $< \theta_{dye} >= 12.4°$) with thick white lines and the average boundaries of the 'core' (half-spreading angle, $7°$ starting from $z = 20$d) with thin white lines. Similarly to the constant-flux results presented in figures 4.5(a–c), we can observe that the interaction between the core and the eddies, as described in § 2.5, results in large streamwise dispersion. As we explained earlier, we model this streamwise dispersion using an enhanced turbulent eddy diffusive coefficient $D_{zz} \propto b\overline{w}_m$.

We present the laterally-integrated experimental concentration $\phi_{B,exp}(z, t)$ in figure 4.5(e) in normalized and re-distributed form using

$$C(x, z, t) = \begin{cases} \dfrac{\phi_{B,exp}(z, t)}{2l(z)}, & -l(z) \leq x \leq l(z) \\ 0, & \text{otherwise} \end{cases}, \tag{4.9}$$

where $l(z) = \tan\left(< \theta_{dye} >\right)(z - z_0)$, as defined in (4.5), is the local lateral distance between the average dye edges (plotted with thick white lines in figure 4.5d), and z_0 is the space virtual origin defined in (4.7a). Alongside in figure 4.5(f), we show the equivalent theoretical prediction $\phi_{T_0}(z, t)$ computed from equation (3.88) and based on the assumption of a finite volume being released at a constant-flux during a finite period of time $T_0 = 183 \ (d^2/Q_0)$ (we discuss this value in more detail below). To compute ϕ_{T_0}, we use $K_a = 1.65$ and $K_d = 0.09$ for the advection and dispersion parameters, respectively (the reference values obtained in the constant-

flux case for y_F, see figure 4.7). Before plotting the theoretical prediction ϕ_{T_0} in figure 4.5(f), we normalize it (similarly to $\phi_{B,exp}(z,t)$) with the local distance $2l(z)$ between the average dye edges, and finally re-distribute it uniformly, assuming a top-hat spatially-averaged profile, within these boundaries, i.e.

$$C(x,z,t) = \begin{cases} \dfrac{\phi_{T_0}(z,t)}{2l(z)}, & -l(z) \le x \le l(z) \\ 0, & \text{otherwise} \end{cases}, \tag{4.10}$$

where $l(z)$ is defined in (4.5).

Although the comparison between the experimental data in figure 4.5(e) and the theoretical prediction in figure 4.5(f) is not perfect at early times and near the origin (the theoretical concentration seems to travel slightly slower than the experimental concentration for $\tilde{t} \le 222$), it improves at later times as the jet advects and diffuses the dye. As we mentioned above, this mismatch is probably due to the zone of flow establishment of the jet. There is a necessary time and distance of adjustment before the experimental data can match the theoretical prediction, because the theoretical prediction is based around the assumption that the jet characteristic properties are given by the similarity power laws (2.5a,b).

In these experiments, we naturally are not able to release finite volumes of dye instantaneously. Aspects of the experimental dye release are revealed in figure 4.11(a), where we show the evolution in time of the integral of the dye concentration over the whole domain $\int_0^\infty \phi_{B,exp}(z,t)\,\mathrm{d}z$ (plotted with pluses). These data represent the total volume of dye 'seen' by the imaging analysis in the window frame $-40 \le x/d \le 40$ and $0 \le z/d \le 100$. The dashed line indicates the time instant $\tilde{t}_{90} = 183$, when approximately 90 % of the total volume of dye has entered the tank. We can see that the total volume of dye increases almost steadily for $\tilde{t} \le \tilde{t}_{90}$. Then, the total volume of dye reaches a maximum at $\tilde{t} \approx 290$ before decreasing smoothly as the dye is transported outside the window frame. These data clearly show that the release of dye occurs over a finite period of time and not instantaneously.

The effect of the spreading in time of the release of dye can also be seen in the evolution in time of the concentration distribution in the jets. In figure 4.11(b), we show the non-dimensional experimental concentration in similarity form $y_{B,exp}$ (computed from $\phi_{B,exp}$ using (3.66) at each instant in time). We normalize $y_{B,exp}$
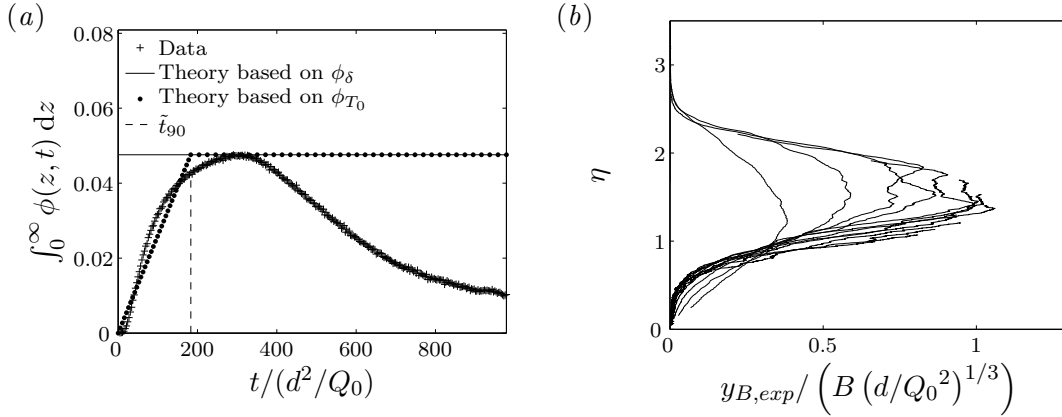
FIGURE 4.11: (*a*) Evolution in time of the integral of the dye concentration over the whole domain for: the experimental data $\phi_{B,exp}$ (pluses); the theoretical prediction ϕ_δ (solid line), defined by (3.73); and the theoretical prediction ϕ_{T_0} (dotted line), defined by (3.88). The dashed line indicates the time instant $\tilde{t}_{90} = 183$ when approximately 90 % of the total integrated concentration of dye has entered the tank. (*b*) Plots of the variation with similarity variable $\eta = z/\left(t^{2/3}\left(Q_0{}^2/d\right)\right)$ of the evolution in time of the normalized ensemble-averaged laterally-integrated experimental concentration plotted in similarity form, $y_{B,exp}$ (computed from $\phi_{B,exp}$ using (3.66)), in the case of finite-volume releases of dye. The data are plotted at 12 different time instants for $0 \leq \tilde{t} \leq 979$, with time increasing as the amplitude of the data increases.

with the total injected volume B and plot it at 12 different instants in time for $0 \leq \tilde{t} \leq 979$, with time increasing as the amplitude of the data increases. The space and time virtual origins described in (4.7*a*) and (4.7*b*) are used to compute $y_{B,exp}$. Ideally, if the dye were released instantaneously at the origin (as described in the integral and initial boundary conditions (3.65*a–c*)) all the curves should be identical and collapse on a single profile. Instead, we observe a gradual increase of the area under the curves. The data do not appear to have yet reached an asymptotic distribution. It can also be noticed that the curves at late times (for $290 \leq \tilde{t}$) are not plotted over the whole range $0 \leq \eta \leq 3.5$, but stop at some values $\eta < 3.5$. These curves are incomplete because for $290 \leq \tilde{t}$, the front of the dye (located at the height z_f) has already moved outside the image frame, i.e. $z_f/d > 100$, and thus we cannot visualize the full distribution of the dye in space.

It is clear from both figures 4.11(*a*) and 4.11(*b*) that the release of the dye is not instantaneous and that the data have not yet reached an asymptotic distribution in similarity space. Thus, we cannot use the theoretical prediction y_δ defined in (3.73) to model these experiments (as we did in the case of finite-volume releases

of virtual particles presented above) because the fundamental solution y_δ assumes an instantaneous release of the finite volume of tracers (see the integral and initial boundary conditions (3.65a–c)). Therefore, we compare the experimental data $\phi_{B,exp}(z,t)$ with the general solution $\phi_g(z,t)$, described in (3.85) and based on the convolution of the fundamental solution ϕ_δ with a source function $f(t) = \phi_g(0,t)$. The source function can model the more general and realistic case of a time-dependent release.

To compute the general solution $\phi_g(z,t)$, we need to define the source function $f(t)$, which represents the rate at which the overall integrated volume of tracers changes with time. In figure 4.11(a), we observe that the total integrated concentration of dye $\int_0^\infty \phi_{B,exp}(z,t)\,\mathrm{d}z$ increases almost linearly with time for $\tilde{t} \leq \tilde{t}_{90}$. Hence, we choose to model the source function as simply a non-zero constant for $0 \leq \tilde{t} \leq \tilde{t}_{90}$ and zero for $\tilde{t}_{90} \leq \tilde{t}$,

$$f_{\tilde{t}_{90}}(\tilde{t}) = \frac{H(\tilde{t}) - H(\tilde{t} - \tilde{t}_{90})}{\tilde{t}_{90}}, \tag{4.11}$$

where H is the Heaviside function. Using such a rectangular source function, the general solution $\phi_g(z,t)$ corresponds to the particular solution ϕ_{T_0} (with $T_0 = t_{90}$), described in (3.88). We plot the resulting theoretical integrated concentration $\int_0^\infty \phi_{T_0}(z,t)\,\mathrm{d}z$ with a dotted curve in figure 4.11(a). We can see that the match with the data (plotted with pluses) is, at least until the dye is advected beyond the spatial range of the camera (for $\tilde{t} \leq 290$), better than for the model assuming an instantaneous release ϕ_δ (plotted with a solid line).

We compute the theoretical prediction ϕ_{T_0}, based on the source function $f_{\tilde{t}_{90}}$ with $T_0 = t_{90} = 183(d^2/Q_0)$, using the virtual origins described in (4.7a,b). We compare the distribution of the experimental data $\phi_{B,exp}$ (plotted with pluses) and the theoretical prediction ϕ_{T_0} (plotted with solid curves) in figure 4.12 at nine different times for $0 \leq \tilde{t} \leq 418$. We compute ϕ_{T_0} using the advection and dispersion parameters $K_a = 1.65$ and $K_d = 0.09$, respectively (the reference values obtained in the constant-flux case for y_F, see figure 4.7). We also show the best least-squares fit $\phi_{T_0,fit}$ (plotted with dashed curves in figure 4.12), computed using the theoretical formula (3.88) and the source function $f_{\tilde{t}_{90}}$ (see equation (4.11)) with $T_0 = t_{90} = 183(d^2/Q_0)$. The advection and dispersion parameters $K_{a,fit}$ and $K_{d,fit}$, respectively, are optimized under the finite-volume constraint (3.65c).

The best least-squares fit between $\phi_{B,exp}$ and $\phi_{T_0,fit}$ is obtained for $K_{a,fit} = 1.75$ and $K_{d,fit} = 0.09$, still quite close to the reference values. Overall, we observe a reasonable agreement between ϕ_{T_0} and $\phi_{B,exp}$. At early time, for $\tilde{t} \leq 100$, the match between the data and the model is not perfect because the experimental concentration profile adjusts partially due to the lack of self-similarity in the jet (this issue is related to the zone of flow establishment discussed previously). Then, both the advection (location of the peak in time) and the dispersion (width of the curve) seem to agree. There is a consistent mismatch at the rear where the data seem to be more spread out. This is probably due to some residue of dye in the tube still being injected in the jet at late time, and apparently stretching and diffusing the experimental dye concentration.

According to equation (3.89), the solution $\phi_{T_0}(z,t)$ converges in time towards $\phi_\delta(z,t)$. Hence, we also expect the data $\phi_{B,exp}(z,t)$ to converge in time towards $\phi_\delta(z,t)$. We demonstrate this convergence by plotting in figure 4.13 the similarity form of the theoretical prediction ϕ_{T_0} at $\tilde{t} = 150$ (plotted with a thin solid curve), $\tilde{t} = 300$ (plotted with a dotted curve) and $\tilde{t} = 450$ (plotted with a dashed curve). We also show the asymptotic solution y_δ, defined by (3.73) and computed using the (reference) advection and dispersion parameters $K_a = 1.65$ and $K_d = 0.09$. We can measure the absolute deviation, based on equation (3.91), between y_{T_0} at $\tilde{t} = 300$ (when the integrated concentration of dye is approximately maximum, see figure 4.11a) and the asymptotic solution y_δ. We find $dev = 0.85$, computed for $\tilde{t}/\tilde{T}_0 = 300/183 \approx 1.64$ and using (3.91). If we consider that convergence is 'achieved' if $dev \leq 0.1$, then we find that our experimental data would be expected to achieve convergence for $\tilde{t}/\tilde{T}_0 \geq 13.6$, or at $\tilde{t} \geq 2488$. We can estimate that the distance at which we should observe the concentration distribution of the finite volumes of dye converge towards an asymptotic distribution is $z \geq \eta_a (13.6\tilde{T}_0)^{2/3}\, d \approx 2\,\text{m}$ (based on the location of the concentration peak at convergence). Finally, we can predict the key characteristics of y_δ, the asymptotic distribution of $y_{B,exp}$ (the similarity form of $\phi_{B,exp}$ computed using (3.66)), which are actually identical to the characteristics of the theoretical prediction found for the virtual particles because the advection and dispersion parameters are the same. So, we can expect that the maximum concentration of the asymptotic distribution of $y_{B,exp}$ is located at $\eta_a = 1.83$, based on (3.40) with $K_a = 1.65$. The position of the centroid relative to η_a is $\mu_B = 1.03$ (shown with a cross in
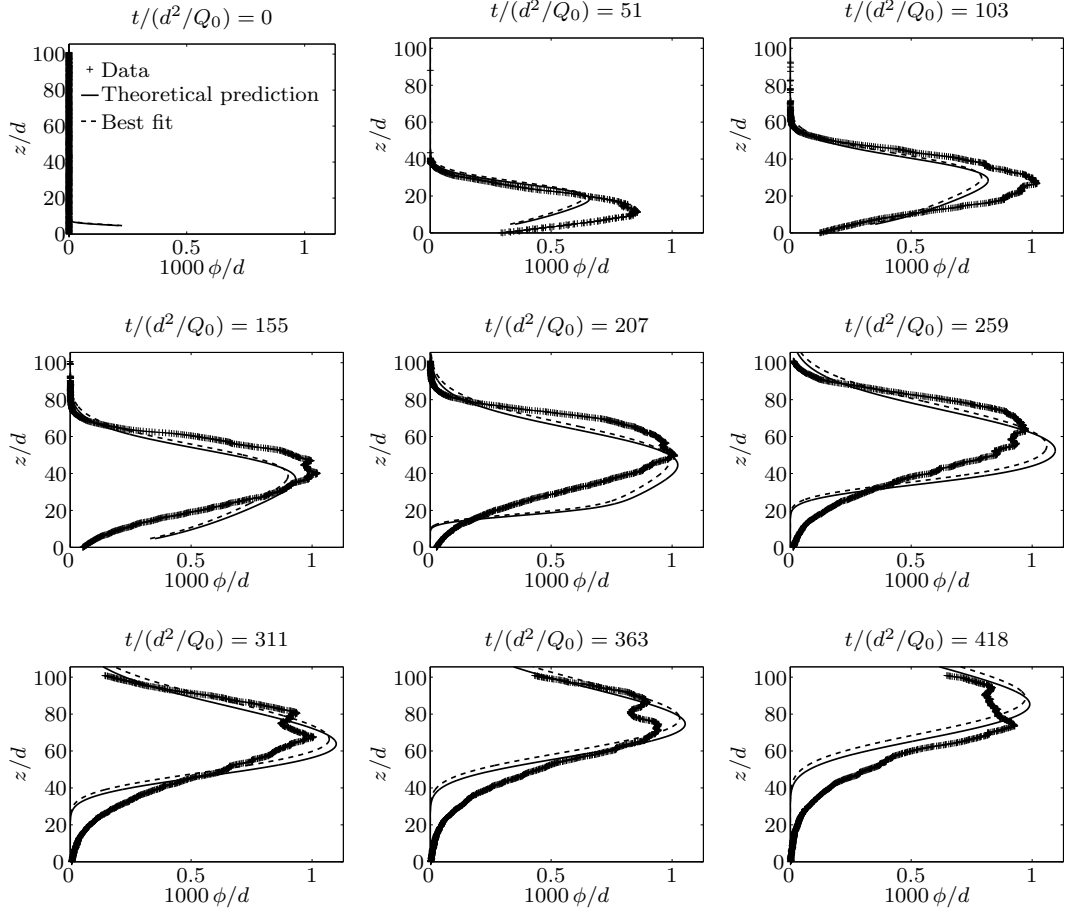
FIGURE 4.12: Plots at various times of the streamwise distribution of the laterally-integrated concentration of dye against the non-dimensional distance z/d in the case of finite-volume releases for: ensemble-averaged experimental data $\phi_{B,exp}$ (pluses); theoretical prediction ϕ_{T_0} (solid curves), based on equation (3.88) using the reference advection and dispersion parameters $K_a = 1.65$ and $K_d = 0.09$, respectively, and the source function $f_{\tilde{t}_{90}}(t)$ as defined in (4.11); and best least-squares fit $\phi_{T_0,fit}$ (dashed curves), based on equation (3.88) using the advection and dispersion parameters $K_{a,fit} = 1.75$ and $K_{d,fit} = 0.09$, respectively, and the source function $f_{\tilde{t}_{90}}(t)$ as defined in (4.11).

figure 3.8a and computed using (3.77) with $K_a/K_d = 18.3$). The theoretically predicted standard deviation is $\sigma_B = 0.19$ (shown with a cross in figure 3.8b and computed using (3.79) with $K_a/K_d = 18.3$). The portion of the virtual particles which travels ahead of the advective front is $\beta_B = 0.54$ (shown with a cross in figure 3.9a), based on the ratio $K_a/K_d = 18.3$ and using (3.81). The average location of the volume of tracers travelling ahead of the advective front is $\xi_B = 0.17$ (shown with a cross in figure 3.9b), based on the ratio $K_a/K_d = 18.3$ and using (3.83).
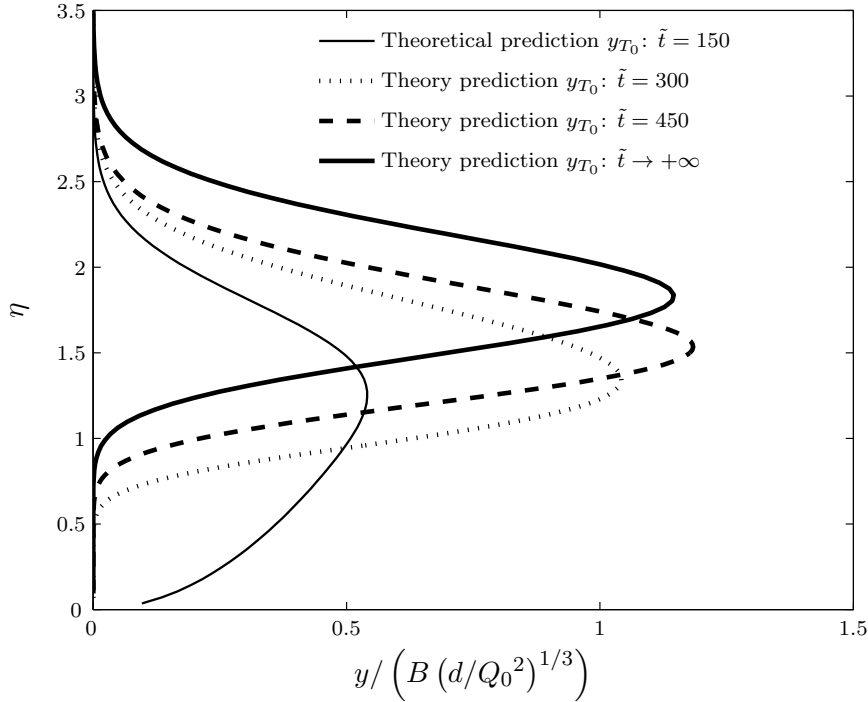
FIGURE 4.13: Finite-volume case, in similarity form: plots of the variation with similarity variable $\eta = z/\left(t^{2/3}\left(Q_0{}^2/d\right)\right)$ of the non-dimensionalized theoretical prediction y_{T_0}, based on equation (3.88), computed at $\tilde{t} = 150$ (thin solid curve), $\tilde{t} = 300$ (dotted curve), and $\tilde{t} = 450$ (dashed curve), using the reference advection and dispersion parameters $K_a = 1.65$ and $K_d = 0.09$, respectively, and the source function $f_{\tilde{t}_{90}}(t)$ as defined in (4.11). The asymptotic distribution of y_{T_0} (thick solid curve) is equal to y_δ and can be computed using (3.73) with $K_a = 1.65$ and $K_d = 0.09$.

4.3 Statistical significance of the experimental results

We investigate the statistical significance of the experimental results, presented in § 4.2 above, for the constant-flux releases of dye and the instantaneous finite-volume releases of virtual particles in quasi-two-dimensional jets. We compute the probability density function (p.d.f.) of all the measurements of the laterally-integrated concentration y (in similarity form) at different values of the similarity variable $\eta \propto z/t^{2/3}$.

We do not compute the p.d.f. of the experimental results found in the case of finite-time finite-volume releases of dye. (We describe the experiments in § 4.1.3 and plot the ensemble-averaged concentration in figure 4.12 with pluses). As we discuss in § 4.2.4, the distribution of the concentration has not yet reached an

asymptotic distribution in similarity form. Therefore, the study of the statistical significance is not meaningful while the concentration profile is in a transient time-dependent regime.

In the problem of river pollution, predicting and assessing the risk of encountering harmful concentration levels is crucial. We show in this section how we can predict and assess this risk for the constant-flux and instantaneous finite-volume cases. Moreover, we discuss how this risk varies in time and space, depending on the p.d.f. of the measurements of the concentration.

4.3.1 Constant-flux release of dye

We compute numerically the p.d.f. f_F of the laterally-integrated experimental concentration $y_{F,exp}$ (in similarity form) for the $N_e = 19$ constant-flux release experiments (presented in § 4.1.1) such that, for all $1 \le l \le N_\eta$ and $1 \le m \le N_y$ (with l and m two integers)

$$f_F(y_m, \eta_l) = \frac{\displaystyle\sum_{i,j,k}^{N_e,N_z,N_t} \Delta_{e_i,z_j,t_k}(y_m, \eta_l)}{\displaystyle\sum_m^{N_y} \sum_{i,j,k}^{N_e,N_z,N_t} \Delta_{e_i,z_j,t_k}(y_m, \eta_l)\, \delta y}, \tag{4.12}$$

where $\delta y = y_2 - y_1$ is the concentration step and, for all $1 \le i \le N_e$, $1 \le j \le N_z$ and $1 \le k \le N_t$ (with i, j and k three integers),

$$\Delta_{e_i,z_j,t_k}(y_m, \eta_l) = \begin{cases} 1 & \text{if} & y_{m-1} \le \dfrac{y_{F,exp}(e_i, z_j, t_k)}{F\left(d/Q_0{}^2(e_i)\right)^{1/3}} < y_m \\ & \text{and} & \eta_{l-1} \le \eta = \dfrac{z_j}{t_k{}^{2/3}\left(Q_0{}^2(e_i)/d\right)^{1/3}} < \eta_l, \\ 0 & \text{otherwise} \end{cases} \tag{4.13}$$

where z_j (the discretized streamwise coordinate) are linearly distributed from approximately 0 to $100\,d$ (depending on the experiment and with $N_z = 756$), t_k (the kth frame of the experiment) are linearly distributed from approximately 0 to t_{N_t} (with N_t of the order of 300, depending on the experiment), η_l (the discretized similarity variable) are linearly distributed from 0 to 3.5 (with $N_\eta = 200$, the number of bins) and y_m (the discretized laterally-integrated concentration
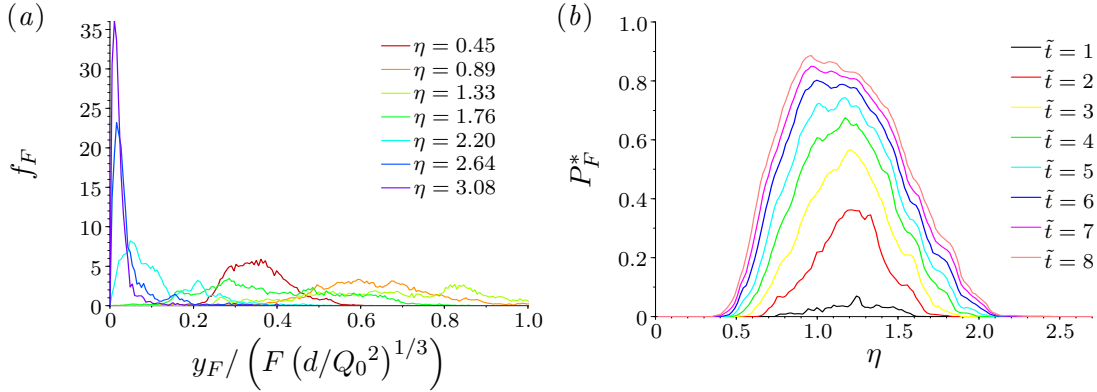
FIGURE 4.14: (*a*) Probability density function of the experimental dye concentration $y_{F,exp}/\left(F\left(d/Q_0{}^2\right)^{1/3}\right)$, non-dimensionalized and in similarity form, at different values of the similarity variable η in the case of constant-flux releases. We describe the experiments in § 4.1.1 and plot the ensemble-averaged concentration $\overline{y}_{F,exp}$ in figure 4.7 with pluses. (*b*) Distribution against the similarity variable η at different non-dimensional times (plotted with different colours) of the probability that the concentration of tracers $\phi_{F,exp}$ is greater than a critical value ϕ^* in the case of a constant-flux release in a quasi-two-dimensional jet.

in similarity form) are linearly distributed from 0 to 1.07 (with $N_y = 200$, the number of bins).

In figure 4.14(*a*), we show the p.d.f. f_F, computed in (4.12), at seven different values of the similarity variable η for $0.45 \leq \eta \leq 3.08$ (plotted with different colours).The distribution of the ensemble-averaged concentration $\overline{y}_{F,exp}$ is plotted in figure 4.7 with pluses. As we can see in figure 4.14(*a*), the p.d.f. f_F decreases with increasing concentration $y_{F,exp}$. In figure 4.7, the maximum of $\overline{y}_{F,exp}$ is found at $\eta = 1.17$, which corresponds, in figure 4.14(*a*), to the rightmost and lowest profile of f_F (see light green curve at $\eta = 1.33$). The amplitude of f_F is large for either large values of η or small values: $\eta > 2.20$ and $\eta < 0.45$. In fact, we find that the standard deviation of the p.d.f. of $y_{F,exp}$ grows approximately linearly with its average value, although with a hysteresis between the values before the concentration peak (i.e. $\eta < 1.17$) and the values after the concentration peak (i.e. $\eta > 1.17$).

In the case of a constant-flux release of pollutants in a quasi-two-dimensional turbulent jet, the probability P_F^* to find concentrations of pollutants larger than a critical concentration level ϕ^* (laterally-integrated concentration) at a given value

η is for $t > 0$

$$P_F^*(\eta, \tilde{t}) = \int_{\tilde{t}^{-1/3}\tilde{\phi}^*}^{\infty} f_F(\tilde{y}_{F,exp}, \eta) \, \mathrm{d}\tilde{y}_{F,exp}, \tag{4.14}$$

where tildes denote non-dimensional values (see $(4.1a,b)$), and where we use equation (3.25), $\phi(z,t) = t^{1/3}y(\eta)$. It is interesting to note that the distribution of P_F^* increases in time, starting from 0 at $t = 0$. The increase in time of P_F^* is due to the constant flux of tracer concentration at the source of the jet and to the decrease (like $z^{-1/2}$) of the velocity of the jet with distance. Thus, the laterally-integrated tracer concentration tends to increase at a fixed value of $\eta \propto z/t^{2/3}$ as time increases (i.e. for z increasing).

As an example, we have plotted P_F^* in figure $4.14(b)$ against η at eight different non-dimensional times $1 \leq \tilde{t} \leq 8$ (plotted with different colours), for the critical non-dimensional concentration $\tilde{\phi}^* = 1$. We can clearly see that the probability P_F^* increases rapidly in time. As time increases, the maximum value of P_F^* appears to move to the left, towards $\eta = 0$, and is found in the range $0.9 \leq \eta \leq 1.3$ (the peak of $\overline{y}_{F,exp}$, in figure $4.14a$, is found at $\eta = 1.17$). We find that, in this example, the peak of the probability P_F^* first becomes greater than 0.05 (i.e. statistically significant) from $\tilde{t} \geq 1.0$ at the location $\eta = 1.24$, corresponding to $\tilde{z} = 1.2$. The peak of the probability P_F^* becomes greater than 0.95 from $\tilde{t} \geq 12.0$ at the location $\eta = 0.95$, corresponding to $\tilde{z} = 5.0$.

4.3.2 Instantaneous finite-volume release of virtual particles

Similarly to the constant-flux case presented above, we compute numerically the p.d.f. f_v of the laterally-integrated numerical concentration $y_{v,exp}$ (in similarity form), for the $N_e = 256$ clusters, representing 2,624,256 virtual particles, released instantaneously in the velocity field of quasi-two-dimensional jets (see § 4.1.2). The p.d.f. f_v is, for all $1 \leq l \leq N_\eta$ and $1 \leq m \leq N_y$ (with l and m two integers),

$$f_v(y_m, \eta_l) = \frac{\displaystyle\sum_{i,j,k}^{N_e, N_z, N_t} \Delta_{e_i, z_j, t_k}(y_m, \eta_l)}{\displaystyle\sum_{m}^{N_y} \sum_{i,j,k}^{N_e, N_z, N_t} \Delta_{e_i, z_j, t_k}(y_m, \eta_l) \, \delta y}, \tag{4.15}$$

where $\delta y = y_2 - y_1$ is the concentration step and, for all $1 \leq i \leq N_e$, $1 \leq j \leq N_z$ and $1 \leq k \leq N_t$ (with i, j and k three integers),

$$\Delta_{e_i, z_j, t_k}(y_m, \eta_l) = \begin{cases} 1 & \text{if} \qquad y_{m-1} \leq \dfrac{y_{v,exp}(e_i, z_j, t_k)}{B \left(d/Q_0{}^2(e_i) \right)^{1/3}} < y_m \\[4mm] & \text{and} \qquad \eta_{l-1} \leq \eta = \dfrac{z_j}{t_k{}^{2/3} \left(Q_0{}^2(e_i)/d \right)^{1/3}} < \eta_l, \\[4mm] 0 & \text{otherwise} \end{cases} \tag{4.16}$$

where z_j (the discretized streamwise coordinate) are linearly distributed from approximately $47\,d$ to $128\,d$ (depending on the experiment and with $N_z = 1022$), t_k (the kth frame of the experiment) are linearly distributed from approximately 0 to t_{N_t} (with N_t of the order of 300, depending on the experiment), η_l (the discretized similarity variable) are linearly distributed from 0 to 5 (with $N_\eta = 200$, the number of bins) and y_m (the discretized laterally-integrated concentration in similarity form) are linearly distributed from 0 to 5 (with $N_y = 400$, the number of bins).

We present in figure 4.15(a) the p.d.f. f_v, computed in (4.15), at eight different values of the similarity variable η for $1.52 \leq \eta \leq 3.50$ (plotted with different colours). The distribution of the ensemble-averaged concentration $\overline{y}_{v,exp}$ is plotted in figure 4.10 with pluses. As we can see in figure 4.15(a), the p.d.f. f_v decreases even more rapidly than f_F (shown in figure 4.14a) with increasing concentration $y_{v,exp}$. In figure 4.10, the maximum of $\overline{y}_{v,exp}$ is found at $\eta = 1.83$, which is close to the rightmost and lowest profile of f_v in figure 4.15(a) (see curve at $\eta = 2.07$). Similarly to f_F, the amplitude of the f_v is the largest for either large values of η or small values: $\eta > 2.4$ and $\eta < 1.8$. Moreover, we also find that the standard deviation of the p.d.f. of $y_{v,exp}$ grows approximately linearly with its average value, although with more scatter than for the p.d.f. of $y_{F,exp}$ and with a stronger hysteresis between the values before the concentration peak (i.e. $\eta < 1.83$) and the values after the concentration peak (i.e. $\eta > 1.83$).

In the case of an instantaneous finite-volume release of pollutants in a quasi-two-dimensional turbulent jet, the probability P_δ^* to find concentrations of pollutants larger than a critical concentration level ϕ^* at a given value η is for $t > 0$

$$P_\delta^*(\eta, \tilde{t}) = \int_{\tilde{t}^{2/3}\tilde{\phi}^*}^{\infty} f_v(\tilde{y}_{v,exp}, \eta) \, \mathrm{d}\tilde{y}_{v,exp}, \tag{4.17}$$
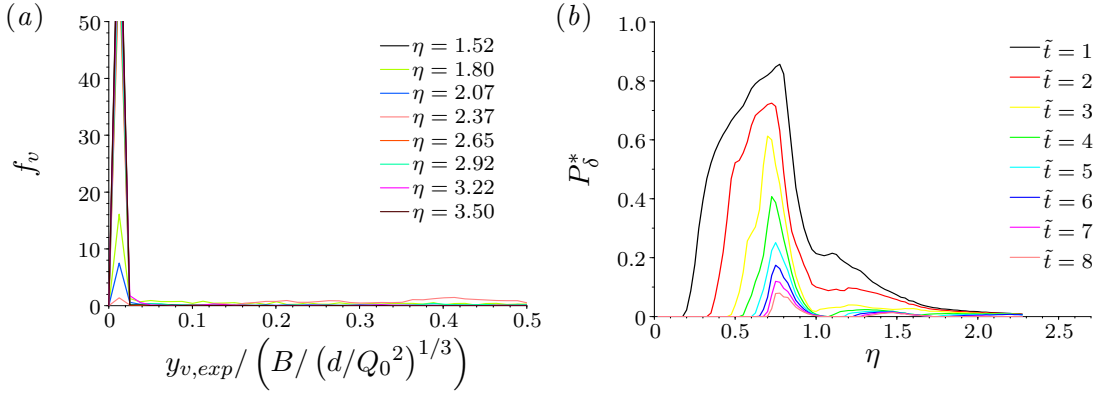
FIGURE 4.15: (*a*) Probability density function of the concentration of virtual particles $y_{v,exp}/\left(B\left(d/Q_0{}^2\right)^{1/3}\right)$, non-dimensionalized and in similarity form, at different values of the similarity variable η in the case of instantaneous finite-volume releases. We describe the experiments in § 4.1.2 and plot the ensemble-averaged concentration $\overline{y}_{v,exp}$ in figure 4.10 with pluses. (*b*) Distribution against the similarity variable η at different non-dimensional times (plotted with different colours) of the probability that the concentration of tracers $\phi_{v,exp}$ is greater than a critical value ϕ^* in the case of an instantaneous finite-volume release in a quasi-two-dimensional jet.

where we use equation (3.66), $\phi(z,t) = t^{-2/3}y(\eta)$. It is interesting to note that, contrary to P_F^*, the probability P_δ^* decreases in time. The probability P_F^* decreases in time because finite volumes of tracers become more dilute, due to the streamwise dispersion, as they are transported by the jet.

As an example, we have plotted P_δ^* in figure 4.15(*b*) against η at eight different non-dimensional times $1 \leq \tilde{t} \leq 8$ (plotted with different colours), for the critical non-dimensional concentration $\tilde{\phi}^* = 1$. We can clearly see that the probability P_δ^* decreases rapidly in time. The maximum value of P_δ^* is located at approximately $\eta = 0.7$, a secondary, much smaller, local maximum is found in the range $1.1 \leq \eta \leq 1.5$. We find that, in this example, the peak of the probability P_δ^* first becomes less than 0.95 from $\tilde{t} \geq 0.3$ at the location $\eta = 0.82$, corresponding to $\tilde{z} = 0.4$. The peak of the probability P_δ^* becomes less than 0.05 (i.e. statistically insignificant) from $\tilde{t} \geq 9.1$ at the location $\eta = 0.77$, corresponding to $\tilde{z} = 3.4$.

4.3.3 Discussion

Owing to the large number of experiments conducted in the cases of constant-flux releases of dye and instantaneous releases of finite volumes of virtual particles,

we have been able to compute the statistical significance of the measurements of the laterally-integrated concentration, in similarity form. We find that, in both cases, the p.d.f. of the concentration tends to decrease and spread rapidly with increasing concentration. This means that near the location of the concentration peak, the difference between the concentration predicted by the model and the experimental (or real) concentration is likely to be much larger than at the tail or front of the distribution where the concentrations are smaller. Therefore, the model is less accurate in the prediction of the values of the largest concentrations than in the prediction of the values of the lowest concentrations.

From the experimental results of the p.d.f. in the constant-flux and instantaneous finite-volume cases, we can determine the probability of having a certain range of tracer concentrations at a certain location in time and space. We discuss the problem, relevant to pollution control, of how to calculate the probability to find concentration levels greater than a critical value in a quasi-two-dimensional jet. We find that in the constant-flux case, the probability increases rapidly in time. On the other hand, the probability decreases for a finite-volume release. In both cases, the location (in terms of the similarity variable η) of the maximum of the probability seems to remain constant in time.

It is important to note that, in this section, we present and discuss the results of the laterally-integrated concentration ϕ instead of the actual concentration C. We observed previously in figure 4.5 that the concentration C tends to disperse linearly with distance across the jet, for both the constant-flux and the finite-volume cases. Therefore, the concentration of tracers is diluted not only because of the streamwise dispersion but also because of the lateral spreading of the jet. As a result, the distribution of the probability P_δ^* to encounter some concentrations C greater than a critical value should decrease more rapidly in time in the case of finite-volume releases of tracers. In the case of constant-flux releases, we believe that instead of increasing in time (for ϕ) the distribution of the probability P_F^* should actually decrease in time for the concentration C. This is related to the fact that, in steady state, the concentration C_F decreases like $z^{-1/2}$ whereas the laterally-integrated concentration ϕ_F increases like $z^{1/2}$ (as discussed in § 3.3.2).

4.4 Conclusion

In Chapters 3 and 4, we have analysed the time-dependent transport and dispersion properties along the streamwise direction of quasi-two-dimensional jets. We model the evolution in time and space of the concentration of passive tracers using a one-dimensional time-dependent effective advection–diffusion equation. We integrate the concentration across the jet in order to be able to solve the effective advection–diffusion equation (3.4). From the analysis of experimental results we find that this simplification appears to be appropriate, because the tracer distribution remains confined within the quasi-two-dimensional jet between two linearly-expanding straight-sided boundaries (see figure 2.4). Neglecting any molecular diffusion, we assume a streamwise turbulent eddy diffusive coefficient D_{zz} proportional to the product of the local half-width of the jet $b(z) \propto z$ and the local time-averaged maximum streamwise velocity $\overline{w}_m(z) \propto z^{-1/2}$ (essentially based on mixing length theory). The streamwise turbulent eddy diffusive diffusion coefficient models physically the interaction between the core and eddy structures of quasi-two-dimensional jets. (In § 2.5, we showed that the core–eddy structure was self-similar with height, with characteristic local length-scale $b(z)$, and with characteristic local velocity scale $\overline{w}_m(z)$.)

Using $D_{zz} \propto z^{1/2}$ we are able to transform the effective advection–diffusion equation into a similarity form. We solve analytically the resulting ordinary differential equation in the cases of a constant-flux release and an instantaneous finite-volume release yielding a 'fundamental solution'. The solutions depend on two parameters, an advection parameter K_a and a dispersion parameter K_d, which we determine using experimental measurements. We also provide an integral formulation for the general problem of an arbitrary time-dependent release of tracers governed by a source function. The integral formulation for this more realistic case is the convolution between the fundamental solution found for the instantaneous finite-volume release and the source function. We present an analytical solution for the general problem in the case of a rectangular source function (i.e. the flux of tracers at the jet source is constant for a finite period of time, T_0, and zero otherwise, thus releasing a finite volume). At large time ($t \gg T_0$), this solution converges towards the fundamental solution found for the instantaneous finite-volume release. On the other hand, for $T_0 \to \infty$, this solution converges towards the solution found for the constant-flux release.

Furthermore, we show theoretically that, owing to dispersion mechanisms, a non-negligible portion of the total volume of tracers released travels ahead of the advective front, in both the finite-volume and the constant-flux cases. The advective front corresponds to the location of the volume of tracers (in the finite-volume case) or the front of the tracer distribution (in the constant-flux case) if all dispersion mechanisms are ignored and $K_d = 0$. We also find that the streamwise dispersion increases in time as $t^{2/3}$.

In this chapter, we compare the theoretical model developed in Chapter 3 with experimental measurements obtained by tracking the concentration of dye or virtual particles in time and space. We conduct both constant-flux and finite-volume releases of dye in quasi-two-dimensional steady turbulent jets. We also release finite volumes of virtual particles (transported as passive tracers) instantaneously in the fully resolved time-dependent velocity fields of quasi-two-dimensional steady turbulent jets. We consider the experimental data for constant-flux releases of dye more accurate because the initial, boundary and integral conditions imposed in the theoretical model are more straightforward to satisfy experimentally. We find that the experimental results agree well with the theoretical prediction, using either the laterally-integrated concentration of dye ϕ or the streamwise concentration flux of dye M_ϕ as defined in (3.6) and (3.50), respectively. The similarity scaling derived from the model $\eta \propto z/t^{2/3}$ is appropriate to study this phenomenon. We find that what we refer to as our 'reference' values for the advection and dispersion parameters are $K_a = 1.65$ and $K_d = 0.09$, respectively, determined from the study of the concentration in the constant-flux dye experiments.

We largely confirm these results by the experimental data obtained with finite-volume releases of virtual particles. The data converge in similarity form towards the fundamental theoretical solution assuming an instantaneous finite-volume release. The similarity scaling $\eta \propto z/t^{2/3}$ is also appropriate in this case. We find that the best fits to the advection and dispersion parameters are $K_a = 1.62$ and $K_d = 0.09$, respectively. In the case of finite-volume releases of dye, we find that the experimental concentration distribution has not converged towards the asymptotic fundamental solution assuming an instantaneous release. We believe that this is principally due to the fact that the dye could not be released instantaneously in the experiment. The duration of the dye release introduces a new time scale T_0, which affects the concentration distribution. Until $t \gg T_0$, the

Case	Theory	K_a	K_d	K_a/K_d	η_a	μ	σ	β	ξ
CF	y_F	1.65	0.09	18.3	1.83	0.65–0.62	0.29–0.30	0.12–0.10	0.16–0.13
CF	y_M	1.55	0.07	23.6	1.83	0.58–0.50	0.31–0.31	0.09–0.06	0.19–0.12
IFV	y_δ	1.62	0.09	18	1.83–1.83	0.99–1.03	0.17–0.19	0.49–0.54	0.13–0.17
FV	ϕ_{T_0}	1.75	0.09	19.4	1.83^a	1.03^a	0.19^a	0.54^a	0.17^a

^{a}Theoretical value after ϕ_{T_0} converges to ϕ_δ.

TABLE 4.1: Summary of the key experimental results found in the constant-flux case (CF) for dye releases, in the instantaneous finite-volume case (IFV) for virtual-particle releases and the finite-volume case (FV) for dye releases. The values for the advection and dispersion parameters K_a and K_d are obtained from the best least-squares fit of the experimental data. On the other hand, η_a, μ, σ, β and ξ are computed theoretically using the 'reference' parameters $K_a = 1.65$ and $K_d = 0.09$, found in the constant-flux case; if two values are indicated: the first value is measured experimentally while the second value is computed theoretically using $K_a = 1.65$ and $K_d = 0.09$.

concentration distribution is in a transition regime, which we model using the general model ϕ_{T_0} defined in (3.88), assuming a rectangular source function. We find that the best fits to the advection and dispersion parameters are $K_a = 1.80$ and $K_d = 0.08$, respectively. We also calculate that, in this case, the distribution should 'converge' (i.e. the normalized absolute deviation between ϕ_{T_0} and ϕ_δ, defined in (3.91), is smaller than 0.1) towards the fundamental solution ϕ_δ defined in (3.73) after a duration equal to approximately 14 times the time of release of the dye (i.e. $t \geq 14T_0$). In other words, the dye distribution should converge towards an asymptotic distribution at $z \approx 2\,\text{m}$ (i.e. at a distance larger than four times the maximum distance of our study area).

Our model appears to be robust to variations in the initial boundary conditions of the experiments. In the experiments with finite-volume releases of virtual particles, even though the particles are released instantaneously but far away from the source, the particle concentration distribution seems to converge rapidly in time towards a stable asymptotic distribution predicted by the model. In the experiments with finite-volume releases of dye, even though the dye is released near the source but not instantaneously, we can prove that the dye concentration distribution will eventually converge in time towards a stable asymptotic distribution predicted by the model. Moreover, we can estimate the time before convergence and provide a model for the transition regime.

Overall, the model largely appears to agree with the data, especially at the dispersive front of the distribution. In table 4.1 we collect all the various key

experimentally determined quantities. By comparing the various models with all the experiments, we are able to give an estimated range for the advection and dispersion parameters. We find that the advection and dispersion parameters are $K_a = 1.65 \pm 0.10$ and $K_d = 0.09 \pm 0.02$ respectively, and the ratio between the two is within the range $18 \leq K_a/K_d \leq 23.6$. For both the constant-flux case and the instantaneous finite-volume case, the location in similarity space of the advective front (as defined in (3.40)) is found at $\eta_a = 1.83$. Then, in the case of constant-flux releases of tracers, we find that the ratio between the centroid and the advective front is approximately $\mu_F = 0.635 \pm 0.015$ with a standard deviation normalized with η_a $\sigma_F = 0.295 \pm 0.005$. At each instant in time, approximately $\beta_F = 11\ \% \pm 1\ \%$ (as defined in (3.47)) of the total volume of tracers having already been released is transported ahead of the advective front, at an averaged normalized distance in similarity space $\xi_F = 0.145 \pm 0.015$ (as defined in (3.49)). In the case of an instantaneous finite-volume release of tracers, the ratio between the centroid and the advective front is approximately $\mu_B = 1.01 \pm 0.02$ with a standard deviation normalized with η_a $\sigma_B = 0.18 \pm 0.01$. At each instant in time, approximately $\beta_B = 51.5\ \% \pm 2.5\ \%$ (as defined in (3.81)) of the total volume of tracers released is transported ahead of the advective front η_a, at an averaged normalized distance in similarity space $\xi_B = 0.15 \pm 0.02$ (as defined in (3.83)).

The analysis of the statistical significance of the experimental measurements of the laterally-integrated concentration reveals that experimental or real concentrations are more likely to differ from the concentrations predicted by the model at large concentration levels than at low concentration levels. We find that the distribution, against the similarity variable η, of the probability to encounter laterally-integrated concentrations greater than a critical value increases in time for the case of constant-flux releases of tracers. On the other hand, the distribution of the analogous probability decreases in time for the case of finite-volume releases of tracers. However, if we study the actual (non-laterally-integrated) concentration, we believe that the probability distribution in the constant-flux case should also decrease in time due to lateral dispersion across the jet with distance.

In § 3.1, we discussed the importance of modelling correctly the transport and dispersion of tracers in quasi-two-dimensional jet flows. We believe that the model developed in Chapter 3 provides not only a strong insight into these mechanisms but also a quantitative basis to predict them. In this chapter, comparisons with

experimental data obtained using different techniques support the predictions of the model. From this comparison, we can also measure accurately the strength of the advection and the strength of the dispersion in quasi-two-dimensional jets, using only an advection parameter K_a and a dispersion parameter K_d, respectively. Finally, we have discovered that the streamwise dispersion increases in time like $t^{2/3}$. In other words, a significant amount of tracers released in quasi-two-dimensional jets is transported faster than the speed predicted by a simple advection model. Such predictions are crucial to many applications, particularly in the event of environmental pollutions in rivers and lakes.

CHAPTER 5

TWO-POINT STATISTICS FOR TURBULENT RELATIVE DISPERSION IN QUASI-TWO-DIMENSIONAL JETS

5.1 Introduction

The dispersion and mixing mechanisms in the turbulent flow of quasi-two-dimensional jets are closely related to the dynamics of the large-scale structures identified as core and eddies. The core and eddy structures display very different flow properties. The velocity field of the core is very high in the streamwise direction, and it appears to be subject to a sinuous instability. The velocity field of the eddies is inherently vortical, with a time-averaged mean component in the streamwise direction. At the interface between the eddies and the core, the streamwise velocity has a large lateral (or cross-jet) gradient. Moreover, the

flow is turbulent everywhere in a quasi-two-dimensional jet. We believe that such distinctive Eulerian characteristics (of the flow in the core, in the eddies and at the interface between the two) also have distinctive dispersive and mixing properties. From the interaction between these structures, in time and space, results the global, mean dispersion mechanism of quasi-two-dimensional jets, which we model in Chapter 3 along the streamwise direction.

Conversely, in this chapter, we adopt a Lagrangian approach to investigate the dispersion and mixing properties of the core and eddy structures of quasi-two-dimensional jets. In figure 4.4 presented in the previous chapter, we showed the evolution in time of clusters of virtual particles (or passive tracers) released in different parts of a quasi-two-dimensional jet: in an eddy (see figure 4.4a), between the eddy and the core (see figure 4.4b), and in the core (see figure 4.4c). We qualitatively described how the clusters of particles disperse and mix, while being transported by the jet. The virtual particles seeded in the eddy travel significantly slower than the virtual particles seeded in the core. The virtual particles seeded in the eddy appear to experience more vigorous stirring than the virtual particles seeded in the core. We also noticed that the virtual particles seeded in the core disperse laterally as they are advected by the flow. On the other hand, the virtual-particle cluster seeded between the eddy and the core display intense streamwise stretching.

The aim of this study is to quantify these observations about the dispersion and mixing of the virtual particles in figure 4.4. We use statistical analysis to understand the underlying physical mechanisms. We study the probability distribution of two-point properties, such as the lateral (or x-) distance between two points, the streamwise (or z-) distance between two points, the distance between two points, and the ratio of the lateral distance to the streamwise distance between two points. We apply these probabilistic tools to clusters of virtual particles released in quasi-two-dimensional jets (such as those in figure 4.4), where the two-point measurements are made between pairs of virtual particles. We compute the probability distribution of the two-point properties at each instant in time to obtain meaningful quantitative insight about the temporal and spatial dispersive dynamics of the jet structures.

The work of Richardson (1926) pioneers the use of two-point statistics to study diffusion in turbulent flows (see e.g. Sawford, 2001; Salazar & Collins, 2009, for

recent reviews). Observing considerable discrepancies (by more than ten orders of magnitude) in the measurements of the atmospheric diffusivity, he argued that two-point statistics are more appropriate to explain diffusion in the atmosphere than single-point statistics (used previously to measure the diffusivity in the sense described by Fick's law). Two-point statistics (such as the time average of the distance between two points) enable the study of the dispersion in the flow at each spatial scale (defined, for example, by the eddy size), without being influenced by the larger scales. From the probability density function of the distance between particles, Richardson derived his famous 4/3 law of diffusion. Batchelor (1952) developed a rigorous mathematical framework for the idea of Richardson (1926) to use two-point statistics in order to study turbulent relative dispersion. He applied two-point statistics to the diffusion of passive scalars in homogeneous isotropic turbulence.

The concept of two-point statistics has then been used to study turbulent dispersion in the ocean and in the atmosphere (see e.g. Monin & Yaglom, 1975, pp. 556–567, for a review). Salazar & Collins (2009) and Yeung (2002) give a summary of experimental and numerical works investigating turbulent relative dispersion. In experimental turbulent flows, two-point statistics can be calculated by tracking Lagrangian particles. According to Toschi & Bodenschatz (2009), the most successful current technique to perform Lagrangian particle tracking is called particle tracking velocimetry. For example, Bourgoin *et al.* (2006) used particle tracking velocimetry to measure the mean square distance between particles in a turbulent flow (generated "between coaxial counter-rotating baffled disks in a closed chamber"). They confirmed the theoretical prediction of Batchelor (1950) that the temporal evolution of the distance between pairs of particles during the superdiffusion stage (i.e. the regime when the mean square distance between particles increases in time like t^α with $\alpha > 1$, Bourgoin *et al.*, 2006) is influenced by the initial distance separation of the particles. Bourgoin *et al.* (2006) also commented on the scarcity of direct experimental evidence for turbulent relative dispersion. Toschi & Bodenschatz (2009) attributed the lack of experimental evidence to the technical difficulties of the implementation of Lagrangian particle tracking in fully turbulent flow.

We believe that applying two-point statistics to the turbulent flow of quasi-two-dimensional jets can give new insight about turbulent relative dispersion in

the case of a non-homogeneous and anisotropic turbulent flow. We use what we believe to be a new method to calculate these two-point statistics, which we call virtual particle tracking (see § 4.1). The virtual-particle-tracking technique (which we use to produce the results shown in figure 4.4, mentioned above) consists of seeding and tracking virtual passive tracers in velocity fields measured using particle image velocimetry. The results presented in this study focus primarily on the dispersion properties of quasi-two-dimensional jets, but not directly on the transport or turbulent mixing properties. By definition, two-point statistics do not depend on mean transport motion, and thus cannot investigate it. (The transport properties of the jet have actually been studied extensively in Chapters 2, 3 and 4.) On the other hand, we believe that mixing properties cannot be directly examined from the results we present in this thesis for technical reasons. The measurements of the velocity fields (performed using particle image velocimetry), though well-resolved in time (the time resolution is one order of magnitude smaller than the Kolmogorov time scale, $\tau_{\eta_K} \approx 40$ ms), do not have the spatial accuracy necessary to investigate the finest scales of turbulence in our flow (the Kolmogorov length scale is of the order of $\eta_K \approx 0.2$ mm, as discussed in § 2.2.2). In Chapter 4, we quantify the mixing through the dilution of the dye concentration. Likewise, in this chapter, we infer indirectly the turbulent mixing processes from the dispersion, stretching and folding of our particle distributions.

In order to comprehend fully the temporal evolution of the probability distributions of two-point properties applied to virtual-particle clusters seeded in the different parts of the flow of quasi-two-dimensional jets, we compare our results with other flow fields. As a preliminary study, we apply our statistical tools to simple distributions of points (such as a circle, an ellipse and a square) evolving in diverging velocity fields. The purpose of this preliminary study is to understand how the probability distributions of two-point properties are related to a given initial distribution of particles, and how they evolve in time. Then, we compare the results for the time-dependent flow field of a quasi-two-dimensional jet with results obtained using the time-averaged flow field of the same jet. This comparison allows us to identify some key dispersive mechanisms due to the core and eddy structures and emphasizes the importance of their time-dependent interactions.

The rest of this chapter is organized as follows. In § 5.2, we describe mathematically how to compute the probability distribution of the two-point properties

stated above, in both the continuous case and the discrete case. In § 5.3, we present a preliminary study of three analytical and numerical test cases: an axisymmetric expansion of a circular domain, a non-axisymmetric expansion of an elliptical domain, and a diffusive expansion of a square domain. In § 5.4, we present the results of the probability distributions for the three clusters of virtual particles seeded in the quasi-two-dimensional jet shown in figure 4.4. We compare these results with similar results obtained in the equivalent time-averaged velocity field of the jet. Finally, we draw our conclusions in § 5.5.

5.2 Mathematical definitions of two-point probability distributions

5.2.1 Continuous formulation

The probability density function (p.d.f.) $f^{\mathcal{Y}}$ of a real-valued random variable $\mathcal{Y}$ is the derivative of the cumulative distribution function (c.d.f.) $F^{\mathcal{Y}}$ (see e.g. Pope, 1985) such that, for any real number y,

$$f^{\mathcal{Y}}(y) = \frac{\mathrm{d}F^{\mathcal{Y}}(y)}{\mathrm{d}y}. \tag{5.1}$$

The c.d.f. can be defined as the probability that the random variable $\mathcal{Y}$ takes on a value less than or equal to y,

$$F^{\mathcal{Y}}(y) = P(\mathcal{Y} \leq y). \tag{5.2}$$

In the present study, we wish to compute the p.d.f. of four characteristic properties between pairs of points $(\mathbf{x_1}, \mathbf{x_2})$ distributed in a domain $\mathscr{A}$. The first characteristic property is the lateral distance between two points:

$$\mathcal{H}(\mathbf{x_1}, \mathbf{x_2}) = |x_1 - x_2|, \quad \text{with} \quad \mathbf{x_1} = (x_1, z_1),\ \mathbf{x_2} = (x_2, z_2) \in \mathscr{A}. \tag{5.3}$$

The second characteristic property is the streamwise distance between two points:

$$\mathcal{V}(\mathbf{x_1}, \mathbf{x_2}) = |z_1 - z_2|, \quad \text{with} \quad \mathbf{x_1} = (x_1, z_1),\ \mathbf{x_2} = (x_2, z_2) \in \mathscr{A}. \tag{5.4}$$

The third characteristic property is the (Euclidean) distance between two points:

$$\mathcal{D}\left(\mathbf{x_1}, \mathbf{x_2}\right) = \|\mathbf{x_1} - \mathbf{x_2}\|, \quad \text{with} \quad \mathbf{x_1} = (x_1, z_1),\ \mathbf{x_2} = (x_2, z_2) \in \mathscr{A}, \quad (5.5)$$

where $\|\mathbf{x_1} - \mathbf{x_2}\| = \left((x_1 - x_2)^2 + (z_1 - z_2)^2\right)^{1/2}$. The fourth characteristic property is the ratio of the lateral distance to the streamwise distance between two points:

$$\mathcal{M}\left(\mathbf{x_1}, \mathbf{x_2}\right) = \frac{|x_1 - x_2|}{|z_1 - z_2|}, \quad \text{with} \quad \mathbf{x_1} = (x_1, z_1),\ \mathbf{x_2} = (x_2, z_2) \in \mathscr{A}. \quad (5.6)$$

The probability that the random variable $\mathcal{Y}\left(\mathbf{x_1}, \mathbf{x_2}\right)$ ($= \mathcal{H}\left(\mathbf{x_1}, \mathbf{x_2}\right)$, $\mathcal{V}\left(\mathbf{x_1}, \mathbf{x_2}\right)$, $\mathcal{D}\left(\mathbf{x_1}, \mathbf{x_2}\right)$ or $\mathcal{M}\left(\mathbf{x_1}, \mathbf{x_2}\right)$), with $\mathbf{x_1}$, $\mathbf{x_2} \in \mathscr{A}$, takes on a value less than or equal to y ($= \hbar$, v, d or m, respectively) is

$$P_{\mathscr{A}}(\mathcal{Y}\left(\mathbf{x_1}, \mathbf{x_2}\right) \le y) = \frac{1}{\displaystyle\int_{\mathscr{A}} \varsigma(\mathbf{x_1}) \mathrm{d}\tau_1} \int_{\mathscr{A}} P_{\mathscr{A}}(\mathcal{Y}\left(\mathbf{x_1}, \mathbf{x_2}\right) \le y | \mathbf{x_1}) \varsigma(\mathbf{x_1})\, \mathrm{d}\tau_1, \quad (5.7)$$

where $\mathrm{d}\tau_1$ is an appropriate differential for the domain $\mathscr{A}$ with respect to the first point $\mathbf{x_1}$, and $\varsigma(\mathbf{x})$ is the density of the probability distribution (i.e. it is a measure of the local probability, which may not be uniform, at the point $\mathbf{x} \in \mathscr{A}$). $P_{\mathscr{A}}(\mathcal{Y}\left(\mathbf{x_1}, \mathbf{x_2}\right) \le y | \mathbf{x_1})$ is the conditional probability that the random variable $\mathcal{Y}\left(\mathbf{x_1}, \mathbf{x_2}\right)$ takes on a value less than or equal to y knowing $\mathbf{x_1}$ and is defined as

$$P_{\mathscr{A}}(\mathcal{Y}\left(\mathbf{x_1}, \mathbf{x_2}\right) \le y | \mathbf{x_1}) = \frac{1}{\displaystyle\int_{\mathscr{A}} \varsigma(\mathbf{x_2}) \mathrm{d}\tau_2} \int_{\mathscr{A} \cap \mathscr{B}(\mathbf{x_1}, y)} \varsigma(\mathbf{x_2})\, \mathrm{d}\tau_2, \quad (5.8)$$

where the domain $\mathscr{B}(\mathbf{x_1}, y)$ is defined such that $\mathbf{x_2} \in \mathscr{B}(\mathbf{x_1}, y)$ if $\mathcal{Y}\left(\mathbf{x_1}, \mathbf{x_2}\right) \le y$ with $\mathbf{x_1}$ known, and $\mathrm{d}\tau_2$ is an appropriate differential for the domain $\mathscr{A}$ with respect to the second point $\mathbf{x_2}$. Finally, according to (5.1) and (5.2), the p.d.f. of the random variable $\mathcal{Y}$ in the domain $\mathscr{A}$ is

$$f_{\mathscr{A}}^{\mathcal{Y}}(y) = \frac{\mathrm{d}P_{\mathscr{A}}(\mathcal{Y}\left(\mathbf{x_1}, \mathbf{x_2}\right) \le y)}{\mathrm{d}y}, \quad (5.9)$$

where the probability $P_{\mathscr{A}}(\mathcal{Y}\left(\mathbf{x_1}, \mathbf{x_2}\right) \le y)$ is defined by (5.7) and (5.8).

5.2.2 Discrete formulation

The probability density functions of the four characteristic properties of the distribution of particles defined in (5.3), (5.4), (5.5), and (5.6), for $\mathcal{H}$, $\mathcal{V}$, $\mathcal{D}$ and $\mathcal{M}$, respectively, can also be formulated in the discrete case. For n particles $\mathbf{x_i} = (x_i, z_i)$ of weight ω_i (similarly to the concept of density ς used previously for the continuous case) distributed in a domain $\mathscr{A}$, the discrete p.d.f. of a random variable $\mathcal{Y}(\mathbf{x_1}, \mathbf{x_2})$ $(= \mathcal{H}(\mathbf{x_1}, \mathbf{x_2})$, $\mathcal{V}(\mathbf{x_1}, \mathbf{x_2})$, $\mathcal{D}(\mathbf{x_1}, \mathbf{x_2})$ or $\mathcal{M}(\mathbf{x_1}, \mathbf{x_2}))$ in this domain is

$$f_{\mathscr{A}}^{\mathcal{Y}}(y_k) = \frac{1}{\displaystyle\sum_{i>j}^{n} \omega_i \omega_j \, \delta y} \sum_{i>j}^{n} \mathfrak{Y}_{i,j}(y_k), \quad k \in \mathbb{N}, \quad 1 \le k \le N, \tag{5.10}$$

with $\delta y = y_1 - y_0$ and, for all $1 \le i \le n$ and $1 \le j \le n$ (where i and j are two integers),

$$\mathfrak{Y}_{i,j}(y_k) = \begin{cases} \omega_i \omega_j & \text{if } y_{k-1} \le \mathcal{Y}(\mathbf{x_i}, \mathbf{x_j}) < y_k \\ 0 & \text{otherwise} \end{cases}. \tag{5.11}$$

Here, y_k are distributed from $y_0 = 0$ to y_N, the maximum value taken by $\mathcal{Y}(\mathbf{x_1}, \mathbf{x_2})$ in the domain $\mathscr{A}$, while N is the number of bins. The distribution of y_k is linear for $\mathcal{Y} = \mathcal{H}$, $\mathcal{V}$ and $\mathcal{D}$, and logarithmic for $\mathcal{Y} = \mathcal{M}$.

5.3 Test studies in diverging velocity fields

We calculate analytically or numerically the time evolution of the p.d.f.s of the two-point properties $\mathcal{H}$, $\mathcal{V}$, $\mathcal{D}$, and $\mathcal{M}$ (as defined in (5.3), (5.4), (5.5) and (5.6), respectively) in the case of continuous or discrete distributions of points in simple two-dimensional domains. Firstly, we study a circular domain expanding axisymmetrically in a diverging velocity field. Secondly, we investigate the non-axisymmetric expansion of an elliptical domain, in order to understand the effect on the p.d.f.s of a variation in the aspect ratio of the domain. Thirdly, we study the effect of molecular diffusion on the p.d.f.s for an initially square distribution of discrete points.

Following the example of Richardson (1926), who derived the p.d.f. of the distance between particles distributed on a straight line, we believe this preliminary

analysis can help us understand the turbulent relative dispersion in quasi-two-dimensional jets, which is studied in § 5.4. In these test studies, the actual velocity fields in which we set our domains (the disc, the ellipse and the square) are not important because we do not intend to relate them directly to the velocity fields of quasi-two-dimensional jets. The velocity fields of the test studies are merely a means to change the shape of our three domains in time. In fact, this is rather the effect of the time evolution of the shape of our domains on the p.d.f.s that we intend to compare with the time evolution of the p.d.f.s for the three particle clusters presented in § 5.4.

5.3.1 Circular domain in an axisymmetric diverging velocity field

We define in $\mathbb{R}^2$ a continuous uniform distribution $\mathscr{D}_t$ where the initial density $\varsigma_{\mathscr{D}_t}(\mathbf{x}, 0) \equiv 1$ for all $\mathbf{x} = (x, z)$ such that $x^2 + z^2 \leq R_0{}^2$ (where R_0 is the initial radius of the disc $\mathscr{D}_t$) and $\varsigma_{\mathscr{D}_t}(\mathbf{x}, 0) \equiv 0$ otherwise. The domain $\mathscr{D}_t$ evolves in time due to a constant diverging radial velocity field (u, w) defined by

$$u(x) = x, \quad w(z) = z. \tag{5.12}$$

Hence, the radius of the disc increases uniformly in time at an exponential rate:

$$R(t) = e^t R_0; \tag{5.13}$$

and the density decreases in time such that

$$\varsigma_{\mathscr{D}_t}(\mathbf{x}, t) = \begin{cases} \dfrac{R_0{}^2}{R^2(t)} = e^{-2t} & \forall \, \mathbf{x} = (x, z), \ x^2 + z^2 \leq R^2(t) \\ 0 & \text{otherwise} \end{cases}. \tag{5.14}$$

Since the domain $\mathscr{D}_t$ is axisymmetric and expands radially at all times, the p.d.f. of the lateral distance between two points is equal to the p.d.f. of the streamwise distance between two points in the same domain, i.e. $f_{\mathscr{D}_t}^{\mathscr{H}} = f_{\mathscr{D}_t}^{\mathscr{V}}$. Moreover, the p.d.f. is self-similar in time and depends only on the radius $R(t)$. Using equations (5.7) and (5.8) with $\mathscr{Y} = \mathscr{H}$ (or $\mathscr{V}$), defined in (5.3) (and (5.4)), $y = \hbar$ (or v),

the c.d.f. of $\mathcal{H}(\mathbf{x_1}, \mathbf{x_2})$ (or $\mathcal{V}(\mathbf{x_1}, \mathbf{x_2})$) with $\mathbf{x_1}$, $\mathbf{x_2}$ in $\mathscr{A} = \mathscr{D}_t$ is, for $h \geq 0$,

$$F_{\mathscr{D}_t}^{\mathcal{H}}(h) = \frac{4}{\pi R^2(t)} \int_0^{R(t)} P_{\mathscr{D}_t}(\mathcal{H}(\mathbf{x_1}, \mathbf{x_2}) \leq h | \mathbf{x_1}) \sqrt{R^2(t) - x_1{}^2} \, dx_1, \qquad (5.15)$$

where we use the fact that the c.d.f. is symmetric with respect to both the x-axis and the z-axis, the conditional probability does not depend on z_1 (as long as $x_1{}^2 + z_1{}^2 \leq R^2(t)$) and the density is uniform over the whole domain $\mathscr{D}_t$. For $0 \leq h \leq R(t)$, the conditional probability is

$$P_{\mathscr{D}_t}(\mathcal{H}(\mathbf{x_1}, \mathbf{x_2}) \leq h | \mathbf{x_1}) = \frac{1}{\pi}\left(\arcsin\left(\frac{x_1+h}{R(t)}\right) + \frac{(x_1+h)}{R(t)}\sqrt{1-\left(\frac{x_1+h}{R(t)}\right)^2} - \arcsin\left(\frac{x_1-h}{R(t)}\right) \right.$$
$$\left. - \frac{(x_1-h)}{R(t)}\sqrt{1-\left(\frac{x_1-h}{R(t)}\right)^2} \right), \quad 0 \leq x_1 \leq R(t)-h, \qquad (5.16)$$

and

$$P_{\mathscr{D}_t}(\mathcal{H}(\mathbf{x_1}, \mathbf{x_2}) \leq h | \mathbf{x_1}) = \frac{1}{\pi}\left(\frac{\pi}{2} - \arcsin\left(\frac{x_1-h}{R(t)}\right) - \frac{(x_1-h)}{R(t)}\sqrt{1-\left(\frac{x_1-h}{R(t)}\right)^2} \right), \quad R(t)-h \leq x_1 \leq R(t).$$
$$(5.17)$$

For $R(t) \leq h \leq 2R(t)$, the conditional probability is

$$P_{\mathscr{D}_t}(\mathcal{H}(\mathbf{x_1}, \mathbf{x_2}) \leq h | \mathbf{x_1}) = 1, \quad 0 \leq x_1 \leq -R(t) + h, \qquad (5.18)$$

and

$$P_{\mathscr{D}_t}(\mathcal{H}(\mathbf{x_1}, \mathbf{x_2}) \leq h | \mathbf{x_1}) = \frac{1}{\pi}\left(\frac{\pi}{2} - \arcsin\left(\frac{x_1-h}{R(t)}\right) - \frac{(x_1-h)}{R(t)}\sqrt{1-\left(\frac{x_1-h}{R(t)}\right)^2} \right), \quad -R(t)+h \leq x_1 \leq R(t).$$
$$(5.19)$$

For $2R(t) \leq h$

$$P_{\mathscr{D}_t}(\mathcal{H}(\mathbf{x_1}, \mathbf{x_2}) \leq h | \mathbf{x_1}) = 1, \quad 0 \leq x_1 \leq R(t). \qquad (5.20)$$

Details about the calculation of the conditional probability $P_{\mathscr{D}_t}(\mathcal{H}(\mathbf{x_1}, \mathbf{x_2}) \leq h | \mathbf{x_1})$ can be found in Appendix B.1. We calculate the c.d.f. $F_{\mathscr{D}_t}^{\mathcal{H}}$ (as defined in (5.15)) by computing the integral numerically. We then obtain the p.d.f. $f_{\mathscr{D}_t}^{\mathcal{H}}$ (or $f_{\mathscr{D}_t}^{\mathcal{V}}$) by differentiating this calculated c.d.f. numerically, i.e.

$$f_{\mathscr{D}_t}^{\mathcal{H}}(h) = \frac{dF_{\mathscr{D}_t}^{\mathcal{H}}(h)}{dh}. \qquad (5.21)$$

We plot the non-dimensional p.d.f. $f_{\mathscr{D}_t}^{\mathcal{H}} R(t)$ in figure 5.1(a) against the non-dimensional variable $h/R(t)$. We can see that $f_{\mathscr{D}_t}^{\mathcal{H}} R(t)$ decreases smoothly from $f_{\mathscr{D}_t}^{\mathcal{H}}(0) = 32/\left(3\pi^2 R(t)\right)$ to $f_{\mathscr{D}_t}^{\mathcal{H}}(2R(t)) = 0$ (see details in Appendices B.2 and B.3).

The p.d.f. $f_{\mathscr{S}_t}^{\mathcal{H}}$ of $\mathcal{H}$ in a square domain $\mathscr{S}_t$ defined by the density $\varsigma_{\mathscr{S}_t}(\mathbf{x}, 0) \equiv 1$ for all $\mathbf{x} = (x, z)$ such that $-R_0 \leq x \leq R_0$ and $-R_0 \leq z \leq R_0$ and 0 otherwise (with $R(t)$ described by (5.13) and $\varsigma_{\mathscr{S}_t}(\mathbf{x}, t) = e^{-2t}$ if $-R(t) \leq x \leq R(t)$ and $-R(t) \leq z \leq R(t)$ and 0 otherwise) is

$$f_{\mathscr{S}_t}^{\mathcal{H}}(h) = \frac{2R(t) - h}{2R^2(t)}. \tag{5.22}$$

The full derivation of (5.22) can be found in Appendix B.4. We can see in figure 5.1(a) that the 'disc' $f_{\mathscr{D}_t}^{\mathcal{H}}$ is somewhat similar to the 'square' $f_{\mathscr{S}_t}^{\mathcal{H}}$ (plotted with a dashed line), which decreases linearly from $f_{\mathscr{S}_t}^{\mathcal{H}}(0) = 1/\left(R(t)\right)$ to $f_{\mathscr{S}_t}^{\mathcal{H}}(2R(t)) = 0$.

Similarly, we can compute the c.d.f. of the distance between two points using equations (5.7) and (5.8) with $\mathcal{Y} = \mathcal{D}$ (defined in (5.5)), $y = d$, with $\mathbf{x_1}, \mathbf{x_2}$ in $\mathscr{A} = \mathscr{D}_t$. We have in polar coordinates, for $d \geq 0$,

$$F_{\mathscr{D}_t}^{\mathcal{D}}(d) = \frac{2}{R^2(t)} \int_0^{R(t)} P_{\mathscr{D}_t}(\mathcal{D}(\mathbf{x_1}, \mathbf{x_2}) \leq d \,|\mathbf{x_1}) r_1 \mathrm{d}r_1, \tag{5.23}$$

where $r_1 = \sqrt{x_1{}^2 + z_1{}^2}$, and where we use the fact that the conditional probability is independent of the angle θ_1 (as long as $r_1 \leq R(t)$) and the density is uniform over the whole domain $\mathscr{D}_t$. For $0 \leq d \leq R(t)$, the conditional probability is

$$P_{\mathscr{D}_t}(\mathcal{D}(\mathbf{x_1}, \mathbf{x_2}) \leq d \,|\mathbf{x_1}) = \frac{d^2}{R^2(t)}, \quad 0 \leq r_1 \leq R(t) - d, \tag{5.24}$$

and

$$P_{\mathscr{D}_t}(\mathcal{D}(\mathbf{x_1}, \mathbf{x_2}) \leq d \,|\mathbf{x_1}) = \frac{d^2}{\pi R^2(t)}\left(\pi - \arccos\left(\frac{x_I - r_1}{d}\right) + \frac{(x_I - r_1)}{d}\sqrt{1 - \left(\frac{x_I - r_1}{d}\right)^2}\right) +$$
$$\frac{1}{\pi}\left(\arccos\left(\frac{x_I}{R(t)}\right) - \frac{x_I}{R(t)}\sqrt{1 - \left(\frac{x_I}{R(t)}\right)^2}\right), \quad R(t) - d \leq r_1 \leq R(t), \tag{5.25}$$

where

$$x_I = \frac{R^2(t) + r_1{}^2 - d^2}{2r_1}, \tag{5.26}$$
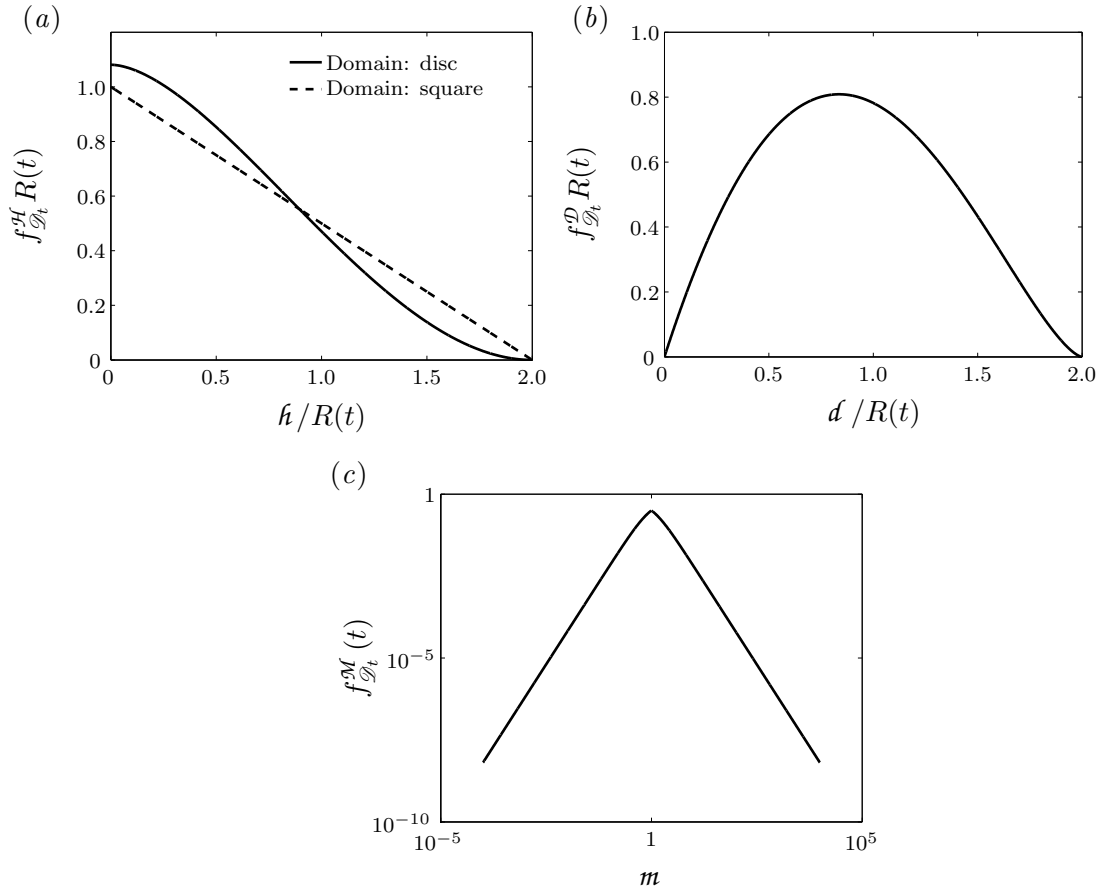
FIGURE 5.1: Probability density functions in the case of a uniformly distributed disc $\mathscr{D}_t$ in an axisymmetric diverging velocity field described in (5.12) for: (a) the lateral (or streamwise) distance between two points $f^{\mathcal{H}}_{\mathscr{D}_t}$ (solid curve), defined in (5.21), the p.d.f. of the lateral (or streamwise) distance between two points in a square $f^{\mathcal{H}}_{\mathscr{S}_t}$ (defined in (5.22)) is plotted with a dashed line for comparison; (b) the distance between two points $f^{\mathcal{D}}_{\mathscr{D}_t}$, defined in (5.30); ($c$) the ratio of the lateral distance to the streamwise distance between two points $f^{\mathcal{M}}_{\mathscr{D}_t}$, defined in (5.34).

is the x-coordinate of the intersection between the perimeter of $\mathscr{D}_t$ and the circle defined by $\mathbf{x} = (x, z)$ such that $(x - r_1)^2 + z^2 = d^2$. For $R(t) \leq d \leq 2R(t)$, the conditional probability is

$$P_{\mathscr{D}_t}(\mathcal{D}(\mathbf{x_1}, \mathbf{x_2}) \leq d \,|\mathbf{x_1}) = 1, \quad 0 \leq r_1 \leq -R(t) + d, \tag{5.27}$$

and

$$P_{\mathscr{D}_t}(\mathscr{D}(\mathbf{x_1}, \mathbf{x_2}) \leq d \, |\mathbf{x_1}) = \frac{d^2}{\pi R^2(t)} \left(\pi - \arccos\left(\frac{x_I - r_1}{d}\right) + \frac{(x_I - r_1)}{d} \sqrt{1 - \left(\frac{x_I - r_1}{d}\right)^2} \right) +$$

$$\frac{1}{\pi} \left(\arccos\left(\frac{x_I}{R(t)}\right) - \frac{x_I}{R(t)} \sqrt{1 - \left(\frac{x_I}{R(t)}\right)^2} \right), \quad -R(t) + d \leq r_1 \leq R(t). \quad (5.28)$$

For $2R(t) \leq d$,

$$P_{\mathscr{D}_t}(\mathscr{D}(\mathbf{x_1}, \mathbf{x_2}) \leq d \, |\mathbf{x_1}) = 1, \quad 0 \leq r_1 \leq R(t). \quad (5.29)$$

Details about the calculation of the conditional probability $P_{\mathscr{D}_t}(\mathscr{D}(\mathbf{x_1}, \mathbf{x_2}) \leq d \, |\mathbf{x_1})$ can be found in Appendix B.5. As before, we calculate the c.d.f. $F_{\mathscr{D}_t}^{\mathscr{D}}$ (as defined in (5.23)) by computing the integral numerically. We then obtain the p.d.f. $f_{\mathscr{D}_t}^{\mathscr{D}}$ by differentiating this calculated c.d.f. numerically, i.e.

$$f_{\mathscr{D}_t}^{\mathscr{D}}(d) = \frac{\mathrm{d}F_{\mathscr{D}_t}^{\mathscr{D}}(d)}{\mathrm{d}d}. \quad (5.30)$$

We plot the non-dimensional p.d.f. $f_{\mathscr{D}_t}^{\mathscr{D}} R(t)$ in figure 5.1(b) against the non-dimensional variable $d/R(t)$. It is interesting to note that the p.d.f. $f_{\mathscr{D}_t}^{\mathscr{D}}$ starts from 0 at $d = 0$ (as can be proved from (5.23), (5.24) and (5.25) using a similar technique to that used in Appendix B.2), increases to a maximum value (which appears to occur for $d/R(t) < 1$) and then vanishes at $d = 2R(t)$ (as can be proved from (5.23), (5.27) and (5.28) using a similar technique to that used in Appendix B.3).

We can also compute the c.d.f. of the ratio of the lateral distance to the streamwise distance between two points using equations (5.7) and (5.8) with $\mathscr{Y} = \mathscr{M}$, defined in (5.6), $y = m$, and with $\mathbf{x_1}$, $\mathbf{x_2}$ in $\mathscr{A} = \mathscr{D}_t$. We have in polar coordinates, for $m \geq 0$,

$$F_{\mathscr{D}_t}^{\mathscr{M}}(m, t) = \frac{4}{\pi R^2(t)} \int_0^{R(t)} \int_0^{\frac{\pi}{2}} P_{\mathscr{D}_t}(\mathscr{M}(\mathbf{x_1}, \mathbf{x_2}) \leq m \, |\mathbf{x_1}) r_1 \, \mathrm{d}r_1 \mathrm{d}\theta_1, \quad (5.31)$$

where $x_1 = r_1 \cos\theta_1$ and $z_1 = r_1 \sin\theta_1$, and where we use the fact that the density is uniform over the whole domain $\mathscr{D}_t$ and that the conditional probability is symmetric with respect to both the x-axis and the z-axis. The conditional

probability, which, in this case, depends on θ_1, is

$$P_{\mathscr{D}_t}(\mathcal{M}(\mathbf{x_1}, \mathbf{x_2}) \leq m \,|\mathbf{x_1}) = \mathscr{F}(\pi - \upsilon) - \mathscr{F}(\upsilon) + \mathscr{F}(-\upsilon) - \mathscr{F}(\upsilon - \pi), \quad (5.32)$$

with $\upsilon = \arctan(1/m)$, and where

$$\mathscr{F}(\theta_2) = \frac{1}{\pi R^2(t)} \left(\frac{R^2(t)}{2}\theta_2 + \frac{r_1^2}{4}\sin(2(\theta_2 - \theta_1)) + \right.$$

$$\left. \frac{R^2(t)}{2} \left(\arccos\left(\frac{r_1}{R(t)}\sin(\theta_2 - \theta_1)\right) - \frac{r_1}{R(t)}\sin(\theta_2 - \theta_1)\sqrt{1 - \left(\frac{r_1}{R(t)}\sin(\theta_2 - \theta_1)\right)^2} \right) \right). \quad (5.33)$$

Details about the calculation of the conditional probability $P_{\mathscr{D}_t}(\mathcal{M}(\mathbf{x_1}, \mathbf{x_2}) \leq m \,|\mathbf{x_1})$ can be found in Appendix B.6. As before, we calculate the c.d.f. $F_{\mathscr{D}_t}^{\mathcal{M}}$ (as defined in (5.31)) by computing the integral numerically. We then obtain the p.d.f. $f_{\mathscr{D}_t}^{\mathcal{M}}$ by differentiating this calculated c.d.f. numerically, i.e.

$$f_{\mathscr{D}_t}^{\mathcal{M}}(m) = \frac{\mathrm{d}F_{\mathscr{D}_t}^{\mathcal{M}}(m)}{\mathrm{d}m}. \quad (5.34)$$

We plot the dimensionless p.d.f. $f_{\mathscr{D}_t}^{\mathcal{M}}$ in figure 5.1(c) against the dimensionless variable m using a logarithmic scale. We can see that the p.d.f. vanishes at $r \to 0$ and $r \to \infty$. Moreover, $f_{\mathscr{D}_t}^{\mathcal{M}}$ is symmetric with respect to $m = 1$, owing to the axisymmetry of the domain $\mathscr{D}_t$ at all time. In other words, $f_{\mathscr{D}_t}^{\mathcal{M}}(m) = f_{\mathscr{D}_t}^{\mathcal{M}}(1/m)$.

5.3.2 Elliptical domain in a non-axisymmetric diverging velocity field

Now, we study the case of a non-axisymmetric diverging velocity field. We define in $\mathbb{R}^2$ a continuous uniform distribution $\mathscr{L}_t$, which is identical to the disc $\mathscr{D}_t$ (described previously) at $t = 0$. The initial density of $\mathscr{L}_t$ is $\varsigma_{\mathscr{L}_t}(\mathbf{x}, 0) \equiv 1$ for all $\mathbf{x} = (x, z)$ such that $x^2 + z^2 \leq R_0^2$ (where R_0 is the initial radius of $\mathscr{L}_t$) and $\varsigma_{\mathscr{D}_t}(\mathbf{x}, 0) \equiv 0$ otherwise. For $t > 0$, the domain $\mathscr{L}_t$ evolves in time due to a constant diverging non-axisymmetric velocity field (u, w) defined by

$$u(x) = x, \quad w(z) = \frac{z}{c}, \quad (5.35)$$

where $c > 1$ is a constant. The case $c = 1$ corresponds to the axisymmetric expansion of the disc studied in the previous section. Also, we do not need to study the case $c < 1$ owing to the symmetry between the x and z spatial coordinates (or u and w components of the velocity field). The domain $\mathscr{L}_t$ has an elliptical contour for $t > 0$, whose semi-major axis and semi-minor axis are denoted a and b in the x- and z-directions, respectively. The semi-axes a and b increase in time at different exponential rates:

$$a(t) = e^t R_0, \quad b(t) = e^{t/c} R_0, \qquad (5.36a,b)$$

and the density decreases in time such that

$$\varsigma_{\mathscr{L}_t}(\mathbf{x}, t) = \begin{cases} \dfrac{R_0{}^2}{a(t)b(t)} = e^{-t(c+1)/c} & \forall \, \mathbf{x} = (x,z), \; \left(\frac{x}{a(t)}\right)^2 + \left(\frac{z}{b(t)}\right)^2 \leq 1 \\ 0 & \text{otherwise} \end{cases} . \quad (5.37)$$

The domain $\mathscr{L}_t$ expands radially at all time but not axisymmetrically. The domain $\mathscr{L}_t$ remains symmetric with respect to both the x-axis and the z-axis. The p.d.f. of the lateral distance between two points $f^{\mathcal{H}}_{\mathscr{L}_t}$ is not equal to the p.d.f. of the streamwise distance between two points $f^{\mathcal{V}}_{\mathscr{L}_t}$, but can be computed in a similar manner by substituting $a(t)$ and $b(t)$. Using equations (5.7) and (5.8) with $\mathcal{Y} = \mathcal{H}$, defined in (5.3), $y = h$, the c.d.f. of $\mathcal{H}(\mathbf{x_1}, \mathbf{x_2})$ with $\mathbf{x_1}$, $\mathbf{x_2}$ in $\mathscr{A} = \mathscr{L}_t$ is, for $h \geq 0$,

$$F^{\mathcal{H}}_{\mathscr{L}_t}(h) = \frac{4}{\pi a(t) b(t)} \int_0^{a(t)} \int_0^{b(t)\sqrt{1-(x_1/a(t))^2}} P_{\mathscr{L}_t}(\mathcal{H}(\mathbf{x_1}, \mathbf{x_2}) \leq h \,|\, \mathbf{x_1}) \, \mathrm{d}z_1 \mathrm{d}x_1, \quad (5.38)$$

where we use the fact that the c.d.f. is symmetric with respect to both the x-axis and the z-axis, and the density is uniform over the whole domain $\mathscr{L}_t$. Since the conditional probability does not depend on z_1 (as long as $(x_1/a(t))^2 + (z_1/b(t))^2 \leq 1$), we can integrate (5.38) with respect to z_1, to obtain

$$F^{\mathcal{H}}_{\mathscr{L}_t}(h) = \frac{4}{\pi a^2(t)} \int_0^{a(t)} P_{\mathscr{L}_t}(\mathcal{H}(\mathbf{x_1}, \mathbf{x_2}) \leq h \,|\, \mathbf{x_1}) \sqrt{a^2(t) - x_1{}^2} \, \mathrm{d}x_1. \qquad (5.39)$$

We can notice that (5.39) is exactly the same as the c.d.f. of the lateral distance between two points in the domain $\mathscr{D}_t$ $F^{\mathcal{H}}_{\mathscr{D}_t}$ (see equation (5.15)), but with $R(t) =$
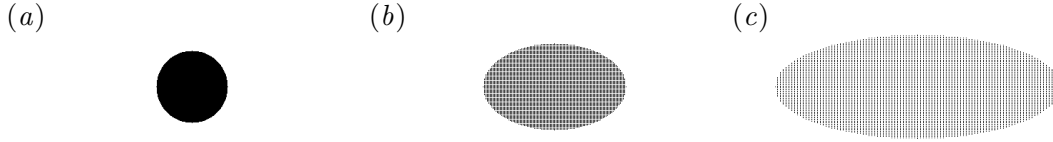
FIGURE 5.2: Distribution of a cluster of virtual particles seeded in the non-axisymmetric diverging velocity field described in (5.35) with $c = 5$ at successive non-dimensional times: (a) $t = 0$; (b) $t = 1$; (c) $t = 2$.

$a(t)$. Thus, the conditional probability in (5.39) is given by equations (5.16), (5.17), (5.18), (5.19) and (5.20) with $R(t) = a(t)$. Therefore, the p.d.f. $f^{\mathcal{H}}_{\mathscr{L}_t}$ is equivalent to $f^{\mathcal{H}}_{\mathscr{D}_t}$, but with $R(t) = a(t)$. Similarly, we find by symmetry that the p.d.f. of the streamwise distance between two points in the domain $\mathscr{L}_t$ (i.e. $f^{\mathcal{V}}_{\mathscr{L}_t}$) is equivalent to $f^{\mathcal{V}}_{\mathscr{D}_t}$, but with $R(t) = b(t)$. We have plotted the non-dimensional p.d.f. $f^{\mathcal{H}}_{\mathscr{L}_t} a(t)$ and $f^{\mathcal{V}}_{\mathscr{L}_t} b(t)$ in figures 5.3(a) and 5.3(b), respectively, with solid curves. We can see that $f^{\mathcal{H}}_{\mathscr{L}_t} a(t)$ and $f^{\mathcal{V}}_{\mathscr{L}_t} b(t)$ are similar when plotted against $\hbar / a(t)$ and $v / b(t)$, respectively. In comparison, we plot the non-dimensional p.d.f. of the lateral (streamwise) distance between two points in a rectangular domain (defined such that $-a(t) \leq x \leq a(t)$ and $-b(t) \leq z \leq b(t)$) with a dashed line in figure 5.3(a) (5.3b, respectively). The p.d.f. of the lateral (streamwise) distance between two points in a rectangular domain is equivalent to the p.d.f. in a square domain, described in (5.22), with $R(t) = a(t)$ ($R(t) = b(t)$, respectively).

The calculation of the p.d.f. of $\mathcal{D}$ (the distance between two points) and $\mathcal{M}$ (the ratio of the lateral to the streamwise distances between two points) in the elliptical domain $\mathscr{L}_t$ is apparently more difficult. Instead of computing $f^{\mathcal{D}}_{\mathscr{L}_t}$ and $f^{\mathcal{M}}_{\mathscr{L}_t}$ analytically using the continuous formulation, we use the discrete formulation described in § 5.2.2. We distribute 7845 virtual passive tracers (or particles) of similar weight $\omega = 1$ uniformly in a disc of initial radius $R_0 = 50$ centred at the origin of a two-dimensional (x, z) infinite domain. The particles are seeded in the non-axisymmetric diverging velocity field described in (5.35), with $c = 5$. Using a discrete time step $\delta t = 1$, we find that the position of a given particle at t is

$$x_t = 2^t x_0, \quad z_t = \left(\frac{c + 1}{c}\right)^t z_0. \tag{5.40}$$

We display in figures 5.2$(a$–$c)$ the distribution of the particles at dimensionless times $t = 0$, $t = 1$ and $t = 2$, respectively.

From the location of all the particles at each instant in time, given by (5.40), we can compute the p.d.f. of the distance between two particles $f^{\mathcal{D}}_{\mathscr{L}_t}$ using the discrete formulation described in (5.10) and (5.11), with $\mathcal{Y}(\mathbf{x_1}, \mathbf{x_2}) = \mathcal{D}(\mathbf{x_1}, \mathbf{x_2})$, $y_k = d_k$ and $N = 100$. We plot the non-dimensional p.d.f. $f^{\mathcal{D}}_{\mathscr{L}_t}a(t)$ in figure 5.3(c) against $d/a(t)$ for $t = 0$ (black), $t = 1$ (blue) and $t = 2$ (red). We can clearly see that the p.d.f. is no longer self-similar in time. The peak of the curve increases and move towards $d = 0$ (i.e. to the left) as time increases. The spurious fluctuations that can be seen in the p.d.f. $f^{\mathcal{D}}_{\mathscr{L}_t}$ are due to discretization issues. These fluctuations, particularly prominent at $t = 0$, are due to the fact that the discrete particle distribution has not enough randomness. Thus, despite a large number of pairs of particles (30,768,090) there cannot be a statistically good partition of all their separation distances among the $N = 100$ bins of the discretized variable d_k.

Again, from the location of all the particles at each instant in time, given by (5.40), we can compute the p.d.f. of the ratio of the lateral distance to the streamwise distance between two particles $f^{\mathcal{M}}_{\mathscr{L}_t}$ using the discrete formulation described in (5.10) and (5.11), with $\mathcal{Y}(\mathbf{x_1}, \mathbf{x_2}) = \mathcal{M}(\mathbf{x_1}, \mathbf{x_2})$, $y_k = m_k$ and $N = 100$. We plot the dimensionless p.d.f. $f^{\mathcal{M}}_{\mathscr{L}_t}$ in figure 5.3(d) against m for $t = 0$ (black), $t = 1$ (blue) and $t = 2$ (red). We can clearly see that for $t > 0$ the p.d.f. is not symmetric with respect to $m = 1$, as it is at $t = 0$ when the domain is circular. The p.d.f. $f^{\mathcal{M}}_{\mathscr{L}_t}$ displaces to the right as the aspect ratio $a(t)/b(t)$ of the domain increases in time. Therefore, the evolution in time of $f^{\mathcal{M}}_{\mathscr{L}_t}$ can reveal a change in the aspect ratio of the domain studied. The spurious fluctuations that can be seen in the p.d.f. $f^{\mathcal{M}}_{\mathscr{L}_t}$ are also due to the discretization issue mentioned previously.

5.3.3 Square cluster of virtual particles in a diffusive velocity field

Now, we study the case of a diffusive velocity field. We distribute 3721 virtual passive tracers (or particles) of similar weight $\omega = 1$ uniformly in a square of unit size centred at the origin of a two-dimensional (x, z) infinite domain. At each time step, the particles move following a two-dimensional random walk of length $500(t+1)$. We designate by $\mathscr{K}_t$ the diffusing distribution of particles. We display in figures 5.4(a–c) the distribution of the particles at dimensionless times $t = 0$, $t = 1$ and $t = 2$, respectively.

From the location of all the particles at each instant in time, we can compute
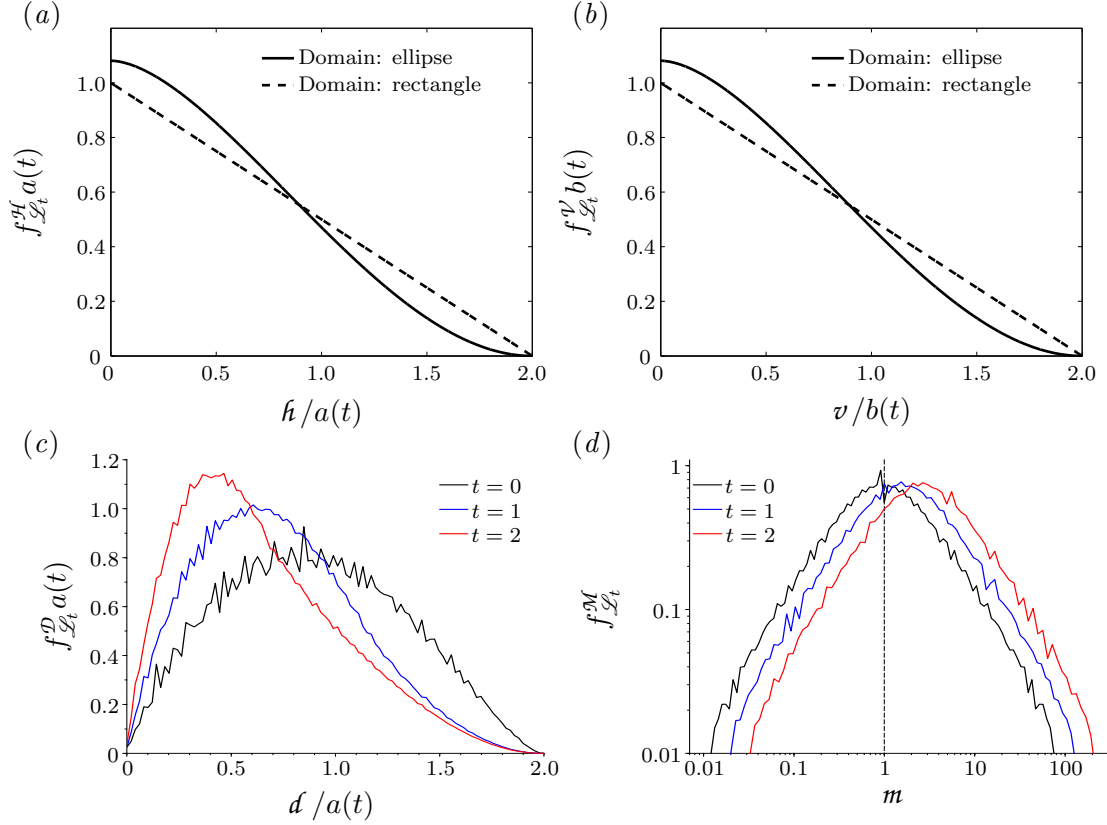
FIGURE 5.3: Evolution in time of the probability density functions in the case of a uniformly distributed elliptical domain $\mathscr{L}_t$ in a non-axisymmetric diverging velocity field described in (5.35) for: (a) the lateral distance between two points $f_{\mathscr{L}_t}^{\mathcal{H}}$ (solid curve) computed in the continuous case using (5.15) with $R(t) = a(t)$, the p.d.f. of the lateral distance between two points in a rectangle (defined in (5.22) with $R(t) = a(t)$) is plotted with a dashed line for comparison; (b) the streamwise distance between two points $f_{\mathscr{L}_t}^{\mathcal{V}}$ (solid curve) computed in the continuous case using (5.15) with $R(t) = b(t)$, the p.d.f. of the streamwise distance between two points in a rectangle (defined in (5.22) with $R(t) = b(t)$) is plotted with a dashed line for comparison; (c) the distance between pairs of particles $f_{\mathscr{L}_t}^{\mathcal{D}}$ computed in the discrete case using (5.10) and (5.11) with $n = 7845$ and $N = 100$ at times $t = 0$ (black), $t = 1$ (blue) and $t = 2$ (red); and (d) the ratio of the lateral distance to the streamwise distance between pairs of particles $f_{\mathscr{L}_t}^{\mathcal{M}}$ computed in the discrete case using (5.10) and (5.11) with $n = 7845$ and $N = 100$ at times $t = 0$ (black), $t = 1$ (blue) and $t = 2$ (red), note that, in this case, the distribution is in a log–log plot.

the p.d.f. of the lateral distance between two particles $f_{\mathscr{K}_t}^{\mathcal{H}}$ using the discrete formulation described in (5.10) and (5.11), with $\mathcal{Y}(\mathbf{x_1}, \mathbf{x_2}) = \mathcal{H}(\mathbf{x_1}, \mathbf{x_2})$, $y_k = \hbar_k$ and $N = 100$. We plot the p.d.f. $f_{\mathscr{K}_t}^{\mathcal{H}}$ in figure 5.5(a) against $\hbar$ for $t = 0$

(a)   (b)   (c)
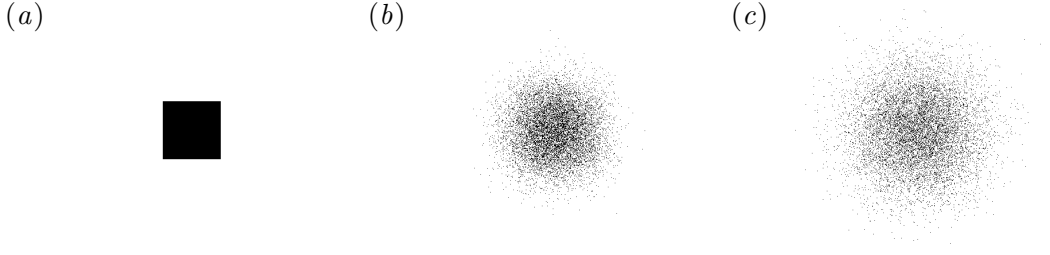
FIGURE 5.4: Time evolution of an initially square distribution of particles following random walks, at successive non-dimensional times: (a) $t = 0$; (b) $t = 1$; (c) $t = 2$.

(black), $t = 1$ (blue) and $t = 2$ (red). We can see that starting from the expected distribution for a square domain, the p.d.f. rapidly drops and becomes smoother (similarly to the p.d.f. for the circular domain $f^{\mathcal{H}}_{\mathscr{D}_t}$ displayed in figure 5.1a).

Similarly, we can compute the p.d.f. of the streamwise distance between two particles $f^{\mathcal{V}}_{\mathscr{K}_t}$ using the discrete formulation described in (5.10) and (5.11), with $\mathcal{Y}(\mathbf{x_1}, \mathbf{x_2}) = \mathcal{V}(\mathbf{x_1}, \mathbf{x_2})$, $y_k = v_k$ and $N = 100$. We plot the p.d.f. $f^{\mathcal{V}}_{\mathscr{K}_t}$ in figure 5.5(b) against v for $t = 0$ (black), $t = 1$ (blue) and $t = 2$ (red). The p.d.f. of the streamwise distance is very similar to the p.d.f. of the lateral distance shown in figure 5.5(a), owing to the axisymmetry of the diffusion process.

Similarly, we can compute the p.d.f. of the distance between two particles $f^{\mathcal{D}}_{\mathscr{K}_t}$ using the discrete formulation described in (5.10) and (5.11), with $\mathcal{Y}(\mathbf{x_1}, \mathbf{x_2}) = \mathcal{D}(\mathbf{x_1}, \mathbf{x_2})$, $y_k = d_k$ and $N = 100$. We plot the p.d.f. $f^{\mathcal{D}}_{\mathscr{K}_t}$ in figure 5.5(c) against d for $t = 0$ (black), $t = 1$ (blue) and $t = 2$ (red). The p.d.f. gradually drops and spreads in time. For $t > 0$, the p.d.f. is similar to the p.d.f. for the circular domain $f^{\mathcal{D}}_{\mathscr{D}_t}$ displayed in figure 5.1(c).

Similarly, we can compute the p.d.f. of the ratio between the lateral distance to the streamwise distance between two particles $f^{\mathcal{M}}_{\mathscr{K}_t}$ using the discrete formulation described in (5.10) and (5.11), with $\mathcal{Y}(\mathbf{x_1}, \mathbf{x_2}) = \mathcal{M}(\mathbf{x_1}, \mathbf{x_2})$, $y_k = m_k$ and $N = 100$. We plot the p.d.f. $f^{\mathcal{M}}_{\mathscr{K}_t}$ in figure 5.5(d) against m for $t = 0$ (black), $t = 1$ (blue) and $t = 2$ (red). It is clear that the distribution of particles remain symmetric as the p.d.f. is centred around $m = 1$ at all time.

Again, the spurious fluctuations that can be observed in the p.d.f.s $f^{\mathcal{H}}_{\mathscr{K}_t}$, $f^{\mathcal{V}}_{\mathscr{K}_t}$, $f^{\mathcal{D}}_{\mathscr{K}_t}$, and $f^{\mathcal{M}}_{\mathscr{K}_t}$ are due to the discretization issue mentioned previously.
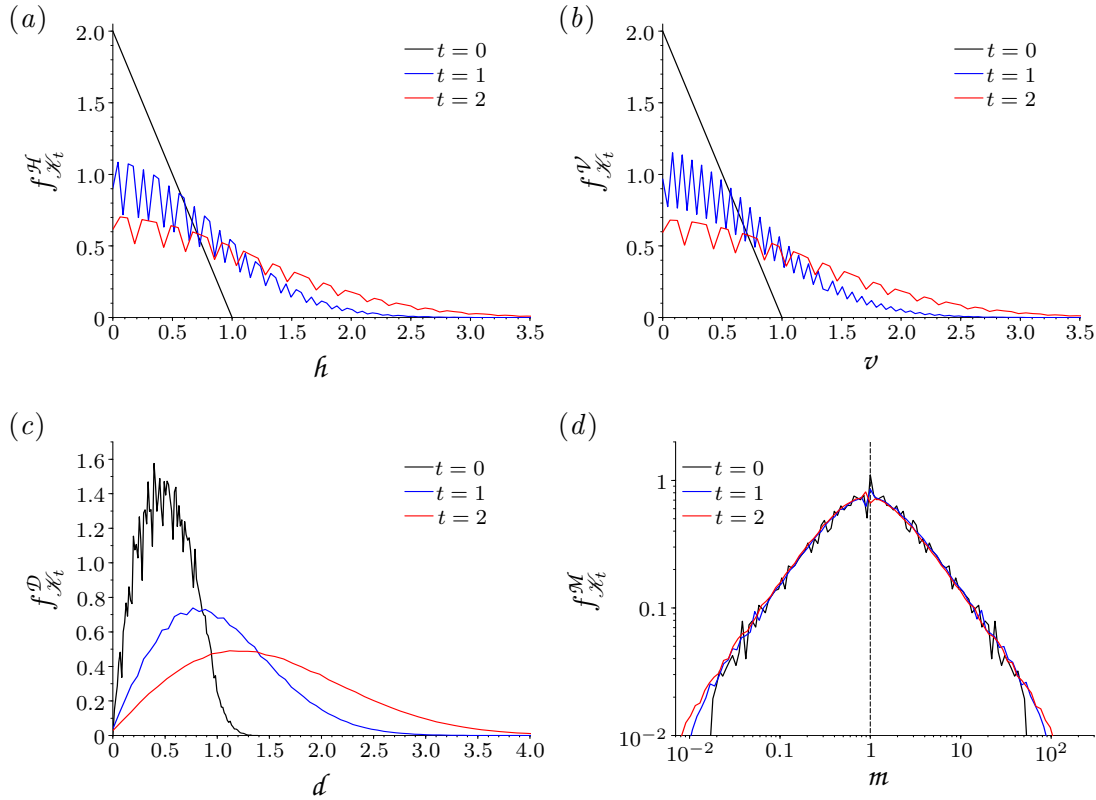
FIGURE 5.5: Evolution in time of the probability density functions in the case of a diffusing domain $\mathcal{K}_t$ of virtual particles for: (a) the lateral distance between pairs of particles $f_{\mathcal{K}_t}^{\mathcal{H}}$ computed in the discrete case using (5.10) and (5.11) with $n = 3721$ and $N = 100$ at times $t = 0$ (black), $t = 1$ (blue) and $t = 2$ (red); (b) the streamwise distance between pairs of particles $f_{\mathcal{K}_t}^{\mathcal{V}}$ computed in the discrete case using (5.10) and (5.11) with $n = 3721$ and $N = 100$ at times $t = 0$ (black), $t = 1$ (blue) and $t = 2$ (red); (c) the distance between pairs of particles $f_{\mathcal{K}_t}^{\mathcal{D}}$ computed in the discrete case using (5.10) and (5.11) with $n = 3721$ and $N = 100$ at times $t = 0$ (black), $t = 1$ (blue) and $t = 2$ (red); and (d) the ratio of the lateral distance to the streamwise distance between pairs of particles $f_{\mathcal{K}_t}^{\mathcal{M}}$ computed in the discrete case using (5.10) and (5.11) with $n = 3721$ and $N = 100$ at times $t = 0$ (black), $t = 1$ (blue) and $t = 2$ (red), note that, in this case, the distribution is in a log–log plot.

5.3.4 Conclusion of the test studies

We have analysed the probability distributions of two-point properties for: a circular domain in axisymmetric expansion, an elliptical domain in non-axisymmetric expansion and a square domain expanding due to a diffusion-like process. From these studies, we have learnt that:

- the p.d.f. of the lateral and streamwise distance between two points, $\mathcal{H}$ and $\mathcal{V}$ respectively, characterizes the extent of the domain along each specific direction. The p.d.f. of $\mathcal{H}$ or $\mathcal{V}$ do not seem to depend on the actual shape of the distribution. In normalized form, the results of $f^{\mathcal{H}}$ or $f^{\mathcal{V}}$ were identical between the disc and the ellipse (see solid curves in figures 5.1a,b and figures 5.3a,b), and were very similar to the results for the square domain and the diffusing domain (see black lines in figures 5.5a,b, and blue and red curves in figures 5.5a,b).

- Regardless of the orientation, the p.d.f. of $\mathcal{D}$ characterizes the average distance between particles, and thus the shape of the domain. The p.d.f. $f^{\mathcal{D}}$ of an axisymmetric domain (i.e. a disc in two dimensions) has its maximum value the furthest away from $d = 0$ (see figure 5.1c). The more elongated the distribution (e.g. an ellipse with large aspect ratio), the closer the peak of $f^{\mathcal{D}}$ is to 0 (see figure 5.3c).

- The ratio between the lateral and the streamwise distance between two points, $\mathcal{M}$ characterizes the symmetry between the x-direction and the z-direction. $f^{\mathcal{M}}$ characterizes the aspect ratio of the extension of the domain along these two directions.

Furthermore, through the evolution in time of these probability distributions we can note that

- stretching or shrinking of the domain along the specific x- and z-directions can be quantified with $f^{\mathcal{H}}$ and $f^{\mathcal{V}}$. This is also characterized by the shifting of the maximum of $f^{\mathcal{M}}$ away from $m = 1$ (see figure 5.3d).

- If $f^{\mathcal{D}}$ remains self-similar in time, then the transformation seems to preserve the form (see the evolution of $f^{\mathcal{D}}$ for the circular domain in figure 5.1c compared with the elliptical domain in figure 5.3c).

- In a diffusion process (see figure 5.4), the distribution of particles tends to become more axisymmetric. In figures 5.5(a,b) the p.d.f. $f^{\mathcal{H}}_{\mathcal{K}_t}$ and $f^{\mathcal{V}}_{\mathcal{K}_t}$ are linear at $t = 0$ and then become smoother at each time step, similarly to $f^{\mathcal{H}}_{\mathcal{L}_t}$ and $f^{\mathcal{V}}_{\mathcal{L}_t}$.

5.4 Analysis of the virtual particles in the jet structures

5.4.1 Virtual particles: time-dependent versus time-averaged velocity fields

In the light of the preliminary study presented above, we analyse the statistical properties of particles seeded in the core and eddy structures of quasi-two-dimensional jets. We use the time-dependent velocity field of the jet shown previously in figure 4.3(b), where we seed a square cluster of $n = 3721$ virtual particles in an eddy (shown in light grey), a rectangular cluster of $n = 7381$ virtual particles and aspect ratio 2 at the interface between the core and the eddy (shown in grey), and a square cluster of $n = 3721$ virtual particles in the middle of the core (shown in dark grey). We have reproduced the time evolution of the particle clusters seeded in this time-dependent velocity field (previously shown in figures 4.4a–c) in figures 5.6(a–c).

We now repeat the same process in the time-averaged velocity field (with an average duration time of 21.8 s, as explained in § 2.2.2) of the jet used in figures 5.6(a–c). We show in figures 5.6(d–f) the time evolution (the colour-scale used is the same to that used in figures 5.6a–c) of three clusters of virtual particles seeded in this time-averaged velocity field. The clusters in figures 5.6(d–f) have the same size and are initially located at the same position in the velocity field as the clusters in figures 5.6(a–c), respectively.

The comparison between the evolution of the particle clusters in the time-dependent and the time-averaged velocity fields reveals crucial information about the dynamics of the core and eddy structures. The cluster seeded at the location of an eddy in the time-averaged velocity field (see figure 5.6d) stretches in the streamwise direction and rotates counter-clockwise. The evolution of the corresponding cluster in the time-dependent velocity field (see figure 5.6a) does not display the same streamwise stretching, but rather expands isotropically. Strong stirring and turbulent mixing at the location of the eddy also seem to be features of the time-dependent velocity field only. At the interface between the eddy and the core, the time-averaged velocity field (see figure 5.6e) merely stretches the particle cluster in the streamwise direction. On the other hand, the cluster

seeded in the time-dependent velocity field (see figure 5.6*b*) not only experiences streamwise dispersion (clear at early times, shown with dark and red colours), but also divides into two as some particles are drawn into the neighbouring eddy. The particles drawn into the eddy experience the same isotropic dispersion and strong turbulent stirring as observed for the cluster in figure 5.6(*a*), whereas the particles that remain in the core are rapidly transported away. The particle cluster seeded in the core of the time-dependent velocity field (see figure 5.6*c*) has a similar evolution as the corresponding particle cluster seeded in the time-averaged velocity field (see figure 5.6*f*). We can observe slightly more streamwise dispersion in the time-averaged velocity field, whereas the time-dependent velocity field rather seems to stretch the particles in the cross-jet direction.

5.4.2 Two-point statistics: time-dependent versus time-averaged velocity fields

We now study the time evolution of the two-point statistics of the three particle clusters evolving in the time-dependent velocity field (presented in figures 5.6*a–c*), as well as the three particle clusters evolving in the time-averaged velocity field of the same jet (presented in figures 5.6*d–f*). For every cluster of both velocity fields, we compute the p.d.f., using the discrete formulation (5.10) and (5.11) (with $N = 100$, the number of bins), for the lateral distance $\mathcal{H}$ (except at $\tilde{t} = t/(d^2/Q_0) = 0$ where we use the theoretical prediction defined in (5.22) for a rectangular domain), the streamwise distance $\mathcal{V}$ (except at $\tilde{t} = 0$ where we use the theoretical prediction defined in (5.22) for a rectangular domain), the (Euclidean) distance $\mathcal{D}$, and the ratio of the lateral distance to the streamwise distance between pairs of particles $\mathcal{M}$, as defined in (5.3), (5.4), (5.5) and (5.6), respectively. We present the distributions of the p.d.f.s at three or four different times, linearly distributed from $\tilde{t} = 0$ (the time we initially seed the particle cluster in the velocity field) to the time instant a particle of the cluster reaches the top boundary of the velocity field (this time varies between each cluster).

In the eddy

In figures 5.7(*a–d*), we present the non-dimensional p.d.f. of the lateral distance $f_{\mathcal{E}_t}^{\mathcal{H}} d$ (where $d = 0.5$ cm is the nozzle width of the experimental appara-
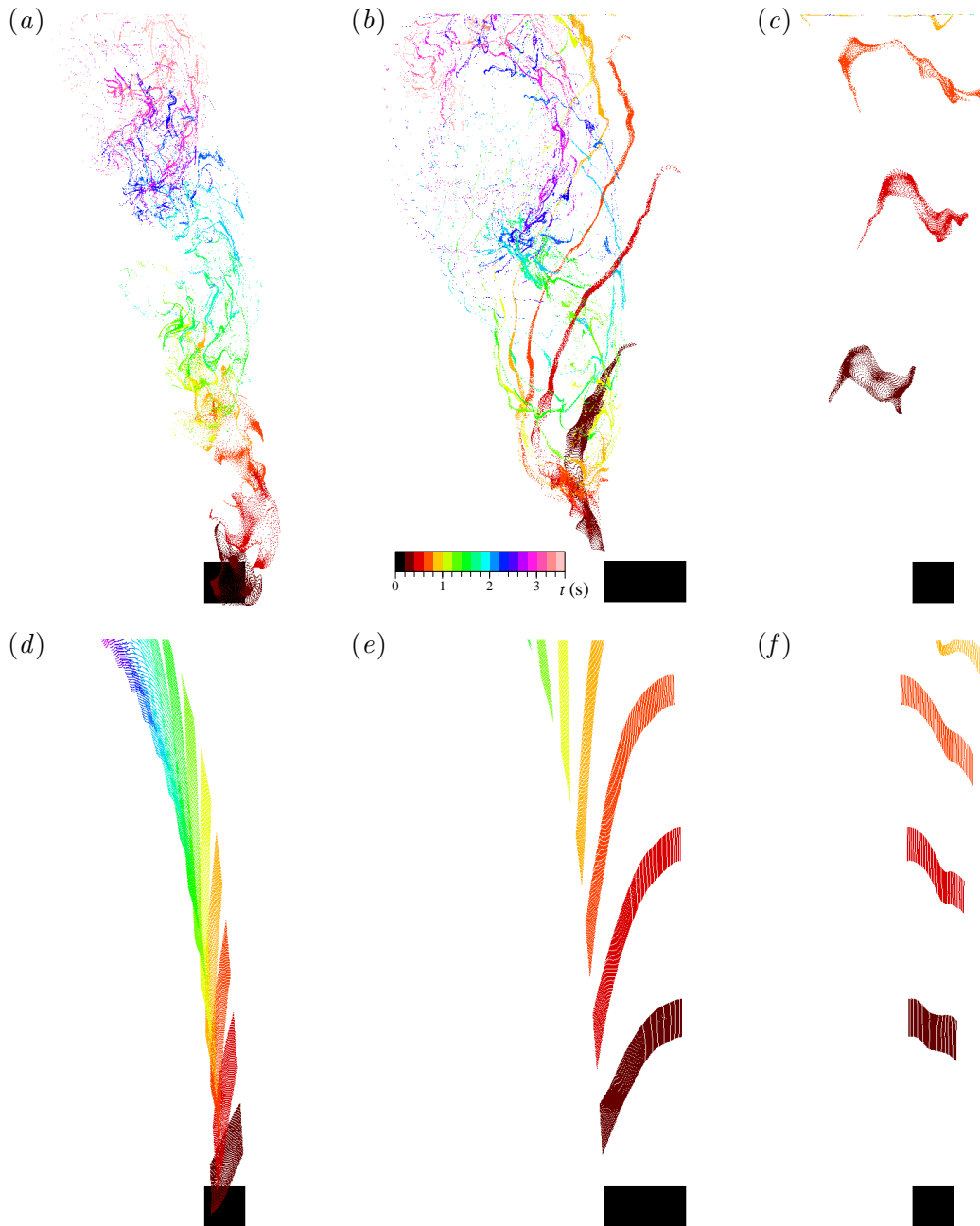
FIGURE 5.6: Comparison of the evolution in time of the virtual particles seeded in the velocity field shown in figure 4.3(*b*): (*a*–*c*) correspond to the time-dependent velocity field, while (*d*–*f*) correspond to the time-averaged velocity field. (*a*,*d*) Particle cluster initially distributed at the centre of an eddy and shown in light grey in figure 4.3(*b*). (*b*,*e*) Particle cluster initially distributed between the eddy and the core and shown in grey in figure 4.3(*b*). (*c*,*f*) Particle cluster initially distributed in the core of the jet and shown in dark grey in figure 4.3(*b*). Each colour corresponds to a time period of $\Delta t = 0.2\,\mathrm{s}$ (or $\Delta \tilde{t} = 33$ in dimensionless time), the colour scale shown at the bottom of (*b*) is the same to that used in figure 4.3(*b*).

tus presented in figure 4.1), the streamwise distance $f^{\mathcal{V}}_{\mathcal{E}_t} d$, the ratio between the lateral and streamwise distances between pairs of virtual particles $f^{\mathcal{M}}_{\mathcal{E}_t}$ and the distance $f^{\mathcal{D}}_{\mathcal{E}_t} d$ for the cluster initially seeded at the location of an eddy in the time-dependent velocity field (see figure 5.6a). We plot the p.d.f. against the non-dimensional variables $\hbar/d$, v/d, m and d/d in figures 5.7(a–d), respectively. The p.d.f.s are plotted at four different times, from $\tilde{t} = 0$ to 392, using different colours. The colour scale used here is the same as shown in figure 5.6(b). Similarly, we show in figures 5.7(e–h) the evolution in time of the non-dimensional p.d.f.s $f^{\mathcal{H}}_{\mathcal{E}_t} d$, $f^{\mathcal{V}}_{\mathcal{E}_t} d$, $f^{\mathcal{D}}_{\mathcal{E}_t} d$ and $f^{\mathcal{M}}_{\mathcal{E}_t}$ for the cluster initially seeded at the location of an eddy in the time-averaged velocity field (see figure 5.6d).

As we can see in figure 5.7(a), the range of $f^{\mathcal{H}}_{\mathcal{E}_t} d$ increases slightly in time from approximately $0 \leq \hbar/d \leq 5$ at $\tilde{t} = 0$ to $0 \leq \hbar/d \leq 7$ at $\tilde{t} = 392$. In the streamwise direction, the distribution of particles stretches more than in the lateral direction, as the range of $f^{\mathcal{V}}_{\mathcal{E}_t} d$ (shown in figure 5.7b) increases from approximately $0 \leq v/d \leq 5$ at $\tilde{t} = 0$ to $0 \leq v/d \leq 13$ at $\tilde{t} = 392$. The small change in aspect ratio can also be observed in figure 5.7(c), where $f^{\mathcal{M}}_{\mathcal{E}_t}$ is no longer exactly symmetric with $m = 1$ for $\tilde{t} > 0$. Moreover, the smooth profile of $f^{\mathcal{M}}_{\mathcal{E}_t}$ at $\tilde{t} = 0$ seems to be disturbed near $m = 1$ for $\tilde{t} > 0$. This disturbance could suggest changes in the distribution of the particles with time. The evolution in time of the p.d.f. of the distance between two points $f^{\mathcal{D}}_{\mathcal{E}_t}$, shown in figure 5.7($d$), also reveals important changes in the distribution of the particles. The increase in the range of $f^{\mathcal{D}}_{\mathcal{E}_t}$ (from approximately $0 \leq d/d \leq 6$ at $\tilde{t} = 0$ to $0 \leq d/d \leq 13$ at $\tilde{t} = 392$) means that the particles have been spread over a larger domain. Moreover, the characteristic profile of $f^{\mathcal{D}}_{\mathcal{E}_t}$ at $\tilde{t} = 0$ (which corresponds to a square domain) quickly vanishes, thus suggesting a radical change in the shape of the domain. Finally, for $\tilde{t} > 0$, $f^{\mathcal{D}}_{\mathcal{E}_t}$ displays large fluctuations and peaks (different from the small fluctuations at $\tilde{t} = 0$ which are due to the resolution problem mentioned previously), which vary in amplitude and location with time.

In the light of the observations made in § 5.4.1, we can notice some major differences between the p.d.f.s for the time-dependent flow field (shown in figures 5.7a–d) and the p.d.f.s for the time-averaged flow field (shown in figures 5.7e–h). Firstly, the aspect ratio of the distribution in the time-averaged flow field deviates considerably in time from the aspect ratio of the distribution in the time-dependent flow field. In figure 5.7(e), the range of $f^{\mathcal{H}}_{\mathcal{E}_t} d$ decreases slightly in

time from approximately $0 \leq \hbar/d \leq 5$ at $\tilde{t} = 0$ to $0 \leq \hbar/d \leq 3$ at $\tilde{t} = 196$. In figure 5.7(f), the range of $f^{\mathcal{V}}_{\mathscr{E}_t} d$ increases considerably in time from approximately $0 \leq \hbar/d \leq 5$ at $\tilde{t} = 0$ to $0 \leq v/d \leq 35$ at $\tilde{t} = 196$. The aspect ratio (between the lateral and streamwise extent) drops from 1 to less than 0.1, as clearly shown by $f^{\mathcal{M}}_{\mathscr{E}_t}$ plotted in figure 5.7(g). Secondly, the distribution of the p.d.f. of the distance $f^{\mathcal{D}}_{\mathscr{E}_t}$ for the time-averaged velocity field (plotted in figure 5.7h) is much smoother than for the time-dependent velocity field (plotted in figure 5.7d). We believe these continuous and rapid variations in time of the profile of $f^{\mathcal{D}}_{\mathscr{E}_t}$ for the time-dependent flow field can be related to the intense stirring effect of the turbulent eddy. The chaotic dynamics of the turbulent flow in the eddy perturbs the distribution of particles. This manifests itself in the rapid displacement of the peaks in the distribution of $f^{\mathcal{D}}_{\mathscr{E}_t}$, for the time-dependent flow field.

At the interface between the core and the eddy

In figures 5.8(a–d), we present the non-dimensional p.d.f. of the lateral distance $f^{\mathcal{H}}_{\mathscr{I}_t} d$, the streamwise distance $f^{\mathcal{V}}_{\mathscr{I}_t} d$, the ratio between the lateral and streamwise distances between pairs of virtual particles $f^{\mathcal{M}}_{\mathscr{I}_t}$ and the distance $f^{\mathcal{D}}_{\mathscr{I}_t} d$ for the cluster initially seeded at the interface between the eddy and the core (see figure 5.6b). We plot the p.d.f. against the non-dimensional variables $\hbar/d$, v/d, m and d/d in figures 5.8(a–d), respectively. The p.d.f.s are plotted at four different times, from $\tilde{t} = 0$ to 98, using different colours. The colour scale used here is the same as shown in figure 5.6(b). Similarly, we show in figures 5.8(e–h) the evolution in time of the non-dimensional p.d.f.s $f^{\mathcal{H}}_{\mathscr{I}_t} d$, $f^{\mathcal{V}}_{\mathscr{I}_t} d$, $f^{\mathcal{D}}_{\mathscr{I}_t} d$ and $f^{\mathcal{M}}_{\mathscr{I}_t}$ for the cluster initially seeded at the interface between the eddy and the core in the time-averaged velocity field (see figure 5.6e).

In figure 5.8(a), the range of $f^{\mathcal{H}}_{\mathscr{I}_t} d$ first decreases in time from approximately $0 \leq \hbar/d \leq 10$ at $\tilde{t} = 0$ to $0 \leq \hbar/d \leq 5$ at $\tilde{t} = 33$ before increasing to $0 \leq \hbar/d \leq 13$ at $\tilde{t} = 98$. On the other hand, the distribution of particles steadily stretches in the streamwise direction, as the range of $f^{\mathcal{V}}_{\mathscr{I}_t} d$ (shown in figure 5.8b) increases from approximately $0 \leq v/d \leq 5$ at $\tilde{t} = 0$ to $0 \leq v/d \leq 55$ at $\tilde{t} = 98$. This considerable change in the aspect ratio of the distribution, from 2 to less than 1/4 is also clearly revealed in figure 5.8(c), where the peak of $f^{\mathcal{M}}_{\mathscr{I}_t}$ rapidly moves from the right-hand side of $m = 1$ to the left-hand side. The evolution in time of the p.d.f. of the distance between two points $f^{\mathcal{D}}_{\mathscr{I}_t}$, shown in figure 5.8($d$), is different
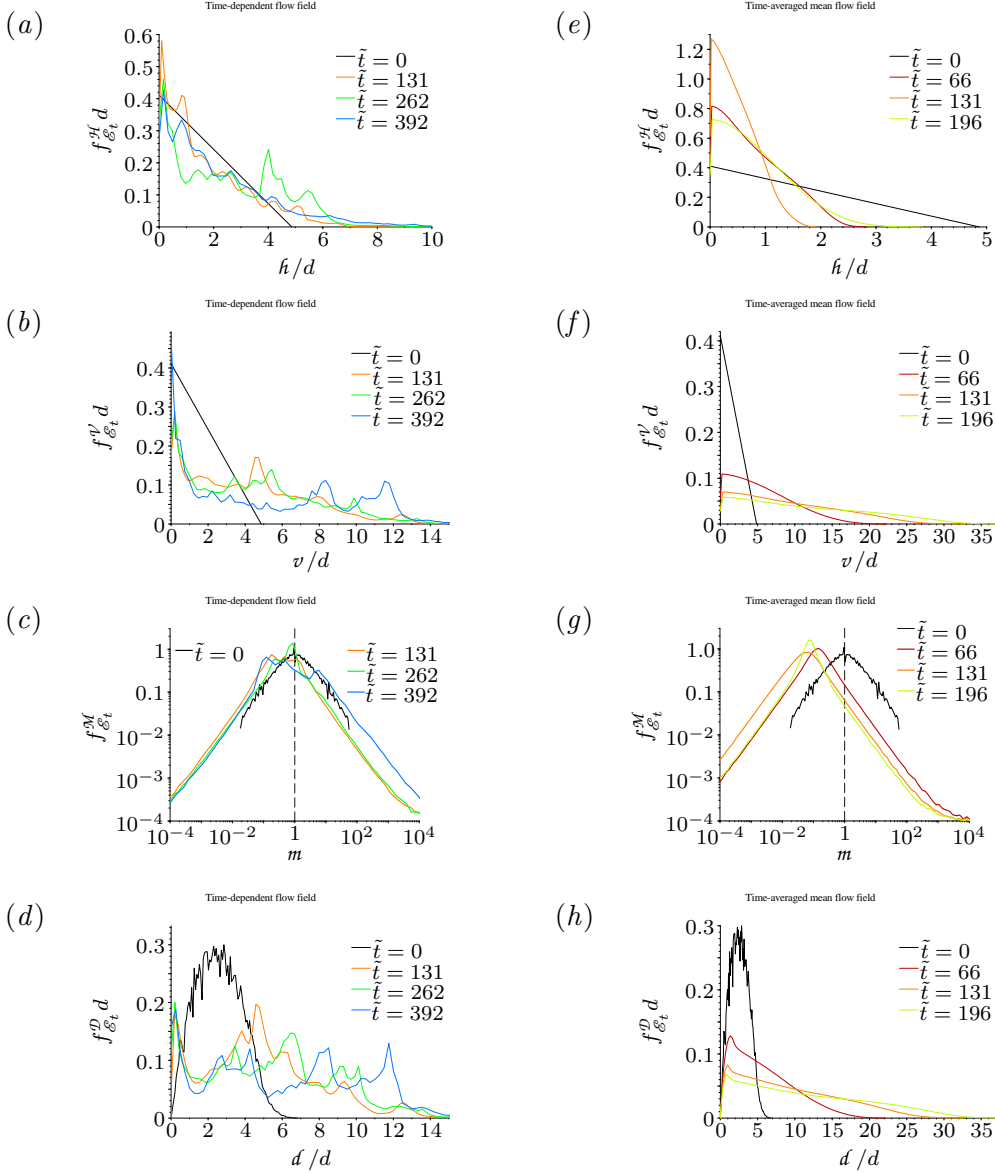
FIGURE 5.7: Comparison between the time evolutions (the colour-scale used is the same to that used in figure 5.6) of the p.d.f.s in the case of the cluster of virtual particles initially seeded in the eddy of the time-dependent $(a–d)$ (see figure 5.6a) and the time-averaged $(e–h)$ (see figure 5.6d) velocity fields, for: (a,e) the dimensionless lateral distance between pairs of particles $f_{\mathscr{E}_t}^{\mathcal{H}} d$ computed using (5.10) and (5.11) with $n = 3721$ and $N = 100$; (b,f) the dimensionless streamwise distance between pairs of particles $f_{\mathscr{E}_t}^{\mathcal{V}} d$ computed using (5.10) and (5.11) with $n = 3721$ and $N = 100$; (c,g) the ratio of the lateral distance to the streamwise distance between pairs of particles $f_{\mathscr{E}_t}^{\mathcal{M}}$ computed using (5.10) and (5.11) with $n = 3721$ and $N = 100$ (in a log–log plot); and (d,h) the dimensionless distance between pairs of particles $f_{\mathscr{E}_t}^{\mathcal{D}} d$ computed using (5.10) and (5.11) with $n = 3721$ and $N = 100$.

from the evolution of $f_{\mathscr{E}_t}^{\mathscr{D}}$ for the cluster seeded in the eddy (shown in figure 5.7d). The increase in the range of $f_{\mathscr{I}_t}^{\mathscr{D}}$ (from approximately $0 \leq d/d \leq 10$ at $\tilde{t} = 0$ to $0 \leq d/d \leq 55$ at $\tilde{t} = 98$) means that the particles have been spread over a larger domain very rapidly. Contrary to $f_{\mathscr{E}_t}^{\mathscr{D}}$, the characteristic profile of $f_{\mathscr{I}_t}^{\mathscr{D}}$ at $\tilde{t} = 0$ (which corresponds to a square domain) does not completely change. The main peak recedes towards $d \to 0$ as time increases, thus suggesting a significant thinning of the distribution, probably owing to the intense lateral shear at the interface between the core and the eddy. Note that, in this case, the statistical study stops at $\tilde{t} \approx 98$, which corresponds to the time when the first particle reaches the top of the visualization window (see figure 5.6b).

We can notice one major difference between the p.d.f.s for the time-dependent flow field (shown in figures 5.8a–d) and the p.d.f.s for the time-averaged flow field (shown in figures 5.8e–h). The distribution of the p.d.f.s $f_{\mathscr{I}_t}^{\mathscr{H}}$, $f_{\mathscr{I}_t}^{\mathscr{V}}$ and $f_{\mathscr{I}_t}^{\mathscr{D}}$ are smoother for the time-averaged velocity field (plotted in figures 5.8e,f,h, respectively) than for the time-dependent flow field (plotted in figures 5.8a,b,c, respectively). We believe that the jaggedness observed for the time-dependent flow field is, similarly to the case of the eddy, related to the unstable and turbulent flow of the shear layer at the interface between the eddy and the core.

In the core

In figures 5.9(a–d), we present the non-dimensional p.d.f. of the lateral distance $f_{\mathscr{C}_t}^{\mathscr{H}} d$, the streamwise distance $f_{\mathscr{C}_t}^{\mathscr{V}} d$, the ratio between the lateral and streamwise distances between pairs of virtual particles $f_{\mathscr{C}_t}^{\mathscr{M}}$ and the distance $f_{\mathscr{C}_t}^{\mathscr{D}} d$ for the cluster initially seeded in the core (see figure 5.6c). We plot the p.d.f. against the non-dimensional variables h/d, v/d, m and d/d in figures 5.9(a–d), respectively. The p.d.f.s are plotted at four different times, from $\tilde{t} = 0$ to 98, using different colours. The colour scale used here is the same as shown in figure 5.6(b). Similarly, we show in figures 5.9(e–h) the evolution in time of the non-dimensional p.d.f.s $f_{\mathscr{C}_t}^{\mathscr{H}} d$, $f_{\mathscr{C}_t}^{\mathscr{V}} d$, $f_{\mathscr{C}_t}^{\mathscr{D}} d$ and $f_{\mathscr{C}_t}^{\mathscr{M}}$ for the cluster initially seeded at the location of the core in the time-averaged velocity field (see figure 5.6f).

The p.d.f. of the lateral distance $f_{\mathscr{C}_t}^{\mathscr{H}}$, presented in figure 5.9(a), seems to remain linear until approximately $\tilde{t} = 66$, and then becomes bimodal at $\tilde{t} = 98$ with a peak close to $h = 0$ and the other one near $h = 13$. The p.d.f. of the streamwise distance $f_{\mathscr{C}_t}^{\mathscr{V}}$, shown in figure 5.9($b$), decreases approximately linearly

(a) Time-dependent flow field

(e) Time-averaged mean flow field

(b) Time-dependent flow field

(f) Time-averaged mean flow field

(c) Time-dependent flow field

(g) Time-averaged mean flow field

(d) Time-dependent flow field

(h) Time-averaged mean flow field
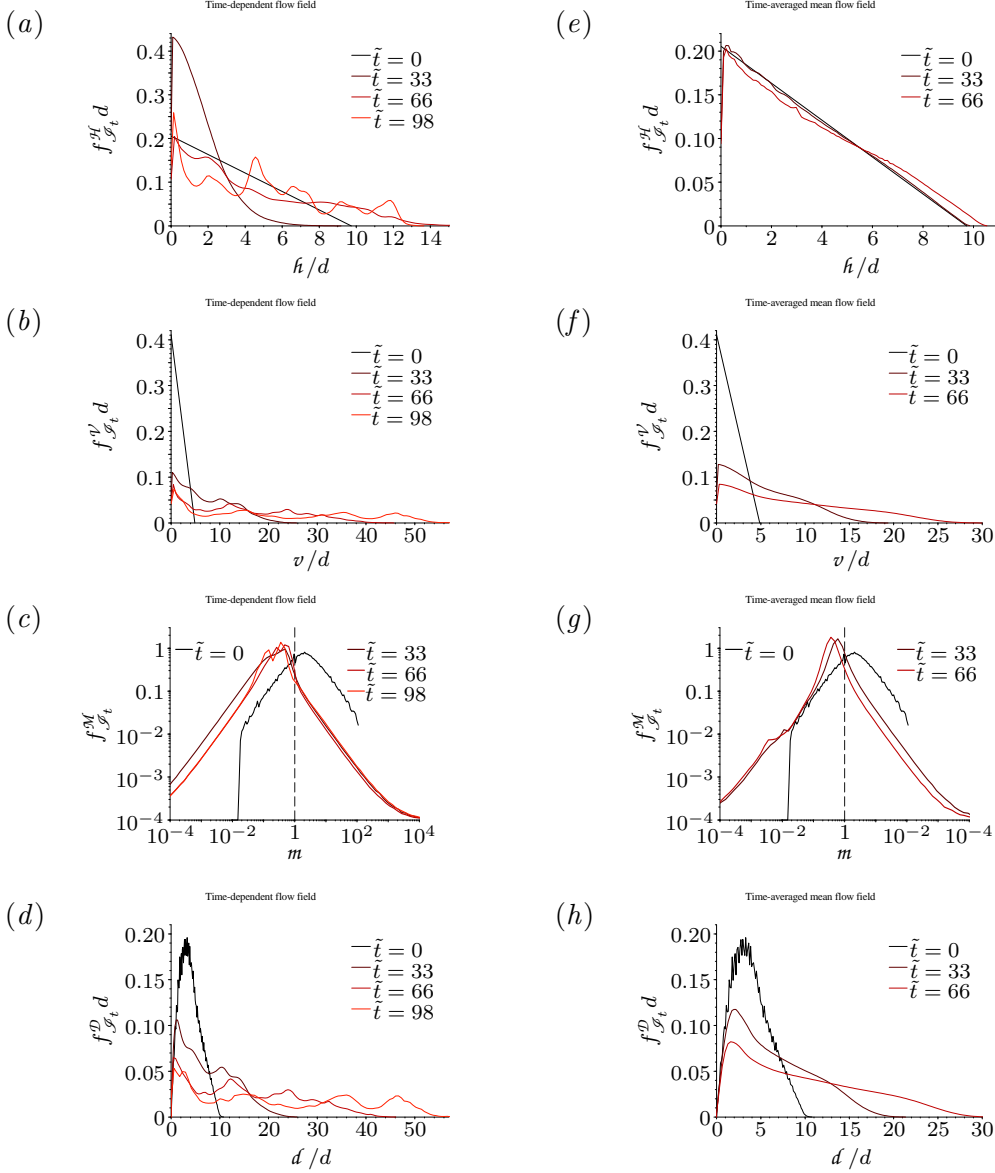
FIGURE 5.8: Comparison between the time evolutions (the colour-scale used is the same to that used in figure 5.6) of the p.d.f.s in the case of the cluster of virtual particles initially seeded between an eddy and the core of the time-dependent $(a$–$d)$ (see figure 5.6b) and the time-averaged $(e$–$h)$ (see figure 5.6e) velocity fields, for: (a,e) the dimensionless lateral distance between pairs of particles $f^{\mathcal{H}}_{\mathscr{I}_t} d$ computed using (5.10) and (5.11) with $n = 7381$ and $N = 100$; (b,f) the dimensionless streamwise distance between pairs of particles $f^{\mathcal{V}}_{\mathscr{I}_t} d$ computed using (5.10) and (5.11) with $n = 7381$ and $N = 100$; (c,g) the ratio of the lateral distance to the streamwise distance between pairs of particles $f^{\mathcal{M}}_{\mathscr{I}_t}$ computed using (5.10) and (5.11) with $n = 7381$ and $N = 100$ (in a log–log plot); and (d,h) the dimensionless distance between pairs of particles $f^{\mathcal{D}}_{\mathscr{I}_t} d$ computed using (5.10) and (5.11) with $n = 7381$ and $N = 100$.

at all time, with its range increasing only slightly (from $0 \leq v/d \leq 5$ at $\tilde{t} = 0$ to approximately $0 \leq v/d \leq 8$ at $\tilde{t} = 98$). The p.d.f. of the ratio between the lateral and streamwise distances $f_{\mathscr{C}_t}^{\mathcal{M}}$, shown in figure 5.9($c$), moves away to the right of the axis of symmetry $m = 1$. Therefore, the distribution stretches in the cross-jet or lateral direction, conversely to the cluster of particles seeded between the core and the eddy discussed above. This lateral stretching is probably due to the linear time-averaged lateral spreading of the jet velocity field with z. Finally, we can notice that, similarly to $f_{\mathscr{C}_t}^{\mathcal{H}}$, the p.d.f. of the distance $f_{\mathscr{C}_t}^{\mathcal{D}}$, shown in figure 5.9($d$), also becomes more and more bimodal with time. The bimodality can be related to the gradual splitting of the cluster of virtual particles, as it becomes thinner along the centreline of the jet (see figure 5.6c). This effect must originate from the divergence of the lateral mean flow along the jet axis.

We point out two minor differences between the p.d.f.s for the time-dependent flow field (shown in figures 5.9a–d) and the p.d.f.s for the time-averaged flow field (shown in figures 5.9e–h). Firstly, the range of the p.d.f. $f_{\mathscr{C}_t}^{\mathcal{H}}$ for the time-averaged velocity field (plotted in figure 5.9e) increases less (from $0 \leq h/d \leq 5$ at $\tilde{t} = 0$ to approximately $0 \leq h/d \leq 7$ at $\tilde{t} = 66$) than for the time-dependent flow field (plotted in figure 5.9a). The spurious fluctuations, which can be noticed in the distribution of $f_{\mathscr{C}_t}^{\mathcal{H}}$ in figure 5.9(e) at $\tilde{t} = 33$ and 66 (and also, to some extent, in figures 5.9d,h at $\tilde{t} = 0$), are due to the discretization issue mentioned previously (the problem does not occur at $\tilde{t} = 0$ where we plot the theoretical prediction defined in (5.22)). Secondly, the bimodality of the distribution of the p.d.f. $f_{\mathscr{C}_t}^{\mathcal{D}}$ for the time-dependent flow field (shown in figure 5.9d) is not clear for the time-averaged flow field (shown in figure 5.9h), though it may develop at later time due to the time-averaged mean diverging lateral velocity near the centreline of the jet.

5.5 Discussion and Conclusion

In this chapter, we investigate turbulent relative dispersion in the flow field of quasi-two-dimensional jets using two-point statistics. To obtain the data necessary to compute these two-point statistics, we have developed what we believe to be a new method which allows us to perform effectively Lagrangian particle tracking in the turbulent flow of the jets. We use virtual particle tracking, which
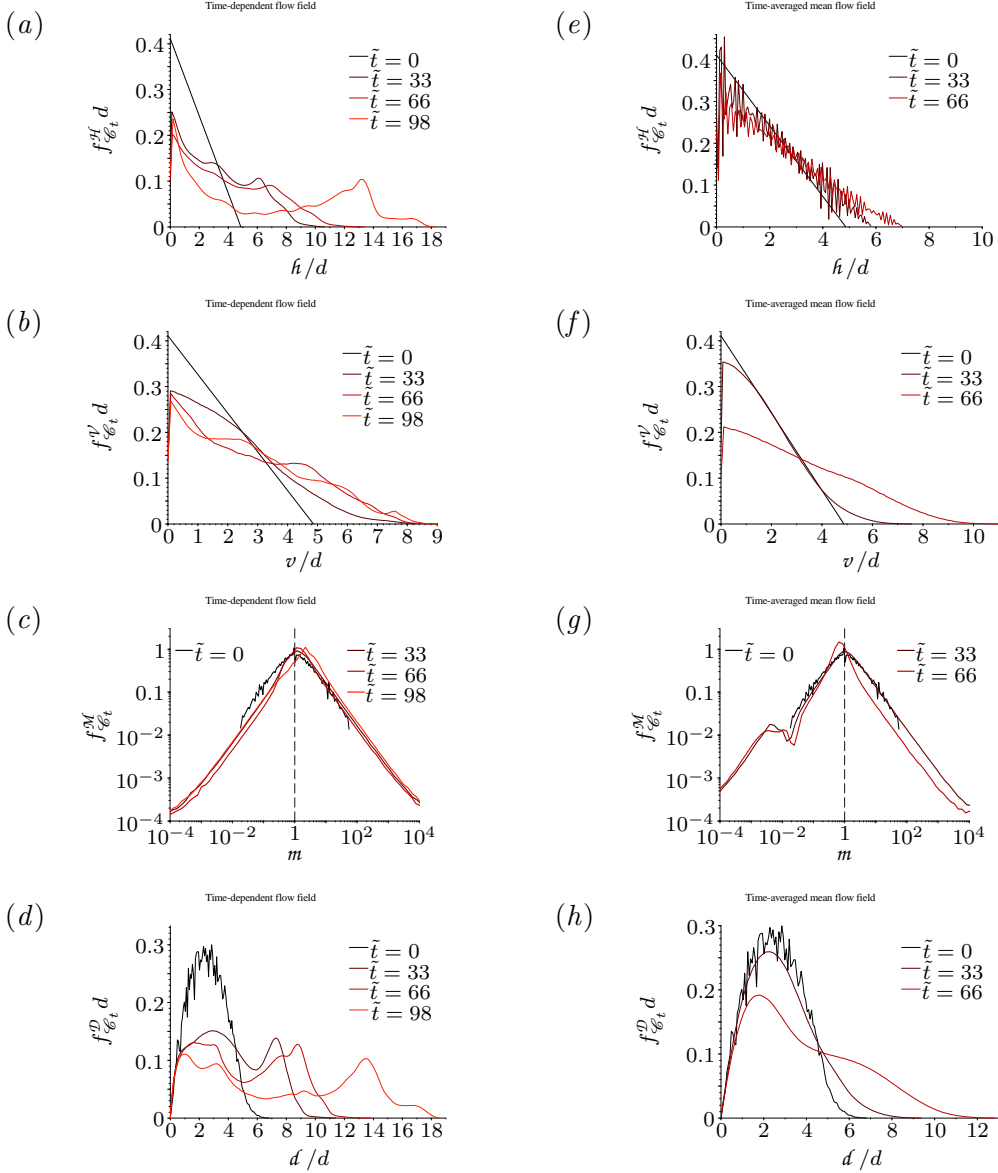
FIGURE 5.9: Comparison between the time evolutions (the colour-scale used is the same to that used in figure 5.6) of the p.d.f.s in the case of the cluster of virtual particles initially seeded in the core of the time-dependent $(a–d)$ (see figure 5.6c) and the time-averaged $(e–h)$ (see figure 5.6f) velocity fields, for: (a,e) the dimensionless lateral distance between pairs of particles $f_{\mathscr{C}_t}^{\mathscr{H}} d$ computed using (5.10) and (5.11) with $n = 3721$ and $N = 100$; (b,f) the dimensionless streamwise distance between pairs of particles $f_{\mathscr{C}_t}^{\mathscr{V}} d$ computed using (5.10) and (5.11) with $n = 3721$ and $N = 100$; (c,g) the ratio of the lateral distance to the streamwise distance between pairs of particles $f_{\mathscr{C}_t}^{\mathscr{M}}$ computed using (5.10) and (5.11) with $n = 3721$ and $N = 100$ (in a log–log plot); and (d,h) the dimensionless distance between pairs of particles $f_{\mathscr{C}_t}^{\mathscr{D}} d$ computed using (5.10) and (5.11) with $n = 3721$ and $N = 100$.

consists of seeding and tracking clusters of virtual particles (or passive tracers) in experimentally-measured velocity fields. As we discussed in the previous chapter (see § 4.1.2), there are numerous advantages to using this technique. The spatial and temporal resolutions are only limited by the resolution of the acquisition technique used to measure the velocity field.[1] Virtual particle tracking can potentially be applied to any laboratory flows, with a possible range of Reynolds numbers, Schmidt numbers or Prandtl numbers far exceeding the capabilities of numerical simulations. A large quantity of virtual particles can be seeded instantaneously in the flow field, with any arbitrary initial distribution, and then tracked over a spatial range only limited by the size of the measured velocity field. One could argue that virtual particle tracking is not adapted to the study of three-dimensional flow fields. With only a two-dimensional velocity field of a three-dimensional flow field, it is true that virtual particle tracking cannot give meaningful information, because the trajectories of real Lagrangian particles are also three-dimensional. We believe that the recent development of volumetric particle image velocimetry to measure the three components of the velocity in three-dimensional domains (see e.g. Kitzhofer *et al.*, 2011; Cierpka & Kaehler, 2012, for recent reviews) can address this shortcoming.

The flow in quasi-two-dimensional jet is appropriate for the application of particle tracking velocimetry because the three-dimensionality of the flow can be considered insignificant in the first order. In § 4.1.2 we report that the mean divergence of the flow is small compared with the mean vorticity. Moreover, Dracos *et al.* (1992) found that the flow of quasi-two-dimensional jets is primarily governed by a two-dimensional inverse cascade of turbulence, except at scales of the order of (or less than) the gap width of the tank W. Therefore, we believe that particle tracking velocimetry can give physically meaningful information about the dispersion in quasi-two-dimensional jets. However, the three-dimensional small-scale turbulence, typically of the order of $W = 1\,\mathrm{cm}$ or less, cannot be adequately resolved in this study, with only a two-dimensional velocity field.

Bearing in mind the limited spatial resolution of our data, we have probed the large-scale dispersion of the (large-scale) eddy and core structures of the flow.

---

[1]It can be noted that particle image velocimetry, a common technique to measure velocity fields, is considered technically less demanding than experimental Lagrangian particles tracking techniques, such as particle tracking velocimetry or other optical particle tracking techniques (Kitzhofer, Nonn & Brücker, 2011)

The time evolution of the probability distributions of key two-point properties (such as the lateral distance, the streamwise distance, the Euclidean distance and the ratio of the lateral distance to the streamwise distance between two points) in the main structures of quasi-two-dimensional jets has shown different behaviours for the different parts of the flow. We compare the results of the two-point statistics obtained in the time-dependent velocity field with results obtained in the time-averaged velocity field of the same jet and results obtained with simple geometrical distributions of points (a circle, an ellipse and a square). From the study of these simple geometrical distributions, we have been able to understand how the variation in time of general shape characteristics of the distribution affects the p.d.f.s of the two-point properties. In particular, we have been able to measure that, in the eddy, the distribution of particles disperses slowly and in a rather axisymmetric manner. At the interface between the core and the eddy, the distribution of particles stretches considerably in the streamwise direction at a high rate. This is accompanied by thinning of the particle cluster. In the core of the jet, the particle distribution disperses slowly in the cross-jet direction and splits along the jet axis. Finally, we believe that the comparison between the p.d.f.s for the time-averaged flow field and the p.d.f.s for the time-dependent flow field demonstrates the intense stirring (and potentially the resulting vigorous turbulent mixing) occurring within the eddy and, to some extent, at the interface between the eddy and the core. This aspect is revealed by the rapid displacement through time of the peaks in the distribution of $f_{\mathscr{E}_t}^{\mathcal{D}}(t)$ (the time evolution of the p.d.f. of the distance between two particles initially seeded in the eddy) for the time-dependent velocity field of the eddy. The chaotic dynamics of the turbulent flow in the eddy strongly perturbs the distribution of the virtual particles, which manifests itself in the time evolution of the p.d.f. for the separation distance between particles.

Future research about the turbulent relative dispersion of the flow of quasi-two-dimensional jets could investigate the ideas of Richardson (1926) and Batchelor (1952) to describe the relative dispersion in the jet by a differential equation based on the p.d.f.s of two-point properties. In Chapter 3, we propose a model for the transport and streamwise dispersion in the jet, based on the Eulerian description of the flow. Forming the connection between the Eulerian and the Lagrangian descriptions of the turbulent dispersion could provide invaluable insight in the

physics of anisotropic turbulent processes. One particular question of interest is to relate the streamwise turbulent eddy diffusivity $K_d M_0^{1/2} z^{1/2}$ in the general effective advection–diffusion equation (3.15) (obtained using a mixing length hypothesis) to the p.d.f. of the streamwise distance between two points obtained directly from virtual particle tracking, in an effort to identify and parameterize the cumulative quantitative effect of the complex time-dependent flow on streamwise dispersion.

Another possible avenue of research would be to improve the spatial resolution of the velocity field, and perhaps to measure a truly three-dimensional velocity field of the flow. With a fully resolved velocity field in time (i.e. resolving Kolmogorov time scale $\tau_{\eta_K} \approx 40\,\mathrm{ms}$) and in space (i.e. resolving Kolmogorov length scale $\eta_K \approx 0.2\,\mathrm{mm}$), we could explore, for instance, the two-point dispersion model of Batchelor (1950). As Bourgoin *et al.* (2006) pointed out, there is a need for more experimental evidence. A comparison between the results of two-point statistics for the flow field of quasi-two-dimensional jets with the results for three-dimensional turbulent flows could shed new light on the physics of turbulent relative dispersion.

CHAPTER 6

FLOW INDUCED BY A QUASI-TWO-DIMENSIONAL JET IN A CONFINED RECTANGULAR DOMAIN

6.1 Introduction

A turbulent momentum jet induces a flow towards the jet in the surrounding ambient fluid. The entrainment of the ambient fluid, which is the result of a complex turbulent dynamics at the boundary of the jet, was modelled by Morton *et al.* (1956). Using dimensional analysis, they related the lateral velocity of the entrained fluid at the boundary of the jet as simply being proportional to the time-averaged maximum axial (or streamwise) velocity in the jet. Contrary to round axisymmetric jets, the velocity of the fluid entrained by a plane jet does not decay with distance away from the jet axis. The flow induced by plane

jets is important in industrial applications such as chemical reactors and mixing chambers (Jirka & Harleman, 1979). As we discuss in the introduction of Chapter 2 (see § 2.1) rivers flowing into lakes or oceans can be modelled as quasi-two-dimensional turbulent jets (Giger *et al.*, 1991; Dracos *et al.*, 1992; Rowland *et al.*, 2009). Studying the flow induced by rivers emerging into lakes or oceans, Joshi & Taylor (1983) revealed the impact on the local sediment transport and the possible coastal erosion.

Taylor (1958) calculated the stream function of the flow in the ambient of plane jets and axisymmetric jets, when emerging from either a plane wall into a semi-infinite domain or directly into unbounded space, and for both buoyant and non-buoyant jets. Assuming an inviscid incompressible potential flow in the ambient, using a slip boundary condition at the wall (if present) and modelling the jet as a distribution of sinks, he solved Laplace's equation to obtain the stream function. However, Schneider (1981) demonstrated that the hypothesis of an inviscid fluid and the use of a slip boundary condition at the wall gave an incorrect result for the streamlines in the ambient of axisymmetric jets. Comparing Taylor (1958)'s analytical solution and Schneider (1981)'s numerical solution in the case of a laminar axisymmetric jet, Zauner (1985) confirmed experimentally the importance of viscosity in the ambient flow and the need to satisfy the condition of zero tangential velocity at the wall. Nevertheless, inviscid potential theory using slip boundary conditions at the walls is still valid in the case of the flow induced by plane turbulent jets, because the Reynolds number in the ambient flow is comparable to the jet Reynolds number (Schneider, 1981).

The flow induced by a turbulent jet can also influence the axial momentum flux of the jet (Kotsovinos, 1978; Schneider, 1985; Kotsovinos & Angelidis, 1991). According to Kotsovinos & Angelidis (1991), this influence occurs through two factors. The momentum flux of the induced flow can contribute positively or negatively to the jet momentum flux depending on the angle between the streamlines of the induced flow and the direction of the jet flow at the jet boundary. The pressure field at the boundary of the jet contributes negatively to the jet momentum flux. Therefore, predicting the streamlines of the induced flow is important to determine the rate of change of the jet momentum flux. In the case of a plane jet emerging from a wall into a semi-infinite domain, the streamlines of the induced potential flow form two sets of confocal parabolas with axes perpendicular to the

jet axis (Taylor, 1958). Thus, the streamlines are opposed to the jet flow and the jet momentum flux slowly decays with distance. However, the more realistic case of a plane jet emerging from a wall into a confined domain does not seem to have been solved in the literature.

The case of a plane jet emerging from a wall into a domain confined in the axial, lateral and spanwise directions is a common problem, because, in practice, semi-infinite domains or fully unbounded domains (as assumed by Taylor, 1958; Schneider, 1981) do not exist. In his model, Schneider (1981) analysed how the angle between the jet axis and the wall (from which the jet emerged) influences the streamlines of the induced flow. Revuelta, Sánchez & Liñán (2002) investigated numerically the case of an axisymmetric laminar jet confined in an axisymmetric domain. They predicted the size and the induced pressure drop of a long recirculating region surrounding the jet, before the jet expands across the whole domain. Jirka & Harleman (1979) studied experimentally and theoretically the stability and mixing of plane jets confined in the axial direction, but unconfined in the lateral (or cross-stream) direction. For non-buoyant jets, they observed on both sides of the jet the formation of alternating recirculation cells. The cell closer to the jet is driven by two distinct mechanisms. As the vertical upward jet impinges on the free surface at the top, the flow spreads laterally outwards along the free surface. Along the bottom boundary, the flow is driven inwards by the jet entrainment process. The size and the total mass flow of the cell are controlled by the growth characteristics of the jet and the associated entrainment mechanism. Moreover, Jirka & Harleman (1979) noted that if passive tracers are injected at the source of the jet, their concentration in the jet increases due to the recirculation in the cell.

In this chapter, we are interested in the flow induced by a quasi-two-dimensional turbulent jet emerging from a plane wall into a fully confined domain (see experimental apparatus presented in figure 2.1). In this domain, the distance between the source and the lateral or axial boundaries is much larger than the nozzle width, $d = 0.5$ cm. As we discuss in Chapter 2, the flow in the jet does not seem to be affected by the streamwise confinement for $0 \leq z/d \leq h_i/d \approx 120$, where h_i is the height at which the impingement region starts (see § 2.4). For $h_i/d \leq z/d \leq h_f/d = 183$ (where h_f is the height of the free surface), the flow experiences a transition as it impinges on the free surface. The vertical upward

flow from the jet spreads laterally outwards, symmetrically with respect to the jet axis. Two overflows, located close to the lateral walls, maintain the free surface at a constant $h_f = 91.5$ cm. A large portion of the flow spreading along the free surface recirculates inside the tank as it reaches the lateral boundaries and produces the counterflow mentioned in § 2.4 (with volume flux Q_r). Somewhat similarly to the recirculation cells observed by Jirka & Harleman (1979), the flow in our experimental apparatus also displays a recirculation cell on either side of the jet, but in our case, the recirculation cells are confined laterally by rigid walls.

In this study, we do not model the flow in the impingement region located directly above the jet nor the recirculation flow at the lateral boundaries near the free surface (i.e. the region ranging $h_i \leq z \leq h_f$ in the streamwise direction and spanning the entire domain in the lateral (or x-) direction and the spanwise (or y-) direction). We only model the flow on the left-hand side of the jet axis (the flow on the right-hand side can be obtained by symmetry), before the transition from a jet flow to an impingement flow. We assume that the jet is a distribution of sinks. The domain of study, which we designate as $\mathscr{D}_s$, ranges $0 \leq x/d \leq x_j/d = 90$ in the lateral or cross jet direction (where x_j represents the lateral coordinate of the jet nozzle, considering the origin of the domain ($x = 0, y = 0, z = 0$) at the bottom left-hand-side corner of the tank), $0 \leq z \leq h_i$ in the streamwise direction, and spans the entire domain in the spanwise (or y-) direction, $W/2 \leq y \leq W/2$ (where $W = 1$ cm is the gap width). We distinguish two aspect ratios in this study: the aspect ratio of the inner dimensions of the experimental apparatus, $(2x_j)/h_f \approx 1$; and the aspect ratio of the domain $\mathscr{D}_s$, $\zeta = x_j/h_i = 3/4$, or the jet aspect ratio.

In § 6.2, we develop a model of the ambient flow field in the domain $\mathscr{D}_s$ using two-dimensional potential theory. We present the results for the potential field, the stream function, and the velocity field. In § 6.3, we compare the theoretical results with results from dyed quasi-two-dimensional turbulent jets and particle image velocimetry experiments for the stream function, the velocity field, the volume flux and the momentum flux of the induced flow. We draw our conclusions in § 6.4.

6.2 Potential flow model

6.2.1 Description of the entrainment problem

We consider a similar experimental apparatus to that which is depicted in figure 2.1. We model the ambient flow field at the left-hand side of a quasi-two-dimensional turbulent jet using potential theory. We assume a steady laminar plane flow in the rectangular domain $\mathscr{D}_s$. In Cartesian coordinates (x, z) with the origin at the bottom left-hand corner of the inside of the experimental apparatus,[1], the domain is bounded at the bottom ($z = 0\,\mathrm{m}$) and on the left-hand side ($x = 0\,\mathrm{m}$) by rigid walls. For the top boundary, we do not wish to consider the impingement region observed by Jirka & Harleman (1979) near the free surface (located at $z = h_f = 0.915\,\mathrm{m}$). So, instead of choosing the free surface as the top boundary, we choose the height of transition between the jet region and the impingement region, which is at $z = h_i \approx 0.6\,\mathrm{m}$ (see § 2.4 and figure 2.4). On the right-hand side, the domain is delimited by the jet boundary, which we assume to be along the jet axis (Taylor, 1958) at $x = x_j \approx 0.45\,\mathrm{m}$. Although the distance between the jet boundary and the axis increases with z, we believe that this assumption is valid because the jet velocity spread rate $b(z)$ (which is of the same order of magnitude as the jet boundary) is much smaller than the lateral dimension of the domain at all height: $b/x_j \leq 0.2$ for $0 \leq z \leq h_i$ according to (2.5a) using an entrainment coefficient $\alpha = 0.068$. Since we assume a two-dimensional plane flow in the domain (similarly to the model in § 2.4), we do not consider the boundaries in the spanwise (or y-) direction in this model.

The domain $\mathscr{D}_s$ is delimited by: $0 \leq x \leq x_j$ and $0 \leq z \leq h_i$. We use the following boundary conditions for the velocity field $\mathbf{u} = (u, w)$. The normal velocity vanishes at the walls, $u(x = 0, z) = 0$ and $w(x, z = 0) = 0$, and the slip condition applies for the tangential velocity at the walls (Taylor, 1958). At $z = h_i$, we assume a uniform constant line source, the flux per unit length is

$$w(x, z = h_i) = -\ell, \tag{6.1}$$

where $\ell \geq 0$ is a constant, which is determined below. The boundary condition (6.1) represents the recirculation of the flow in the experimental apparatus. The

---

[1]Note that in the model developed in § 2.4 the origin of the domain is in the middle of the bottom wall of the experimental apparatus.

last boundary condition corresponds to the jet at $x = x_j$. Similarly to Taylor (1958), we assume that, in the ambient, the influence of the jet can be considered as a line sink along the z-axis of strength $j(z)$, varying with height,

$$j(z) = u(x = x_j, z) = \alpha \overline{w}_m, \tag{6.2}$$

where we use the entrainment assumption of Morton *et al.* (1956), and where $\overline{w}_m$ is defined by (2.5b) (which assumes a constant momentum flux). Hence, the strength of the line sink is

$$j(z) = \frac{K_j \sqrt{d}}{\sqrt{z - z_0}}, \quad \text{with} \quad K_j = \left(\frac{\alpha M_0}{2\sqrt{2}d} \right)^{1/2}, \tag{6.3}$$

where M_0 is the initial momentum of the jet at $z = 0$, and z_0 the space virtual origin defined in (2.6). By continuity, the volume flux of the line source must equal the volume flux of the line sink

$$\int_0^{x_j} \ell \, \mathrm{d}x = \int_0^{h_i} j(z) \, \mathrm{d}z. \tag{6.4}$$

Finally, we assume that the flow is irrotational and incompressible in the domain. Therefore, the velocity field $\mathbf{u} = (u, w)$ derives from a potential φ, such that $\mathbf{u} = \boldsymbol{\nabla}\varphi$ (where $\boldsymbol{\nabla}$ is the gradient operator), which must satisfy Laplace's equation in the domain:

$$\boldsymbol{\nabla}^2\varphi = 0 \quad \text{for} \quad 0 \leq x \leq x_j, \quad 0 \leq z \leq h_i. \tag{6.5}$$

We scale all spatial variables with the height of the impingement region h_i, such that $\widetilde{x} = x/h_i$ and $\widetilde{z} = z/h_i$ (where wide tildes denote non-dimensional variables). We define $\zeta = x_j/h_i = 3/4$, the jet aspect ratio of the domain $\mathscr{D}_s$ corresponding to our particular experimental problem. (As mentioned previously, we distinguish the jet aspect ratio ζ from the aspect ratio of the apparatus $2x_j/h_f \approx 1$.) We scale velocities with K_j (which is proportional to the streamwise velocity at the nozzle) defined in (6.3), such that $\widetilde{u} = u/K_j$ and $\widetilde{w} = w/K_j$.

We summarize the entrainment problem in figure 6.1. The non-dimensional

potential $\widetilde{\varphi}$ is the solution to Laplace's equation in the domain $\mathscr{D}_s$:

$$\widetilde{\boldsymbol{\nabla}}^2 \widetilde{\varphi} = 0 \quad \text{for} \quad 0 \le \widetilde{x} \le \zeta, \quad 0 \le \widetilde{z} \le 1, \tag{6.6}$$

subject to the Neumann boundary conditions

$$\begin{cases} \dfrac{\partial \widetilde{\varphi}}{\partial \widetilde{x}} &=& 0 \quad \text{for} \quad \widetilde{x} = 0, \quad 0 \le \widetilde{z} \le 1, \\[2ex] \dfrac{\partial \widetilde{\varphi}}{\partial \widetilde{x}} &=& \widetilde{j} \quad \text{for} \quad \widetilde{x} = \zeta, \quad 0 \le \widetilde{z} \le 1, \\[2ex] \dfrac{\partial \widetilde{\varphi}}{\partial \widetilde{z}} &=& 0 \quad \text{for} \quad 0 \le \widetilde{x} \le \zeta, \quad \widetilde{z} = 0, \\[2ex] \dfrac{\partial \widetilde{\varphi}}{\partial \widetilde{z}} &=& -\widetilde{\ell} \quad \text{for} \quad 0 \le \widetilde{x} \le \zeta, \quad \widetilde{z} = 1 \end{cases} \tag{6.7}$$

and with the continuity condition (from (6.4))

$$\int_0^1 \widetilde{j}(\widetilde{z}) \, \mathrm{d}\widetilde{z} = \zeta \widetilde{\ell}, \tag{6.8}$$

where

$$\widetilde{j}(\widetilde{z}) = \left(\frac{\widetilde{d}}{\widetilde{z} - \widetilde{z}_0} \right)^{1/2}, \tag{6.9}$$

according to (6.3). Therefore, the strength of the line source is, in non-dimensional form,

$$\widetilde{\ell} = \frac{2\sqrt{\widetilde{d}}}{\zeta} \left(\sqrt{1 - \widetilde{z}_0} - \sqrt{-\widetilde{z}_0} \right). \tag{6.10}$$

6.2.2 Decomposition of the problem

To simplify our problem and to eventually improve the convergence of the numerical calculation of our analytical solution, we split the non-dimensional potential $\widetilde{\varphi}$, by virtue of the superposition principle for linear problems, into two components:

$$\widetilde{\varphi} = \widetilde{\varphi}_u + \widetilde{\varphi}_p, \tag{6.11}$$
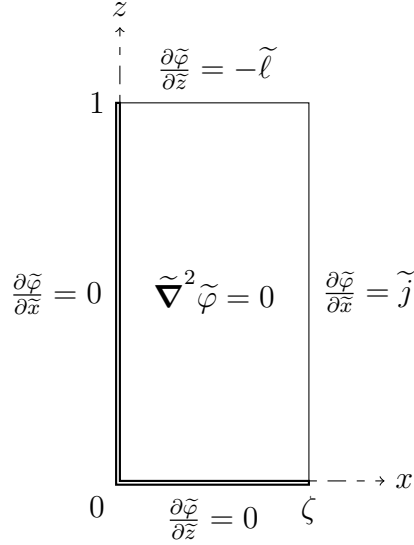
FIGURE 6.1: Description of the entrainment problem of which $\widetilde{\varphi}$ is solution.

where $\widetilde{\varphi}_u$ is the solution of a 'uniform problem' in the domain $\mathscr{D}_s$, with a non-dimensional uniform line source of strength $\widetilde{\ell}$ at $\widetilde{z} = 1$ and a non-dimensional uniform line sink of strength $\zeta\widetilde{\ell}$ at $\widetilde{x} = \zeta$, as described in figure 6.2(a), and where $\widetilde{\varphi}_p$ is defined as a perturbation to this uniform problem. The 'perturbation problem' is represented in figure 6.2(b). In the perturbation problem, we have no-flux boundary conditions at $\widetilde{x} = 0$, $\widetilde{z} = 0$ and $\widetilde{z} = 1$, and a varying flux at $\widetilde{x} = \zeta$ such that

$$\frac{\partial\widetilde{\varphi}_p}{\partial\widetilde{x}}\left(\widetilde{x} = \zeta, \widetilde{z}\right) = \widetilde{j}\left(\widetilde{z}\right) - \zeta\widetilde{\ell}. \tag{6.12}$$

6.2.3 Solution to the uniform problem $\widetilde{\varphi}_u$

Solving Laplace's equation in the domain described in figure 6.2(a), the solution to the uniform problem, with a uniform line source at $\widetilde{z} = 1$ and a uniform line sink at $\widetilde{x} = \zeta$, is

$$\widetilde{\varphi}_u = \frac{1}{2}\left(\widetilde{x}^2 - \widetilde{z}^2\right) \quad \text{for} \quad 0 \le \widetilde{x} \le \zeta, \quad 0 \le \widetilde{z} \le 1. \tag{6.13}$$

As a solution of Laplace's equation under Neumann boundary conditions, $\widetilde{\varphi}_u$ is the unique solution, to within a constant, to the uniform problem.

In a two-dimensional inviscid and incompressible flow, we can also define a
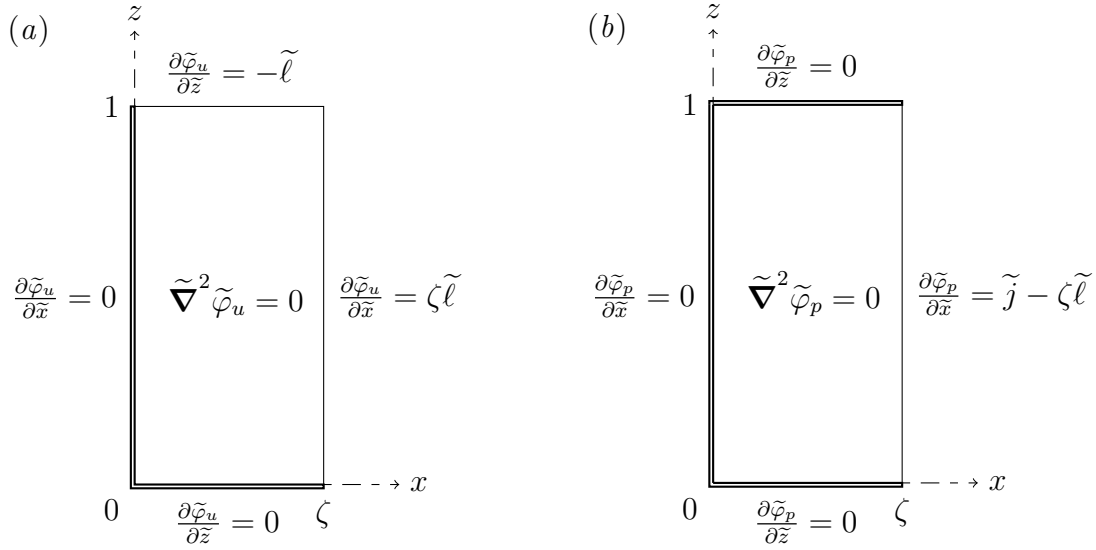
FIGURE 6.2: We decompose the entrainment problem into two problems (see equation (6.11)): (a) a uniform problem of which $\widetilde{\varphi}_u$ is solution; (b) a perturbation problem of which $\widetilde{\varphi}_p$ is solution.

stream function ψ such that

$$\boldsymbol{\nabla}\psi \cdot \boldsymbol{\nabla}\varphi = 0, \tag{6.14}$$

i.e. the streamlines are orthogonal to the equipotential lines in the domain. The corresponding non-dimensional stream function $\widetilde{\psi}_u$ for the uniform problem described in figure 6.2(a) is

$$\widetilde{\psi}_u = \widetilde{x}\widetilde{z} \quad \text{for} \quad 0 \leq \widetilde{x} \leq \zeta, \quad 0 \leq \widetilde{z} \leq 1. \tag{6.15}$$

In figures 6.3(a,b), we show the non-dimensional potential $\widetilde{\varphi}_u$ and the non-dimensional stream function $\widetilde{\psi}_u$, respectively, for the uniform problem described in figure 6.2(a). For the aspect ratio, we use $\zeta = x_j/h_i = 3/4$, the jet aspect ratio of our particular case. The flow field in the right-hand-side half of the tank can be found by symmetry with respect to the jet axis. As we can see in figure 6.3(b), the streamlines are hyperbolas.

By definition we have $\mathbf{u} = \boldsymbol{\nabla}\varphi$, so the velocity field of the uniform problem $\widetilde{\mathbf{u}}_u = (\widetilde{u}_u, \widetilde{w}_u)$ can be derived from the potential $\widetilde{\varphi}_u$ described in (6.13). We find

$$\widetilde{u}_u = \widetilde{x}, \quad \widetilde{w}_u = -\widetilde{z} \quad \text{for} \quad 0 \leq \widetilde{x} \leq \zeta, \quad 0 \leq \widetilde{z} \leq 1. \tag{6.16a,b}$$

(a)

(b)
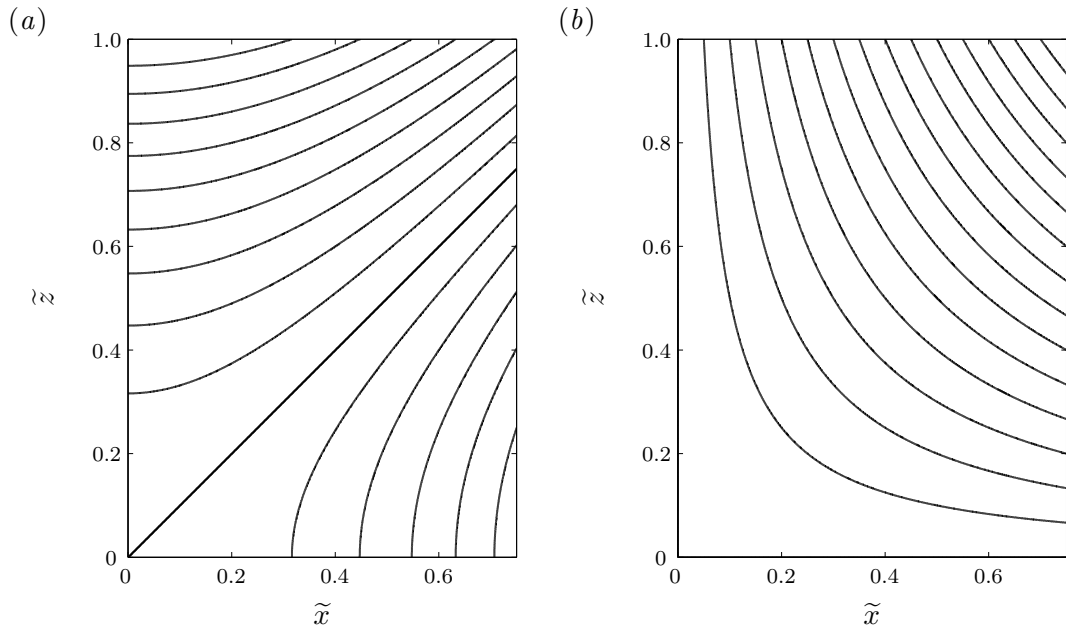
FIGURE 6.3: (a) Non-dimensional potential $\widetilde{\varphi}_u$ (defined by (6.13)), and (b) non-dimensional stream function $\widetilde{\psi}_u$ (defined by (6.15)) for the uniform problem described in figure 6.2(a), using $\zeta = x_j/h_i = 3/4$.

The velocity components are linear in their coordinate direction and constant in the orthogonal direction. The non-dimensional velocity field $(\widetilde{u}_u, \widetilde{w}_u)$ is presented in figures 6.4(a,b), respectively.

(a)

(b)
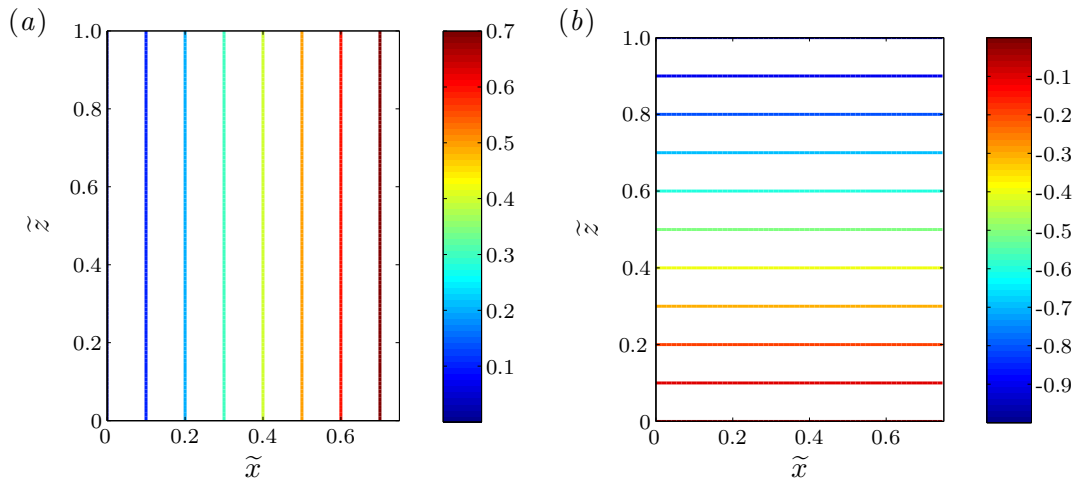
FIGURE 6.4: (a) Non-dimensional lateral velocity $\widetilde{u}_u$ (defined by (6.16a)), and (b) non-dimensional streamwise velocity $\widetilde{w}_u$ (defined by (6.16b)) for the uniform problem described in figure 6.2(a), using $\zeta = x_j/h_i = 3/4$.

6.2.4 Solution to the perturbation problem $\widetilde{\varphi}_p$

A solution to the perturbation problem can be found by the method of separation of variables. The solution $\widetilde{\varphi}_p$ consists of an infinite linear combination of the product of hyperbolic cosines and cosines, i.e.

$$\widetilde{\varphi}_p = \sum_{n=1}^{\infty} A_n \cosh\left(n\pi\widetilde{x}\right) \cos\left(n\pi\widetilde{z}\right) \quad \text{for} \quad 0 \leq \widetilde{x} \leq \zeta, \quad 0 \leq \widetilde{z} \leq 1, \tag{6.17}$$

where A_n are coefficients which can be determined using the non-homogeneous boundary condition at $\widetilde{x} = \zeta$,

$$\left.\frac{\partial\widetilde{\varphi}_p}{\partial\widetilde{x}}\right|_{\widetilde{x}=\zeta} = \sum_{n=1}^{\infty} A_n n\pi \sinh\left(n\pi\zeta\right) \cos\left(n\pi\widetilde{z}\right) = \widetilde{j}(\widetilde{z}) - \zeta\widetilde{\ell} \quad \text{for} \quad 0 \leq \widetilde{z} \leq 1, \tag{6.18}$$

according to (6.12). We define the coefficients B_n such that

$$B_n = A_n n\pi \sinh\left(n\pi\zeta\right) \quad \text{for} \quad n \geq 1. \tag{6.19}$$

Re-writing equation (6.18),

$$\sum_{n=1}^{\infty} B_n \cos\left(n\pi\widetilde{z}\right) = \widetilde{j}(\widetilde{z}) - \zeta\widetilde{\ell} \quad \text{for} \quad 0 \leq \widetilde{z} \leq 1, \tag{6.20}$$

we can clearly see that the coefficients B_n are the Fourier coefficients of an even function $\widetilde{E}$ defined as

$$\widetilde{E}(\widetilde{z}) = \widetilde{j}(|\widetilde{z}|) - \zeta\widetilde{\ell} \quad \text{for} \quad -1 \leq \widetilde{z} \leq 1. \tag{6.21}$$

Therefore, we can calculate the coefficients B_n as follows

$$B_n = \int_{-1}^{1} \widetilde{E}(\widetilde{z}) \cos\left(n\pi\widetilde{z}\right) \mathrm{d}\widetilde{z} \quad \text{for} \quad n \geq 1, \tag{6.22}$$

which simplifies to

$$B_n = 2 \int_{0}^{1} \widetilde{j}(\widetilde{z}) \cos\left(n\pi\widetilde{z}\right) \mathrm{d}\widetilde{z}, \tag{6.23}$$

because $\widetilde{j}(|\widetilde{z}|)$ and $\cos\left(n\pi\widetilde{z}\right)$ are even functions for $-1 \leq \widetilde{z} \leq 1$ and $\zeta\widetilde{\ell}\cos\left(n\pi\widetilde{z}\right)$ integrates to zero in the interval $-1 \leq \widetilde{z} \leq 1$ for $n \geq 1$. Using equation (6.9), we

have

$$B_n = 2\sqrt{\widetilde{d}} \int_0^1 \frac{\cos{(n\pi\widetilde{z})}}{\sqrt{\widetilde{z} - \widetilde{z}_0}} \, \mathrm{d}\widetilde{z}. \tag{6.24}$$

Then, applying the transformation $q = n\pi(\widetilde{z} - \widetilde{z}_0)$ we find

$$B_n = \frac{2\sqrt{\widetilde{d}}}{\sqrt{n\pi}} \left(\cos{(n\pi\widetilde{z}_0)} \int_{-n\pi\widetilde{z}_0}^{n\pi(1-\widetilde{z}_0)} \frac{\cos{q}}{\sqrt{q}} \, \mathrm{d}q - \sin{(n\pi\widetilde{z}_0)} \int_{-n\pi\widetilde{z}_0}^{n\pi(1-\widetilde{z}_0)} \frac{\sin{q}}{\sqrt{q}} \, \mathrm{d}q \right). \tag{6.25}$$

Finally, we can apply another transformation $s = \sqrt{2q/\pi}$, which gives

$$B_n = \frac{2\sqrt{2\widetilde{d}}}{\sqrt{n}} \left(\cos{(n\pi\widetilde{z}_0)} \Big[\mathcal{C}(y) \Big]_{\sqrt{-2n\widetilde{z}_0}}^{\sqrt{2n(1-\widetilde{z}_0)}} - \sin{(n\pi\widetilde{z}_0)} \Big[\mathcal{S}(y) \Big]_{\sqrt{-2n\widetilde{z}_0}}^{\sqrt{2n(1-\widetilde{z}_0)}} \right) \tag{6.26}$$

for $n \geq 1$, where we have introduced the Fresnel $\mathcal{C}$ and $\mathcal{S}$ integrals (see e.g. Abramowitz & Stegun, 1972) defined as

$$\mathcal{C}(y) = \int_0^y \cos{\left(\frac{\pi}{2} s^2 \right)} \, \mathrm{d}s \quad \text{and} \quad \mathcal{S}(y) = \int_0^y \sin{\left(\frac{\pi}{2} s^2 \right)} \, \mathrm{d}s. \tag{6.27}$$

It can be noted that the coefficient B_0 equals zero from the condition of continuity stated in equation (6.8). Therefore, we have found a unique solution $\widetilde{\varphi}_p$ (defined by equations (6.17), (6.19) and (6.26)) to the perturbation problem described in figure 6.2(b). According to (6.14), the corresponding non-dimensional stream function $\widetilde{\psi}_p$ for the perturbation problem described in figure 6.2(b) is

$$\widetilde{\psi}_p = \sum_{n=1}^{\infty} A_n \sinh{(n\pi\widetilde{x})} \sin{(n\pi\widetilde{z})} \quad \text{for} \quad 0 \leq \widetilde{x} \leq \zeta, \quad 0 \leq \widetilde{z} \leq 1, \tag{6.28}$$

where the coefficients A_n are given by (6.19) and (6.26).

We present in figures 6.5(a,b) the non-dimensional potential $\widetilde{\varphi}_p$ and the non-dimensional stream function $\widetilde{\psi}_p$, respectively, for the perturbation problem described in figure 6.2(b). We compute the series $\widetilde{\varphi}_p$ (defined by equations (6.17), (6.19) and (6.26)) and $\widetilde{\psi}_p$ (defined by equations (6.28), (6.19) and (6.26)) numerically for $n_{max} = 100$, the (finite) number of terms of both series. We use the jet aspect ratio $\zeta = x_j/h_i = 3/4$ of our particular case, and the space virtual origin $z_0 = -4.7\,d$ (computed from (2.6) using $\alpha = 0.068$, $<\overline{M}>/\left(Q_0{}^2/d\right) = 0.55$).

Similarly to $\widetilde{\mathbf{u}}_u$, the velocity field of the perturbation problem $\widetilde{\mathbf{u}}_p = \left(\widetilde{u}_p, \widetilde{w}_p\right)$ can

(a)

(b)
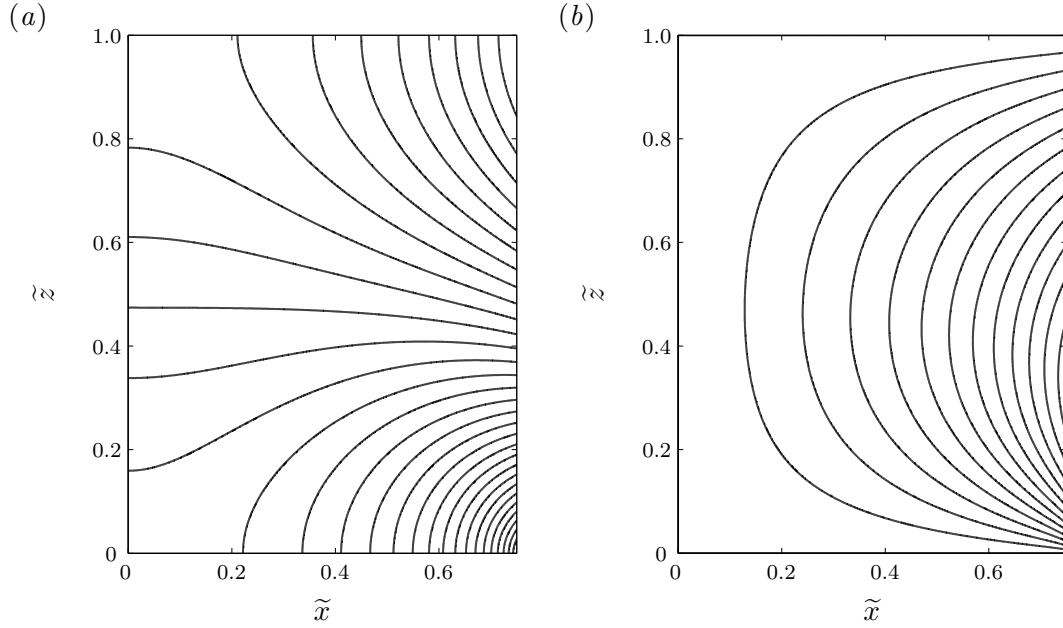
FIGURE 6.5: (a) Non-dimensional potential $\widetilde{\varphi}_p$ (defined by equations (6.17), (6.19) and (6.26) with $n_{max} = 100$ the number of terms of the series, and $z_0 = -4.7\,d$ the space virtual origin), and (b) non-dimensional stream function $\widetilde{\psi}_p$ (defined by (6.28), (6.19) and (6.26) with $n_{max} = 100$, the number of terms of the series, and $z_0 = -4.7\,d$ the space virtual origin) for the perturbation problem described in figure 6.2(b), using $\zeta = x_j/h_i = 3/4$.

be derived from the potential $\widetilde{\varphi}_p$ defined by equations (6.17), (6.19) and (6.26). We find for $0 \leq \widetilde{x} \leq \zeta$, $0 \leq \widetilde{z} \leq 1$,

$$\widetilde{u}_p = \sum_{n=1}^{\infty} n\pi A_n \sinh(n\pi\widetilde{x}) \cos(n\pi\widetilde{z}), \qquad (6.29)$$

$$\widetilde{w}_p = -\sum_{n=1}^{\infty} n\pi A_n \cosh(n\pi\widetilde{x}) \sin(n\pi\widetilde{z}), \qquad (6.30)$$

where the coefficients A_n are given by (6.19) and (6.26). We present the non-dimensional velocities $\widetilde{u}_p$ and $\widetilde{w}_p$ for the perturbation problem in figures 6.6(a,b), respectively. Similarly to $\widetilde{\varphi}_p$ and $\widetilde{\psi}_p$, we compute the series $\widetilde{u}_p$ (defined by equations (6.29), (6.19) and (6.26)) and $\widetilde{w}_p$ (defined by equations (6.30), (6.19) and (6.26)) numerically for $n_{max} = 100$, the number of terms of both series. We use the aspect ratio $\zeta = x_j/h_i = 3/4$, and the space virtual origin $z_0 = -4.7\,d$ (computed from (2.6) using $\alpha = 0.068$, $< \overline{M} > / \left(Q_0^2/d \right) = 0.55$). We note that both the lateral and the streamwise velocities are strongly affected by the origin of the

(a)

(b)
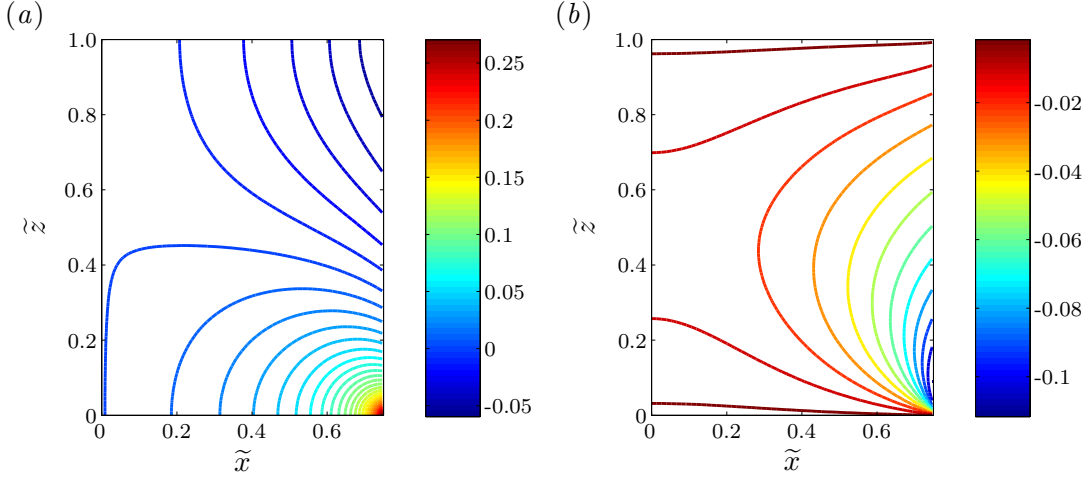
FIGURE 6.6: (a) Non-dimensional lateral velocity $\widetilde{u}_p$ (defined by (6.29), (6.19) and (6.26) with $n_{max} = 100$ the number of terms of the series, and $z_0 = -4.7\,d$ the space virtual origin), and (b) non-dimensional streamwise velocity $\widetilde{w}_p$ (defined by (6.30), (6.19) and (6.26) with $n_{max} = 100$ the number of terms of the series, and $z_0 = -4.7\,d$ the space virtual origin) for the perturbation problem described in figure 6.2(b), using $\zeta = x_j/h_i = 3/4$.

line sink at $(\widetilde{x} = \zeta, \widetilde{z} = 0)$. This is due to the singularity at the virtual origin $\widetilde{z} = \widetilde{z}_0 < 0$. We can see in figure 6.6(a) that the lateral velocity $\widetilde{u}_p$ is maximum at the bottom right-hand corner, $(\widetilde{x} = \zeta, \widetilde{z} = 0)$. In figure 6.6(b), we can see that, along the right-hand side boundary $\widetilde{x} = \zeta$, the streamwise velocity $\widetilde{w}_p$ sharply decreases from the bottom boundary $\widetilde{z} = 0$ to approximately $\widetilde{z} \approx 0.1$. Then, $\widetilde{w}_p$ slowly increases again for $\widetilde{z} > 0.1$, to eventually vanish at the top boundary $\widetilde{z} = 1$.

Since there is no flux inwards or outwards at the boundaries $\widetilde{x} = 0$, $\widetilde{z} = 0$ and $\widetilde{z} = 1$, by continuity, the total integrated flux along the right-hand side boundary at $\widetilde{x} = \zeta$ must also be zero,

$$\int_0^1 \frac{\partial \widetilde{\varphi}_p}{\partial \widetilde{x}} (\widetilde{x} = \zeta, \widetilde{z}) \; \mathrm{d}\widetilde{z} = 0, \tag{6.31}$$

according to equation (6.8) and (6.12), thus

$$\frac{\partial \widetilde{\varphi}_p}{\partial \widetilde{x}} (\widetilde{x} = \zeta, \widetilde{z}) = \sqrt{\widetilde{d}} \left(\frac{1}{\sqrt{\widetilde{z} - \widetilde{z}_0}} - 2 \left(\sqrt{1 - \widetilde{z}_0} - \sqrt{-\widetilde{z}_0} \right) \right), \tag{6.32}$$

according to (6.12), with $\widetilde{j}(\widetilde{z})$ defined by (6.9) and $\widetilde{\ell}$ defined by (6.10). There is

a local non-uniform flux along the right-hand side boundary at $\widetilde{x} = \zeta$ oriented inwards for $z \geq \widetilde{z}_c$ and outwards for $z \leq \widetilde{z}_c$, where $\widetilde{z}_c$ is defined by

$$\frac{\partial \widetilde{\varphi}_p}{\partial \widetilde{x}} (\widetilde{x} = \zeta, \widetilde{z}_c) = 0. \tag{6.33}$$

Hence, the non-dimensional height $\widetilde{z}_c$ is

$$\widetilde{z}_c = \frac{1}{4 \left(\sqrt{1 - \widetilde{z}_0} - \sqrt{-\widetilde{z}_0} \right)^2} + \widetilde{z}_0. \tag{6.34}$$

We show in figure 6.7 the distribution of the non-dimensional perturbation flux $\partial \widetilde{\varphi}_p / \partial \widetilde{x}(\widetilde{x} = \zeta, \widetilde{z}) = \widetilde{j}(\widetilde{z}) - \zeta \widetilde{\ell}$ along the right-hand side boundary. The analytical formula (6.32), for the flux along the right-hand side boundary, is plotted with a solid curve. We can see the relative importance of the line sink and the line source. The varying line sink $\widetilde{j}(\widetilde{z})$ is stronger than the line source $\zeta \widetilde{\ell}$ and oriented outwards (i.e. in the positive direction) for $\widetilde{z} < \widetilde{z}_c$ (where $\widetilde{z}_c \approx 0.33$, defined in (6.34), is marked with dashed lines). The flux $\partial \widetilde{\varphi}_p / \partial \widetilde{x}(\widetilde{x} = \zeta, \widetilde{z})$ increases steeply approaching the origin, i.e. as $\widetilde{z} \to 0$, as expected near the singularity at $\widetilde{z} = \widetilde{z}_0 < 0$. For $\widetilde{z} > \widetilde{z}_c$, the uniform line source dominates and the local flux is oriented inwards (i.e. in the negative direction). The exchange flow at the right-hand-side boundary is also depicted clearly by the distribution of the streamlines shown in figure 6.5(b).

We compute the potential $\widetilde{\varphi}_p$ (defined in (6.17)), the stream function $\widetilde{\psi}_p$ (defined in (6.28)), and the velocity field $\widetilde{\mathbf{u}}_p = (\widetilde{u}_p, \widetilde{w}_p)$ (defined in (6.29) and (6.30), respectively) numerically and we truncate their infinite series to a finite number of terms n_{max}. In order to test the accuracy of the numerical computation of these truncated series, we compare the numerical computation of the truncated series of the lateral velocity along the right-hand side boundary, designated by $\widetilde{u}_p^{n_{max}}(\widetilde{x} = \zeta, \widetilde{z})$ for the first n_{max} terms of the series (6.29), with the analytical formula (6.32) of the flux imposed at the same boundary, the perturbation flux $\partial \widetilde{\varphi}_p / \partial \widetilde{x}(\widetilde{x} = \zeta, \widetilde{z})$. We measure the mismatch (introduced by the truncation) between the truncated series and the analytical formula by calculating their standard deviation, as a function of the number of terms of the series n_{max}. The standard deviation is
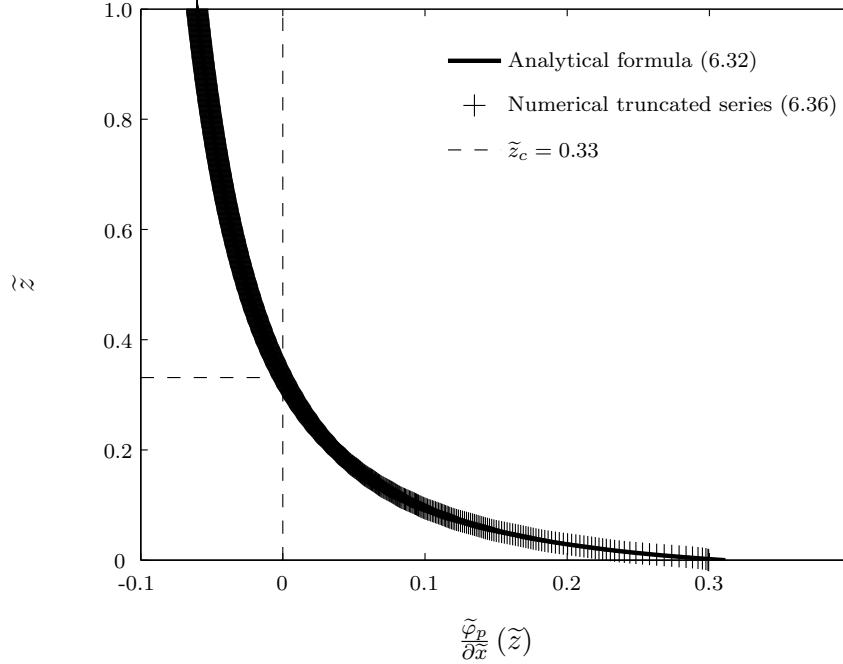
FIGURE 6.7: Distribution of the non-dimensional flux along the right-hand side boundary. The analytical formula of the imposed boundary condition, $\partial\widetilde{\varphi}_p/\partial\widetilde{x}(\widetilde{x} = \zeta, \widetilde{z})$ defined by (6.32), is plotted with a solid curve. We plot the numerical truncated series of the flux $\widetilde{u}_p^{n_{max}}$ (defined in (6.36), with $n_{max} = 100$ the number of terms of the truncated series, and $z_0 = -4.7\,d$ the space virtual origin) with pluses. The location $\widetilde{z}_c$ (defined by (6.34)), where the flux vanishes and changes sign, is marked with dashed lines.

defined, in discrete form, by

$$\sigma_p(n_{max}) = \left(\frac{1}{N_z} \sum_{i=1}^{N_z} \left(\widetilde{u}_p^{n_{max}}(\zeta, \widetilde{z}_i) - \frac{\partial\widetilde{\varphi}_p}{\partial\widetilde{x}}(\zeta, \widetilde{z}_i) \right)^2 \right)^{1/2}, \qquad (6.35)$$

where $\widetilde{z}_i$ are linearly distributed from $\widetilde{z}_1 = 0$ to $\widetilde{z}_{N_z} = 1$, with $N_z = 1001$ the discretization number, and

$$\widetilde{u}_p^{n_{max}}(\zeta, \widetilde{z}_i) = \sum_{n=1}^{n_{max}} B_n \cos\left(n\pi\widetilde{z}_i\right), \quad \text{for all} \quad 1 \leq i \leq N_z, \qquad (6.36)$$

according to (6.29) and (6.19), where the coefficients B_n are described by (6.26) for $n \geq 1$.

We plot in figure 6.8(a) the standard deviation σ_p (defined in (6.35)) against

n_{max}. We can see that σ_p decreases rapidly and monotonically as n_{max} increases. Thus, the numerical truncated series $\widetilde{u}_p^{n_{max}}(\zeta, \widetilde{z}_i)$ converges rapidly towards the analytical formula for $\partial\widetilde{\varphi}_p/\partial\widetilde{x}(\zeta, \widetilde{z}_i)$. We find that for $n_{max} = 100$ the standard deviation is very small, $\sigma_p \leq 0.1\,\%$. As a comparison with the analytical formula (6.32) for the perturbation flux $\partial\widetilde{\varphi}_p/\partial\widetilde{x}(\widetilde{x} = \zeta, \widetilde{z})$, we plot in figure 6.7 the numerical truncated series $\widetilde{u}_p^{n_{max}}(\zeta, \widetilde{z})$ (defined in (6.36), for $n_{max} = 100$) with pluses. As expected, the match is excellent.

To study the smoothness of the (non-truncated) Fourier series $\widetilde{u}_p^{\infty}(\zeta, \widetilde{z})$, we present in a log–log plot in figure 6.8(b) the coefficients of the series B_n (described by (6.26) and shown with pluses), for $1 \leq n \leq 200$. As we can observe, the coefficients B_n appear to fall off like $O(1/n^2)$ (the function $1/n^2$ is plotted with a red line) rather than $O(1/n)$ (the function $1/n$ is plotted with a black line). A decrease of $O(1/n^2)$ means that the Fourier series $\widetilde{u}_p^{\infty}(\zeta, \widetilde{z})$ is continuous while its first derivative (with respect to $\widetilde{z}$) is discontinuous over the interval $0 \leq \widetilde{z} \leq 1$. The Fourier series $\widetilde{u}_p^{\infty}(\zeta, \widetilde{z})$ (defined in (6.36), with $n_{max} = \infty$) converges precisely to the even continuous function $E(\widetilde{z}) = \widetilde{j}(|\widetilde{z}|) - \zeta\widetilde{\ell}$ (except perhaps on a set of measure zero, see e.g. Körner, 1988) defined in the periodic interval $-1 \leq \widetilde{z} \leq 1$, according to (6.20) and (6.21). The function E is continuous over this interval, but its first derivative is discontinuous at $\widetilde{z} = 0 \mod T_p = 2$ (where T_p is the period of the function E) owing to the absolute value, and at $\widetilde{z} = 1 \mod T_p$ by construction of the periodic function E. Since the Fourier series $\widetilde{u}_p^{\infty}(\zeta, \widetilde{z})$ also satisfies Dirichlet's conditions (see e.g. Kahane & Lemarié-Rieusset, 1998), then it converges to the analytical formula (6.32) for the right-hand side boundary condition $\partial\widetilde{\varphi}_p/\partial\widetilde{x}(\widetilde{x} = \zeta, \widetilde{z})$, for all point $0 \leq \widetilde{z} \leq 1$, with a smoothness of order 2.

We believe that the numerical computations of the truncated series for the potential $\widetilde{\varphi}_p$ (defined in (6.17)), the stream function $\widetilde{\psi}_p$ (defined in (6.28)), and the velocity field $\widetilde{\mathbf{u}}_p = (\widetilde{u}_p, \widetilde{w}_p)$ (defined in (6.29) and (6.30), respectively) should all be sufficiently accurate with $n_{max} = 100$.

6.2.5 Solution to the entrainment problem

According to the superposition principle (6.11), we can combine the potential for the uniform solution $\widetilde{\varphi}_u$ (defined by (6.13)) with the potential for the perturbation solution $\widetilde{\varphi}_p$ (defined by (6.17), (6.19) and (6.26)). We find a unique analytical

(a) (b)
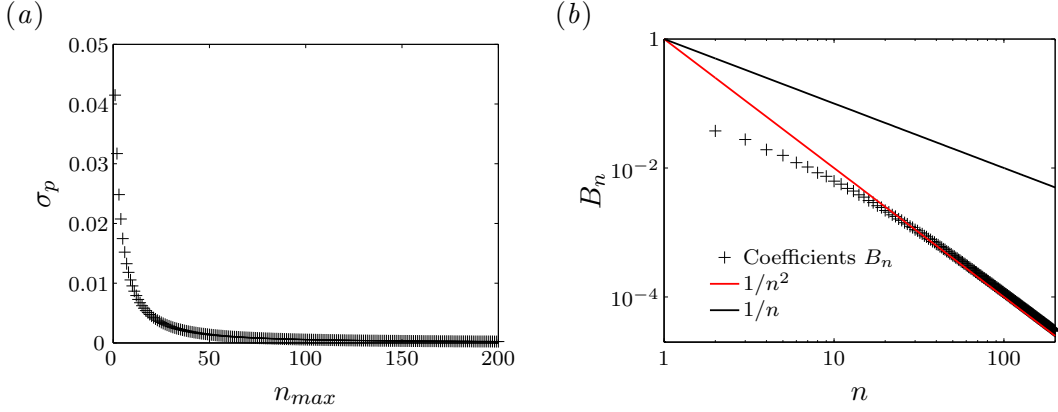
FIGURE 6.8: (a) Standard deviation σ_p (defined in (6.35)) between the truncated series $\widetilde{u}_p^{n_{max}}(\zeta, \widetilde{z})$ (defined in (6.36)) and the analytical formula $\partial \widetilde{\varphi}_p / \partial \widetilde{x}(\zeta, \widetilde{z}_i)$ (defined in (6.32)). (b) Log-log plot of the coefficients B_n (defined in (6.26) and plotted with pluses) of the series $\widetilde{u}_p^{n_{max}}(\zeta, \widetilde{z})$ (defined in (6.36)) versus n. The function $1/n$ is plotted with a black curve and the function $1/n^2$ is plotted with a red curve.

solution, to within a constant, for the potential of the entrainment problem

$$\widetilde{\varphi} = \frac{1}{2}\left(\widetilde{x}^2 - \widetilde{z}^2\right) + \sum_{n=1}^{\infty} A_n \cosh\left(n\pi\widetilde{x}\right)\cos\left(n\pi\widetilde{z}\right) \quad \text{for} \quad 0 \leq \widetilde{x} \leq \zeta, \quad 0 \leq \widetilde{z} \leq 1.$$

(6.37)

where A_n are given by (6.19) and (6.26). Again, applying the superposition principle, the corresponding stream function is

$$\widetilde{\psi} = \widetilde{x}\widetilde{z} + \sum_{n=1}^{\infty} A_n \sinh\left(n\pi\widetilde{x}\right)\sin\left(n\pi\widetilde{z}\right) \quad \text{for} \quad 0 \leq \widetilde{x} \leq \zeta, \quad 0 \leq \widetilde{z} \leq 1, \quad (6.38)$$

where the coefficients A_n are given by (6.19) and (6.26).

We show in figures 6.9(a,b) the non-dimensional potential $\widetilde{\varphi}$ (defined by (6.37), (6.19) and (6.26)) and the non-dimensional stream function $\widetilde{\psi}$ (defined by (6.38), (6.19) and (6.26)) for the entrainment problem described in figure 6.1. We compute the series $\widetilde{\varphi}$ and $\widetilde{\psi}$ numerically for $n_{max} = 100$, the number of terms of both series. Again, we use the jet aspect ratio $\zeta = x_j/h_i = 3/4$ of our particular case, and the space virtual origin $z_0 = -4.7\,d$ (computed from (2.6) using $\alpha = 0.068$, $< \overline{M} > / \left(Q_0^2/d\right) = 0.55$). The streamlines are very similar to those found in the uniform problem in figure 6.3(b). The difference is that they are slightly steeper along the right-hand-side boundary, probably due to the singularity at the virtual origin $\widetilde{z}_0$ of the line sink. In figure 6.9(b), we also plot with red curves the Taylor's

solution for the streamlines $\widetilde{\psi}_T$ (Taylor, 1958)

$$\widetilde{\psi}_T = \left(\sqrt{\widetilde{x}^2 + \widetilde{z}^2} - \widetilde{z}\right)^{1/2} \quad \text{for} \quad 0 \le \widetilde{x} \le \zeta, \quad 0 \le \widetilde{z} \le 1. \qquad (6.39)$$

The stream function $\widetilde{\psi}_T$ corresponds to the two-dimensional incompressible and irrotational flow induced by a plane jet emerging from a plane wall (at $\widetilde{x} = \zeta$) into a semi-infinite domain. As we can observe in figure 6.9(b), the streamlines predicted by Taylor (1958) are qualitatively different from our solution. The stream function $\widetilde{\psi}_T$ produces concave streamlines, whereas our solution $\widetilde{\psi}$ produces convex streamlines. The discrepancy between Taylor's stream function $\widetilde{\psi}_T$ and our stream function $\widetilde{\psi}$ is due to the fact that we consider a fully confined domain, which induces a recirculation flow on either side of the jet, whereas Taylor (1958) considered fully unbounded domains or the case of a jet emerging from a wall into a semi-infinite domain, thus ignoring the possibility of recirculation in the ambient flow. Nevertheless, the streamlines of both stream functions are pointing downwards, i.e. opposite to the jet direction.

The velocity field for the entrainment problem is, for $0 \le \widetilde{x} \le \zeta$, $0 \le \widetilde{z} \le 1$,

$$\widetilde{u} = \widetilde{x} + \sum_{n=1}^{\infty} n\pi A_n \sinh(n\pi\widetilde{x}) \cos(n\pi\widetilde{z}), \qquad (6.40)$$

$$\widetilde{w} = -\widetilde{z} - \sum_{n=1}^{\infty} n\pi A_n \cosh(n\pi\widetilde{x}) \sin(n\pi\widetilde{z}), \qquad (6.41)$$

where the coefficients A_n are given by (6.19) and (6.26).

We show in figures 6.10(a,b) the non-dimensional lateral velocity $\widetilde{u}$ (defined by (6.40), (6.19) and (6.26)) and the non-dimensional streamwise velocity $\widetilde{w}$ (defined by (6.41), (6.19) and (6.26)) for the entrainment problem described in figure 6.1. We compute the series $\widetilde{u}$ and $\widetilde{w}$ numerically for $n_{max} = 100$, the number of terms of both series. We use the aspect ratio $\zeta = x_j/h_i = 3/4$, and the space virtual origin $z_0 = -4.7\,d$ (computed from (2.6) using $\alpha = 0.068$, $< \overline{M} > / \left(Q_0^2/d\right) = 0.55$). As we can see, the velocity field $\widetilde{\mathbf{u}}$ is very similar to the velocity field of the uniform problem $\widetilde{\mathbf{u}}_u$ presented in figure 6.4(a,b). The influence of the varying line sink mainly appears in its vicinity (i.e. along the right-hand-side boundary at $\widetilde{x} = \zeta$). The perturbation of the velocity field is stronger near the source of the jet due to the singularity at the virtual origin ($\widetilde{x} = \zeta, \widetilde{z} = \widetilde{z}_0$).
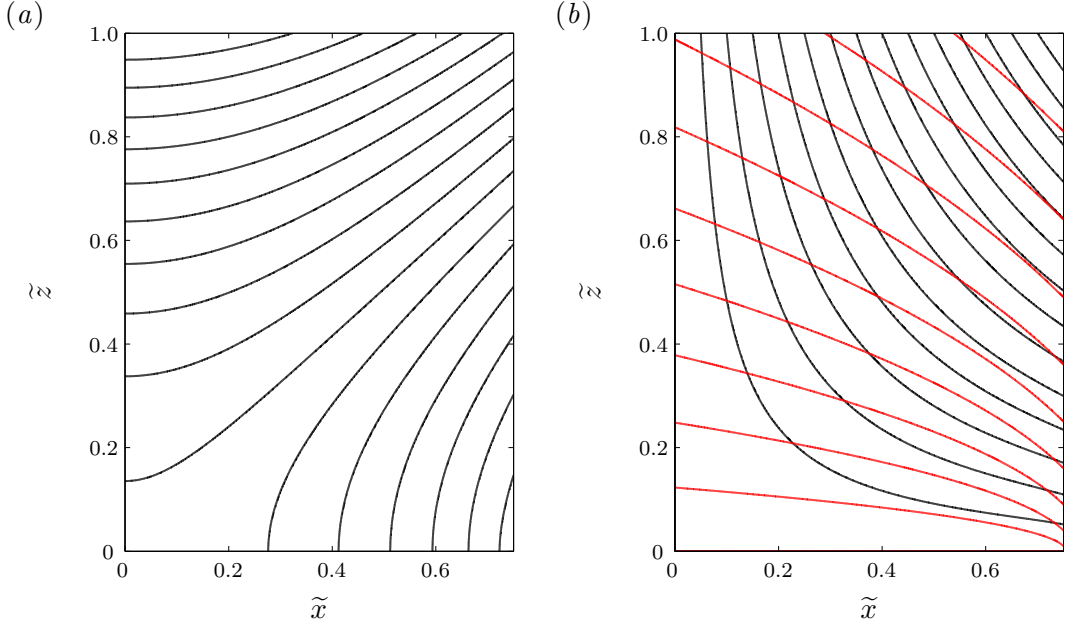
FIGURE 6.9: (*a*) Non-dimensional potential $\widetilde{\varphi}$ (defined by equations (6.37), (6.19) and (6.26) with $n_{max} = 100$ the number of terms of the series, and $z_0 = -4.7\,d$ the space virtual origin), and (*b*) non-dimensional stream function $\widetilde{\psi}$ (defined by (6.38), (6.19) and (6.26) with $n_{max} = 100$, the number of terms of the series, and $z_0 = -4.7\,d$ the space virtual origin) for the entrainment problem described in figure 6.1, using $\zeta = x_j/h_i = 3/4$. We also plot with red curves in (*b*) the Taylor's solution (defined by (6.39)) for the streamlines of a flow induced by a plane jet emerging from a plane wall (at $\widetilde{x} = \zeta$) into a semi-infinite domain (Taylor, 1958).

The aspect ratio ζ and the virtual origin z_0 influence the flow field of the full problem only through the perturbation part of the problem. The aspect ratio ζ and the virtual origin z_0 appear only in the coefficients A_n of the series, in (6.19) and in (6.26) respectively. We find that, qualitatively, increasing the aspect ratio (i.e. stretching the domain $\mathscr{D}_s$ in the x-direction) tends to 'stretch' the streamlines in the lateral direction throughout the domain and decrease the angle (with respect to the x-axis) made by the streamlines at the right-hand side boundary (i.e. the ambient fluid enters the jet more perpendicular to the jet axis). Decreasing the aspect ratio produces the opposite effects. Changing the virtual origin has only a local impact along the right-hand side boundary. An increase in $|z_0|$ (i.e. the virtual origin is further away below the right-hand side bottom corner) diminishes the influence of the singularity on the flow field, decreases the strength of the sink line, and thus decreases the angle (with respect to the x-axis) made by the streamlines at the right-hand side boundary. Decreasing $|z_0|$ (i.e.
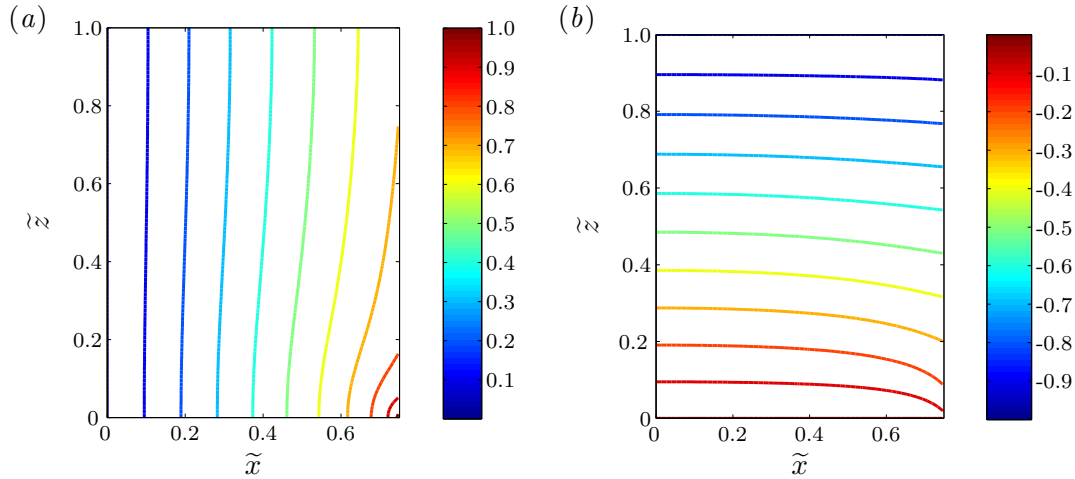
FIGURE 6.10: (*a*) Non-dimensional lateral velocity $\widetilde{u}$ (defined by (6.40), (6.19) and (6.26) with $n_{max} = 100$ the number of terms of the series, and $z_0 = -4.7\,d$ the space virtual origin), and (*b*) non-dimensional streamwise velocity $\widetilde{w}$ (defined by (6.41), (6.19) and (6.26) with $n_{max} = 100$ the number of terms of the series, and $z_0 = -4.7\,d$ the space virtual origin) for the entrainment problem described in figure 6.1, using $\zeta = x_j/h_i = 3/4$.

the virtual origin is closer to the right-hand side bottom corner), has the opposite effect.

Our model, and in particular the assumption of a uniform flux at the top boundary, cannot apply for all ranges of aspect ratios. In the case of a very large aspect ratio, Jirka & Harleman (1979) observed alternating recirculation cells on either side of the jet. Thus, the assumption of a uniform flux at the top boundary seems to be incorrect for approximately $\zeta > 3$, from the measurements of the size of the primary recirculation cells made by Jirka & Harleman (1979). In the case of a small aspect ratio, we believe that the width of the jet (whose boundary expands at a rate of approximately 0.22 from the z-axis) could also affect the flux at the top boundary for $\zeta < 2/3$.

6.3 Experimental results

6.3.1 Experimental procedure

The experimental procedure is almost identical to the experimental procedure described in § 2.2. The main difference concerns the location of the PIV study areas. To investigate the flow induced by the jet, we choose two PIV study areas
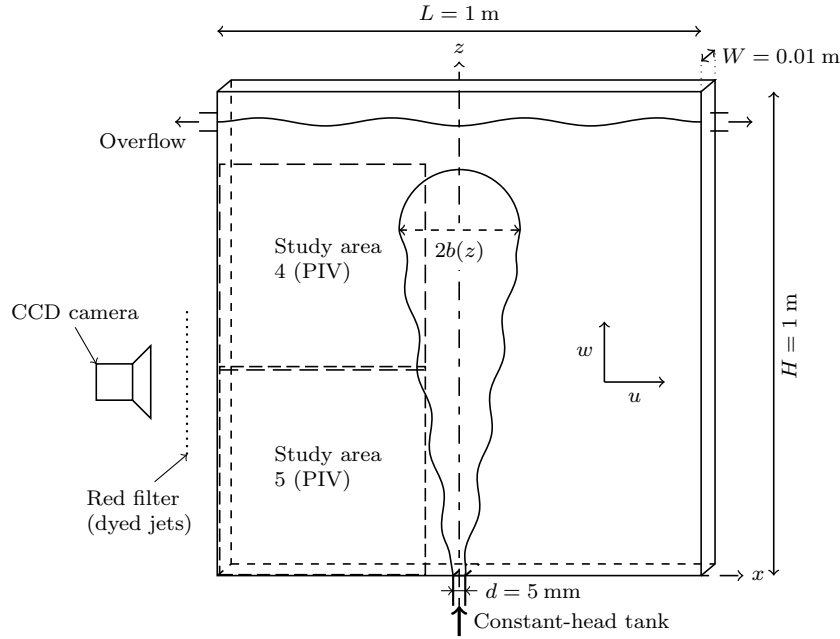
FIGURE 6.11: Schematic diagram of the experimental apparatus. The two PIV study areas are shown with dashed lines along the left-hand-side inner wall.

located on the left-hand-side of the jet axis along the left-hand side inner wall, as shown in figure 6.11. Study area 4 covers a height from $z = 0.425$ to 0.85 m, while study area 5 covers a height from $z = 0$ to 0.425 m. Both study areas cover a width from $x = 0$ to 0.425 m. We analyse three steady turbulent jets in each study area. In study area 4, the jet flow rates are 32.2, 36.8 and 40.3 cm^3 s^{-1} . The corresponding jet Reynolds number (based on the jet source characteristics, such that $Re_j = dw_s/\nu$) are in the range $3220 \leq Re_j \leq 4030$. In study area 5, the jet flow rates are 33.5, 37.5 and 40.3 cm^3 s^{-1} . The corresponding jet Reynolds number are in the range $3350 \leq Re_j \leq 4030$. The frequency of image acquisition is set at 60 frames per second for both study areas. The duration of every experiment is approximately 91 s.

6.3.2 Qualitative observations

In figure 6.12(a), a superposition of 20 images (i.e. a duration of 0.33 s) of the filming of two experiments, where passive tracers (0.23 mm Pliolite VTAC particles) were mixed with a quasi-two-dimensional jet ($Re_j = 4030$), depicts the tracers as streaks. One experiment is filmed in the PIV study area 5 (see figure

6.11) located at $0 \leq x/d \leq 85$, $0 \leq z/d \leq 85$. The other experiment is filmed in the PIV study area 4 (see figure 6.11) located at $0 \leq x/d \leq 85$, $85 \leq z/d \leq 170$. In figure 6.12(a), we can visualize the recirculation of the flow on the left-hand side of the jet. Along the right-hand side border of the picture ($x/d \approx 80$), we can see three characteristic eddies (located at approximately $z/d = 45$, $z/d = 75$ and $z/d = 110$) of the flow in a quasi-two-dimensional jet (the axis of the jet, not visible in the experiment, is plotted with a dot-dashed line at $x = x_j$.). The top eddy ($z/d = 110$) is close to the boundary between the jet region and the impingement region, shown with a red dashed line at $z = h_i = 120\,d$. As it approaches the free surface (not visible in this experiment, but identified with a black dashed line at $z = h_f$), the flow spreads laterally. The flow is eventually redirected downwards along the wall at $x = 0$, before being re-entrained by the jet. The location of the transition height $h_i = 120\,d$, between the jet region and the impingement region, was chosen in § 2.4 because we found that the jet was no longer self-similar beyond this height. In figure 6.12(a), we can see that h_i also corresponds approximately to the location of the last eddy of the quasi-two-dimensional jet. We actually have not seen eddies beyond this height. The size of the eddies approaching the height h_i is around $30\,d$. This size is still small compared with the distance between the left-hand-side wall and the jet axis, $x_j/d = 90$, but the eddy may start becoming affected by the left-hand-side wall. Jirka & Harleman (1979) found a transition height between the jet region and the impingement region at approximately 85 % of the total depth h_f. In our experiment, we find that the ratio between the transition height and the free surface is $h_i/h_f \approx 65$ %. We believe that this discrepancy is due to the lateral confinement, which was insignificant in the experiments of Jirka & Harleman (1979).

In figure 6.12(b), we show a picture of a quasi-two-dimensional turbulent dyed jet ($Re_j \approx 4000$) in the region delimited by $-40 \leq (x - x_j)/d \leq 40$ and $0 \leq z/d \leq 100$. The dye was injected at a constant rate for approximately 3 s in a steady jet, following the experimental procedure detailed in § 2.2.1. We took the picture approximately 4.2 s after the injection of the dye, hence the brighter intensity of the non-dyed fluid in the jet compared with the ambient flow. The dye streaks outside the jet reveal the re-entrainment process of the flow owing to the recirculation in the domain. As Jirka & Harleman (1979) noted, the re-

entrainment process leads to an increase in dye concentration in the jet. The boundary between the jet and the ambient fluid can be identified by the sharp contrast between the light intensity in the induced ambient flow and the light intensity in the turbulent jet flow. We find in figure 2.4 that the location of the average dye edge of quasi-two-dimensional jets is a linear function of height with a slope equal to 0.22 from the z-axis (calculated for $20 \leq z/d \leq 120$), this corresponds to an average angle of approximately 12° from the z-axis. Kotsovinos (1978) also defined the jet boundary as the separation between the turbulent jet flow and the ambient flow field. He too used the sharp contrast between dyed jets and the ambient fluid to determine the boundaries of plane turbulent jets. In figure 2.14, we can observe that the location of the jet boundary is almost at the location $x_0(z)$, where the time-averaged streamwise velocity vanishes and changes sign. It means that, in average, the flow velocity is purely lateral at the jet boundary. Therefore, we choose $x_0(z) \approx 0.22z$ as the location of the jet boundary in this study. We can also see that, at the jet boundary, the streamlines of the induced ambient flow are oriented in the opposite direction to the jet flow, thus producing a counterflow which can affect the momentum flux of the jet (Kotsovinos & Angelidis, 1991).

6.3.3 Quantitative results

In figure 6.13, we compare the streamlines predicted theoretically in equations (6.38), (6.19) and (6.26) (plotted with solid curves) with the streamlines of an ensemble-averaged experimental flow field (plotted with dotted curves). The experimental flow field is the ensemble average of the time-averaged flow fields of the three jets studied (see § 6.3.1). Both the experimental and theoretical streamlines start at the same locations along the top boundary of the PIV study area 5, i.e. at $z/d = 85$. As we can see, the theory and the data agree in the far field away from the jet axis. The streamlines of the experimental data, which point downwards in the ambient fluid, change direction at the boundary of the jet to point upwards.

In figure 6.14(a), we compare the time-averaged lateral velocity predicted theoretically in equations (6.40), (6.19) and (6.26) (plotted with solid curves) with the time-averaged lateral velocity (plotted with dotted curves) of the ensemble-averaged experimental flow field shown in figure 6.13. We show the experimen-

(a)   (b)
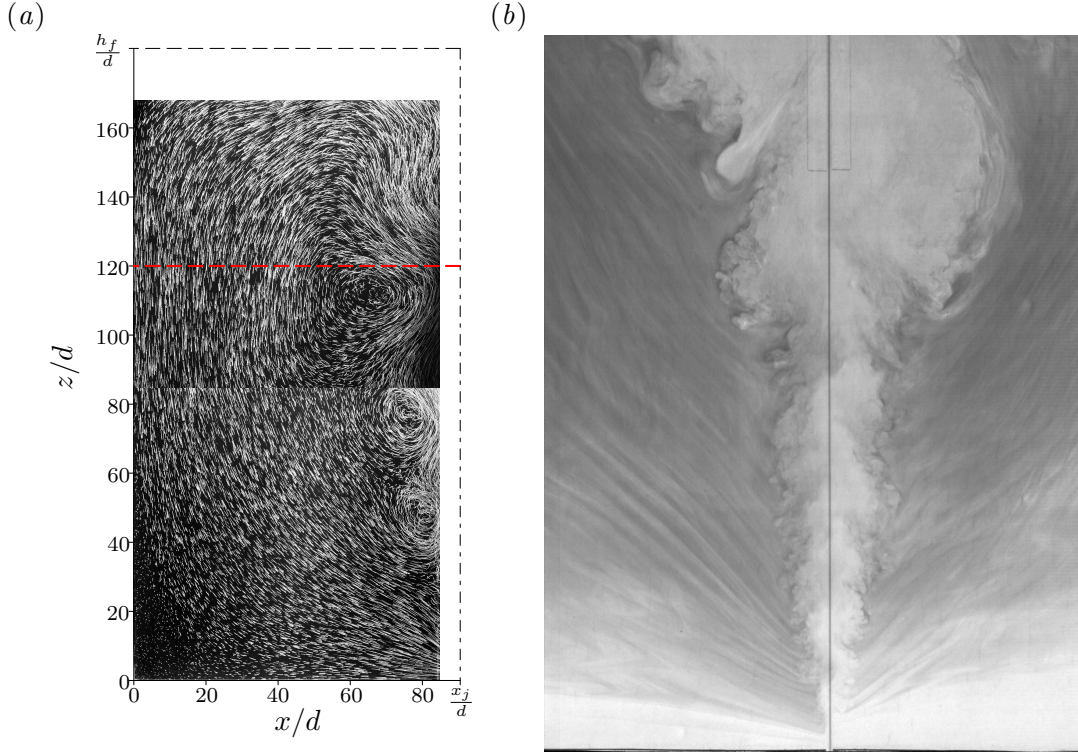
FIGURE 6.12: (a) Passive tracers (Pliolite particles) shown as streaks in a typical jet ($Re_j = 4030$). The axis of the jet is plotted with a dot-dashed line at $x = x_j$. The free surface is plotted with a black dashed line at $z = h_f$. The transition between the jet region and the impingement region is shown with a red dashed line at $z = h_i$. (b) Grey-scale picture of a turbulent quasi-two-dimensional dyed jet ($Re_j \approx 4000$) and the induced flow in the region delimited by $-40 \leq (x - x_j)/d \leq 40$ and $0 \leq z/d \leq 100$.

tal and theoretical lateral distributions of the lateral velocity at four different heights (indicated by dashed lines) in the PIV study area 5 ($0 \leq x/d \leq 85$, $0 \leq z/d \leq 85$). We normalize the time-averaged lateral velocity $\overline{u}$ with the maximum time-averaged streamwise velocity $\overline{w}_{max}$ measured in the domain (at height $z/d \approx 75$, see figure 6.14b). The normalized velocity $\overline{u}/\overline{w}_{max}$ is then scaled so that the maximum amplitude (i.e. $\overline{w}_{max}/\overline{w}_{max} = 1$) matches the z-separation between two heights of measurement (shown with dashed lines in figures 6.14a). Similarly to the streamlines, the theory and the data agree in the far field away from the jet boundary, except for the lowest curve at $z/d = 10$. We believe that the difference at $z/d = 10$ is due to the fact that the jet is very close to the source, and thus the flow of the quasi-two-dimensional jet (as well as its induced flow) is not yet established (see § 2.4).
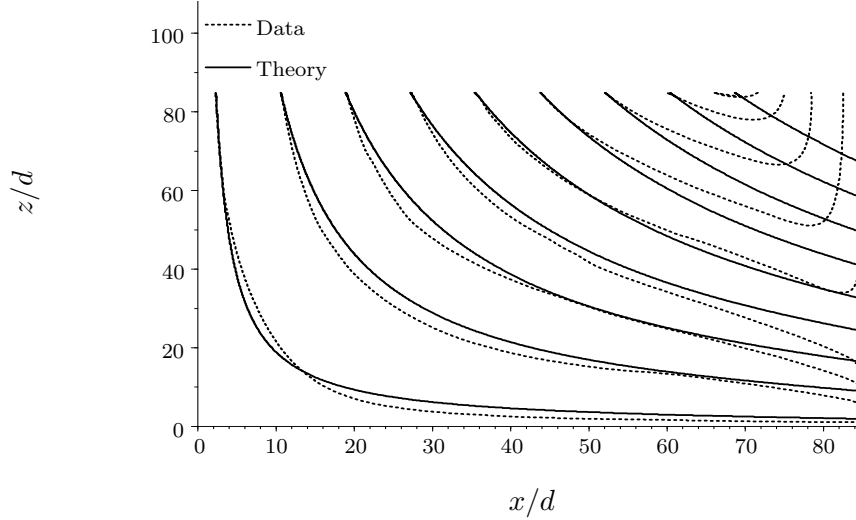
FIGURE 6.13: Experimental (dotted curves) and theoretical (solid curves) distributions of the time-averaged streamlines of the flow induced by quasi-two-dimensional jets in the PIV study area 5, $0 \leq x/d \leq 85$, $0 \leq z/d \leq 85$ (see equations (6.38), (6.19) and (6.26) for the theoretical curve).

In figure 6.14(*b*), we compare the time-averaged streamwise velocity predicted theoretically in equations (6.41), (6.19) and (6.26) (plotted with solid curves) with the time-averaged streamwise velocity (plotted with dotted curves) of the ensemble-averaged experimental flow field shown in figure 6.13. We show the experimental and theoretical lateral distributions of the lateral velocity at four different heights (indicated by dashed lines) in the PIV study area 5 ($0 \leq x/d \leq 85$, $0 \leq z/d \leq 85$). Similarly to the time-averaged lateral velocity, we normalize the time-averaged streamwise velocity $\overline{w}$ with the maximum time-averaged streamwise velocity $\overline{w}_{max}$ measured in the domain (at height $z/d \approx 75$). The normalized velocity $\overline{w}/\overline{w}_{max}$ is then scaled so that the maximum amplitude (i.e. $\overline{w}_{max}/\overline{w}_{max} = 1$) matches the z-separation between two heights of measurement (shown with dashed lines in figures 6.14*b*). The theory seems to agree with the data in the far field away from the jet boundary at least to leading order. However, we can see that the experimental time-averaged streamwise velocity is not exactly uniform across the study area. In particular, the experimental streamwise velocity vanishes along the right-hand-side boundary at $x = 0$, contrary to the theoretical streamwise velocity which assumes a slip-boundary condition.

In figure 6.15(*a*), we plot the non-dimensional time-averaged volume flux $\overline{Q}_r/Q_0$
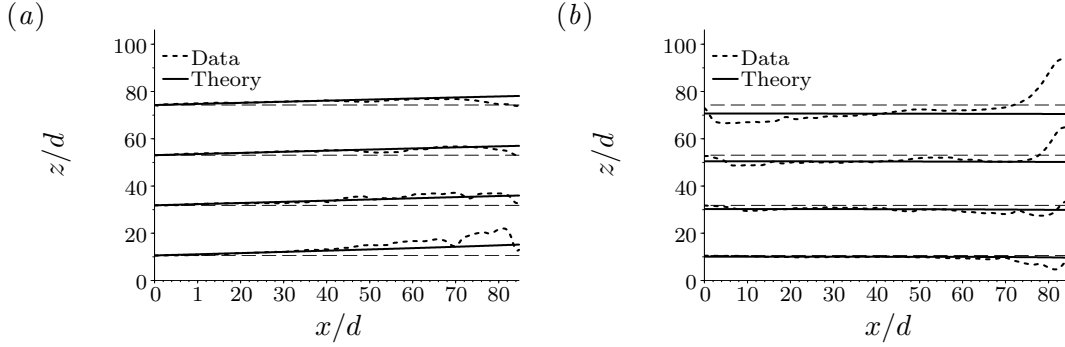
FIGURE 6.14: Experimental (dotted curves) and theoretical (solid curves) lateral distributions of the time-averaged velocity field of the flow induced by quasi-two-dimensional jets in the PIV study area 5 ($0 \leq x/d \leq 85$, $0 \leq z/d \leq 85$) at four different heights (plotted with dashed lines) for: (a) the normalized time-averaged lateral velocity $\overline{u}/\overline{w}_{max}$ (see equations (6.40), (6.19) and (6.26) for the theoretical curve), with $\overline{w}_{max}$ the maximum time-averaged streamwise velocity measured in the domain (at height $z/d \approx 75$, see b); (b) the normalized time-averaged streamwise velocity $\overline{w}/\overline{w}_{max}$ (see equations (6.41), (6.19) and (6.26) for the theoretical curve).

of the return flow (combining the two sides of the jet) versus non-dimensional height z/d. The experimental data, plotted with a dotted curve, are computed from the streamwise velocity of the ensemble-averaged experimental flow field shown in figure 6.14(b), such that

$$\overline{Q}_{r,exp}(z) = -2 \int_0^{x_j - x_0(z)} \overline{w}(x,z) \, \mathrm{d}x, \tag{6.42}$$

where $x_0(z) \approx 0.22z$ defines the location where $\overline{w} = 0$, as discussed in § 6.3.2. The first theoretical prediction, plotted with a solid curve, is computed using the streamwise velocity predicted by potential theory and defined in equations (6.41), (6.19) and (6.26), such that

$$\overline{Q}_{r,pot}(z) = -2 \int_0^{x_j} \overline{w}(x,z) \, \mathrm{d}x. \tag{6.43}$$

Note the difference between the top boundaries of the integral (6.42), where we choose the boundary of the jet, and the integral (6.43), where we choose the jet axis (because the jet is modelled as a line sink). Using equation (6.41), we find that the volume flux $\overline{Q}_{r,pot}$ increases linearly with distance z. However, equation

(6.43) is valid only in the region where the jet is self-similar and the momentum flux of the jet is conserved, i.e. for $z \leq h_i$. The second theoretical prediction, plotted with a dashed curve, is computed using conservation of volume flux at every height. By continuity, the downward volume flux of the return flow on both sides of the jet $\overline{Q}_{r,cont}$ is equal to the upward volume flux of the jet $\overline{Q}$ (defined in (2.4b)) minus the source volume flux Q_0, at every height: $\overline{Q}_{r,cont}(z) = \overline{Q}(z) - Q_0$. We find

$$\overline{Q}_{r,cont}(z) = Q_0 \left(4\sqrt{2}\alpha \frac{M_0 z}{Q_0{}^2} + 1 \right)^{1/2} - Q_0. \tag{6.44}$$

The volume flux $\overline{Q}_{r,cont}$ increases like $z^{1/2}$ with distance. However, similarly to $\overline{Q}_{r,pot}$, $\overline{Q}_{r,cont}$ can only model the return flow for $z \leq h_i$. The theoretical predictions $\overline{Q}_{r,pot}$ and $\overline{Q}_{r,cont}$ have different growth rates because of the difference in the boundary conditions. $\overline{Q}_{r,pot}$ is computed with fixed boundary conditions (the jet is modelled as a line sink located at $x = x_j$), whereas the boundary conditions for $\overline{Q}_{r,cont}$ change linearly with distance (the jet boundary is a function of height, $x_0(z) \propto z$).

We can see in figure 6.15(a) that the experimental return-flow volume flux is increasing between the two theoretical curves. The first prediction (6.43), based on potential theory, underestimates the volume flux, whereas the second prediction (6.44), based on continuity, overestimates the volume flux. We can also note that the volume flux of the return flow becomes rapidly larger than the initial volume flux, $\overline{Q}_r/Q_0 \approx 3$ at mid-height in the tank $z = h_f/2$. Therefore, the volume flux of the return flow is of the order of magnitude of the jet volume flux away from the source, i.e. $\overline{Q}_r \approx \overline{Q}$ for $z \geq h_f/2$. As predicted, $\overline{Q}_{r,pot}$ increases linearly while $\overline{Q}_{r,cont}$ increases like $z^{1/2}$ with distance. We believe that the assumption we make to model the jet as a fixed line sink is valid only if the distance between the jet axis and the lateral wall (at $x = 0$) is large. The trend of the experimental data $\overline{Q}_{r,exp}$ is not accurate enough in figure 6.15(a) to distinguish a linear growth rate, as predicted by $\overline{Q}_{r,pot}$, or a growth rate of $z^{1/2}$, as predicted by $\overline{Q}_{r,cont}$.

Similarly to the volume flux, we plot in figure 6.15(b) the non-dimensional time-averaged momentum flux $\overline{M}_r / \left(Q_0{}^2/d \right)$ of the return flow (combining the two sides of the jet) versus non-dimensional height z/d. The experimental data, plotted with a dotted curve, are computed from the time-averaged streamwise

velocity of the ensemble-averaged experimental flow field shown in figure 6.14(b), such that

$$\overline{M}_{r,exp}(z) = 2 \int_0^{x_j - x_0(z)} (\overline{w})^2 (x, z) \, \mathrm{d}x. \tag{6.45}$$

The first theoretical prediction, plotted with a solid curve, is computed using the streamwise velocity predicted by potential theory and defined in equations (6.41), (6.19) and (6.26), such that

$$\overline{M}_{r,pot}(z) = 2 \int_0^{x_j} (\overline{w})^2 (x, z) \, \mathrm{d}x. \tag{6.46}$$

Using equation (6.41), we find that the momentum flux $\overline{M}_{r,pot}$ increases like z^2 with distance. However, as we mentioned for the volume flux, equation (6.47) is valid only in the region where the jet is self-similar and the momentum flux of the jet is conserved, i.e. for $z \leq h_i$. The second theoretical prediction, plotted with a dashed curve, is computed using the volume flux $\overline{Q}_{r,cont}$ defined in (6.44) and assuming a uniform velocity outside the jet (with slip boundary condition at the walls). We find

$$\overline{M}_{r,cont}(z) = \frac{\left(\overline{Q}_{r,cont}\right)^2 (z)}{2 \left(x_j - x_0(z)\right)}. \tag{6.47}$$

The momentum flux $\overline{M}_{r,cont}$ increases like z^2 with distance for $x_0(z)/x_j \ll 1$. But, unlike $\overline{M}_{r,pot}$, we find that in the limit $x_0(z)/x_j \to 1$, $\overline{M}_{r,cont}$ increases like $1/(1 - x_0(z)/x_j)$ with distance z. Nevertheless, and similarly to $\overline{M}_{r,pot}$, $\overline{M}_{r,cont}$ can only model the return flow for $z \leq h_i$, so that $x_0(z)/x_j < 1$ and $\overline{M}_{r,cont}$ only increases like z^2. This discrepancy between the asymptotic behaviours of the two theoretical predictions $\overline{M}_{r,pot}$ and $\overline{M}_{r,cont}$ is, again, due to the difference between the boundary conditions.

Similarly to the volume flux, we can see in figure 6.15(b) that the experimental return-flow momentum flux is increasing between the two theoretical curves. The first prediction (6.46), based on potential theory, underestimates the momentum flux, whereas the second prediction (6.47), based on continuity, overestimates the momentum flux. As predicted, we can observe that both $\overline{M}_{r,pot}$ and $\overline{M}_{r,cont}$ increases like z^2, which seems to be also the case for the experimental momentum flux $\overline{M}_{r,exp}$. From consideration of figure 2.6, we find that the time-averaged momentum flux of the jet is approximately constant with height at an average

(a)

(b)
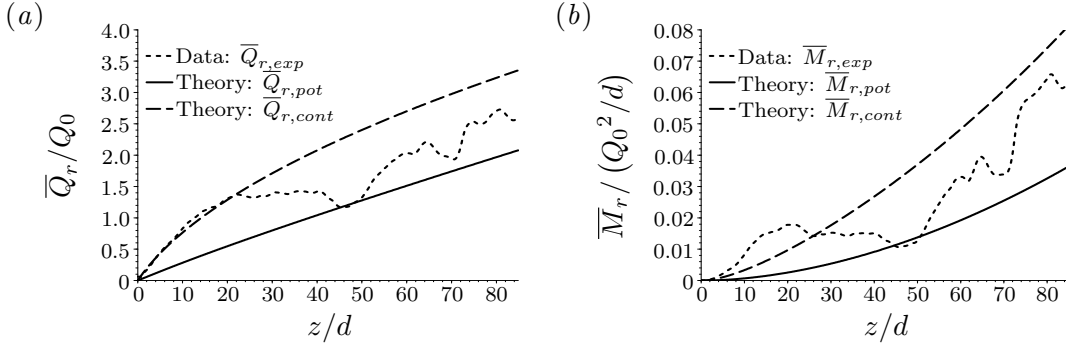
FIGURE 6.15: Experimental and theoretical distributions against non-dimensional height z/d of: (a) the experimental normalized time-averaged volume flux $\overline{Q}_{r,exp}/Q_0$ (dotted curve) computed using (6.42), the theoretical prediction based on potential theory $\overline{Q}_{r,pot}/Q_0$ (solid curve) and computed using (6.43), the theoretical prediction based on continuity $\overline{Q}_{r,pot}/Q_0$ (dashed curve) and computed using (6.44); (b) the experimental normalized time-averaged momentum flux $\overline{M}_{r,exp}/\left(Q_0{}^2/d\right)$ (dotted curve) computed using (6.45), the theoretical prediction based on potential theory $\overline{M}_{r,pot}/\left(Q_0{}^2/d\right)$ (solid curve) and computed using (6.46), the theoretical prediction based on continuity $\overline{M}_{r,cont}/\left(Q_0{}^2/d\right)$ (dashed curve) and computed using (6.47).

value of $< \overline{M} > /\left(Q_0{}^2/d\right) = 0.55$. The non-dimensional momentum flux of the return flow increases from $\overline{M}_r/\left(Q_0{}^2/d\right) = 0$ at $z/d = 0$ to approximately 0.06 at $z/d = 80$. Therefore, in our domain, the momentum flux of the return flow is rather insignificant compared with the jet momentum flux. This finding is completely different from the results for the volume flux of the return flow, which is not insignificant because it has to balance the volume flux of the flow. This crucial difference, which enables us to neglect the influence of the momentum flux of the return flow on the jet flow, is related to the distance between the jet and the lateral boundaries (i.e. to the lateral confinement of the jet) and justifies the assumptions we make in Chapter 2 that the return flow has a weak effect on the dynamics of the evolving jet.

6.4 Conclusion

In this chapter, we study the flow induced by a steady quasi-two-dimensional turbulent jet in a confined rectangular domain. Using two-dimensional potential theory, we determine the induced flow in a representative domain $\mathscr{D}_s$ of aspect

ratio $\zeta = x_j/h_i = 3/4$ (corresponding to our particular case) between the streamwise dimension and the cross-stream dimension. The domain is delimited by the jet axis at the right-hand-side boundary (at $x = x_j$), the walls of the experimental apparatus at the left-hand-side and bottom boundaries and the transition height h_i between the jet flow region and the impingement region, at the top boundary. The jet is modelled as a line sink (located on the jet axis) with a lateral flux per unit length varying with height in a similar way to the entrainment velocity due to a quasi-two-dimensional jet. The transition height h_i is modelled as a uniform line source, whose total inwards flux matches the total outwards flux of the line sink.

To solve Laplace's equation in the domain $\mathscr{D}_s$, we decompose the problem into a uniform problem with a uniform line source and a uniform line sink, and a perturbation problem accounting for the varying line sink condition at the jet boundary. We find an analytical solution for the potential field, the stream function and the velocity field in the domain $\mathscr{D}_s$. It appears that in the far field, away from the jet, the results are dominated by the uniform problem with uniform boundary conditions. The influence of the varying line sink (i.e. the entrainment process of the jet) is strong near the source of the jet, because of the singularity at the virtual origin of the jet (located outside the domain below the bottom boundary).

We observe qualitative discrepancies between our analytical solution for the streamlines of the induced flow compared with the solutions of Taylor (1958) or Schneider (1981). The second derivative of the streamlines with respect to the lateral or cross-jet coordinate (x) have a different sign. Our streamlines are convex, whereas the streamlines of Taylor (1958) or Schneider (1981) are concave. This difference is due to the fact that we consider a fully confined domain, which induces a recirculation flow on either side of the jet, whereas Taylor (1958) or Schneider (1981) considered fully unbounded domains or the case of a jet emerging from a wall into a semi-infinite domain, thus ignoring the possibility of recirculation in the ambient flow.

We compare our theoretical flow field with experimental data from quasi-two-dimensional turbulent jets in a confined experimental apparatus of aspect ratio 1 (the ratio between the inner dimensions of the tank). The theoretical streamlines agree with the data in the far-field, away from the boundary of the jet. We find

that the boundary of the jet, defined as the boundary between the turbulent jet flow and the ambient flow (Kotsovinos, 1978), also corresponds to the location $x_0(z) \approx 0.22z$ where the flow is, in average, purely lateral because the time-averaged streamwise velocity vanishes and changes sign at $x_0(z)$. In our model, we assume that the jet boundary coincides exactly with the jet axis, instead of being at an angle of approximately $12°$. We find that this assumption is valid in the far-field away from the jet boundary and for $z \leq h_i$.

We find that, to the leading order, the experimental velocity field agrees with the model. Differences are seen near the rigid boundaries, where the experimental time-averaged tangential velocity vanishes at the walls, contrary to the theoretical tangential velocity which is assumed to satisfy a slip boundary condition. Also, near the jet source, the experimental data differ from the model because the flow of the jet is not yet fully established. Finally, the experimental measurements for the volume flux and the momentum flux of the return flow agree to leading order with the model based on potential theory and a model based on volume conservation. In particular, we find that the time-averaged momentum flux of the return flow increases like z^2 to approximately $10\,\%$ of the jet momentum flux at mid-height in the experimental apparatus.

We believe that a jet emerging from a wall into a fully confined domain is a more realistic case than the case of a jet in an unbounded or semi-infinite domain. The streamlines of the induced flow are strongly modified by the recirculation cells observed on either side of the jet. This phenomenon is important in mixing problems because the re-entrainment process tends to increase the concentration in the jet of passive tracers injected in the fluid. The momentum flux of the jet can also become negatively affected by the counter-flow after a certain distance. The core and eddy structures also become affected by the confinement at a distance h_i approximately equal to $65\,\%$ of the depth of the flow, for an experimental apparatus of aspect ratio 1 (i.e. the ratio between the inner dimensions of the tank) or a jet aspect ratio $\zeta = x_j/h_i = 3/4$ (i.e. the ratio of the distance between the jet and the lateral boundary to the transition height of the impingement region). We believe that our model, and in particular the assumption of a uniform flux at the top boundary and the assumption of a jet boundary parallel to the z-axis on the right-hand side of the domain, is valid for a range of jet aspect ratios $2/3 < \zeta = x_j/h_i < 3$. At higher aspect ratios, secondary recirculation cells could

form on either side of the jet (Jirka & Harleman, 1979), thus affecting the flux at the top boundary. On the other hand, at lower aspect ratios, the expansion of the jet boundary becomes significant compared with the size of the domain, and thus can influence the flux at the top boundary.

DYNAMICS OF PARTICLE-LADEN JETS IN QUASI-TWO-DIMENSIONAL ENVIRONMENTS

7.1 Introduction

Two-phase flows involving mixtures of solid particles and liquids are common in industrial applications. One example can be found in the coking process of the residue, or heavy-tar, from the refinement of crude oil, which serves to produce graphite electrodes for smelting applications (see e.g. Lee *et al.*, 1997). During the coking, chemical reactions normally provoke a gradual phase transition of the heavy-tar into solid sponge coke; however, this process can also occasionally lead to the formation of a less valuable product called shot coke (Eser *et al.*, 1986). Eser *et al.* (1986) reproduced the chemical reactions that can cause the production of shot coke, but much less is known about the dynamics of the flow and its mixing properties, when the heavy-tar is injected into the reactor. Another important

industrial application of particle-laden jets is for fluidized beds, which are used in chemical reactors or in the transport of granular material (see e.g. Zoueshtiagh & Merlen, 2007). The study of particle-laden jets is also relevant to geophysical applications such as volcanic eruptions (see e.g. Sparks, 1986; Ernst *et al.*, 1996; Veitch & Woods, 2000; Walters *et al.*, 2006), and the transport and resuspension of sediments by jets (see e.g. Neves & Fernando, 1995; Colomer & Fernando, 1996; Colomer, Casamitjana & Fernando, 1998; Cardoso & Zarrebini, 2002; Jiang, Law & Cheng, 2005).

We have conducted different experiments in which a vertical water jet is discharged below a flat bed of particles immersed in water. Similarly to the experiments described in § 2.2 and § 4.1, these experiments are performed in a quasi-two-dimensional environment. The jet and the bed are constrained between two close walls in the spanwise (*y*-) direction. Typically, the dimension of the gap is two orders of magnitude smaller than the other dimensions. This particular geometry allows us to visualize and study the evolution of the system inside the bed of particles. Rich dynamical behaviours, characteristically different from the three-dimensional case, appear in two dimensions. For instance, the quasi-two-dimensional particle-laden jet (Q2DPL jet) presents an unreported instability occurring at intermediate flow rates.

The objective is to understand and analyze the succession of regimes shown by the evolution of the system while the jet flow rate is changed. We are interested in the interaction between the jet and the bed of particles. The entrainment and recirculation of the particles in the jet reveal an interesting coupling with the geometry of the eroded bed. The maximum height reached by the particles is a key parameter to understand the dynamics of the whole system. As a model of the Q2DPL jet, we draw a comparison with the non-buoyant quasi-two-dimensional momentum jet studied in the previous chapters. We discuss the assumptions and conditions under which the model holds on the basis of experimental and theoretical results. Future work will be to compare Q2DPL jets with heavy fountains in a quasi-two-dimensional environment, in order to model the regimes where the density difference between the Q2DPL jet and the ambient fluid is important.

The rest of this chapter is organized as follows. In § 7.2, we describe the experimental procedure. In § 7.3, we describe the different phenomenological regimes observed in the experiment, as the jet flow rate increases. In § 7.4, we

discuss a model to predict the maximum height reached by the particles in the final dilute regime, based on the model for the time-averaged mean momentum jet (presented in § 2.4). We draw our conclusions in § 7.5 and suggest new avenues of research.

7.2 Experimental procedure

The 0.5 m $(L) \times 0.01$ m $(W) \times 0.5$ m (H) quasi-two-dimensional experimental apparatus is presented in figure 7.1.[1] The (heavy) particles we use are 0.5 mm glass beads (density: $\rho_p = 2.5$ g cm^{-3}). The initial thickness of the bed ranges from $h_0 = 1.75$ to 8 cm. At the beginning of an experiment, we lay the bed flat at the bottom of the tank, which is filled with water. The water jet, injected through a circular nozzle of diameter $d = 6$ mm located at the middle of the bottom of the tank, has a source flow rate ranging from $Q_0 = 0$ to 33 cm^3 s^{-1} . We generate the flow either by gravity or using a peristaltic pump (the pulsing of the pump had no influence on the system for $Q_0 > 4$ cm^3 s^{-1}). We increase the flow rate in a stepwise manner, with typical step 1 cm^3 s^{-1} . After each increase in the flow rate, we allow the system to reach steady state (characterized by a fixed shape of the bed and by an approximately constant amount of particles in circulation in the jet, i.e. particles no longer sediment in the far field). This typically takes 5 to 30 minutes. At steady state, we take (with a ruler) some characteristic geometric measurements of the shape of the bed: the size of the cone formed by the erosion of the bed, the thickness of the bed above the nozzle (h_{source}) and the angle of the slopes of the cone (with accuracy of approximately ± 5 mm for the lengths and $\pm 5°$ for the angle). Moreover, we measure the maximum height reached by the particles in the jet h_{max} (accuracy of ± 5 to ± 20 mm) and the oscillation frequency of the Q2DPL jet (accuracy of ± 15 %).

---

[1]Note that the length L and the height H of the experimental apparatus used in this chapter are half the length and half the height of the experimental apparatus used in Chapters 2 to 6.
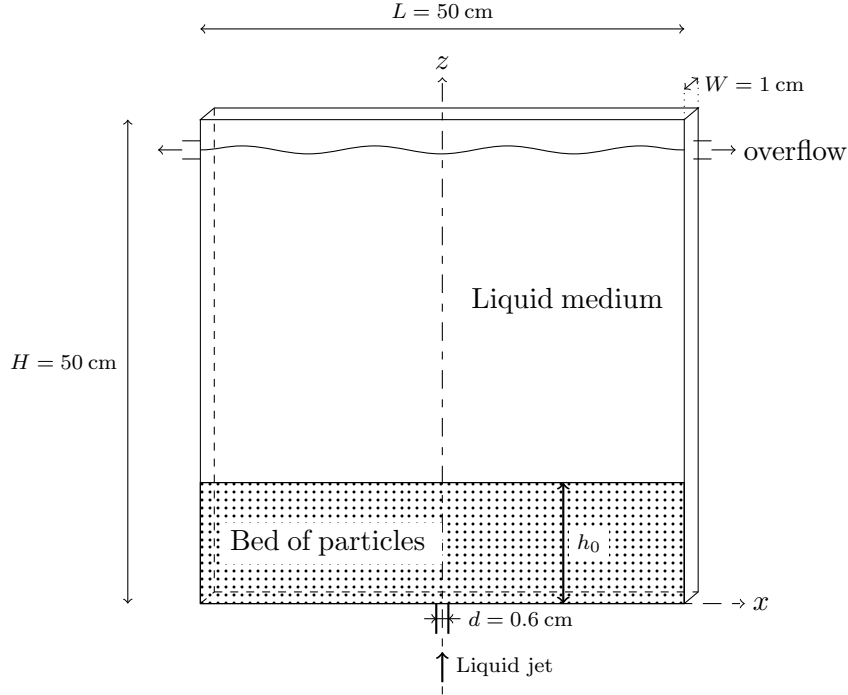
FIGURE 7.1: Sketch of the experimental apparatus. The evolution of the system is analyzed when a water jet of variable flow rate is injected at the bottom of the bed of particles (0.5 mm glass beads).

7.3 Phenomenological description

7.3.1 Regime diagram

In figure 7.2, we present a schematic diagram of the successive regimes displayed by the system (bed of particles and jet) as the jet flow rate Q_0 increases, and for various initial bed thicknesses h_0.

We start with $Q_0 = 0$ and a flat bed of particles. At very low flow rates, the bed remains motionless because the pressure of the flow is insignificant compared with the weight of the bed of particles per unit area. In this pre-regime (not represented in figure 7.2), we have a porous medium flow, which can be modelled using Darcy's law (Zoueshtiagh & Merlen, 2007)

$$W = -\frac{\kappa}{\mu}\nabla P, \tag{7.1}$$

where W is the superficial velocity, κ is the permeability of the bed, μ is the dynamic viscosity of the liquid and P the pressure. From this model, Zoueshtiagh
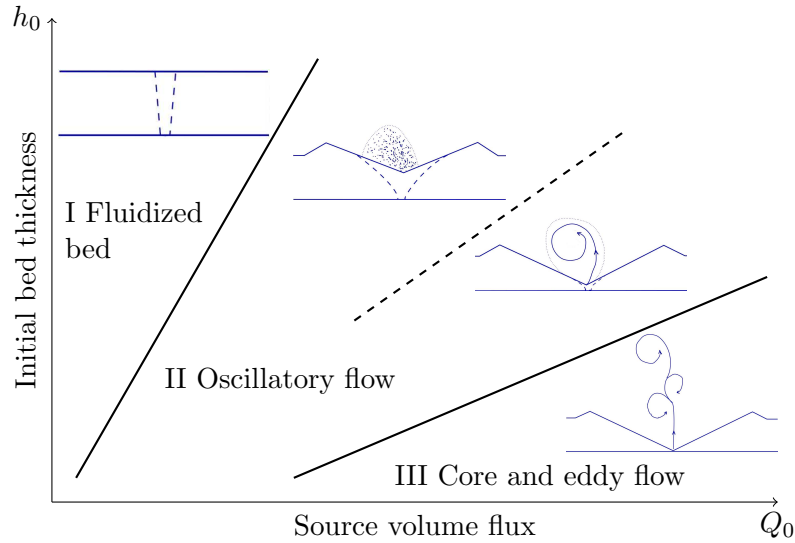
FIGURE 7.2: Schematic diagram showing the boundaries between the three different phenomenological regimes observed as the source flow rate is increased from $Q_0 = 0$ to $33 \, \text{cm}^3 \, \text{s}^{-1}$.

& Merlen (2007) deduced the flow velocity at the surface of the bed. Their experimental measurements of the flow velocity at the bed surface agreed with the theoretical prediction as long as the configuration could be considered as a point source in an infinite domain (i.e. $d/h_0 \leq 0.2$).

As we increase the source flow rate (for a given bed thickness), the system displays very different regimes, which we describe in detail below. At low flow rates, we observe a fluidization regime after the Darcy flow regime (see regime I in figure 7.2). Then, the jet starts eroding the bed if we increase Q_0 further. In this "oscillatory flow" regime (see regime II in figure 7.2), the Q2DPL jet is unstable and oscillates in the eroded bed with respect to the vertical axis. Finally, at large Q_0 the bed is fully eroded and the jet can lift particles higher in the water above the bed. The motion of the particles in the jet flow shows the same core and eddy structures as we observe in particle-free quasi-two-dimensional jets. So, in reference to the flow in particle-free quasi-two-dimensional jets, we name this regime the "core and eddy flow" regime (see regime III in figure 7.2).

7.3.2 Regime I: fluidized bed

At low flow rates, the jet fluidizes the bed, which maintains a flat surface (see figure 7.3). We observe a strong recirculation of the particles inside a chimney, or narrow cone, located above the nozzle (see the dashed blue lines in regime I, fluidized bed, in figure 7.2). In fluidization models, the basic hypothesis states that the pressure gradient of the flow inside the chimney is balanced by the weight of the particles in the chimney (see e.g. Zoueshtiagh & Merlen, 2007), i.e.

$$\Delta p = \phi_b \Delta \rho g h_0, \tag{7.2}$$

where $\Delta p = (p(0) - p(h_0))$ is the pressure difference between the bottom of the bed (at $z = 0$) and the top surface of the bed (at $z = h_0$), ϕ_b is the volume fraction of the bed,[2] $\Delta \rho = \rho_p - \rho$ is the difference between the density of the particles and the density of the liquid, and g is the constant of gravity. In the rest of the bed, the flow follows Darcy's law (described in (7.1)). Therefore, the total flow rate at the nozzle exit is equal to the sum of the flow rate in the fluidized chimney and the flow rate in the unfluidized part of the bed.

Zoueshtiagh & Merlen (2007) conducted a similar experiment in three dimensions. It is interesting to note that our observations about the fluidization of the bed in the quasi-two-dimensional case agree qualitatively with their report. They also proposed a model for the fluidization process and the formation of the chimney. However, they could not obtain any experimental evidence to validate or invalidate the model because their experimental apparatus did not allow them to visualize and measure the interior of the bed where the fluidization process occurred. We believe that our quasi-two-dimensional experiment, which gives a clear picture of the dynamics inside the bed, could provide quantitative data to verify the fluidization model of Zoueshtiagh & Merlen (2007).

7.3.3 Regime II: oscillatory flow

As we increase the flow rate, the opening angle of the cone increases by an erosion process, as depicted in figure 7.4. At an intermediate range of flow rates the

---

[2]Ojha, Menon & Durian (2000) determined experimentally the volume fraction of a slowly defluidized bed of particles. They found that the volume fraction ϕ_b is independent of the size or shape of the particles and is approximately equal to $\phi_b = 0.59$.
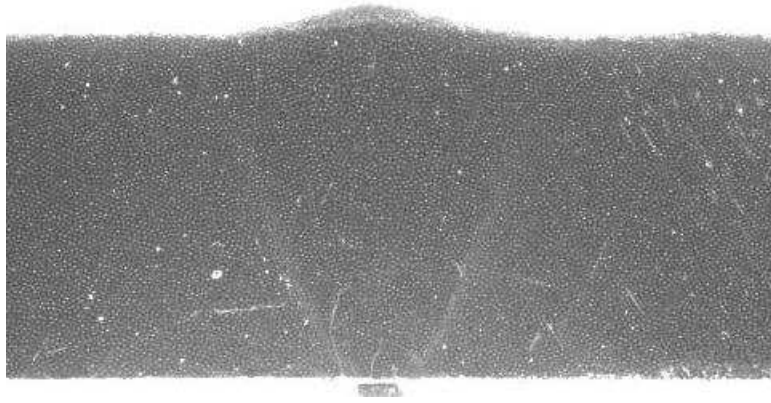
FIGURE 7.3: Illustration of regime I, $Q_0 = 2.5\,\mathrm{cm}^3\,\mathrm{s}^{-1}$ and the initial height $h_0 = 4\,\mathrm{cm}$. At very low flow rates the jet coming through the bed at the bottom center of the picture fluidizes the particles above it. The surface of the bed remains almost flat (only a small hump is observed), showing almost no activity.

Q2DPL jet builds a mound of particles on each side of the cone. For every increase in the flow rate, the mounds grow and move away from the cone until they reach a steady state (i.e. a fixed position). In addition, we can observe a surprising behaviour in this regime: the Q2DPL jet does not maintain a vertical axis, but oscillates in the (x, z) plane about the z-axis (the origin of the domain $(0, 0, 0)$ is at the centre of the nozzle). As we can see in figure 7.5, a large vortical structure develops alternately on each side of the z-axis at each semi-oscillation. As an explanation of this oscillating phenomenon, we believe that the Q2DPL jet becomes unstable as it emerges out of the bed and is no longer bounded by the steep walls of the cone. An oscillation can start when some disturbance breaks the symmetry of the sedimentation process. This leads to an asymmetry of the avalanching process occurring on the slopes of the cone. The stronger avalanche deflects the jet to the opposite side of the cone. This has the effect of reversing the asymmetric avalanching process, which can then deflect the jet back to the initial side of the oscillation, thus completing a whole cycle. The oscillation of the jet is sustained by the kinetic energy of the jet. The oscillation frequency of the jet appears to be steady for a given source flow rate and to decrease with increasing source flow rate.
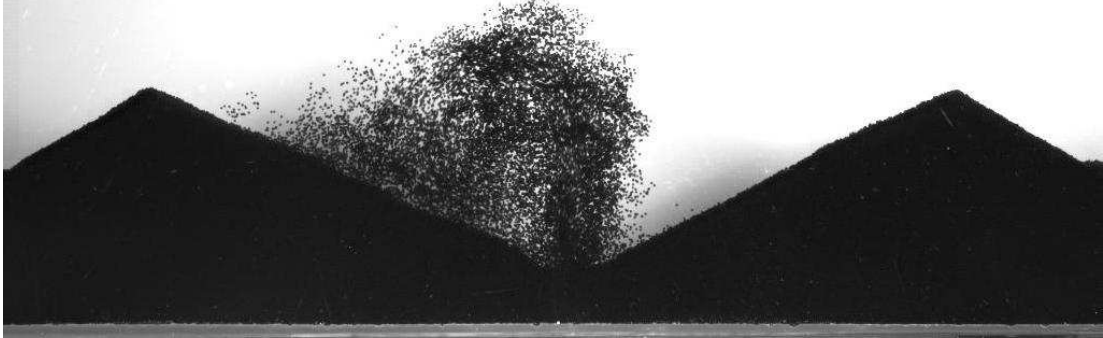
FIGURE 7.4: Illustration of regime II, the jet flow rate is $Q_0 = 15 \ \mathrm{cm^3\,s^{-1}}$ and the frequency of image acquisition is 500 frames per second. At medium-high flow rates, a mound of particles forms on each side of the cone. The opening angle of the cone increases rapidly with the flow rate. The jet oscillates from side to side in the crater. A steady state is reached when the jet cannot eject any particles above the mounds.
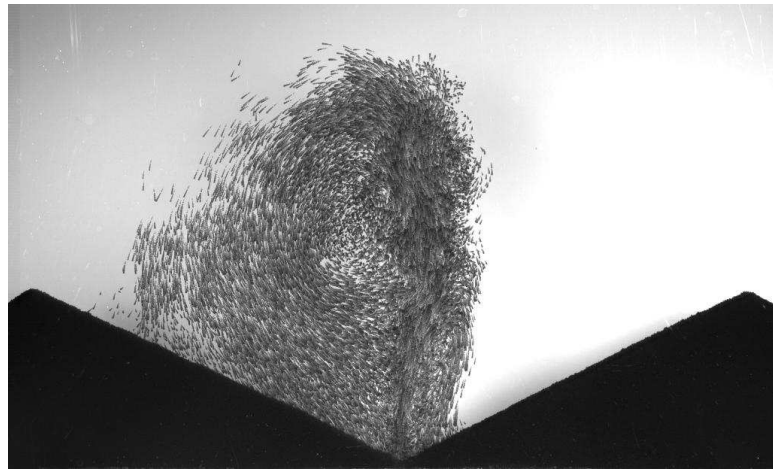
FIGURE 7.5: Illustration of the vortical structure in regime II, $Q_0 = 18.5 \ \mathrm{cm^3\,s^{-1}}$ and $h_0 = 4 \ \mathrm{cm}$. The Q2DPL jet displays a large vortex as it oscillates alternately on each side of the z-axis (several images are superimposed on this picture to show particles as streaks).

7.3.4 Regime III: core and eddy flow

As we can see in figure 7.6(a), the final regime of the system is characterized by a fixed final shape of the bed. The bed forms a crater, whose slopes are at the angle of repose (approximately 26° for our particles). Moreover, it is flanked by two pyramidal mounds, whose added volumes (computed above the initial height of the bed, i.e. for $z > h_0$) account for the volume of the crater. In this regime, the jet still entrains some particles, but the volume fraction is much lower. Unlike in regime II, the flow in the jet does not seem to be very strongly affected by the particles in this regime. We observe a sharp decrease in the frequency and amplitude of the oscillations of the Q2DPL jet, and also an increase in the rate of change of the particle maximum height h_{max} (plotted with triangles in figure 7.7) with the source flow rate Q_0.

The trajectory of the particles in the jet flow (shown as streaks in figure 7.6a, where the velocity is large) reveals three large eddies (identified with yellow circular arrows) and a high speed core (identified with a yellow arrowed curve). The resemblance to the core and eddy structures in a quasi-two-dimensional turbulent jet (depicted with yellow circular arrows and a yellow arrowed curve, respectively, in the picture of a dyed quasi-two-dimensional jet in figure 7.6b) is strong. From our qualitative observations, we can report that the size of the eddies in the Q2DPL jet also grows with distance z. Therefore, it appears that in the case of a dilute concentration of particles, the momentum of the jet is not strongly affected by the negative bulk density of the two-phase flow.

7.4 Core and eddy flow model

The experiment described above reveals the complexity of the interaction between the jet and the bed of particles. In this section, we are interested in the final regime, or core and eddy flow regime, which has strong similarities with the flow in a quasi-two-dimensional jet, described in the previous chapters. Assuming that the density of the particles does not affect the flow of the jet we propose a model for the maximum height reached by the particles transported by the jet.

From the study of non-buoyant quasi-two-dimensional momentum jets presented in Chapter 2, we know the velocity field of a quasi-two-dimensional jet in our apparatus. If we assume that, in the final regime (i.e. regime III), the con-
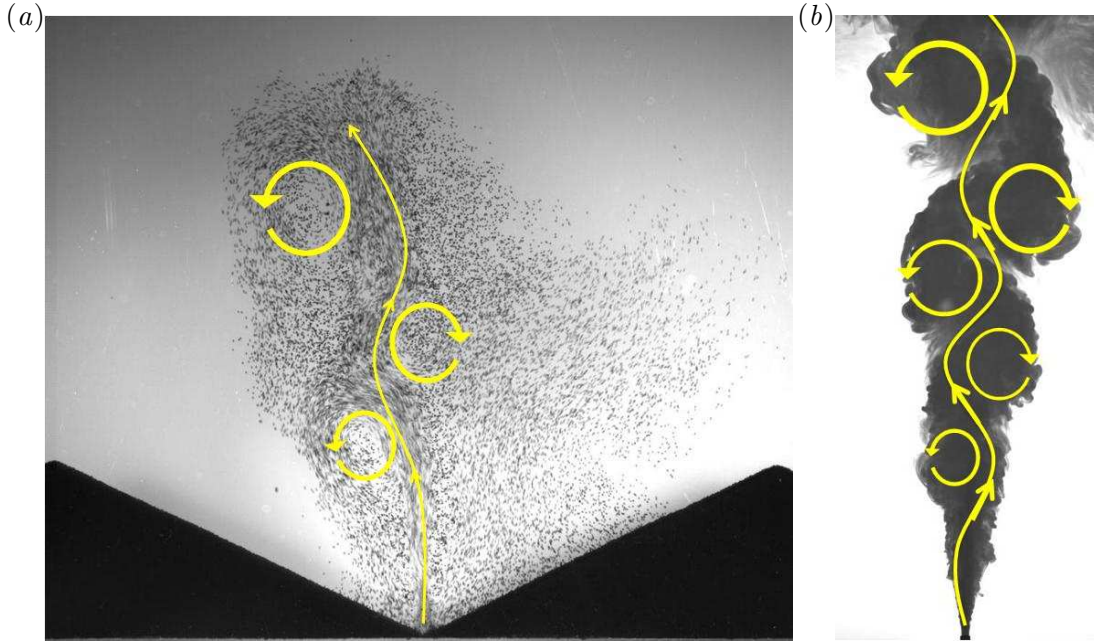
FIGURE 7.6: (a) Illustration of the core and eddy structures in regime III, $Q_0 = 23 \text{ cm}^3 \text{ s}^{-1}$ and $h_0 = 4 \text{ cm}$. At very high flow rates, the slopes of the cone are at the angle of repose and the bed has a fixed shape. The Q2DPL jet displays three large growing eddies (identified with yellow circular arrows), which are advected upwards by the flow, as well as a high speed core (identified with a yellow arrowed curve). In this picture, the maximum height reached by the particles is approximately 20 cm. (b) Grey-scale picture of a dyed steady quasi-two-dimensional turbulent jet rising in the tank over a height of approximately 40 cm (this dyed jet was produced in the apparatus depicted in figure 7.1, following the experimental procedure described in § 2.2.1). Similarly to (a), the eddies are identified with yellow circular arrows and the core is identified with a yellow arrowed curve.

centration of the particles in the Q2DPL jets does not strongly affect the liquid phase of the jet, the particles are passively advected by the flow. Therefore, we can theoretically compute the maximum height reached by the particles h_{max}^t. We make the simplifying assumption that the theoretical particle maximum height h_{max}^t is equal to the height at which the maximum vertical velocity of the pure momentum jet matches the particle settling velocity. For our particles, the settling velocity is $v_s \approx 7.2 \pm 0.4 \text{ cm s}^{-1}$ in the tank at rest. We further assume that the maximum vertical velocity of the jet is approximately equal to its maximum time-averaged vertical velocity $\overline{w}_m$, described by (2.5b). Solving

$$\overline{w}_m(z = h_{max}^t) = v_s, \tag{7.3}$$

we find

$$h^t_{max} = \frac{Q_0{}^2}{4\sqrt{2}\alpha} \left(2\left(\frac{M_0}{v_s Q_0}\right)^2 - 1 \right),$$ (7.4)

where $\alpha = 0.068$ is the entrainment coefficient (Morton *et al.*, 1956) measured in § 2.4, and M_0 is the source momentum flux. As discussed in § 2.4, we have the relationship $M_0/\left(Q_0{}^2/d\right) \approx 0.55$.

In figure 7.7, we present the experimental results for the evolution of the non-dimensional particle maximum height h_{max}/d against the non-dimensional source flow rate $Q_0/(v_s d)$. The experimental data are obtained for an initial bed thickness $h_0 = 1.85$ cm. The data plotted with triangles for h_{max} are obtained with increasing Q_0 (in the stepwise manner described in § 7.2). The data plotted with pluses for h_{max} are obtained with decreasing Q_0. We conduct this second phase directly after the Q_0-increasing phase, after having reached the maximum source flow rate (which can lift the particles to the free surface) and the experiment has reached a steady state (as described in § 7.2).

We also plot in figure 7.7 the thickness of the bed of particles above the nozzle h_{source} (in the Q_0-increasing phase of the experiment) with blue squares (multiplied by a factor 15, for clarity, and non-dimensionalized by d). The evolution of h_{source} with Q_0 indicates the transitions between the three regimes I, II and III described in § 7.3. From $Q_0/(v_s d) \approx 0$ to 0.8, h_{source} remains constant and the bed is fluidized by the jet (regime I, on the left-hand side of the first dotted line plotted in figure 7.7). In regime II (within the two dotted lines), or from $Q_0/(v_s d) \approx 0.8$ to 3.6, h_{source} decreases because of the erosion process above the jet nozzle. In regime II, we can also notice that the Q_0-increasing data for h_{max} are increasing slowly, i.e. the particles rise only slightly higher than the initial bed thickness. For $Q_0 > 3.6$, or regime III (on the right-hand side of the second dotted line in figure 7.7), the erosion process is finished. In regime III, the Q_0-increasing data for h_{max} are in a new regime: the rate of increase of h_{max} with Q_0 is larger than in regime II. Moreover, we show in figure 7.7 the impingement transition height $h_i = 3/4H$ (plotted with a black dashed line), which we discuss in Chapter 6. The transport of the particles by the jet is perturbed beyond this height because the flow changes from a jet flow to an impingement flow. We can see that, for $z > h_i$, h_{max} no longer shows the same increasing trend, but approximately plateaus.

We plot in figure 7.7 the range of the non-dimensional theoretical prediction $h_{max}^t/d \pm 12\,\%$ (computed using (7.4)) between two red dashed curves. We allow a variation of $\pm 12\,\%$ in the calculation of h_{max}^t to account for the typical $0.4/7.2 = 5.5\,\%$ standard deviation in the measurements of the particle settling velocity v_s. As we can see, the theoretical curves lie above the Q_0-increasing data for h_{max} (plotted with triangles) and slightly below the Q_0-decreasing data for h_{max} (plotted with pluses). Moreover, we can observe a strong hysteresis between the two data sets: the particles rise lower in the Q_0-increasing phase than in the Q_0-decreasing phase of the experiment. We believe that the main reason for this hysteresis is because during the Q_0-increasing phase the bulk density of the Q2DPL jet is larger than during the Q_0-decreasing phase. During the Q_0-increasing phase, the Q2DPL jet loses particles because, at each increase of the source flow rate, particles in the jet can settle outside the cone of recirculation until the steady state is reached. On the other hand, once the system has reached a steady state at the maximum flow rate, no more particles can settle out of the recirculation cone as the source flow rate is reduced. Therefore, the assumption that the particle concentration does not affect the jet flow appears to be incorrect in the Q_0-increasing phase of the experiment. In the Q_0-decreasing phase, the 'dilute' assumption seems to be valid because the theoretical prediction underestimates the experimental data only slightly. This small mismatch could be related to the (second) assumption that the time-dependent vertical velocity is approximately equal to the time-averaged vertical velocity. Indeed, we find in Chapter 2 that the vertical velocity in the high-speed core of the jet is different from the Gaussian profile of the time-averaged vertical velocity, and we are unable to investigate whether the maximum height h_{max} reached by the particles is attained exclusively with flow in the high-speed core.

7.5 Conclusion

7.5.1 Summary

We have studied the dynamics of quasi-two-dimensional particle-laden jets in the case of a vertical jet injected below a bed of particles confined in a quasi-two-dimensional environment. We have observed several regimes as we increase the source flow rate and vary the initial bed thickness. Initially, we find the well-
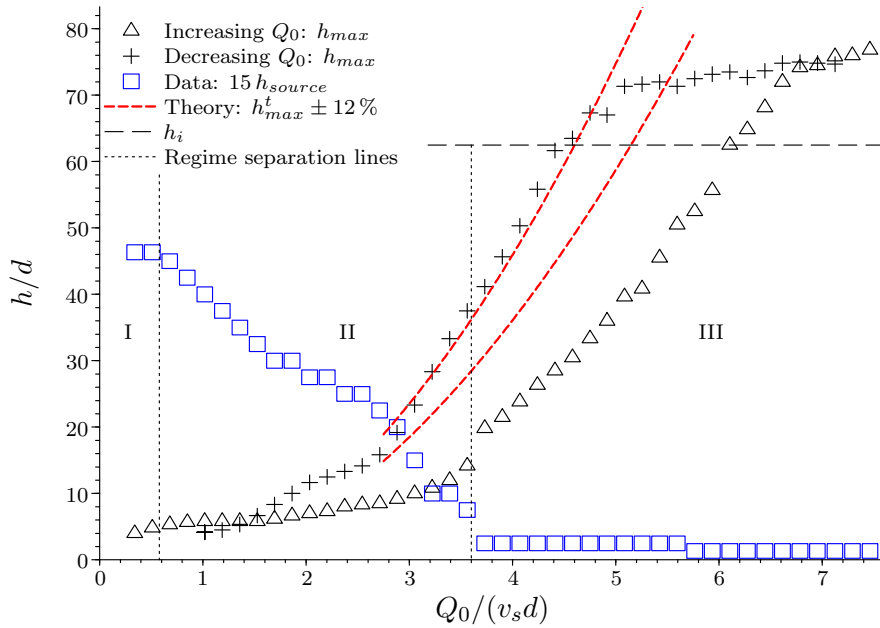
FIGURE 7.7: Evolution against the non-dimensional source flow rate $Q_0/(v_s d)$ of: the non-dimensional experimental particle maximum height h_{max}/d for increasing source flow rate (black triangles), the non-dimensional experimental particle maximum height for decreasing source flow rate (black pluses), the non-dimensional theoretical particle maximum height plus or minus 12 percent $h^t_{max}/d \pm 12\%$ (red dashed curves), and the non-dimensional experimental bed thickness (measured above the nozzle) $15\,h_{source}/d$ (plotted with blue squares). We plot the non-dimensional impingement transition height h_i/d with a black dashed line. The different regimes (I, II and III), presented in the regime diagram shown in figure 7.2 and discussed in § 7.3, are delimited with dotted lines.

known Darcy flow regime and fluidization regime for low flow rates (or large initial bed thicknesses). Then, the bed of particles evolves towards a triangular shape because the jet erodes the bed of particles gradually. The jet entrains particles above the bed, which settle and avalanche on the slope of the triangular eroded bed. In this regime, we observe an instability characterized by the oscillation of the Q2DPL jet. Finally, at large flow rates the particles are transported higher by the jet and their bulk concentration in the jet decreases.

We propose a model for the final regime, in which the flow of the Q2DPL jet displays the same characteristic core and eddy structure as the flow of the non-buoyant quasi-two-dimensional momentum jet. Assuming that the concentration

191

of the particles does not affect the flow of the jet and that the time-dependent vertical velocity is approximately equal to the time-averaged vertical velocity, we calculate the maximum height reached by the particles by equating their settling velocity with the maximum time-averaged vertical velocity of non-buoyant quasi-two-dimensional jets (as described in Chapter 2). The comparison with experimental results shows that the order of magnitude and the trend (with source flow rate) of the particle maximum height are predicted by the model. However, in the phase where the source flow rate increases, the assumption of a dilute suspension of particles in the jet appears to be incorrect because the theoretical prediction overestimates the maximum height reached by the particles. On the other hand, in the (hysteretic) phase where the source flow rate decreases, the dilute assumption appears to be correct because the theoretical prediction only slightly underestimates the maximum height reached by the particles. The small mismatch is thought to be due to the difference between the time-dependent vertical velocity in the high-speed core of the jet and the time-averaged vertical velocity, which we assume in the simplified model presented here.

7.5.2 Future work

Study of heavy fountains

The next step in the understanding of the different regimes is to model the Q2DPL jet as a heavy fountain in a quasi-two-dimensional environment. We believe that a heavy fountain can account for the non-dilute regimes of the flow: the oscillatory flow regime, or regime II, and the Q_0-increasing phase of regime III.

A heavy fountain is a vertical upward jet with negative buoyancy (see e.g. Baines, Turner & Campbell, 1990, for an introduction to the theory of heavy fountains). From dimensional analysis, its maximum height is related to its initial momentum flux M_0 and its initial buoyancy flux B_0

$$z_{max} = A \frac{M_0}{|B_0|^{2/3}}, \tag{7.5}$$

with

$$M_0 = 2b_0 \overline{w}_0{}^2, \quad B_0 = 2b_0 \frac{(\rho_f - \rho_h)}{\rho_f} g \overline{w}_0, \tag{7.6}$$

and where A is a constant of proportionality which can be determined experimen-

tally (Bower *et al.*, 2008), ρ_f is the density of the ambient fluid, ρ_h is the density of the heavy fountain, b_0 is the initial half-width of the fountain, and $\overline{w}_0$ is the initial time-averaged vertical velocity of the fountain. Then, we can re-write the density of the fountain in terms of the densities of the fluid and the particles, and the initial volume fraction of the particles ϕ_0 in the fountain:

$$\rho_h = \phi_0\,\rho_p + (1 - \phi_0)\rho_f. \tag{7.7}$$

Therefore, the particle maximum height is

$$z_{max} = A \left(\phi_0 \frac{(\rho_f - \rho_p)}{\rho_f} g \right)^{-2/3} (2b_0)^{1/3} \overline{w}_0^{4/3}. \tag{7.8}$$

A future aim could be to apply this model to regime II and the Q_0-increasing phase of regime III of the Q2DPL jet and to verify it experimentally. We could inject a homogenous heavy buoyant fluid in the quasi-two-dimensional tank in order to investigate the maximum height reached by the particles as a function of M_0 and B_0, and to measure the experimental constant A. However, relating the heavy-fountain model to the Q2DPL jet is particularly challenging because it requires an estimation of the initial buoyancy flux of the Q2DPL jet, and in particular the initial volume fraction ϕ_0. The rate of entrainment of the particles at the source is one of the most critical and intriguing points: the recirculation of the particles denotes the coupling between the solid phase and the flow of the jet. Both the shape of the crater and the deposition of the particles determine the avalanching flux feeding the jet. The jet entrains these particles, which in turn affect the momentum of the jet by changing its bulk density. Thereafter, the particles rise to the height where their settling velocity matches the vertical velocity of the fluid. In order to close the recirculation problem, we must relate the sedimentation rate of the particles to both the settling time of the particles and their rising time inside the jet. In conclusion, a robust model accounting for the recirculation of the particles is needed to understand the full dynamics of the system.

Changing the viscosity of the medium

To improve our model of the motivating industrial application (the problem of shot-coke formation in a late-stage oil-refining process), the viscosity of the medium in which the bed of particles is prepared could be different from the viscosity of the jet. This experiment is expected to have very rich dynamics because instabilities such as finger-like structures can occur when viscous forces and gravity forces play a key role (Stöhr & Khalili, 2006).

Study of the oscillation of the Q2DPL jet

Another puzzling and interesting issue in this study is our discovery of an instability at intermediate flow rates. The Q2DPL jet oscillates steadily at a fixed flow rate and about a vertical axis. It also produces a large vortex as it tilts sideways at every half oscillation. From these observations, we can wonder what sets the frequency of the oscillation and why the frequency decreases with Q_0. There are different time scales that can influence the frequency: the rising time of the particles in the jet, the settling time of the particles and the avalanching time of the particles. Even the vortex recirculation time could be considered part of the problem; however, the vorticity tends to increase with the flow rate, which seems to be in contradiction with the fact that the oscillation frequency actually decreases with it. Finally, we also noticed that the frequency rapidly drops at the transition between regimes II and III, thus suggesting a different model for the evolution of the frequency in these two regimes.

Injecting water and particles through the nozzle

As a further step in the understanding of the experiments, we could change the experimental procedure by injecting both liquid and particles through the nozzle. The experimental results should be closer to real applications, such as industrial two-phase flows and volcanic eruptions. The complexity of this problem is likely to increase: for example, there cannot be a steady state at fixed flow rate because of the continuous injection of particles in the tank. We might find that the shape of the bed evolves in the reverse order from that which occurs in the present experiment as we increase the flow rate, i.e. passing through regime III, then regime II and finally regime I as shown on figure 7.2. From preliminary experiments, we

observe the formation of an open and flatter crater from the sedimentation of the particles (Jiang *et al.*, 2005; Neves & Fernando, 1995). Moreover, we find that the crater grows in size and its slopes become steeper, thus blocking the rise of the Q2DPL jet. The final stages could also show a fluidization regime and eventually a porous medium flow. An interesting issue is to determine the mechanisms accounting for the transition from one regime to the next.

Study of the three-dimensional case

Three-dimensional particle-laden jets have been studied by many scientists (see e.g. Cardoso & Zarrebini, 2002; Colomer *et al.*, 1998; Colomer & Fernando, 1996; Ernst *et al.*, 1996; Jiang *et al.*, 2005; Neves & Fernando, 1995; Walters *et al.*, 2006; Zoueshtiagh & Merlen, 2007). However, our understanding of the quasi-two-dimensional experiment gives us the opportunity to analyze the three-dimensional case from a different perspective. When comparing the two cases, it is possible to consider a wide variety of interesting issues: the dynamics of the particle-laden jet, the interaction between the particle-laden jet and the bed, the mechanisms of recirculation of the particles, their mixing properties, and the three-dimensional manifestation of the periodic oscillation observed in the quasi-two-dimensional environment.

CONCLUSION AND FUTURE WORK

8.1 Review

In this thesis, we have studied experimentally and theoretically the dynamics of steady quasi-two-dimensional turbulent jets. In Chapter 1, we present a brief summary of past studies on quasi-two-dimensional jets, as well as some motivations for this study. Giger *et al.* (1991) and Dracos *et al.* (1992) gave the first clear description of this particular type of jets, which occurs in the far field of a plane turbulent jet confined between two close boundaries separated by a gap width W (i.e. for $z > 10W$, where z is the streamwise coordinate). They observed that, in the far field, the unstable flow develops into a meandering core with large counter-rotating eddies developing on alternate sides of the core. They found an inverse cascade of quasi-two-dimensional turbulence, which affects not only the structure of the flow but also the transport, dispersion and mixing properties.

One particular application relevant to this study concerns the flow of rivers discharging into lakes or oceans. Various phenomena are related to this type of flow: sediment transport, coastal erosion, and the transport and dispersion of passive tracers such as pollutants. Understanding the physics of the flow is crucial to the prediction and assessment of the environmental impact.

In Chapter 2, we describe the phenomenology of the core and eddy structure of the jet using detailed experimental measurements of the velocity field, obtained with particle image velocimetry. We observe an inverse cascade typical of quasi-two-dimensional turbulence where both the core and the eddies grow linearly with z and travel at an average speed proportional to $z^{-1/2}$. We find that quasi-two-dimensional jets are self-similar and their mean properties are consistent with both experimental results and theoretical models of the time-averaged properties of fully unconfined planar two-dimensional jets. The experimental results for the spatial statistical distribution of the core and eddy structure led us to believe that the dynamics of the interacting core and large eddies accounts for the Gaussian profile of the mean streamwise velocity. The lateral excursions (caused by the propagating eddies) of the high-speed central core produce a Gaussian distribution for the time-averaged streamwise velocity. In addition, we find that approximately 75% of the total momentum flux of the jet is contained within the core. The eddies travel substantially slower (at approximately 25 % of the maximum speed of the core) at each height and their growth is primarily attributed to entrainment of ambient fluid. The frequency of occurrence of the eddies decreases in a stepwise manner due to merging, with a well-defined minimum value of the corresponding Strouhal number $St = fb/\overline{w}_m \geq 0.07$ (where f is the eddy frequency, b is the velocity spread rate of the jet and $\overline{w}_m$ is the maximum time-averaged streamwise velocity in the jet).

In Chapter 3, we investigate theoretically the streamwise transport and dispersion properties of quasi-two-dimensional jets. We model the evolution in time and space of the concentration of passive tracers released in these jets using a one-dimensional time-dependent effective advection–diffusion equation. Based on the study of the flow field presented in Chapter 2, we make a mixing length hypothesis to model the streamwise turbulent eddy diffusivity $D_{zz} \propto b\overline{w}_m$, where b is the jet velocity spread rate, $\overline{w}_m$ is the maximum time-averaged streamwise velocity, and D_{zz} is the streamwise component of the turbulent eddy diffusive

tensor. Under these assumptions, the effective advection–diffusion equation for $\phi(z, t)$, the cross-stream integral of the ensemble-averaged concentration, is of the form:

$$\partial_t \phi + K_a M_0^{1/2} \partial_z \left(\phi/z^{1/2} \right) = K_d M_0^{1/2} \, \partial_z \left(z^{1/2} \partial_z \phi \right), \tag{8.1}$$

where t is time, K_a (the advection parameter) and K_d (the dispersion parameter) are empirical dimensionless parameters which quantify the importance of advection and dispersion, respectively, and M_0 is the source momentum flux. We find analytical solutions to this equation for ϕ in the cases of a constant-flux release and an instantaneous finite-volume release. We also give an integral formulation for the more general case of a time-dependent release, which we solve analytically when tracers are released at a constant flux over a finite period of time.

In Chapter 4, we compare the theoretical predictions of the streamwise advection and dispersion model, derived in Chapter 3, with experimental evidence. From our experimental results, whose concentration distributions agree with the model, we find that $K_a = 1.65 \pm 0.10$ and $K_d = 0.09 \pm 0.02$, for both finite-volume releases and constant-flux releases using either dye or virtual passive tracers. The experiments also show that streamwise dispersion increases in time as $t^{2/3}$. As a result, in the case of finite-volume releases, more than $50\,\%$ of the total volume of tracers is transported ahead of the purely advective front (i.e. the front location of the tracer distribution if all dispersion mechanisms are ignored, corresponding formally to the assumption of 'top-hat' velocity profiles in the jet); and in the case of constant-flux releases, at each instant in time, approximately $10\,\%$ of the total volume of tracers is transported ahead of the advective front. Finally, we assess the statistical significance of our results. We find that experimental or real concentrations are more likely to differ from the concentrations predicted by the model at large concentration levels than at low concentration levels. These findings are important in problems of pollution control in rivers because they show that pollutants can travel faster than expected and their concentration may be higher than predicted.

In Chapter 5, we investigate turbulent relative dispersion in quasi-two-dimensional turbulent jets. Following the seminal paper of Richardson (1926), we use two-point statistics to describe the dispersion properties of the core and eddy structure of the jet. The experimental data are obtained using what we believe to be a novel Lagrangian-particle-tracking technique, which we refer to as vir-

tual particle tracking. Virtual particle tracking, first introduced in Chapter 4, consists of tracking (numerically) virtual passive tracers seeded in the experimentally measured velocity field of a flow. We demonstrate that this technique can yield valuable experimental data to compare with turbulent relative dispersion models. We calculate the time evolution of the probability distributions of key two-point properties (such as the lateral distance, the streamwise distance, the Euclidean distance and the ratio of the lateral distance to the streamwise distance between two points) in three different parts of the flow of quasi-two-dimensional jets. We find that in the eddy, the distribution of particles disperses slowly and in a rather axisymmetric manner. At the interface between the core and the eddy, the distribution of particles stretches considerably in the streamwise direction at a high rate. In the core of the jet, the particle distribution disperses slowly in the cross-jet direction and splits along the jet axis. Finally, we believe that the rapid change in time of the jagged distribution of the p.d.f. for the distance between two points in the eddy reveals the intense stirring (and potentially the resulting vigorous turbulent mixing) occurring within the eddy.

In Chapter 6, we use potential theory to describe the ambient flow induced by a quasi-two-dimensional jet discharged vertically upwards in a fully confined rectangular domain. In our experimental apparatus (of aspect ratio 1), we can observe that at a height $h_i \approx 0.65 h_f$ (where h_f is the distance of the free surface from the source) the jet flow becomes an impingement flow which spreads laterally along the free surface, recirculates downwards along the lateral boundaries of the apparatus, and is eventually re-entrained by the jet. In the domain, spanning from the lateral rigid boundary to the jet axis in the x-direction and from the bottom rigid boundary to the impingement transition height h_i in the streamwise direction, we solve Laplace's equation. We assume slip boundary conditions at the rigid boundaries, a sink link with varying strength proportional to $(z - z_0)^{-1/2}$ (where z_0 is the space virtual origin of the jet) at the jet axis, and a uniform source line (whose integrated volume flux matches the integrated volume flux of the sink line) at the impingement transition height. The analytical stream function and velocity field agree with our experimental measurements, except near the boundary of the jet. We also find that (contrary to the volume flux) the time-averaged momentum flux of the induced return flow is insignificant compared with the time-averaged momentum flux of the jet, typically less than 10 %. We believe

that this means that the induced return flow in our experimental apparatus has little impact on the flow structures of the quasi-two-dimensional jet studied in the previous chapters.

In Chapter 7, we study the case of a momentum jet discharged below a bed of particles in a quasi-two-dimensional environment. As the jet flow rate increases, the interaction between the jet and the bed of particles evolves through three main different regimes. At low flow rates or large initial bed thicknesses, the jet fluidizes the bed. At intermediate flow rates, the jet erodes the bed and form a pyramidal mound on either side of the jet axis. The particle-laden jet is also unstable and oscillates about a vertical axis. At large flow-rates, the bed is fully eroded and the flow of the particle-laden jet shows the same core and eddy structure as the particle-free quasi-two-dimensional jet observed in Chapter 2. We propose a model to predict the maximum height of rise reached by the particles in the jet based on the time-averaged vertical velocity of a particle-free quasi-two-dimensional jet. We find that the model agrees with experimental data for a dilute suspension of particles in the jet.

8.2 Future work

This study has raised questions for future research. We highlight below the various possible directions already discussed throughout the thesis. For instance, the streamwise advection and dispersion model (developed in Chapter 3) could be extended to include advection and dispersion in the cross-jet direction of quasi-two-dimensional jets. With a two-dimensional time-dependent model, the distribution of the concentration of passive tracers in quasi-two-dimensional jets would be fully resolved. Such a model would provide more accurate predictions for dispersion and transport in river flows.

A relationship between the two-point statistics in the jet and our streamwise advection and dispersion model (i.e. connecting Chapters 3 and 4 with Chapter 5) could improve our understanding of relative dispersion in turbulent flows. Furthermore, the spatial resolution of the results obtained with the technique of virtual particle tracking (described in § 4.1.2 and used in Chapters 4 and 5) could be enhanced to resolve the finest scale of turbulence. This would provide crucial experimental data for comparison with the vast number of turbulent dispersion

models.

We also believe that the technique of virtual particle tracking, developed in this study, can be successfully applied to other flow problems. Virtual particle tracking can resolve Lagrangian particle tracking (as shown in Chapter 5), as well as identify Eulerian features in the flow (as performed in § 2.5 to study quantitatively the core and eddy structures of quasi-two-dimensional jets).

The study of particle-laden jets in quasi-two-dimensional environments has also opened many avenues of research. An analogy with heavy fountains could give a basis to model the flow regimes with large concentrations of particles, and potentially explain the physics of the oscillatory instability displayed by quasi-two-dimensional particle-laden jets. Changing the viscosity of the liquid phase, or injecting solid particles with the liquid phase at the source would show very rich dynamics relevant to many industrial applications, such as coking, and geophysical applications, such as volcanic eruptions.

The influence of quasi-two-dimensional confinement on buoyant jets or plumes could also be studied. This problem is relevant to the study of natural ventilation in buildings with line sources of heat. The question of the stability of the flow and the conditions of emergence of the core and eddy structure can be raised when buoyancy forces play an important role. Moreover, one might investigate whether the entrainment, transport, dispersion and mixing mechanisms in quasi-two-dimensional buoyant jets or quasi-two-dimensional plumes are analogous to those in the non-buoyant case studied in this thesis.

Finally, the fundamental modelling of the turbulence in the flow of quasi-two-dimensional jets could be investigated. Dracos *et al.* (1992) found an inverse cascade of turbulence at scales larger than the gap width W and a three-dimensional cascade of turbulence at smaller scales. Thus, the turbulence in quasi-two-dimensional jets is neither purely two-dimensional nor exactly three-dimensional. The study of the transfer of energy in this quasi-two-dimensional cascade of turbulence could provide some insight about the general problem of turbulence.

ADVECTION−DIFFUSION MODEL FOR QUASI-TWO-DIMENSIONAL JETS

A.1 Proof of equation (3.89)

If $t > T_0$, we have, according to (3.88),

$$\phi_{T_0}(z, t) = \frac{K_{T_0}}{T_0} z^{1/2} \left(\int_{s(t)}^{+\infty} h^{a-1} e^{-h} \, \mathrm{d}h - \int_{s(t-T_0)}^{+\infty} h^{a-1} e^{-h} \, \mathrm{d}h \right), \qquad (A.1)$$

with

$$K_{T_0} = \frac{2B}{3 K_d M_0^{1/2} \Gamma[a+1]}, \quad a = \frac{2}{3} \left(\frac{K_a}{K_d} - \frac{1}{2} \right) \quad \text{and} \quad s(t) = \frac{4 z^{3/2}}{9 K_d M_0^{1/2} t}.$$
$$(A.2a\text{–}c)$$

Combining the two integrals, in the limit $t \gg T_0$, (A.1) becomes

$$\phi_{T_0}(z,t) \quad \sim \quad \frac{K_{T_0}}{T_0} z^{1/2} \left(s(t)\right)^{a-1} e^{-s(t)} \left(s(t-T_0) - s(t)\right) \tag{A.3}$$

$$\sim \quad K_{T_0} \frac{z^{1/2}}{t} \left(s(t)\right)^a e^{-s(t)} \tag{A.4}$$

Using $\eta = z/\left(t^{2/3} M_0^{1/3}\right)$, (A.2$b$) and (A.2$c$), we obtain

$$\phi_{T_0}(z,t) \sim t^{-2/3} K_{T_0} M_0^{1/6} \left(\frac{4}{9K_d}\right)^a \eta^{K_a/K_d} \exp\left[-\frac{4}{9K_d}\eta^{3/2}\right]. \tag{A.5}$$

Finally, using (A.2a), we find

$$\phi_{T_0}(z,t) \sim t^{-2/3} \frac{B}{\left(\frac{3}{2}\right)^{2a+1} \left(K_d\right)^{a+1} \Gamma\left[a+1\right] M_0^{1/3}} \eta^{K_a/K_d} \exp\left[-\frac{4}{9K_d}\eta^{3/2}\right] \tag{A.6}$$

$$= t^{-2/3} y_\delta(\eta), \tag{A.7}$$

where y_δ is defined in (3.73), and hence (3.89) follows.

Two-point statistics in circular distributions

B.1 Conditional probability for the x-distance between two points in a disc

In equation (5.15), the conditional probability for the x- or lateral distance between two points $\mathcal{H}(\mathbf{x_1}, \mathbf{x_2})$ (with $0 \leq x_1 \leq R(t)$ fixed and $x_1{}^2 + z_1{}^2 \leq R^2(t)$) is, using Cartesian coordinates,

$$P_{\mathscr{D}_t}(\mathcal{H}(\mathbf{x_1}, \mathbf{x_2}) \leq h \,|\, \mathbf{x_1}) = \frac{1}{\pi R^2(t)} \iint_{\mathscr{D}_t \cap \mathscr{H}(\mathbf{x_1}, h)} \mathrm{d}z_2 \mathrm{d}x_2, \qquad \text{(B.1)}$$

where the domain $\mathscr{H}(\mathbf{x_1}, h)$ is defined such that $\mathbf{x_2} \in \mathscr{H}(\mathbf{x_1}, h)$ if $|x_1 - x_2| \leq h$. Since $\mathscr{H}(\mathbf{x_1}, h)$ does not depend on z_2 (as long as $x_2{}^2 + z_2{}^2 \leq R^2(t))$ and

$\mathscr{D}_t \cap \mathscr{H}(\mathbf{x_1}, \hbar)$ is symmetric with respect to the x-axis, (B.1) becomes, for $0 \leq \hbar \leq R(t)$,

$$P_{\mathscr{D}_t}(\mathscr{H}(\mathbf{x_1}, \mathbf{x_2}) \leq \hbar \,|\mathbf{x_1}) = \frac{2}{\pi R^2(t)} \int_{x_1 - \hbar}^{x_1 + \hbar} \sqrt{R^2(t) - x_2{}^2} \,\mathrm{d}x_2, \ 0 \leq x_1 \leq R(t) - \hbar$$

(B.2)

and

$$P_{\mathscr{D}_t}(\mathscr{H}(\mathbf{x_1}, \mathbf{x_2}) \leq \hbar \,|\mathbf{x_1}) = \frac{2}{\pi R^2(t)} \int_{x_1 - \hbar}^{R(t)} \sqrt{R^2(t) - x_2{}^2} \,\mathrm{d}x_2, \ R(t) - \hbar \leq x_1 \leq R(t);$$

(B.3)

for $R(t) \leq \hbar \leq 2R(t)$,

$$P_{\mathscr{D}_t}(\mathscr{H}(\mathbf{x_1}, \mathbf{x_2}) \leq \hbar \,|\mathbf{x_1}) = \frac{2}{\pi R^2(t)} \int_{-R(t)}^{R(t)} \sqrt{R^2(t) - x_2{}^2} \,\mathrm{d}x_2, \ 0 \leq x_1 \leq -R(t) + \hbar,$$

(B.4)

and

$$P_{\mathscr{D}_t}(\mathscr{H}(\mathbf{x_1}, \mathbf{x_2}) \leq \hbar \,|\mathbf{x_1}) = \frac{2}{\pi R^2(t)}$$
$$\times \int_{x_1 - \hbar}^{R(t)} \sqrt{R^2(t) - x_2{}^2} \,\mathrm{d}x_2, \ -R(t) + \hbar \leq x_1 \leq R(t);$$

(B.5)

and for $2R(t) \leq \hbar$,

$$P_{\mathscr{D}_t}(\mathscr{H}(\mathbf{x_1}, \mathbf{x_2}) \leq \hbar \,|\mathbf{x_1}) = \frac{2}{\pi R^2(t)} \int_{-R(t)}^{R(t)} \sqrt{R^2(t) - x_2{}^2} \,\mathrm{d}x_2, \ 0 \leq x_1 \leq R(t).$$

(B.6)

Solving the integrals in (B.2), (B.3), (B.4), (B.5) and (B.6), we obtain the results described in (5.16), (5.17), (5.18), (5.19) and (5.20), respectively.

B.2 Value at the origin for the p.d.f. of the lateral distance between two points in a disc

The value at the origin for the p.d.f. of the lateral distance between two points in a disc $f_{\mathscr{D}_t}^{\mathcal{H}}$ is defined as

$$f_{\mathscr{D}_t}^{\mathcal{H}}(0) = \lim_{\delta h \to 0} \frac{f_{\mathscr{D}_t}^{\mathcal{H}}(\delta h)}{\delta h} \tag{B.7}$$

$$= \lim_{\delta h \to 0} \frac{4}{\pi R^2(t)} \int_0^{R(t)} \frac{P_{\mathscr{D}_t}(\mathcal{H}(\mathbf{x_1}, \mathbf{x_2}) \leq \delta h \,|\mathbf{x_1})}{\delta h} \sqrt{R^2(t) - x_1{}^2} \, \mathrm{d}x_1 \tag{B.8}$$

$$\approx \frac{4}{\pi R^2(t)} \int_0^{R(t)} \lim_{\delta h \to 0} \frac{P_{\mathscr{D}_t}(\mathcal{H}(\mathbf{x_1}, \mathbf{x_2}) \leq \delta h \,|\mathbf{x_1})}{\delta h} \sqrt{R^2(t) - x_1{}^2} \, \mathrm{d}x_1, \tag{B.9}$$

where we use (5.15). According to (5.16), the conditional probability is, for $\delta h \to 0$,

$$\lim_{\delta h \to 0} \frac{P_{\mathscr{D}_t}(\mathcal{H}(\mathbf{x_1}, \mathbf{x_2}) \leq \delta h \,|\mathbf{x_1})}{\delta h} = \lim_{\delta h \to 0} \frac{1}{\pi \delta h} \left(\arcsin\left(\frac{x_1 + \delta h}{R(t)}\right) + \frac{(x_1 + \delta h)}{R(t)} \sqrt{1 - \left(\frac{x_1 + \delta h}{R(t)}\right)^2} \right.$$

$$\left. - \arcsin\left(\frac{x_1 - \delta h}{R(t)}\right) - \frac{(x_1 - \delta h)}{R(t)} \sqrt{1 - \left(\frac{x_1 - \delta h}{R(t)}\right)^2} \right) \tag{B.10}$$

$$= \frac{2}{\pi R(t)} \frac{\mathrm{d}}{\mathrm{d}\left(\frac{x_1}{R(t)}\right)} \left[\arcsin\left(\frac{x_1}{R(t)}\right) + \left(\frac{x_1}{R(t)}\right) \sqrt{1 - \left(\frac{x_1}{R(t)}\right)^2} \right] \tag{B.11}$$

$$= \frac{4}{\pi R(t)} \sqrt{1 - \left(\frac{x_1}{R(t)}\right)^2}. \tag{B.12}$$

We can replace (B.12) in (B.9), and integrate to find

$$f_{\mathscr{D}_t}^{\mathcal{H}}(0) = \frac{32}{3\pi^2 R(t)}. \tag{B.13}$$

B.3 Value at $2R(t)$ for the p.d.f. of the lateral distance between two points in a disc

The value at $h = 2R(t)$ for the p.d.f. of the lateral distance between two points in a disc, $f_{\mathscr{D}_t}^{\mathcal{H}}$ is defined as

$$
\begin{aligned}
f_{\mathscr{D}_t}^{\mathcal{H}}\left(2R(t)\right) &= \lim_{\delta h \to 0} \frac{f_{\mathscr{D}_t}^{\mathcal{H}}\left(2R(t)\right) - f_{\mathscr{D}_t}^{\mathcal{H}}\left(2R(t) - \delta h\right)}{\delta h} &\text{(B.14)}\\
&= \lim_{\delta h \to 0} \frac{1 - f_{\mathscr{D}_t}^{\mathcal{H}}\left(2R(t) - \delta h\right)}{\delta h}, &\text{(B.15)}
\end{aligned}
$$

where we use (5.20), then using to (5.18) and (5.19) we can show that for $\delta h \ll 1$

$$
f_{\mathscr{D}_t}^{\mathcal{H}}\left(2R(t) - \delta h\right) = 1 + O\left[\delta h\right]^{3/2}. \tag{B.16}
$$

Therefore, replacing (B.16) in (B.15), we obtain

$$
f_{\mathscr{D}_t}^{\mathcal{H}}\left(2R(t)\right) = 0. \tag{B.17}
$$

B.4 P.d.f of the x-distance between two points in a square domain

The c.d.f. of the $x-$ or lateral distance between two points in a square domain $\mathscr{S}_t$ (described in § 5.3.1) is, using Cartesian coordinates,

$$
F_{\mathscr{S}_t}^{\mathcal{H}}(h) = P_{\mathscr{S}_t}(\mathcal{H}\left(\mathbf{x_1}, \mathbf{x_2}\right) \le h) = \frac{1}{R(t)} \int_0^{R(t)} P_{\mathscr{S}_t}(\mathcal{H}\left(\mathbf{x_1}, \mathbf{x_2}\right) \le h | \mathbf{x_1}) \, \mathrm{d}x_1, \tag{B.18}
$$

based on the general definition (5.7), and where we use the fact that the domain $\mathscr{S}_t$ is symmetric with respect to the z-axis, the density is uniform over the whole domain $\mathscr{D}_t$ and the conditional probability does not depend on z_1 (as long as $-R(t) \le z_1 \le R(t)$). Similarly to the conditional probability for the disc described

in § B.1, the conditional probability for the domain $\mathscr{S}_t$ is

$$P_{\mathscr{S}_t}(\mathcal{H}(\mathbf{x_1}, \mathbf{x_2}) \leq h | \mathbf{x_1}) = \frac{1}{4R^2(t)} \int_{\mathscr{S}_t \cap \mathcal{H}(\mathbf{x_1}, h)} \mathrm{d}z_2 \mathrm{d}x_2, \qquad \text{(B.19)}$$

where the domain $\mathcal{H}(\mathbf{x_1}, h)$ is defined such that $\mathbf{x_2} \in \mathcal{H}(\mathbf{x_1}, h)$ if $|x_1 - x_2| \leq h$. We can integrate (B.19) with respect to both x_1 and z_1. We find, for $0 \leq h \leq R(t)$,

$$P_{\mathscr{S}_t}(\mathcal{H}(\mathbf{x_1}, \mathbf{x_2}) \leq h | \mathbf{x_1}) = \begin{cases} \dfrac{h}{R(t)} & 0 \leq x_1 \leq R(t) - h \\ \dfrac{R(t) - (x_1 - h)}{2R(t)} & R(t) - h \leq x_1 \leq R(t) \end{cases} ; \quad \text{(B.20)}$$

for $R(t) \leq h \leq 2R(t)$,

$$P_{\mathscr{S}_t}(\mathcal{H}(\mathbf{x_1}, \mathbf{x_2}) \leq h | \mathbf{x_1}) = \begin{cases} \dfrac{1}{2R(t)} & 0 \leq x_1 \leq -R(t) + h \\ \dfrac{R(t) - (x_1 - h)}{2R(t)} & -R(t) + h \leq x_1 \leq R(t) \end{cases} ; \quad \text{(B.21)}$$

and for $2R(t) \leq h$,

$$P_{\mathscr{S}_t}(\mathcal{H}(\mathbf{x_1}, \mathbf{x_2}) \leq h | \mathbf{x_1}) = \frac{1}{2R(t)}. \qquad \text{(B.22)}$$

Using (B.20), (B.21) and (B.22) we can integrate (B.18) to find

$$F_{\mathscr{S}_t}^{\mathcal{H}}(h) = \frac{4R(t)h - h^2}{4R^2(t)}. \qquad \text{(B.23)}$$

Finally, we can differentiate (B.23) with respect to h to obtain the p.d.f. $f_{\mathscr{S}_t}^{\mathcal{H}}$ described in (5.22).

B.5 Conditional probability for the Euclidean distance between two points in a disc

In equation (5.23), the conditional probability for the distance between two points $\mathcal{D}(\mathbf{x_1}, \mathbf{x_2})$ (with $0 \leq x_1 \leq R(t)$ fixed and $x_1^2 + z_1^2 \leq R^2(t)$) is, using Cartesian

coordinates,

$$P_{\mathcal{D}_t}(\mathcal{D}(\mathbf{x_1}, \mathbf{x_2}) \leq d \,|\mathbf{x_1}) = \frac{1}{\pi R^2(t)} \iint_{\mathcal{D}_t \cap \mathcal{J}(\mathbf{x_1}, d)} \mathrm{d}z_2 \mathrm{d}x_2, \qquad (\text{B.24})$$

where the domain $\mathcal{J}(\mathbf{x_1}, h)$ is defined such that $\mathbf{x_2} \in \mathcal{J}(\mathbf{x_1}, d)$ if $(x_1 - x_2)^2 + z_2{}^2 \leq d^2$ (we can fix $z_1 = 0$ by axisymmetry). (B.24) becomes, for $0 \leq d \leq R(t)$,

$$P_{\mathcal{D}_t}(\mathcal{D}(\mathbf{x_1}, \mathbf{x_2}) \leq d \,|\mathbf{x_1}) = \frac{1}{\pi R^2(t)} \int_0^d \int_0^{2\pi} r_2 \mathrm{d}r_2 \mathrm{d}\theta_2, \quad 0 \leq r_1 \leq R(t) - d, \ (\text{B.25})$$

with $r_1 = \sqrt{x_1{}^2 + z_1{}^2}$ and $r_2 = \sqrt{x_2{}^2 + z_2{}^2}$, and

$$P_{\mathcal{D}_t}(\mathcal{D}(\mathbf{x_1}, \mathbf{x_2}) \leq d \,|\mathbf{x_1}) = \frac{2}{\pi R^2(t)} \left(\int_{r_1 - d}^{x_I} \sqrt{d^2 - (x_2 - r_1)^2} \, \mathrm{d}x_2 \right.$$
$$\left. + \int_{x_I}^{R(t)} \sqrt{R^2(t) - x_2{}^2} \, \mathrm{d}x_2 \right), \ R(t) - d \leq r_1 \leq R(t),$$
$$(\text{B.26})$$

where x_I is defined in (5.26); for $R(t) \leq d \leq 2R(t)$,

$$P_{\mathcal{D}_t}(\mathcal{D}(\mathbf{x_1}, \mathbf{x_2}) \leq d \,|\mathbf{x_1}) = \frac{1}{\pi R^2(t)} \int_0^{R(t)} \int_0^{2\pi} r_2 \, \mathrm{d}r_2 \mathrm{d}\theta_2, \ 0 \leq r_1 \leq -R(t) + d,$$
$$(\text{B.27})$$

and

$$P_{\mathcal{D}_t}(\mathcal{D}(\mathbf{x_1}, \mathbf{x_2}) \leq d \,|\mathbf{x_1}) = \frac{2}{\pi R^2(t)} \left(\int_{r_1 - d}^{x_I} \sqrt{d^2 - (x_2 - r_1)^2} \, \mathrm{d}x_2 \right.$$
$$\left. + \int_{x_I}^{R(t)} \sqrt{R^2(t) - x_2{}^2} \, \mathrm{d}x_2 \right), \ -R(t) + d \leq r_1 \leq R(t);$$
$$(\text{B.28})$$

and for $2R(t) \leq d$,

$$P_{\mathcal{D}_t}(\mathcal{D}(\mathbf{x_1}, \mathbf{x_2}) \leq d \,|\mathbf{x_1}) = \frac{1}{\pi R^2(t)} \int_0^{R(t)} \int_0^{2\pi} r_2 \, \mathrm{d}r_2 \mathrm{d}\theta_2, \quad 0 \leq r_1 \leq R(t). \ (\text{B.29})$$

Solving the integrals in (B.25), (B.26), (B.27), (B.28) and (B.29), we obtain the results described in (5.24), (5.25), (5.27), (5.28) and (5.29), respectively.

B.6 Conditional probability for the ratio of the lateral distance to the streamwise distance between two points in a disc

In equation (5.31), the conditional probability for the ratio of the lateral distance to the streamwise distance between two points $\mathcal{M}\left(\mathbf{x_1}, \mathbf{x_2}\right)$ (with $0 \leq r_1 \leq R(t)$ and $0 \leq \theta_1 \leq \pi/2$ fixed) is, using polar coordinates,

$$P_{\mathscr{D}_t}(\mathcal{M}\left(\mathbf{x_1}, \mathbf{x_2}\right) \leq m \,|\mathbf{x_1}) = \frac{1}{\pi R^2(t)} \iint_{\mathscr{D}_t \cap \mathscr{G}(\mathbf{x_1}, m)} r_2 \, \mathrm{d}r_2 \mathrm{d}\theta_2, \tag{B.30}$$

where the domain $\mathscr{G}(\mathbf{x_1}, m)$ is defined such that $\mathbf{x_2} \in \mathscr{G}(\mathbf{x_1}, d)$ if $|x_1 - x_2|/|z_1 - z_2| \leq m$. (B.30) becomes, for $0 \leq m$,

$$P_{\mathscr{D}_t}(\mathcal{M}\left(\mathbf{x_1}, \mathbf{x_2}\right) \leq m \,|\mathbf{x_1}) = \frac{1}{\pi R^2(t)} \left(\int_{\upsilon}^{\pi-\upsilon} \int_0^l r_2 \, \mathrm{d}r_2 \mathrm{d}\theta_2 + \int_{-\pi+\upsilon}^{-\upsilon} \int_0^l r_2 \, \mathrm{d}r_2 \mathrm{d}\theta_2 \right),$$
$$\tag{B.31}$$

with $\upsilon = \arctan\left(1/m\right)$, and where

$$l = r_1 \cos\left(\theta_2 - \theta_1 - \pi\right) + \sqrt{R^2(t) - r_1{}^2 \sin^2\left(\theta_2 - \upsilon - \pi\right)} \tag{B.32}$$

is the equation of the perimeter of $\mathscr{D}_t$ in polar coordinates with the origin at $\mathbf{x_1}$. We can then integrate (B.31) with respect to r_2. We obtain

$$P_{\mathscr{D}_t}(\mathcal{M}\left(\mathbf{x_1}, \mathbf{x_2}\right) \leq m \,|\mathbf{x_1}) = \frac{1}{\pi R^2(t)} \left(\int_{\upsilon}^{\pi-\upsilon} \frac{l^2}{2} \, \mathrm{d}\theta_2 + \int_{-\pi+\upsilon}^{-\upsilon} \frac{l^2}{2} \, \mathrm{d}\theta_2 \right). \tag{B.33}$$

Finally, replacing (B.32) into (B.33) and integrating (B.33) with respect to θ_2, we find equations (5.32) and (5.33).

Bibliography

Abramowitz, M. & Stegun, I. A. 1972 *Handbook of Mathematical Functions with Formulas, Graphs, and Mathematical Tables,* 10th Edition. Dover Publications.

Albertson, M. L., Dai, Y. B., Jensen, R. A. & Rouse, H. 1950 Diffusion of submerged jets. *Transactions of the American Society of Civil Engineers* **115**, 639–664.

Antonia, R. A., Satyaprakash, B. R. & Hussain, A. K. M. F. 1980 Measurements of dissipation rate and some other characteristics of turbulent plane and circular jets. *Physics of Fluids* **23**, 695–700.

Baines, W. D., Turner, J. S. & Campbell, I. H. 1990 Turbulent fountains in an open chamber. *Journal of Fluid Mechanics* **212**, 557–592.

Batchelor, G. K. 1950 The application of the similarity theory of turbulence to atmospheric diffusion. *Quarterly Journal of the Royal Meteorological Society* **76**, 133–146.

Batchelor, G. K. 1952 Diffusion in a field of homogeneous turbulence. 2 The relative motion of particles. *Proceedings of the Cambridge Philosophical Society* **48**, 345–362.

Bird, R. B., Stewart, W. E. & Lightfoot, E. N. 2007 *Transport Phenomena,* 2nd Edition. John Wiley & Sons.

Bourgoin, M., Ouellette, N. T., Xu, H. T., Berg, J. & Bodenschatz, E. 2006 The role of pair dispersion in turbulent flow. *Science* **311**, 835–838.

Bower, D. J., Caulfield, C. P., Fitzgerald, S. D. & Woods, A. W. 2008 Transient ventilation dynamics following a change in strength of a point source of heat. *Journal of Fluid Mechanics* **614**, 15–37.

Cardoso, S. S. S. & Zarrebini, M. 2002 Sedimentation from surface currents generated by particle-laden jets. *Chemical Engineering Science* **57**, 1425–1437.

Cenedese, C. & Dalziel, S. B. 1998 Concentration and depth fields determined by the light transmitted through a dyed solution. In *Proceedings of the 8th International Symposium on Flow Visualization*.

Chen, D. & Jirka, G. H. 1998 Linear stability analysis of turbulent mixing layers and jets in shallow water layers. *Journal of Hydraulic Research* **36**, 815–830.

Chen, D. & Jirka, G. H. 1999 LIF study of plane jet bounded in shallow water layer. *Journal of Hydraulic Engineering – ASCE* **125**, 817–826.

Cierpka, C. & Kaehler, C. J. 2012 Particle imaging techniques for volumetric three-component (3D3C) velocity measurements in microfluidics. *Journal of Visualization* **15**, 1–31.

Colomer, J., Casamitjana, X. & Fernando, H. J. S. 1998 Resuspension and sedimentation of particles from a sediment bed by turbulent jets. *Applied Scientific Research* **59**, 229–242.

Colomer, J. & Fernando, H. J. S. 1996 Resuspension of particle bed by round vertical jet. *Journal of Environmental Engineering – ASCE* **122**, 864–869.

Coomaraswamy, I. A. 2011 Natural ventilation of buildings: time-dependent phenomena. PhD thesis, University of Cambridge, Cambridge, UK.

DALZIEL, S. B. 1992 Decay of rotating turbulence - Some particle tracking experiments. *Applied Scientific Research* **49**, 217–244.

DALZIEL, S. B., PATTERSON, M. D., CAULFIELD, C. P. & COOMARASWAMY, I. A. 2008 Mixing efficiency in high-aspect-ratio Rayleigh–Taylor experiments. *Physics of Fluids* **20** (065106).

DE YOUNG, D. S. 1997 Growth of large scale structures in two-dimensional mixing layers. *Physics of Fluids* **9**, 2168–2170.

DIMOTAKIS, P. E., MIAKE-LYE, R. C. & PAPANTONIOU, D. A. 1983 Structure and dynamics of round turbulent jets. *Physics of Fluids* **26**, 3185–3192.

DRACOS, T., GIGER, M. & JIRKA, G. H. 1992 Plane turbulent jets in a bounded fluid layer. *Journal of Fluid Mechanics* **241**, 587–614.

DRAYTON, M. J. 1993 Eulerian and Lagrangian studies of inhomogeneous turbulence generated by an oscillating grid. PhD thesis, University of Cambridge, Cambridge, UK.

DUTKIEWICZ, S., GRIFFA, A. & OLSON, D. B. 1993 Particle diffusion in a meandering jet. *Journal of Geophysical Research–Oceans* **98**, 16,487–16,500.

ERNST, G. G. J., SPARKS, R. S. J., CAREY, S. N. & BURSIK, M. I. 1996 Sedimentation from turbulent jets and plumes. *Journal of Geophysical Research* **101**, 5575–5589.

ESER, S., JENKINS, R. G., DERBYSHIRE, F. J. & MALLADI, M. 1986 Carbonization of coker feedstocks and their fractions. *Carbon* **24**, 77–82.

FOSS, J. F. & JONES, J. B. 1968 Secondary flow effects in a bounded rectangular jet. *Transactions of the ASME: Journal of Basic Engineering* **90**, 241–248.

FUNG, J. C. H. 1990 Kinematic simulation of turbulent flow and particle motion. PhD thesis, University of Cambridge, Cambridge, UK.

GIGER, M., DRACOS, T. & JIRKA, G. H. 1991 Entrainment and mixing in plane turbulent jets in shallow water. *Journal of Hydraulic Research* **29**, 615–642.

CERVANTES DE GORTARI, J. & GOLDSCHMIDT, V. W. 1981 The apparent flapping motion of a turbulent plane jet – further experimental results. *Transactions of the ASME: Journal of Fluids Engineering* **103**, 119–126.

GRADSHTEYN, I. S. & RYZHIK, I. M. 2007 *Table of Integrals, Series, and Products,* 7th Edition. Elsevier Academic Press.

HOLDEMAN, J. D. & FOSS, J. F. 1975 Initiation, development, and decay of secondary flow in a bounded jet. *Transactions of the ASME: Journal of Fluids Engineering* **97**, 342–352.

HUSSEIN, H. J., CAPP, S. P. & GEORGE, W. K. 1994 Velocity measurements in a high-Reynolds number, momentum-conserving, axisymmetric, turbulent jet. *Journal of Fluid Mechanics* **258**, 31–75.

ITÔ, S. 1992 *Diffusion Equations*. American Mathematical Society.

JIANG, J. S., LAW, A. W. K. & CHENG, N. S. 2005 Two-phase analysis of vertical sediment-laden jets. *Journal of Engineering Mechanics – ASCE* **131**, 308–318.

JIRKA, G. H. 2001 Large scale flow structures and mixing processes in shallow flows. *Journal of Hydraulic Research* **39**, 567–573.

JIRKA, G. H. 2006 Integral model for turbulent buoyant jets in unbounded stratified flows. Part 2. Plane jet dynamics resulting from multiport diffuser jets. *Environmental Fluid Mechanics* **6**, 43–100.

JIRKA, G. H. & HARLEMAN, D. R. F. 1979 Stability and mixing of a vertical plane buoyant jet in confined depth. *Journal of Fluid Mechanics* **94**, 275–304.

JIRKA, G. H. & UIJTTEWAAL, W. S. J. 2004 Shallow flows: a definition. In *Shallow Flows* (ed. G. H. Jirka & W. S. J. Uijttewaal), pp. 3–11. Taylor & Francis.

JOSHI, P. B. & TAYLOR, R. B. 1983 Circulation induced by tidal jets. *Journal of Waterway Port Coastal and Ocean Engineering – ASCE* **109**, 445–464.

KAHANE, J.-P. & LEMARIÉ-RIEUSSET, P.-G. 1998 *Séries de Fourier et Ondelettes*. Cassini.

KITZHOFER, J., NONN, T. & BRÜCKER, C. 2011 Generation and visualization of volumetric PIV data fields. *Experiments in Fluids* **51**, 1471–1492.

KÖRNER, T. W. 1988 *Fourier Analysis*. Cambridge University Press.

KOTSOVINOS, N. E. 1975 A study of the entrainment and turbulence in a plane buoyant jet. PhD thesis, California Institute of Technology, Pasadena, USA.

KOTSOVINOS, N. E. 1976 A note on the spreading rate and virtual origin of a plane turbulent jet. *Journal of Fluid Mechanics* **77**, 305–311.

KOTSOVINOS, N. E. 1978 A note on the conservation of the axial momentum of a turbulent jet. *Journal of Fluid Mechanics* **87**, 55–63.

KOTSOVINOS, N. E. & ANGELIDIS, P. B. 1991 The momentum flux in turbulent submerged jets. *Journal of Fluid Mechanics* **229**, 453–470.

KOTSOVINOS, N. E. & LIST, E. J. 1977 Plane turbulent buoyant jets. Part 1. Integral properties. *Journal of Fluid Mechanics* **81**, 25–44.

KUANG, J., HSU, C.-T. & QIU, H. 2001 Experiments on vertical turbulent plane jets in water of finite depth. *Journal of Engineering Mechanics – ASCE* **127**, 18–26.

LANDEL, J. R., CAULFIELD, C. P. & WOODS, A. W. 2012a Meandering due to large eddies and the statistically self-similar dynamics of quasi-two-dimensional jets. *Journal of Fluid Mechanics* **692**, 347–368.

LANDEL, J. R., CAULFIELD, C. P. & WOODS, A. W. 2012b, *sub judice* Streamwise dispersion and mixing in quasi-two-dimensional steady turbulent jets. *Journal of Fluid Mechanics.* .

LAW, A. W. K. 2006 Velocity and concentration distributions of round and plane turbulent jets. *Journal of Engineering Mathematics* **56**, 69–78.

LEE, J. M., BAKER, J. J., MURRAY, D., LLERENA, R. & ROLLE, J. G. 1997 Quality analysis of petroleum cokes and coals for export specifications required in use of specialty products and utility fuels. In *Preprints of Symposia, 214th National Meeting, American Chemical Society* **42**, pp. 844–853.

LIST, E. J. 1982 Turbulent jets and plumes. *Annual Review of Fluid Mechanics* **14**, 189–212.

LUO, K., KLEIN, M., FAN, J.-R. & CEN, K.-F. 2006 Effects on particle dispersion by turbulent transition in a jet. *Physics Letters A* **357**, 345–350.

MATHIEU, J. & SCOTT, J. 2000 *An Introduction to Turbulent Flow*. Cambridge University Press.

MONIN, A. S. & YAGLOM, A. M. 1975 *Statistical Fluid Mechanics,* Volume 2. MIT Press.

MORTON, B. R., TAYLOR, G. I. & TURNER, J. S. 1956 Turbulent gravitational convection from maintained and instantaneous sources. *Proceedings of the Royal Society of London.* Series A **234**, 1–23.

NATIONAL INSTITUTE OF STANDARDS AND TECHNOLOGY 2011-08-29 Digital Library of Mathematical Functions. http://dlmf.nist.gov/.

NEVES, M. J. & FERNANDO, H. J. S. 1995 Sedimentation of particles from jets discharged by ocean outfalls: a theoretical and laboratory study. *Water Science and Technology* **32**, 133–139.

OJHA, R., MENON, N. & DURIAN, D. J. 2000 Hysteresis and packing in gas-fluidized beds. *Physical Review E* **62**, 4442–4445.

PARANTHOËN, P., FOUARI, A., DUPONT, A. & LECORDIER, J. C. 1988 Dispersion measurements in turbulent flows (boundary layer and plane jet). *International Journal of Heat and Mass Transfer* **31**, 153–165.

PICANO, F., SARDINA, G., GUALTIERI, P. & CASCIOLA, C. M. 2010 Anomalous memory effects on transport of inertial particles in turbulent jets. *Physics of Fluids* **22** (051705).

POPE, S. B. 1985 Pdf methods for turbulent reactive flows. *Progress in Energy and Combustion Science* **11**, 119–192.

POPE, S. B. 2000 *Turbulent Flows*. Cambridge University Press.

218

PRANDTL, L. 1925 A report on testing for built-up turbulence. *Zeitschrift für Angewandte Mathematik und Mechanik* **5**, 136–139.

RAMAPRIAN, B. R. & CHANDRASEKHARA, M. S. 1985 LDA measurements in plane turbulent jets. *Transactions of the ASME: Journal of Fluids Engineering* **107**, 264–271.

REVUELTA, A., SÁNCHEZ, A. L. & LIÑÁN, A. 2002 Confined axisymmetric laminar jets with large expansion ratios. *Journal of Fluid Mechanics* **456**, 319–352.

RICHARDSON, L. F. 1926 Atmospheric diffusion shown on a distance-neighbour graph. *Proceedings of the Royal Society of London.* Series A **110**, 709–737.

ROBINSON, S. K. 1991 Coherent motions in the turbulent boundary layer. *Annual Review of Fluid Mechanics* **23**, 601–639.

ROWLAND, J. C., STACEY, M. T. & DIETRICH, W. E. 2009 Turbulent characteristics of a shallow wall-bounded plane jet: experimental implications for river mouth hydrodynamics. *Journal of Fluid Mechanics* **627**, 423–449.

SALAZAR, J. P. L. C. & COLLINS, L. R. 2009 Two-particle dispersion in isotropic turbulent flows. *Annual Review of Fluid Mechanics* **41**, 405–432.

SAWFORD, B. 2001 Turbulent relative dispersion. *Annual Review of Fluid Mechanics* **33**, 289–317.

SCHEFER, R. W., KERSTEIN, A. R., NAMAZIAN, M. & KELLY, J. 1994 Role of large-scale structure in a nonreacting turbulent CH4 jet. *Physics of Fluids* **6**, 652–661.

SCHNEIDER, W. 1981 Flow induced by jets and plumes. *Journal of Fluid Mechanics* **108**, 55–65.

SCHNEIDER, W. 1985 Decay of momentum flux in submerged jets. *Journal of Fluid Mechanics* **154**, 91–110.

SHINNEEB, A.-M., BUGG, J. D. & BALACHANDAR, R. 2011 Coherent structures in shallow water jets. *Transactions of the ASME: Journal of Fluids Engineering* **133**, 011203.

SPARKS, R. S. J. 1986 The dimensions and dynamics of volcanic eruption columns. *Bulletin of Volcanology* **48**, 3–15.

STANLEY, S. A., SARKAR, S. & MELLADO, J. P. 2002 A study of the flow-field evolution and mixing in a planar turbulent jet using direct numerical simulation. *Journal of Fluid Mechanics* **450**, 377–407.

STÖHR, M. & KHALILI, A. 2006 Dynamic regimes of buoyancy-affected two-phase flow in unconsolidated porous media. *Physical Review E* **73**, 036301.

SVEEN, J. K. & DALZIEL, S. B. 2005 A dynamic masking technique for combined measurements of PIV and synthetic schlieren applied to internal gravity waves. *Measurement Science and Technology* **16**, 1954–1960.

TAYLOR, G. I. 1953 Dispersion of soluble matter in solvent flowing slowly through a tube. *Proceedings of the Royal Society of London.* Series A **219**, 186–203.

TAYLOR, G. I. 1958 Flow induced by jets. *Journal of the Aero/Space Sciences* **25**, 464–465.

THOMAS, F. O. & BREHOB, E. G. 1986 An investigation of large-scale structure in the similarity region of a two-dimensional turbulent jet. *Physics of Fluids* **29**, 1788–1795.

TOSCHI, F. & BODENSCHATZ, E. 2009 Lagrangian properties of particles in turbulence. *Annual Review of Fluid Mechanics* **41**, 375–404.

TURNER, J. S. 1986 Turbulent entrainment: the development of the entrainment assumption, and its application to geophysical flows. *Journal of Fluid Mechanics.* **173**, 431–471.

UBEROI, M. S. & SINGH, P. I. 1975 Turbulent mixing in a two-dimensional jet. *Physics of Fluids* **18**, 764–769.

VEITCH, G. & WOODS, A. W. 2000 Particle recycling and oscillations of volcanic eruption columns. *Journal of Geophysical Research* **105**, 2829–2842.

WALTERS, A. L., PHILLIPS, J. C., BROWN, R. J., FIELD, M., GERNON, T., STRIPP, G. & SPARKS, R. S. J. 2006 The role of fluidisation in the

formation of volcaniclastic kimberlite: grain size observations and experimental investigation. *Journal of Volcanology and Geothermal Research* **155**, 119–137.

WANG, H. W. & LAW, A. W.-K. 2002 Second-order integral model for a round turbulent buoyant jet. *Journal of Fluid Mechanics* **459**, 397–428.

WOODS, A. W. & CAULFIELD, C. P. 1992 A laboratory study of explosive volcanic eruptions. *Journal of Geophysical Research* **97**, 6699–6712.

XU, H. & BODENSCHATZ, E. 2008 Motion of inertial particles with size larger than Kolmogorov scale in turbulent flows. *Physica D* **237**, 2095–2100.

YANG, Y., CROWE, C. T., CHUNG, J. N. & TROUTT, T. R. 2000 Experiments on particle dispersion in a plane wake. *International Journal of Multiphase Flow* **26**, 1583–1607.

YANNOPOULOS, P. & NOUTSOPOULOS, G. 1990 The plane vertical turbulent buoyant jet. *Journal of Hydraulic Research* **28**, 565–580.

YANNOPOULOS, P. C. 2006 An improved integral model for plane and round turbulent buoyant jets. *Journal of Fluid Mechanics* **547**, 267–296.

YEUNG, P. K. 2002 Lagrangian investigations of turbulence. *Annual Review of Fluid Mechanics* **34**, 115–142.

ZAUNER, E. 1985 Visualization of the viscous flow induced by a round jet. *Journal of Fluid Mechanics* **154**, 111–119.

ZOUESHTIAGH, F. & MERLEN, A. 2007 Effect of a vertically flowing water jet underneath a granular bed. *Physical Review E* **75**, 056313–1.